

Human Cochlear Nerve Model: Data Collection and Simulation

DISSERTATION

submitted in partial fulfillment of the requirements for the degree of

Doktor/in der technischen Wissenschaften

by

Thomas Potrusil

Registration Number 0842434

to the Faculty of Informatics
at the Vienna University of Technology

Advisor: Ao.Univ.Prof. Dipl.Ing. DDDr. Frank Rattay

The dissertation has been reviewed by:

(Prof. DDDr. Frank Rattay)

(Prof. Dr. Anneliese Schrott-Fischer)

Vienna, October 08, 2013

(Thomas Potrusil)

Erklärung zur Verfassung der Arbeit

Thomas Potrusil
Schlossergasse 13
6060 Hall

Hiermit erkläre ich, dass ich diese Arbeit selbständig verfasst habe, dass ich die verwendeten Quellen und Hilfsmittel vollständig angegeben habe und dass ich die Stellen der Arbeit - einschließlich Tabellen, Karten und Abbildungen -, die anderen Werken oder dem Internet im Wortlaut oder dem Sinn nach entnommen sind, auf jeden Fall unter Angabe der Quelle als Entlehnung kenntlich gemacht habe.

(Ort, Datum)

(Unterschrift)

Acknowledgments

First and foremost, I want to thank Prof. Frank Rattay who has been a great advisor and motivating factor all the years. Your ideas and never-ending support had a major influence on this thesis. He spent a lot of time in front of his email client (several hundred mails) answering my questions and guiding this work in the right direction. Frank, it was a great honor to work with you!

I would also like to thank Prof. Anneliese Schrott-Fischer and Dr. Rudolph Glueckert for giving me the chance to do this PhD-thesis and to conduct the methodical part in their Laboratory for Inner Ear Biology of the University Clinic of Ear, Nose and Throat Medicine, Innsbruck Medical University. Thanks for all the valuable techniques I learned during this time and that you allowed and always supported me to work on new ideas.

Since a PhD-thesis is never the result of a single's person effort I would also like to thank all my colleagues, especially Dr. Cornelia Wenger for introducing me to the field of computer simulations. Thank you so much for your open ears and immediate help with every idea. My very special thanks go to Christian Pritz. I'm overwhelmed by your unbelievable knowledge! You helped me seeing problems with the necessary distance and humor. Thank you my friend for this awesome time! Additionally, thanks to Mario Bitsche, Dr. Soumen Roy, Dr. Agung Dewanto, Letizia Marvaldi for all the discussions and fun during work. Thanks to Dr. Volker Kuhn, the man on the microCT in Innsbruck, who always supported realizing my ideas.

My deepest thank appertains to my beloved wife Michaela for her priceless support and precious encouragement for the last amazing decade! And of course, to my kids Maja, Elias and Greta...thanks a lot for countless fun times and keeping me balanced. This thesis is dedicated to you, my dearly beloved family!

Thomas Potrusil

Abstract

Objectives. Human auditory neurons show micro-anatomical peculiarities which differ considerably from other mammalian species. Their unmyelinated cell bodies as well as their appearance in clusters featuring direct cell-to-cell contact, compose unique morphological characteristics rising questions concerning the spiking pattern of these human sensory neurons. Besides, the anatomical composition of the cochlea representing an inhomogeneous structure as well as the three dimensional (3D) pathways of the action potential (AP) transmitting neural parts mainly affect the excitability of neurons to micro-stimulation induced by electrodes of cochlear implants (CI). Histological methods combined with imaging and visualization techniques were used to gain morphometrical features of human cochlear neurons which were subsequently implemented to a computational model of an auditory neuron to test its excitability and spiking pattern to intra- as well as extracellular stimulation.

Methods. The anatomical findings presented in this thesis are based on several human cochleae and compose the fundament of the subsequent computer simulations which provide an appropriate method for single cell analysis since vital human auditory neurons are not experimentally accessible. Immunohistochemical staining and confocal laser scanning microscopy enabled to acquire 3D image stacks of cochlear neurons where geometrical parameters were quantified systematically along the cochlear spiral. However, this method requires sectioning of the specimen which causes loss of information of the whole analyzed structure making accurate computational reconstruction virtually impossible. To overcome this limitation, one human inner ear was digitalized using ultra-high resolution micro-CT imaging. Visualization and segmentation of data enabled to reconstruct the 3D pathways of tonotopical aligned cochlear neurons. CT data was subsequently used to develop an anatomical exact finite element model (FEM) of the human cochlea which was deployed to calculate the resulting distribution of electrical potentials induced by electrodes along the reconstructed auditory nerve fibers. Implementation of finite element data to a compartment model of a human cochlear neuron enabled to analyze its excitability and temporal behavior to different stimulation strategies.

Results. Hierarchical cluster analysis of acquired volumetric data of unmyelinated human auditory cell somata indicates the existence of four distinct populations of auditory neurons within the human hearing organ. The volume varies enormously resulting in delay differences of the generated AP while passing the somatic region which consequently influences the temporal parameters of signal transduction to the central nervous system. Moreover, these temporal parameters as well as the conduction velocity of APs are additionally depending on peripheral- and central process diameters and process length. Due to the narrowing anatomy of this coiled organ, apical neurons show highly spiral 3D pathways and feature significantly longer peripheral processes compared to middle- or basal turn neurons. As a consequence, finite element- and compartment model analysis suggests varying excitation profiles for nerve fibers originating from different frequency regions and the breach of the tonotopical principle by active electrodes of CIs located in the middle turn region.

Conclusion. The combination of biological data collection methods, visualization of their results, mathematical modeling and computer simulation becomes increasingly important in the field of neuroscience or when refining bionic devices. Taking the human anatomical occurrences for CIs into account will tremendously improve the development of new electrode array configurations and stimulation strategies to restore the hearing sense more accurate. However, the results presented in this thesis provide new insights into the morphometrical and anatomical structure of the human cochlea and demonstrate the behavior of cochlear neurons in an anatomically precise computational environment.

Kurzfassung

Motivation. Neurone des menschlichen Hörsystems weisen mikroanatomische Besonderheiten auf, welche sie von denen anderer Säugetierarten signifikant unterscheiden. Ihre unmyelinisierten Zellsomata gemeinsam mit ihrem gelegentlichen Auftreten als Cluster mit direktem Zellmembrankontakt führen zu Vermutungen, dass diese die neuronalen Muster bei der Signalweiterleitung erheblich beeinflussen. Des Weiteren wird die Anregbarkeit der Neurone bei extrazellulärer Stimulation mittels Cochlea-Implantate durch den inhomogenen anatomischen Aufbau der Cochlea als auch durch den 3D Verlauf der Neurone selbst, stark beeinflusst. Histologische Methoden, kombiniert mit bildgebenden Verfahren und Visualisierungstechniken wurden in der vorliegenden Arbeit genutzt, um morphometrische Eigenschaften des menschlichen Hörnervs zu eruieren. Diese geometrischen Parameter wurden anschließend in ein Computermodell eines auditiven Neurons implementiert um seine Anregbarkeit sowie sein Feuerungsverhalten bei intra- als auch extrazellulärer Stimulation zu analysieren.

Methodik. Die präsentierten anatomischen Ergebnisse basieren auf mehreren menschlichen Hörschnecken und bilden das Fundament für die anschließend durchgeführten Simulationen. Da gesunde und lebende menschliche Hörneurone experimentell nicht zugänglich sind, bilden Computersimulationen eine adäquate Methode um mehr über ihr Verhalten zu erfahren. Immunhistochemische Färbungen in Kombination mit Konfokalmikroskopie ermöglichen die Akquirierung von 3D-Daten von Hörneuronen, um verschiedenste geometrische Parameter systematisch entlang der Cochlea zu quantifizieren. Diese Methode hat jedoch den großen Nachteil, dass die Probe in dünne Schnitte aufgeteilt werden muss, was einerseits zu Informationsverlust, andererseits eine computergestützte Rekonstruktion nahezu unmöglich gestaltet. Deshalb wurde eine menschliche Cochlea in einem hochauflösendem mikroCT gescannt. Datensegmentierung und Visualisierung ermöglichten die 3D-Rekonstruktion von Nervenverläufen. Der CT Datensatz wurde weiters verwendet, um ein anatomisch präzises Finite-Elemente-Modell der menschlichen Cochlea zu entwickeln. Dieses wurde genutzt um die von aktiven Elektroden induzierten elektrischen Potentiale entlang der rekonstruierten Faserverläufe zu bestimmen. Die resultierenden Daten wurden anschließend in das biophysikalische Modell implementiert, um die Anregbarkeit und das zeitliche Verhalten eines Neurons bei verschiedenen Stimulationsstrategien zu testen.

Resultate

Hierarchische Clusteranalyse an volumetrischen Daten von unmyelinisierten Hörneuronen lieferte Hinweise auf die Existenz von vier verschiedenen Populationen beim Menschen. Die rekonstruierten Volumina variieren erheblich was zu unterschiedlichen Laufzeiten von Aktionspotentialen über das Zellsoma führt. Dies impliziert wiederum unterschiedliche zeitliche Parameter bei der Signalweiterleitung ins zentrale Nervensystem. Die zeitlichen Parameter als auch die Geschwindigkeit der generierten elektrischen Signale sind vor allem vom Durchmesser des peripheren- und zentralen Axons und von der Neuronlänge abhängig. Aufgrund der sich nach oben hin verengenden Anatomie der Hörschnecke, zeigen apikale Neurone einen sehr spiraligen Verlauf und haben signifikant längere periphere Axone verglichen mit Neuronen aus dem mittleren bzw. basalen Bereich. Aus diesem Grund weisen die durchgeführten Finite-Elemente- und Kompartimentmodell Analysen auf unterschiedliche Anregungsprofile bei Neuronen aus verschiedenen Frequenzbereichen hin. Außerdem wurde die Verletzung des tonotopischen Prinzips von aktiven Elektroden, welche sich im mittleren Bereich der Hörschnecke befinden, festgestellt.

Schlussfolgerung

Die Kombination von biologischen Datengewinnungsmethoden, Visualisierung der Resultate, mathematischer Modellierung und Computersimulationen gewinnt in den Neurowissenschaften und der bionischen Produktentwicklung immer mehr an Bedeutung. Die Berücksichtigung der anatomischen Beschaffenheit der menschlichen Cochlea kann zur Verbesserung bzw. Entwicklung neuer Elektroden(anordnung) und Stimulationsstrategien genutzt werden, um den künstlich erzeugten Höreindruck des Menschen weiter zu verbessern. Die in dieser Arbeit präsentierten und diskutierten Ergebnisse geben neue Einblicke in die morphometrische und anatomische Struktur der Cochlea und zeigen das Verhalten von Hörneuronen in einer anatomisch präzisen computergestützten Umgebung.

Contents

Acknowledgments	iii
Abstract	V
Kurzfassung	Vii
1 Introduction	1
1.1 Motivation	1
1.2 Problem Definition	4
1.3 Contributions.....	5
1.4 Organization of the Thesis.....	5
2 Anatomical and Physiological Basics of the Human Cochlea and description of the Compartment- and Finite Element Model.....	8
2.1 Anatomy of the Cochlea.....	8
2.2 Physiology of Hearing.....	13
2.2.1 Outer Ear	13
2.2.2 Middle Ear	13
2.2.3 Inner Ear	14
2.3 Hearing loss	15
2.4 Cochlea Implants	16
2.5 Compartment Model of a Cochlear Neuron	18
2.6 Finite Element Model of the Human Cochlea	22
3 Data Collection and Preparation.....	26
3.1 Fixation and Sectioning of Specimens.....	26
3.2 Staining with Biomarker	27
3.3 Acquisition of Data	28
3.4 Data Processing	31
3.5 Data Visualization.....	31
3.6 Measurement of Distances within Medical Imaging Data and Extraction of xyz-Coordinates.....	32
3.7 Imaging and Data Processing Hardware	33
3.8 Statistics	34
4 Morphometric Classification and Spatial Organization of Spiral Ganglion Neurons in the Human Cochlea: Consequences for Single Fiber Response to Electrical Stimulation	36
4.1 Abstract	36
4.2 Introduction	37
4.3 Materials and Methods.....	38
4.3.1 Specimens	38

4.3.2	Immunohistochemistry	38
4.3.3	Acquisition of confocal data	38
4.3.4	Image processing	39
4.3.5	Statistical analysis	39
4.4	Computational model	40
4.5	Results	42
4.5.1	Descriptive Statistics	42
4.5.2	Perikarya	42
4.5.3	Nuclei	45
4.6	Hierarchical Clustering	45
4.6.1	Specimen 1	45
4.6.2	Specimen 2	47
4.6.3	Individual differences	49
4.6.4	Pooled Data of Both Specimens	49
4.7	Computer Simulation	51
4.7.1	Intracellular Stimulation	51
4.7.2	Extracellular Stimulation with Electrodes E1 and E2	51
4.7.3	Extracellular Stimulation with Electrodes E3 and E4	53
4.8	Discussion	58
5	Impact of Morphometry, Myelination and Synaptic Current Strength on Spike Conduction in Human and Cat Spiral Ganglion Neurons	62
5.1	Abstract	62
5.2	Introduction	63
5.3	Materials and Methods	64
5.3.1	Specimens	64
5.3.2	Immunohistochemistry	65
5.3.3	Electron microscopy	65
5.3.4	Confocal imaging and processing	66
5.3.5	Measurement of nerve length	66
5.3.6	Statistical analysis	66
5.3.7	Computer simulation	67
5.4	Results	69
5.4.1	Myelination and soma sizes of SGNs in cat and man	69
5.4.2	SGN lengths in human and cat	74
5.4.3	Type I process diameters of SGN in human and cat	75
5.4.4	Computer Simulation	76

5.5	Discussion.....	85
5.5.1	Spike duration	85
5.5.2	Simulated conduction times correlate with ABR	86
5.5.3	How myelin accelerates signaling	87
5.5.4	Synaptic hair cell currents	88
5.5.5	Significance for natural hearing and cochlear implants.....	88
6	Clustering of Human Spiral Ganglion Neurons: An Morphometrical Analysis and Computational Model Study of Ephaptic Coupling Effects to Intra- and Extracellular Stimulation	90
6.1	Abstract	90
6.2	Introduction	91
6.3	Material and Methods.....	92
6.3.1	Specimens	92
6.3.2	Immunohistochemistry	92
6.3.3	Confocal Imaging and Processing.....	93
6.3.4	Statistical Analysis	93
6.3.5	Computational Model	93
6.4	Results	96
6.4.1	Clusters along the Cochlear Spiral.....	96
6.4.2	Cluster Arrangements	97
6.4.3	Satellite Glial Cells	99
6.4.4	Computer Simulation	101
6.5	Discussion.....	113
7	Finite Element Analysis and Three-Dimensional Reconstruction of Tonotopically Aligned Human Auditory Fiber Pathways:.....	117
7.1	Abstract	117
7.2	Introduction	118
7.3	Methods	119
7.3.1	Human Cochleae Preparation and Fixation.....	119
7.3.2	Micro-CT Imaging	120
7.3.3	Data Processing	120
7.3.4	Segmentation and Visualization.....	121
7.3.5	Data Merging and Nerve Fiber Extrapolation	123
7.3.6	xyz-Coordinates Extraction and Length Measurements of Traced Nerve Fibers.....	123
7.3.7	Length Measurements of Cochleae and Neuron Frequency	124
7.3.8	Electrode Positions based on routinely implanted CIs.....	124
7.3.9	Finite Element Model	125
7.3.10	COMSOL	128

7.3.11	Compartment Model.....	129
7.3.12	Statistical Analysis	130
7.4	Results	130
7.4.1	Cochleae length, width and height – 3D merging and comparison of different individuals.....	130
7.4.2	Cochlea Details and Fiber Bundle Tracing.....	131
7.4.3	Nerve Bundle Lengths	132
7.4.4	Spiral Pathways of Cochlear Neurons	135
7.4.5	Cochlear Implant Electrodes	136
7.4.6	Distribution of the electrical potential based on FE-Analysis	138
7.4.7	Finite Element Solution vs. Homogenous Medium Solution	141
7.4.8	Compartment Model Analysis.....	143
7.4.9	Comparison with Degenerated Neurons.....	146
7.4.10	Excitation pattern of normal neuron population.....	149
7.4.11	Analysis of the normal apical turn.....	153
7.5	Discussion.....	155
	Bibliography	159
	Curriculum Vitae.....	175

List of Abbreviations

ANO	monophasic anodic pulse
ANOVA	one-way analysis of variance
AP	action potential
BIA	biphasic pulse with anodic phase first
BIC	biphasic pulse with cathodic phase first
CAT	monophasic cathodic pulse
CI	cochlear implant
C_m	membrane capacitance
CSLM	confocal laser-scanning microscope
DAPI	4',6-diamidino-2-phenylindole, dihydrochloride
EDTA	ethylenediaminetetraacetic acid
ET	end time
EV	electrode voltage
FEM	finite element model
G_m	membrane conductance
g_E	ephaptic conductance
HH	Hodgkin-Huxley model
IHC	inner hair cell
IHC	immunohistochemistry
IS	Initiation site
LSD	Fisher's least significant difference
MBP	myelin basic protein
NA	numerical aperture
NBF	neutral buffered formaline
NDS	normal donkey serum
OC	organ of Corti
OHC	outer hair cell
OsO_4	osmium tetroxide
PBS	Phosphate buffered saline
PSF	point spread function
PT	peak time
R	intracellular resistance
RC	Rosenthal's canal
RM	Reissner's membrane
SC	Schwann cell
SG	spiral ganglion
SGC	satellite glial cell
SGN	spiral ganglion neuron
SM	scala media
ST	scala tympani
SV	scala vestibuli
TEM	transmission electron microscopy
V_e	extracellular potential
V_i	intracellular potential
V_m	membrane voltage

CHAPTER 1

Introduction

1.1 Motivation

CIs are routinely implanted around the globe and tremendously increase the quality of life of people suffering from deafness or severe sensorineural hearing loss. In 2010, approximately 220 000 people worldwide were treated with CIs (NIDCD, 2011) which offer the possibility to implantees to understand speech, listen to music and to participate in everyday' social life.

The idea to stimulate the human ear with electrical energy is not new. In fact, the extracellular stimulation of the auditory nerve had its beginning in the late 18th century by the Italian scientist Alessandro Volta (1745 - 1827) who invented the voltaic pile – the first electrical battery. He was the first who demonstrated that electric stimulation can directly evoke auditory sensations in humans by connecting a battery of about 50V to two metal rods that were inserted into his ears (Zeng, 2004). After closing the electrical circuit, he observed more than 200 years ago:

'At the moment when the circuit was completed, I received a shock in the head, and some moments after I began to hear a sound, or rather noise in the ears, which I cannot well define: it was a kind of crackling with shocks, as if some paste or tenacious matter had been boiling...The disagreeable sensation, which I believe might be dangerous because of the shock in the brain, prevented me from repeating this experiment.'

It took until the early 1960's where the very first CI was developed. This device featured only one channel which provided input for a five-wire electrode where all contacts applied the same signal to the patients' inner ear. In the following decades, these first CIs were improved continuously and constitute the corner stone for modern multichannel hearing aids (Mudry & Mills, 2013) which are used nowadays to restore human hearing sense. The first patients, which cochlea was electrically stimulated with these first bionic implants, were not able to understand speech or enjoy music. However, it was shown that stimulating different areas within the inner ear results in acoustical perception of different frequencies (Simmons, 1966). This discovery was the first hint that different regions within the cochlea are transducing distinct frequencies acting somehow as a frequency analyzer.

At the same time, biologists and physicians started to analyze their tissue using transmission electron microscopy (TEM) in combination with immunohistochemical methods to get new insights of the ultrastructural composition and to describe morphological features of their fixed specimens within the sub-micrometer range. This trend also slopped to ear biologists who first described the micro-anatomical characteristics of spiral ganglion neurons (SGNs) in man (Kellerhals et al., 1967; Nakai, 1970; Bernard & Spoendlin, 1973) and other mammals (Spoendlin, 1969; Trevisi et al., 1972). It soon became apparent that there are differences in the morphological composition of the signal transmitting auditory neural elements between mammals and humans. The size of the bipolar cell bodies of human cochlear neurons was reported to be larger in man (Kiang et al., 1984; Spoendlin & Schrott, 1989; Nadol et al., 1990) compared to other species (Liberman & Oliver, 1984; Spoendlin, 1984). But there were two more distinct micro-anatomical characteristics reported that have not been identified in other mammalian cochleae so far:

In mammals, the whole cochlear neuron is fairly enwrapped by multiple layers of isolating myelin with the purpose to ensure quick and safe AP propagation. The somatic region (represented by the pre- and postsomatic areas as well as the bipolar cell soma) of the vast majority of human auditory neurons totally lack this isolating dielectric material (Ota & Kimura, 1980; Arnold, 1987; Spoendlin & Schrott, 1989) and are typically surrounded by one or more satellite glial cells (SGC) (Liu et al., 2012). The missing myelin at this distinct region of human cochlear neurons is of prime interest to CI designers: In all other species with the exception of man, the membrane capacitance (C) of the whole neuron is well reduced by many circumjacent myelin layers as C is inversely proportional to the number of covering sheets of cell membranes (Rattay, 1990; Rattay, 1995; Rattay et al., 2001a). This anatomical composition of neurons guarantees fast, safe and energy-efficient electrical signal transmission known as saltatory conduction (Huxley & Stämpfli, 1949). For the human case, problems in successful signal conduction can arise when the small inneraxonal current of the thin peripheral process has to load the large capacitance of an unshielded cell soma (Hossain et al., 2005) which represents the main barrier and acts as an energy dissipater for an AP (chapter 4 and chapter 5) on its way from the sensory epithelium to the auditory cortex (Rattay et al., 2001a).

The described absence of insulating myelin in the somatic region of human auditory neurons forms simultaneously the basis for the second specific characteristic among afferent cochlear neurons. Kellerhals et al. (1967) was the first group who reported in an ultrastructural study that human SGNs can form structural groups or cell clusters of two or more auditory neurons within the spiral ganglion. A more detailed analysis of these unit-like structures (Tylstedt et al., 1997) using a TEM suggest that within the cochlea region featuring maximal innervations density, the cell bodies of neurons were frequently ensheathed by the same SGC so that they are gathered to clusters containing 2 - 4 neurons. These clusters were found to possess signs of physical interaction with their membranes positioned in juxtaposition to each other. In an additional study, this group investigated distinct membrane specializations of these little gaps (Tylstedt & Rask-Andersen, 2001) between closely spaced neurons. They speculate if this unique appearance of SGNs may compose interactive electrotonic or electronic transmission pathways that may increase plasticity and signal acuity related to the coding of speech. Human SGNs have been additionally analyzed using an immunohistochemical approach to provide evidence of certain gap junction proteins to encourage the possibility of the existence of gap junction based electrical interaction. Liu et al. (2009a) identified several connexin proteins within different regions of the human cochlea. Based on their results, the group suggests that some neurons may encode their incoming sound information using nerve signal synchronization with closely adjacent neurons. This would be quite efficient due to much faster responses of electrical- compared to chemical synapses and was also reported to happen within the central nervous system (Bennett & Zukin, 2004). Moreover, this much quicker information exchange may play a crucial role in encoding the quite complex and unique human speech. Connexins were also identified to be expressed by SGCs located in the spiral ganglion (Liu et al.,

2009a) forming the distinct honeycomb alignment (see chapter 4 and chapter 5) that houses the auditory neurons (Liu et al., 2012). The group around Liu additionally discusses the possibility that this unique micro-anatomical setting facilitate the possibility that electric currents from a cell soma may spread over the surrounding SGCs to activate a small population of adjoined neurons simultaneously resulting in synchronization of transmitted encoded signals (Liu et al., 2012).

However, both described peculiarities are supposed to influence crucially the resulting neural coding pattern in human auditory neurons. Since healthy and vital human SGNs are not accessible for experimental investigations, our understanding of physiological auditory coding strategies is essentially based on experiments conducted on various animals. The principle of neural coding of sound and the underlying excitation pattern of the cochlear neuron is mainly based on single cell recordings on cats (Kiang, 1965; Sachs & Abbas, 1974; Liberman, 1982; van den Honert & Stypulkowski, 1984; Ryugo et al., 1998). However, the decisive reported morphological differences of human and cat SGNs, which mainly influences the propagation of the generated APs, ensure that the drawn conclusions of the conducted measurements are not applicable to the unique human case.

To overcome such limitations, mathematical modeling and computer simulations has become an essential part to quantify the effect of varying morphological features or when developing biomedical devices. Many different computational models of human cochlear neurons were developed in the last two decades based on various ion channel kinetic models (Hodgkin & Huxley, 1952; Frankenhaeuser & Huxley, 1964; Sweeney et al., 1987; Mainen & Sejnowski, 1996; Engel & Jonas, 2005; Meeks & Mennerick, 2007; Hu et al., 2009; Fohlmeister, 2009). Besides these voltage-gated channel characterization which describe the behavior of the active parts of auditory neurons, some cochlear models have implemented (for the human case!) a fully enwrapped and electrically shielded somatic region (Frijns et al., 1994) or some do not include the whole soma (Mino et al., 2004). To study the answer of an intra- as well as extracellular stimulated human cochlear neuron, an adapted model was used that was introduced by Rattay et al. (2001a). This is the only model that considers both, various geometrical parameters for the signal transmitting peripheral- and central process and has additionally incorporated the unique unmyelinated somatic region.

Above mentioned human auditory neuron models assume that the whole neuronal structure as well as the stimulating electrode is located in a homogeneous medium with constant resistivity. This implicates that the resulting voltage profile along the modeled neuron is calculated under the same boundary conditions. Due to the quite complex coiled structure of the cochlea which additionally contains several fluid-filled and bony compartments each with varying conductivity, the resulting excitation- and temporal patterns of the modeled structures are of limited suitability to draw final conclusions about the processes within the cochlea during microstimulation. To take the geometry with varying resistivities of the tissues into account and to analyze the neuronal answer to extracellular stimulation, a two-step procedure is required (Rattay et al., 2001b): First, the extracellular potentials along a given neural pathway are determined using e.g. a finite element model to describe the distribution of the electrical potential generated by an active electrode. In a second step, these data is provided as input for a biophysical auditory neuron model (Rattay et al., 2001a) that enables to predict the excitation process induced by varying stimuli pulses along neurons from different cochlear regions. This strategy allows on the one hand analyzing the spreading of the electric potential based on the influence of cochlear anatomy. Otherwise, the electrical circuit model facilitates to analyze and quantify the response and temporal pattern of a single neuron to microstimulation.

The goal of the present thesis is to provide crucial data of the micro-anatomical composition of human auditory neurons which are subsequently incorporated to a computational model of a cochlear neuron. Moreover, a human hearing organ was digitalized using an ultra-high resolution microCT to (i) reconstruct three dimensional pathways of cochlear nerve fiber bundles along the whole coiled structure and (ii) to develop an anatomical precise finite element model of the scanned cochlea. The multidisciplinary approach of combining immunohistochemical methods, various imaging techniques, data visualization, mathematical modeling and computer simulation affords to improve morphometrical and anatomical knowledge of the cochlea and to study the resulting consequences to microstimulation.

Considering the anatomical nature of the complex human cochlea with its auditory neurons that represent different frequency spectra, will contribute to an improved understanding of the signal conduction process. Hence, this knowledge can be used to develop and optimize active electrodes, adjust their position along the intracochlearly located array and to improve stimulation strategies to mimic natural hearing.

1.2 Problem Definition

Present knowledge about the neural coding principles of the auditory nerve is mainly based on single cell recordings conducted on feline cochleae. Due to fundamental differences in morphological composition of auditory neurons from man and other mammals, these measurements and the deduced conclusions concerning neural coding are not representative to humans.

However, complex processes that guarantee speech comprehension in noise, focusing on sounds of interest, attenuation effects or the temporal fine structure of neural auditory coding are not satisfying clear. Numerous questions concerning the physiological processes of human hearing are still open leading to non-proven hypotheses. To shed light on how an acoustic signal is encoded by human auditory neurons, knowledge concerning the anatomical and morphometrical composition of the cochlea and the signal transmitting structures is absolutely essential.

The immunohistochemical studies carried out for this thesis investigated crucial geometrical and spatial parameters of auditory neurons which were implemented to a biophysical model to derive behavioral patterns. The identified parameters include the systematic evaluation along the whole cochlea spiral of the

- volume of unmyelinated human cochlear neurons
- diameter of the peripheral- and central process of auditory neurons from man and cat
- diameter of type II cochlear neurons in man and cat
- diameter of type I neurons in cat
- length of the auditory vestibular nerve from the cochlea to the cochlear nuclei which is located in the brainstem of man and cat
- length of the thinner peripheral process based on three dimensional neuron reconstruction in man

The major drawback of commonly used biophysical models of auditory neurons is their limitation of using two dimensional data sets. Moreover, the investigated model neurons as well as its stimulating electrode are both assumed to be located in a homogeneous medium with constant electrical conductivity. However, this simplified view does not include the complex structure of the human hearing organ influencing the distribution of the electrical potential induced by active electrodes.

Furthermore, the supposed varying spatial pathways of tonotopical aligned SGNs are completely neglected.

To overcome these limitations and to provide data of the 3D spatial arrangement of human auditory neurons, one cochlea was fully scanned using a microCT to

- manually trace multiple cochlear nerve fiber bundles along the cochlea spiral; all originating from different frequency regions
- spatial determination of the somatic region and length measurement of the peripheral process
- segmentation of most important compartments of the cochlea
- development of a Finite Element Model to analyze the induced distribution of the electrical potential by a firing electrode

1.3 Contributions

All presented morphological and morphometrical data which was used for subsequently conducted computer simulations (chapter 4, chapter 5 and chapter 6) were conducted by Thomas Potrusil (TP) at the Laboratory for Inner Ear Biology which is embedded in the University Clinic of Ear, Nose and Throat Medicine, Innsbruck Medical University. This included specimen preparation, immunohistochemical stainings, imaging and data analysis as described. TP analyzed the microCT image stack and developed the FEM which is presented in chapter 7.

The computer simulations presented in chapter 4 were carried out by Dr. Cornelia Wenger (CW), Institute of Analysis and Scientific Computing, Vienna University of Technology. The simulations described in chapter 5 were conducted in equal parts Prof Rattay, TP and CW. The effects of ephaptic coupling of human auditory neurons which are demonstrated in chapter 6 were performed by TP and CW. Computer simulations presented in chapter 7 were conducted by TP.

Note that parts of this thesis are published in:

- Potrusil T, Wenger C, Glueckert R, Schrott-Fischer A, Rattay F. Morphometric classification and spatial organization of spiral ganglion neurons in the human cochlea: consequences for single fiber response to electrical stimulation. *Neuroscience*. 2012 Jul 12;214:120-35.
- Rattay F, Potrusil T, Wenger C, Wise AK, Glueckert R, Schrott-Fischer A. Impact of Morphometry, Myelination and Synaptic Current Strength on Spike Conduction in Human and Cat Spiral Ganglion Neurons. *PLOS ONE*. Accepted on September 23rd, 2013

1.4 Organization of the Thesis

The following **Chapter 2** provides an anatomical overview of the human cochlea (section 2.1) and outlines the physiological process of hearing (section 2.2). This first part offers the reader a summary of the complex organization of the hearing organ, the neural parts that are involved in the hearing process and about the intracochlear activities triggered by incoming airborne sound. Furthermore, some facts concerning hearing loss in humans (section 2.3) and the principle functionality of CIs (section 2.4) are outlined. Information about the general biophysical model (section 2.5) of an auditory neuron is provided by the underlying physical laws of electrical circuits and the derived differential equation. These equations enable to calculate the time course of the transmembrane potential for every functional subunit to study the resulting excitation pattern in respect of time. At

last, this chapter provides information about how to solve the volume conductor problem to calculate the arising distribution of the electrical potential generated by a firing electrode and the composition of the developed FEM (section 2.6).

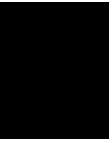
Chapter 3 describes the applied histological (sections 3.1 and 3.2), imaging (section 3.3) and data processing methods (sections 3.4, 3.5, 3.6, 3.7 and 3.8) which were necessary to extract data concerning the microanatomical structure of the human cochlea as well as geometrical and spatial parameters of the AP transmitting SGNs. Furthermore, the information within this chapter depicts a possible workflow to gain quantifiable information of quite complex, small human specimens for further analysis and outlines the delicate handling of well-preserved human tissue.

The first part of **Chapter 4** presents the acquired volumetric data of the unmyelinated cell soma (section 4.5) of human auditory neurons and their corresponding nuclei. The 3D reconstructed perikarya and their nuclei were evaluated systematically along the cochlea spiral and a classification of four distinct groups was introduced. Based on these morphometric data, the subsequent conducted computer simulations (section 4.7) discuss the difference in threshold and properties of generated APs of a single model neuron. The investigated neuron was stimulated by active spherical electrodes located in extracellular space by mono- and biphasic pulses.

Chapter 5 summarizes new systematic collected morphometric data including the diameters of the peripheral- and central process, commonness of myelination and morphology of SGNs along the cochlea spiral of human and cats (sections 5.4.1, 5.4.2 and 5.4.3). These data were implemented to our biophysical model which was subsequently used to quantify the differences of temporal parameters in the electrically stimulated human cochlea compared to the cat cochlea (section 5.4.4). Moreover, the evaluated geometrical parameters enabled to verify the simulated spike conduction times with normal interwave latencies from physiological auditory brainstem response recordings of both species.

The second peculiarity which also concerns the somatic region of human cochlear neurons is presented in **Chapter 6**. Immunohistochemical and imaging techniques enabled to study systematically the commonness of cluster-like arrangement of SGNs based on three individual and independent human cochleae. The result section in this chapter describes the frequency of occurrence of bi- and tricellular neuron arrangements at different frequency regions along the whole spiral organ (section 6.4.1). 3D image stacks acquired with a confocal microscopy facilitate to reconstruct four representative clusters and to quantify the area of direct cell-to-cell contact (section 6.4.2). The following conducted computer simulations explore the ephaptic coupling effects which were studied with altered morphological and geometrical parameters as well as for the intra- and extracellular stimulated case (section 6.4.4).

The first part of **Chapter 7** deals with the digitalization of one human cochlea using ultra-high resolution microCT. Data was subsequently used to reconstruct the three dimensional pathways of 30 nerve fiber bundles that originate from different frequency regions (sections 7.4.3 and 7.4.4). The microCT scan was further used to extract five compartments by manual segmentation. This information was deployed to develop an anatomical precise FEM of this human specimen. The FEM enabled to calculate the distribution of the resulting electrical potential induced by an active electrode along the traced cochlear neurons (section 7.4.6). In a last step, this information about the extracellular potential was implemented to the compartment model to study the temporal and excitation pattern of the traced neurons. The stimuli were applied by electrodes mimicking two routinely implanted CIs with mono- and biphasic stimuli at different positions (sections 7.4.8, 7.4.9, 7.4.10 and 7.4.11).



Anatomical and Physiological Basics of the Human Cochlea and description of the Compartment- and Finite Element Model

This chapter describes the anatomical features and morphological peculiarities of the human cochlea (section 2.1) which were systematically collected and evaluated as a first part of this thesis. These quantified characteristics of human cochlear neurons subsequently provided a solid basis for optimizing the computational model. The physiology of the hearing mechanism in man is provided in section 2.2. The main focus here is addressed to the highly sophisticated system of the cochlea which acts like an analog-to-digital converter encoding sound to neural signals handled by the brain. Section 2.3 of this chapter outlines several aspects concerning hearing loss whereas section 2.4 provides information about the bionic devices used to overcome auditory pathologies. The last two sections (2.5 and 2.6) of this chapter deal with the underlying physics of the compartment- and the FE-model respectively.

2.1 Anatomy of the Cochlea

The human inner ear is composed by the vestibular system which transduces rotational movements (semicircular ducts) and linear accelerations (otolithic organs), and the cochlea – the organ of hearing (Figure 2.1). It is a snail-shaped and fluid filled cavity located within the temporal bone and surrounded by the otic capsule. This compact bone structure is highly mineralized and is known to be the hardest bone in the human body. The compact surrounding increases the stiffness of the inner ear (Bast, 1942) so that vibrations of fluid in the cochlea are reflected and not absorbed by the temporal bone (Rask-Andersen et al., 2012).

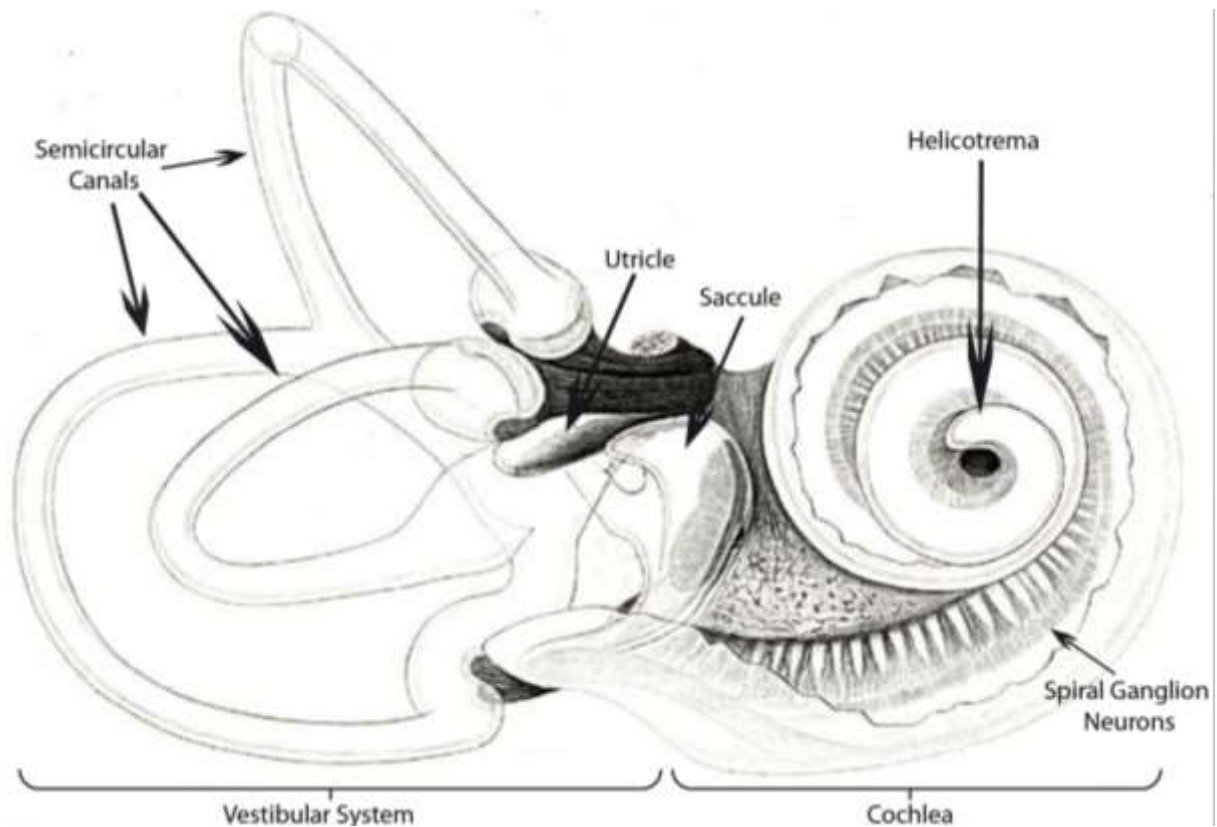


Figure 2.1: Schematic drawing of the human inner ear by Retzius, 1884.

The cochlea coils up for about 2 ½ turns in humans though its dimension and shape can vary enormously which has major influence on insertion depths of CIs used for extracellular stimulation of the cochlear nerve. A study conducted from Erixon et al. (2009) analyzed corrosion casts of 73 human adult inner ears and reported an outer cochlear wall length ranging from 38.6 – 45.6 mm whereas about 53% of the total length are assigned to the basal turn. Furthermore, the coiled and snail-shaped geometry of the cochlea leads to different heights of various turns resulting in narrowing scalae. The basal turn reveal the highest mean height with 2.1 mm, followed by the middle turn region (1.2 mm) and the apical turn which features the smallest height with a mean of only 0.6 mm.

The human hearing organ consists of three fluid filled chambers (Scalae). The most voluminous tract is Scala tympani (ST) and located below the osseous spiral lamina (Figure 2.2). It starts at the round window which marks the most basal part of the hearing organ and coils up to the apical region where Scala vestibuli (SV, second largest) starts as a continuation of the tympanic canal. The transitional region located at the cochlea tip (Apex cochlearis) is called the helicotrema. The SV is located above the osseous spiral lamina and is separated by the Reissner’s membrane, a thin cell membrane based on two cell layers, from the Scala media (SM). It ends at the oval window at the base of the cochlea (Davis & Liu, 2011). Due to their physical connection at the helicotrema, both scalae are filled with perilymph featuring high sodium and a low potassium concentration. The third chamber, SM or ductus cochlearis, is situated between ST and SV sheltering the organ of Corti (OC). It is filled with endolymph which possesses high potassium and low sodium concentrations (Wangemann & Schacht, 1996) and belongs to the endolymphatic system of the inner ear.

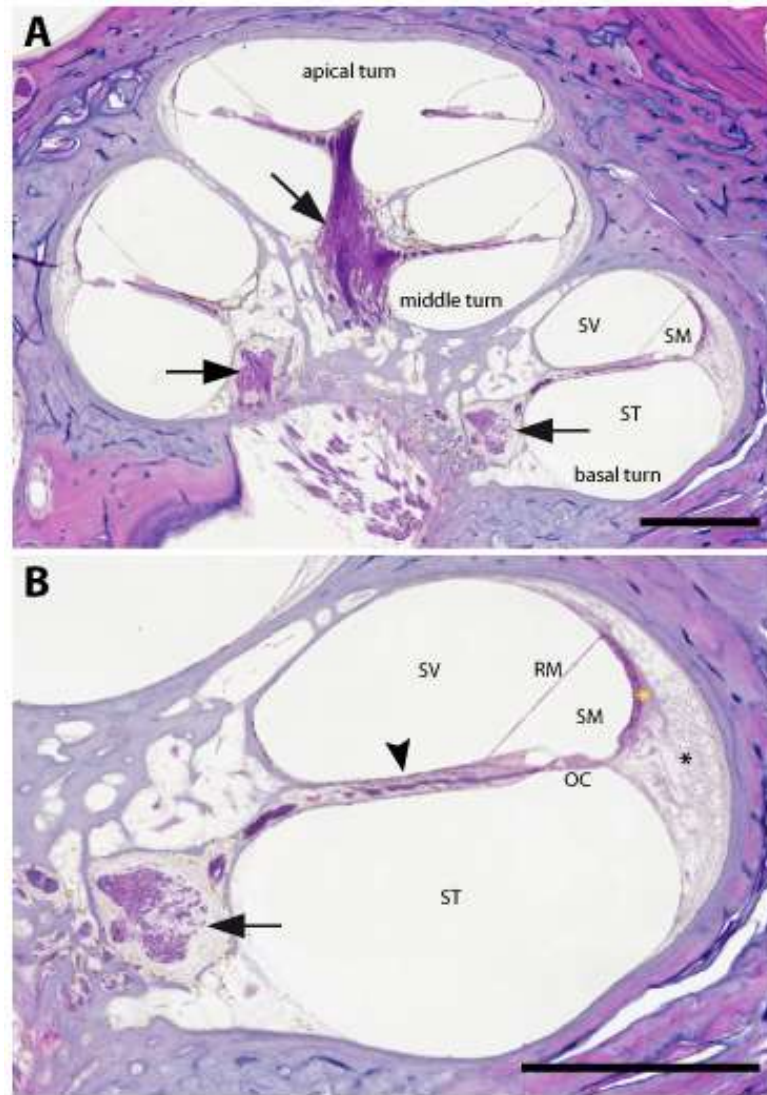


Figure 2.2: Hematoxylin and Eosin stained section of a human cochlea in a mid-modiolar plane. The cochlea (A) consists of three fluid filled chambers (Scalae). Scala vestibuli (SV) is separated by the Reissner's membrane (RM) from the Scala media (SM). The largest chamber is Scala tympani (ST) located below the osseous spiral lamina (B, arrow head). On the lateral end of the inner ear cavity is the stria vascularis (yellow star) which is clearly silhouetted against the loosely arranged cells of the spiral ligament (black star). Additionally, black arrows in both images point to the Rosenthal's canal which shelters the cell bodies of the SGNs. Scale bars indicate in both pictures 1 mm.

The organ of Corti (Figure 2.3) is a highly specialized structure located in the ductus cochlearis and composes the interface between acoustic-mechanical energy and the nerve signals processed by the auditory cortex in the brain. It basically consists of two different types of cells: supporting cells and sensory cells that sit on the basilar membrane (Young & Heath, 2000). The main function of the supporting cells (e.g. Deiter-, Hensen- and Claudius Cells) is to provide mechanical support to hair cells achieving hearing function. In addition, these cells are of prime importance for controlling hearing sensitivity and frequency selectivity (Flock et al., 1999) as they were found to couple on the regulation of outer hair cell electromotility which is influencing and actively contributing the cochlear amplifier (Yu & Zhao, 2009).

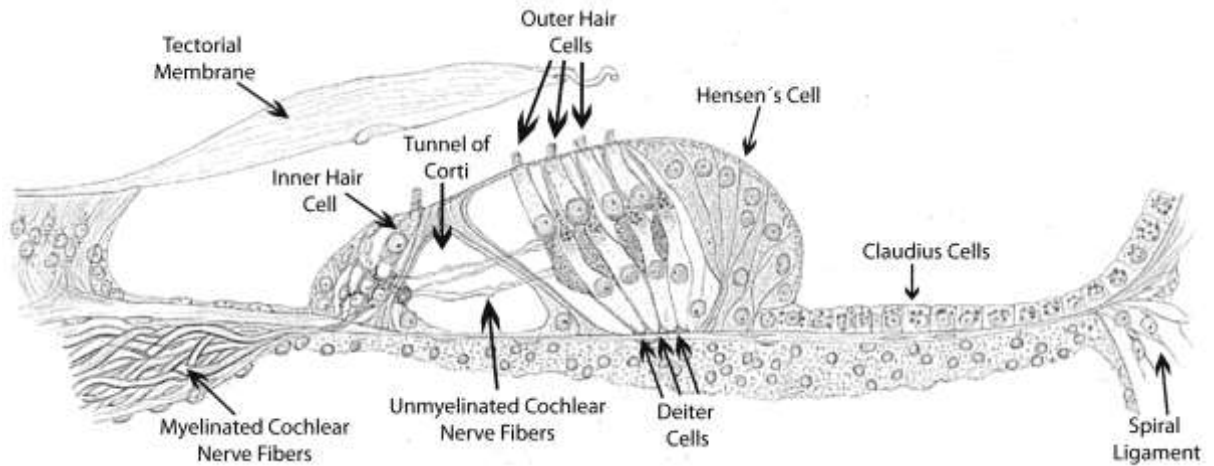


Figure 2.3: Schematic drawing of the organ of Corti by Retzius, 1884.

The cochlea is tonotopically organized (Figure 2.4) along its coiled structure, i.e. the organ of Corti is most sensitive for high frequencies near the base and to increasingly lower frequencies towards the apex (Adams & Liberman, 2010). There are about 15000 hair cells per cochlea in man which can be divided in two groups of mechanotransductive sensory cells: inner hair cells (IHC) and outer hair cells (OHC) (Spoendlin & Schrott, 1990) which differ in size, shape and functionality. IHCs are typically regular arranged in a single row on the organ of Corti whereas OHCs can occur irregularly arranged composing three or four, even five rows which demonstrates striking individual variations. Moreover, the total number of both types of hair cells in humans varies enormously ranging from ~3400 IHCs to ~12000 OHCs (Glueckert et al., 2005a).

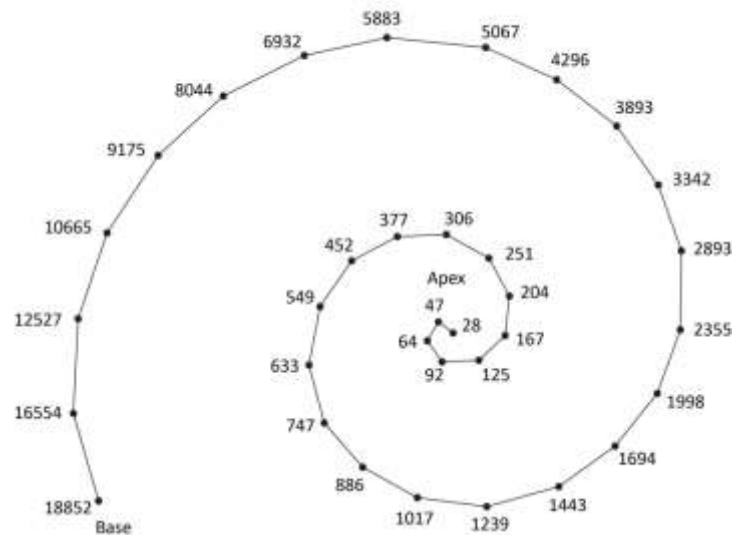


Figure 2.4: Illustration of the tonotopical organisation of the human hearing organ calculated by using the Greenwood function.

One IHC located at the basal end of the hearing organ is composed of 50 to 70 stereocilia and increases to about 100 in the apical region (Wright et al., 1987; Glueckert et al., 2005a) where they are responsible to transduce low frequencies into neural signals. This group of sensory cells provides the majority of afferent auditory signals and each hair cell is innervated by several type I SGNs (Rask-Andersen et al., 2012). Above mentioned numbers suggest that about ten type I cochlear neurons receive input from one IHC though no systematic analysis is available for the human auditory organ. However, findings of about 26 afferents per IHC in other mammalian species (Liberman, 1980a; Liberman, 1980b) support this theory for the human case.

The exact role of OHCs within the cochlea is not completely clear but it is generally assumed that the activation of OHCs adjusts the mechanical properties of the basilar membrane of the organ of Corti (Rusznák & Szucs, 2009). This behavior is attributed to the displacement of OHCs stereocilia leading to length alterations and changes in their stiffness. These activities require prestin, the motor protein of OHCs (Zheng et al., 2000) located in their plasma membrane. Changing the electrical potential at this contractile protein causes mechanical dislocation of OHCs. This dynamic ability, known as electromotility (Frolenkov, 2006), influences the stiffness of the basilar membrane (Dallos & Corey, 1991) which has a bearing on cochlear mechanics. The described feedback mechanism is known as the cochlear amplifier that facilitates sensitivity and frequency selectivity of the hearing epithelium (Dallos, 1992). OHCs are exclusively innervated by smaller type II SGNs composing about 5 % of the afferent projecting cochlear neurons. Contrary to IHCs and type I neurons, a single type II SGN innervates multiple OHCs in an 'en passant' fashion (Rask-Andersen et al., 2012).

Roughly 30000 – 35000 afferent SGNs in the normal hearing human cochleae of young adults (Spoendlin & Schrott, 1989; Spoendlin & Schrott, 1990; Miura et al., 2002) provide transmission of electrically coded sound signals transduced at the sensory epithelium up to the central nervous system. This number decreases progressively with increasing age resulting in age-related primary cochlear neuron degeneration or age-related hearing loss. A recent study (Makary et al., 2011) quantified the decline of SGNs analyzing 100 normal hearing subjects (0-100 years old) at a rate of 100 per year.

The existence of two different types of cochlear neurons within the mammalian cochlea based on morphological and functional criteria is well described. The vast majority of 90-95% is assigned to large type I neurons while only 5-10% are type II SGNs (Kellerhals et al., 1967; Ota & Kimura, 1980; Spoendlin, 1981). Based on characteristics like the cross sectional diameter of human SGN cell bodies as well as their circumference, the mean diameter of type I neurons based on TEM was determined at 30 μm whereas perikarya of small cochlear neurons were measured to be 15 μm (Kiang et al., 1984; Nadol et al., 1990; Rosbe et al., 1996). Because of reported diverging shapes of SGN perikarya (Glueckert et al., 2005b; Rusznák & Szucs, 2009), the use of 2D parameters for drawing appropriate conclusions concerning the size is not sufficient. To overcome these limitations, chapter 4 focused on the volume of human cochlear perikarya using three dimensional image stacks and classified four different populations with a mean diameter of 24.5 μm for the largest- and 13 μm for the smallest population.

One significant difference compared to SGNs of other mammals is, that cell bodies as well as the pre- and post-somatic segments of a standard human type I cochlear neuron totally lack isolating myelination. Only about 5% of these neurons are surrounded by several layers of loose myelin (Ota & Kimura, 1980; Arnold, 1987; Spoendlin & Schrott, 1989). Interestingly, this value is highly variable and seems to be age dependent. Cell bodies of cochlear neurons from babies do not possess any myelinated ganglion cell (Ota & Kimura, 1980; Arnold, 1982) while a total number of 28% of myelinated perikarya were reported from a 75 year old subject (Ota & Kimura, 1980). On the other

hand, the standard type II neuron in the mammalian (including human) cochlea is characterized by the complete absence of myelin resulting in an entirely unmyelinated, electrical signals transmitting neuronal structure (Ota & Kimura, 1980).

Human SGNs are not evenly distributed along the tonotopically organized cochlea. Spoendlin & Schrott (1989) studied human specimens and reported that the spiral lamina of the upper basal- and the lower middle turn region respectively, show the highest density of auditory signal transmitting neurons. Within this region, they counted about 1400 fibers/mm whereas this number decreases to about 330 fibers in basal- as well as in apical direction. Interestingly, the addressed part within the human cochlea is responsible for frequencies from about 3500 to 500 Hz which are of prime importance for speech recognition (Hollien et al., 1971).

2.2 Physiology of Hearing

Hearing composes one of the major senses in mammals that ensure their survival. This sense is responsible for warning of threats on the one hand and enables communication between humans with speech on the other. In order to achieve these sensations, the sound waves arriving at the pinna must be caught, transduced and transmitted via the middle ear to the fluid-filled cochlea. Here, the acoustic energy is transduced into electrochemical nerve impulses which are delivered to the auditory cortex by the VIIIth cranial nerve for further processing. The chapter provides a short overview of this quite complex process.

2.2.1 Outer Ear

As mentioned above, the sound waves that arrive at the outer ear are collected by the angled pinna which protrudes from the side of the skull. It catches sounds better that come from in front than sounds from behind. Consequently, this cartilage structure is quite helpful in sound localizing (Alberti, 2006). Incoming sound energy is further channeled to the ear canal which narrows slightly and widens again towards its inner end where the tube is separated by the ear drum from the middle ear. The ear canal resonates or enhances respectively, sound vibrations best at frequencies which the human ears hear most sharply (Worrall 2000). Vibrating elements resonating at these frequencies (around 1 – 5.5 kHz) are located within the upper basal- and middle turn of the cochlea and are interestingly of prime importance for human speech recognition (Greenwood, 1990, Loizou 1999, Hollien et al, 1971). The resulting resonance which is based on tubes' geometry amplifies the variations of incoming air pressure placing a peak pressure directly at the ear drum. Hence, the sound pressure level at the ear drum is about 10 times higher compared to the sound at the pinna (Worrall, 2000).

The tympanic membrane constitutes the interface between the outer- and the middle ear and is the first part of the sound transducing mechanism. Its shape is reminiscent of a loud speaker cone and covers a round opening of about 1 cm in diameter with a thickness of about 0.1 mm. Here, the airborne sound waves are converted into mechanical vibrations on to the middle ear structures (Worrall, 2000; Alberti, 2006).

2.2.2 Middle Ear

The middle ear is an air filled cavity that houses three little linked bones: the hammer, the anvil and stapes forming a system of quite effective levers driven by the ear drum. These three little bones act as an amplifying unit which is able to triple the vibrational input force coming from the tympanic membrane. Their muscles, which are the smallest in the human body, can modify the performance of

the whole lever system resulting in an automatic volume control. They can reduce the effectiveness of the system with the aim to protect the ear from exceeding vibrations generated by very loud sounds.

The third bone, the stapes, is shaped with an arch and a foot plate that covers the oval window which is an opening into the bony shelter of the cochlea (Alberti, 2006). Its size is about 15 to 30 times smaller compared to the ear drum. This difference in size ensures the needed critical amplification to match the varying impedances between the incoming airborne sound waves to that in the fluid filled cochlea. This concentration of force at this second interface provides an additional amplification of the transduced vibrations of about 15 – 30 times (Worrall, 2000). The stapes ensures that the already encoded sound information is given to the cochlea via the oval window.

In summary, the described amplification mechanisms of the outer- and the middle ear ensure that the sound waves caught by the pinna are boosted about 800 times before entering the liquid filled cochlea (Worrall, 2000).

2.2.3 Inner Ear

The inner ear is the last chain link where the sound information is finally transduced into electrical signals which are subsequently conducted to the auditory cortex in the brain via SGNs. The following paragraphs summarize briefly the principle process of the final signal transduction from vibrational sound information generated by the middle ear to electrical signals which are subsequently transmitted by auditory nerve fibers to higher instances of the brain:

As described above, the stapes produces vibrations representing the encoded sound waves which are applied to the oval window of the cochlea where its membrane is pushed inwardly. This approach induces motion of the windows' membrane which consequently shifts the perilymph, an almost incompressible fluid, of SV that causes a travelling wave in apical direction. As a result, the RM, the endolymph filled SM as well as the OC starts to move towards the subjacent ST. This movement of the mentioned structures leads on the other hand to a displacement of the perilymph of ST (again incompressible) which is compensated by the flexible membrane that seals the round window on its basal end (Zenner, 2005).

The next step of the acoustic vibration causes the recurrence of the mentioned anatomical structures to the initial state which is induced by the contrary movement: stapes and oval window membrane are moved towards the middle ear; RM and the OC show upward movements while the round window membrane goes inward. Since every incoming sound produces numerous movements of the sensory epithelium and the adjacent membranes, the mentioned structures underlie a complex temporal displacement pattern (Zenner, 2005).

Above quoted up- and downward movements' results in a shear movement between the tectorial membrane and the OC where the sensory cells are situated (illustrated in Figure 2.3). If both structures are deflected, the result is a parallel translation between them. Due to the fact that the tips of the longest stereocilia of the OHCs are in direct contact with the tectorial membrane, its relative movement recurve them resulting in the opening of ion channels that generates electrical impulses. These afferent signals are transmitted via the myelinated peripheral process, the unmyelinated bipolar somatic region and the well shielded central process, known as the vestibulocochlear nerve (Kolb & Whishaw, 2011), to the cochlear nuclei located within the brainstem. In contrast, IHCs do not feature direct membrane contact. However, the shear movement causes swaying of the endolymphatic liquid film which is moving between the hair cells and the tectorial

membrane. The resulting motion of the fluid is enough to deflect the hair cells which provoke again the sound-coded APs (Zenner, 2005) which are again sent for processing to the brainstem. The cochlear nuclei are the first relay station in the ascending hearing pathway of mammals (Kandler & Friauf, 1993) sending the incoming afferent signals to higher parts of the brain where they finally arrive in the auditory cortex.

In summary, the cochlea can be seen as a highly sophisticated hydromechanical frequency analyzer that performs nonstop real time spectral decomposition of the incoming acoustic signal. When an acoustic signal pass to the fluid filled cochlea by the stapes of the middle ear, the basilar membrane experiences an oscillatory motion representing the frequency of the input sound. This results in a frequency distinct wave travelling to the apical end inducing above described movements of anatomical components of the cochlea. The peak of the wave is dependent of the incoming frequency resulting in the maximum displacement of the organ of Corti at a distinct spatial region. Here, the auditory receptor cells experience the maximum stimuli generating the highest afferent output along the cochlea spiral. Thus, the hearing organ produces a spatial frequency map sending time-delayed electrical signals to the brain (Dallos, 1992).

2.3 Hearing loss

According to the WHO, around 330 million adults and about 30 million children worldwide are suffering from disabling hearing loss which negatively influences their everyday life. The main reason of hearing loss can be found in irreparable damages of the hair cells due to exposure to loud noise, infectious diseases, ototoxic drugs and ageing but can also be congenital based on genetical defects (WHO, 2013). Hearing loss is classified according to the anatomical structures of the ear that are affected. A surgical intervention or medical treatment can usually cure or at least tremendously improve conductive hearing loss where sound transmission through the outer and/or middle ear is reduced (Moore, 2007).

By far problematic is the irrecoverable loss of anatomical structures responsible for auditory signal transduction and further transmission. The damage or destruction of the outnumbered OHCs raises hearing thresholds and reduces simultaneously the ability of frequency discrimination which greatly influences sound perception (Wilson & Dorman, 2008) and speech understanding. This inner ear pathology is usually found in the elderly suffering from presbycusis and starts in the basal region which is responsible for signal encoding for high frequencies (Nadol, 2010). The missing information can be restored by a CI pursuing an electric-acoustic stimulation approach which amplifies low frequencies acoustically and stimulates the high frequency region within the cochlea electrically (von Ilberg et al., 2011).

Total deafness or profound hearing loss includes all frequency regions of the hearing organ and is caused by the damage of IHCs responsible for signal transduction on the sensory epithelium. The loss of IHC and consequently, the absence of neural stimulation of the auditory nerve induce the degeneration of the peripheral processes of cochlear neurons which connects the bipolar cell body with the sensory cells (Wilson & Dorman, 2008). Interestingly, this neuronal degeneration process usually stops in humans at the level of the unmyelinated cell bodies. It was shown that SGNs can be still alive even after 50 years of documented deafness (Glueckert et al., 2005b). However, the hearing sense, including the ability to understand speech can be brought back to these patients by CIs which electrically stimulate frequency regions along the whole cochlea spiral which substantially improves patients' quality of live.

2.4 Cochlea Implants

The CI is a bionic hearing device that receives sound from the surrounding areas which are subsequently converted in real-time to electrical pulses. These pulses are sent to the electrodes of the intracochlearly located array to stimulate the lateral neuron endings of the auditory nerve. The generated electrical signals are transmitted to the brain which processes and interprets the coded information as sounds.

The active electrode array of CIs is normally located in the perilymph filled ST and delivers electrical currents with the aim to provoke APs which are transmitted by cochlear neurons to the auditory cortex. Their insertion depth is limited by the varying lengths of used arrays, the decreasing diameter in apical direction of this fluid-filled cavity and thirdly, by documented (Erixon et al., 2009) variations in cochlea dimensions and shape. In short, there exist two different groups of CIs which can be classified according to their location within ST:

The vast majority of implanted hearing prostheses are located close to the lateral wall of ST just below the OC where the distance to the peripheral end of SGNs is shortest. The basic concept of a second group of CIs is to mainly apply the electrical current close to the cell bodies of cochlear neurons. As a result, their electrode arrays are situated on the opposite side of ST, its medial wall in close proximity to the Rosenthal's canal minimizing the distance to the unmyelinated human cell somata.

However, both types are constructed quite similar consisting of an external- and an internal part (Figure 2.5). A microphone belonging to the external part catches sound which is analyzed by, e.g. FFT from a microprocessor and subsequently coded to electrical signals. These coded signals are transmitted to the electrodes of the array (usually between 12 and 22 along the electrical active part) which are placed tonotopically along the cochlea spiral by insertion through the round window. Every electrode of this array can stimulate a distinct population of cochlear neurons individually each representing a specific frequency component of the incoming sound. All electrodes of the array can be controlled individually to optimize their output. In monopolar stimulation mode, for example, one active electrode is located intracochlearly while the return (or ground) electrode is usually implemented in the implant case far away from the stimuli receiving cochlea. Consequently, the applied current spreads over a relatively spacious area activating a larger population of neurons (Namasivayam, 2004).

When using bipolar- or tripolar stimulation strategies, two- or three adjacent electrodes (all located within the cochlea) focus their stimulation area on a smaller (Namasivayam, 2004), more distinct and frequency-representing population of auditory nerve fibers. This increases spatial selectivity but requires simultaneously higher current to reach neural activation (Zhu et al., 2012).

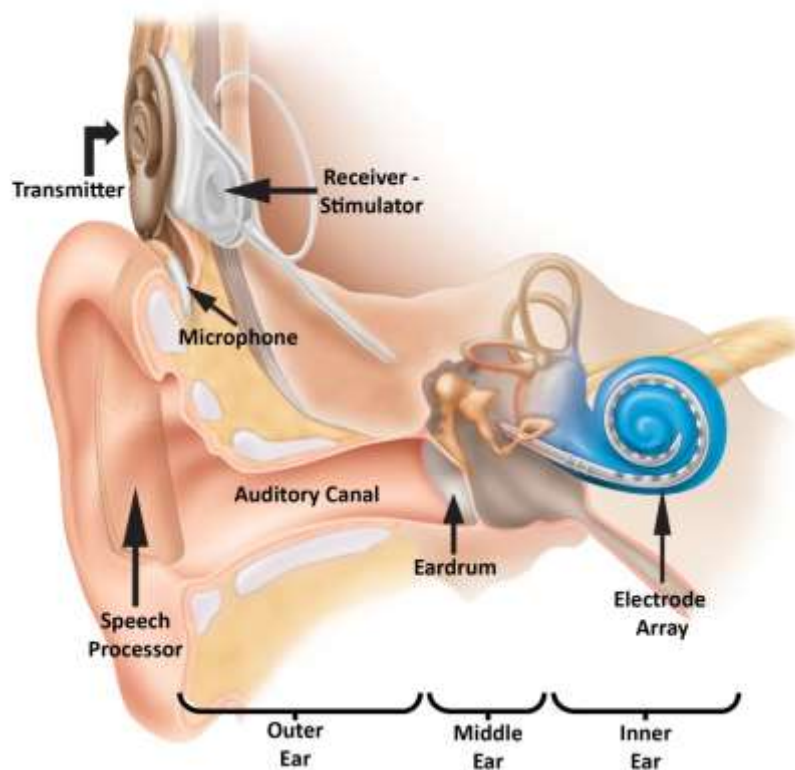


Figure 2.5: Illustration of the human ear with an implanted CI (Aarhus, 2010).

Besides the differences in hardware, location of the active electrodes and used stimulation modes of the routinely implanted CIs, the implemented sound encoding strategy is by far the most important component of these bionic devices (Koch et al., 2004; Wilson & Dorman, 2008). This algorithm determines how the incoming airborne sound energy is digitalized into electrical signals and additionally, how this information is transferred by the electrodes to auditory neurons of distinct regions of the cochlea.

During the last decades, a lot of coding strategies have been developed to encode speech, music and ambient noise. Frequently used in implanted hearing devices nowadays are the continuous interleaved sampling strategy (Wilson & Dorman, 2008) and the advanced combinatorial encoder strategy (Kiefer et al., 2001) which is based on an N of M principle. Both strategies use a fixed number of channels to deliver the encoded acoustic spectrum to the SGNs. To obtain an improved spectral resolution of the active electrode arrays, the virtual channel technique was introduced. The HiRes120 strategy (Koch et al., 2004) for example, creates a virtual channel between two stimulating electrodes that improves the perception of frequencies between these two channels (Charles & Yi-Hsuan, 2012). Besides the above mentioned electrical stimulating approaches, hybrid stimulation strategies or electric acoustic stimulation combines the use of a hearing aid (acoustical stimulation) with a CI (electrical stimulation). This approach is designed for patients suffering from presbycusis (see section 2.3) with poor hearing of high frequencies but good perception of the low frequency portion of incoming sound (von Ilberg et al., 2011).

2.5 Compartment Model of a Cochlear Neuron

In order to simulate the response of a single cochlear neuron stimulated by microelectrodes, a model describing the electrical properties of the conducting neural path is needed. This was realized using a compartment model approach which is commonly used in mathematical modeling of biological systems. The basic idea behind this method is to divide the whole system into subunits for the purpose of reducing the complexity of the analyzed structure.

An ultrastructural drawing of the compartment model of a human SGN is illustrated in Figure 2.6A. Every subunit possesses individual geometric and electric parameters: P0 represents the unmyelinated peripheral terminal, P1 - P5 and C1 - C_n describe the nodes of Ranvier with the intermediate myelinated internodes (grey colored). The unique unmyelinated soma region of human cochlear neurons is composed by three single compartments: the presomatic region, the cell body and the post somatic region (Rattay et al., 2001a).

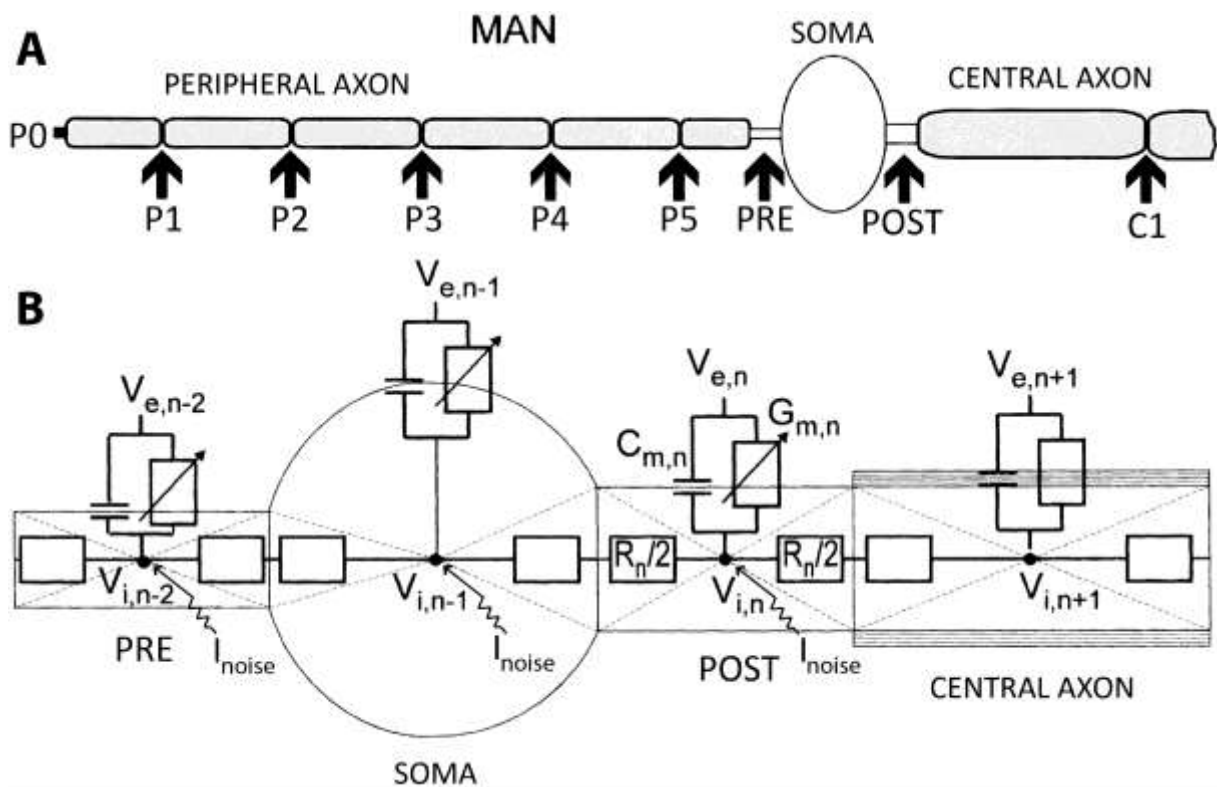


Figure 2.6: Scheme of the ultrastructure of a human cochlear neuron (A) illustrating the compartments of a human cochlear neuron. The corresponding equivalent circuit is shown in (B) with the pre somatic region, a spherical soma, the post somatic region and the first myelinated central internode (partly adapted from (Rattay et al., 2001a))

Every subunit of the model neuron can be seen as an isopotential element. The sum of these elements is described by an electric circuit which is shown in

Figure 2.6B. Analyzing the total current at the central point of an n-th compartment demonstrate that it is composed of the capacitive current $I_{capacitive}$, an ionic transmembrane current I_{ion} , and the ohmic I_{ohm} to the neighboring compartments.

By applying Kirchhoff's Law follows

$$I_{capacitive,n} + I_{ion,n} + I_{ohm,n} = 0 \quad (2.1)$$

According to Ohm's Law, the axial current I_{ax} is given as

$$I_{ohm} = I_{ax} = \frac{V}{R} \quad (2.2)$$

where R is the resistivity in axial direction and V the voltage between two central points of adjacent compartments. The capacitance C of an electrical system is given by $C = \frac{q}{V}$, with q as the charge. This gives the voltage/current relationship

$$I_{capacitive} = C \cdot \frac{dV}{dt} \quad (2.3)$$

As illustrated in

Figure 2.6A, there are two types of compartments: myelinated internodes and the unmyelinated nodes of Ranvier of the peripheral and central process, the peripheral terminal and the somatic region. The internodes are considered to be of the passive type $I_{ion,passive,n}$ where the constant conductance acts as a resistor and reads as

$$I_{ion,passive,n} = G_{int} \cdot V_n \cdot \frac{A_n}{nm_n} \quad (2.4)$$

where G_{int} describes the conductance of one layer of membrane of a internode and nm_n defines the number of myelin layers wrapping the internode. A_n denotes the surface of the cylindrical approximated passive internodes (Rattay et al., 2003).

The remaining unmyelinated compartments are modeled with the inclusion of ionic current flows based on the work of Hodgkin and Huxley (Hodgkin & Huxley, 1952). They found in their experiments that the conductances for sodium and potassium are functions of time and transmembrane voltage. In contrast, the leakage conductance L was found to be constant. On the basis of these equations, the ionic currents IC_n of the unmyelinated n-th compartment $I_{ion,active,n}$ is given as

$$I_{ion,active,n} = A_n \cdot IC_n + I_{noise,n} = A_n \cdot (ic_{Na,n} + ic_{P,n} + ic_{L,n}) + I_{noise,n} \quad (2.5)$$

Further details of the used HH-equations and resulting constants can be found in Rattay et al. (2003) on Table 3.1 and Table 3.2.

The introduced term $I_{noise,n}$ describes ion channel fluctuations which represent measured firing delays even when stimulated with current pulses of constant intensity resulting in stochastic arrival times of APs (jitter). The noisy membrane currents are defined to be proportional to the square root of the number of involved sodium channels and reads as

$$I_{noise,n} = GAUSS \cdot k_{noise,n} \cdot \sqrt{A_n \cdot g_{Na,max}} \quad (2.6)$$

where GAUSS is a Gaussian noise current that changes its value every 2.5 μ s, A_n represents the surface of the compartment and $g_{Na,max}$ stands for the maximum sodium conductance.

The factor $k_{noise,n}$ is common to all compartments representing the fluctuation of the voltage across the resting membrane (Rattay et al., 2003).

HH conducted their experiments on a giant axon from a cold blooded squid. Due to the fact that neurons from humans transmit AP at higher temperatures and most of the nerve fiber is isolated by myelin two modifications were undertaken with respect to the original HH model: (i) the gating processes are sped up by a common factor 12 correcting the temperature and (ii) the sodium, potassium and leakage conductances are multiplied by the factor 10 resulting in a 10-fold channel density in each node (Rattay et al., 2001a).

The membrane capacitance C_m of an n-th compartment is described by

$$C_{m,n} = A_n \cdot c_{m,n} \quad (2.7)$$

where c_m describes the specific membrane capacitance which is reverse proportional to its ensheathing numbers of myelin layers and A_n is again the compartment surface. R_n represents the axoplasmatic resistance to its adjacent compartments. Introducing V_i as the intracellular potential and V_e as the extracellular potential of the n-th compartment, it follows that

$$C_{m,n} * \frac{d(V_{i,n} - V_{e,n})}{dt} + I_{ion,n} + \frac{V_{i,n} - V_{i,n-1}}{R_n/2 + R_{n-1}/2} + \frac{V_{i,n} - V_{i,n+1}}{R_n/2 + R_{n+1}/2} = 0 \quad (2.8)$$

Introducing the reduced membrane voltage $V = V_i - V_e - V_{rest}$ where V_{rest} is the resting potential results in the following system of differential equations for calculating the time-dependend course of the membrane potential V_n for every compartment expressed by

$$\begin{aligned} \frac{dV_n}{dt} = & \left[-I_{ion,n} + \frac{V_{n+1} - V_n}{R_{n+1}/2 + R_n/2} + \frac{V_{n-1} - V_n}{R_{n-1}/2 + R_n/2} + \right. \\ & \left. \frac{V_{e,n+1} - V_{e,n}}{R_{n+1}/2 + R_n/2} + \frac{V_{e,n-1} - V_{e,n}}{R_{n-1}/2 + R_n/2} \right] / C_{m,n} \end{aligned} \quad (2.9)$$

If the neuron is intracellular stimulated it is assumed that $V_e = 0$ because of the absence of an electrode from the extracellular space. Therefore, the equation is reduced to

$$\frac{dV_n}{dt} = \left[-I_{ion,n} + \frac{V_{n+1} - V_n}{R_{n+1}/2 + R_n/2} + \frac{V_{n-1} - V_n}{R_{n-1}/2 + R_n/2} \right] / C_{m,n} \quad (2.10)$$

The direct stimulating influence of the extracellular potential on every n-th compartment is described by the activating function f_n and reads as

$$f_n = \left[\frac{V_{e,n-1} - V_{e,n}}{R_{n-1}/2 + R_n/2} + \frac{V_{e,n+1} - V_{e,n}}{R_{n+1}/2 + R_n/2} \right] / C_{m,n} \quad (2.11)$$

and counts for neurons of arbitrary shape. If a neuron is in the resting state before a stimulating current impulse is applied, this form of the activating function represents the rate of membrane voltage change in every compartment that is activated by the extracellular field. Regions with a positive activating function are candidates for AP initiation whereas a negative activating function causes hyperpolarization (Rattay et al., 2001a).

In order to study the temporal pattern in a target neuron generated by microstimulation, the firing electrode is assumed to be an ideal point source in an infinite homogenous medium with constant conductivity which can be described by

$$V_e = \frac{\rho_e * I_{electrode}}{4 \cdot \pi \cdot r} \quad (2.12)$$

where V_e denotes the extracellular voltage which is measured at a distance r from the electrode; ρ_e is the extracellular resistivity (Rattay et al., 2003).

The described electrical circuit model of an auditory neuron was technically realized using MatLab® 2011a (MathWorks, Natick, Ma, USA) which comprehensively supports object-orientated programming (OOP) since version 2008a. OOP is a formal programming approach combining data and associated actions (methods) into logical structures (objects) (MathWorks, 2013), i.e. the programming problem is divided into single components.

The three fundamental key principles of OOP used to resolve a number of problems that have been experienced with structural languages are: (i) encapsulation, (ii) inheritance and (iii) polymorphism. The first principle ensures that an object is ‘hidden’ or prevented from manipulation respectively, caused by other software components. The second principle describes the possibility that a class can be extended or even created which is built on already existing classes. The third principle represents the ability that various objects act differently (as predefined) to the same input (Bitter et al., 2007).

The cores of object-orientated environment are classes which generally describe and define ‘something’ which represent the main parts of the problem to be solved. Every class needs objects which are instances of the class describing its behavior and how this behavior is performed. Therefore, every class consists of properties (is the object-orientated name for variables) which are mostly private to the class and define characteristics of an object. These attributes of an object are manipulated by the methods which are functions belonging to the class (Bitter et al., 2007).

During the research project, different versions of the model have been developed according to particular questioning. However, the most sophisticated realization of the model comprises the implementation of 3D nerve fiber pathways extracted from a human specimen which was imaged using micro CT. This model was subsequently used in combination with the developed FEM providing the calculated extracellular potentials along the traced nerve fibers influencing the activation thresholds during extracellular microstimulation. The used computational model of a cochlear neuron is based on five classes which are briefly explained in the following. Note that class ‘stimulation’ was adapted when using the FEM for calculation of the extracellular potentials at the traced fiber bundles:

- HH kinetics for sodium channels: this class handles the active electrical properties of the voltage-gated sodium channels which are necessary to describe the unmyelinated compartments of the model. These ion channels are responsible for the rising phase of APs.

- Properties: gating variables (describe the probability for a membrane gating process), temperature coefficient
 - Methods: Calculation of the voltage-gated sodium variables according to the HH model (Rattay et al, 2003, Table 3.1)
- HH kinetics for potassium channels: together with sodium channels, voltage-gated potassium channels play a crucial role during APs; are the driving force for returning the depolarized cell to a resting state
 - Properties: gating variables and temperature coefficient
 - Methods: Calculation of the voltage-gated potassium variables according to the HH model (Rattay et al., 2003, Table 3.1)
- Stimulation (without FEM): the various properties needed for applying a neuron stimulating impulse are handled within this class.
 - Properties: types of impulses, their shape, the position of the electrode in space, extracellular resistivity
 - Methods: calculation of the distance between the electrode and the compartments, calculation of the electrical potential along the cochlear neuron
- Stimulation (with FEM): Chapter 7 presents the development of a FEM which was used to determine the extracellular potentials along reconstructed nerve fiber bundles. Hence, this class was slightly adapted.
 - Properties: types of impulses, their shape, the position of the electrode in space
 - Methods: calculation of the distance between the electrode and the compartments, Import of the electrical potentials along the neural path of the cochlear neurons calculated using the FEM
- Neuron: this class contains the structure and composition of the model neuron
 - Properties: geometrical parameters of the neuron (length and diameters of different compartments, size of cell body, layers of myelin, active and passive compartments, conductivities of ion channels and intracellular resistivity)
 - Methods: calculation of the compartment partitioning
- Segment: determines the temporal behavior of various parameters for each compartment
 - Properties: number and orientation in space of segments, geometrical and morphological parameters
 - Methods: calculation of the temporal behavior of the voltage and gating variables as functions of time for every model compartment

2.6 Finite Element Model of the Human Cochlea

The basic idea behind the finite element method is to simplify a complicated problem with the purpose to find an approximate solution. This approach requires the discretization of the analyzed structure into various compartments each composed of small, interconnected sub-regions which are called finite elements (Rao, 2005). Each compartment is described by its geometrical boundaries and defined properties which represent the composition. According to the problem, these boundary conditions are implemented to a number of partial differential equations describing the physical laws

of the problem. These formulas are solved to derive the approximated solution which can be more precise by increasing the degrees of freedom of the system.

The computational model of a human cochlea was realized using COMSOL Multiphysics® (COMSOL, Inc., Palo Alto, CA, USA) simulation software. The electric currents interface which is integrated in the AC/DC module can solve for three physical quantities: (i) the electric scalar potential V , (ii) the magnetic vector potential A and (iii) the magnetic scalar potential V_m (COMSOL, 2012). Consequently, this interface enabled to study the influence of a current applied by an active electrode in a conductive and capacitive material.

In order to calculate the distribution of the electrical potential in the human cochlea model after single electrode microstimulation, a volume conductor model that precisely represents human inner ear anatomy was developed. The multiple anatomical compartments, each featuring its distinctive electrical conductivity, determine the arising 3D potential distribution. To get the resulting electrical potential it is necessary to solve the volume conductor problem which reads as

$$\nabla \cdot J = I_v \quad (2.13)$$

where ∇ is the vector spatial derivative operator, J describes the current density and I_v denotes the current source.

The current density J in the medium which is linked to the electric field $E[V/m]$ is given by Ohm's law as

$$J = \sigma \cdot E \quad (2.14)$$

where $\sigma[S/m]$ describes the electrical conductivity of the tissue.

If the current density J is known, the electric field E can be calculated from Ohm's law which is expressed as

$$E = -\nabla \cdot v \quad (2.15)$$

where v is the voltage. In the used FEM, E is determined as the difference between the voltage at two points divided by the distance Δd between those points which can be expressed as

$$E = \frac{\delta v}{\delta x} = \frac{v_1 - v_2}{\Delta d} \quad (2.16)$$

As a result, if the electric field is known within the model, the voltage at different points can be calculated (Saba, 2012).

The described compartment model facilitates to study the neural response after injecting a current into the peripheral terminal or to stimulate a nerve fiber by an electrode that is located within the extracellular space. However, the propagation of the electrical potential V_e is assumed to occur in an infinite homogeneous medium with constant extracellular resistivity p_e (see formula 2.12). To overcome this limitation, chapter 7 presents the development of an FEM based on micro CT imaging. The imaging took about five hours resulting in 1062 DICOM slices with a total size of 2.5 GB.

From this data, a total number of five compartments were extracted by using both, manual and threshold segmentation. The model is finally composed by the following compartments:

- Scala tympani: filled with perilymph, usually the location of CI electrodes
- Scala vestibuli: filled with perilymph; directly connected with Scala Tympani in the helicotrema
- Scala media: filled with endolymph
- Bone: surrounding and encapsulating the scalae
- Modiolus: highly porous bony labyrinth with numerous nerve fibers crossing

Surfaces of the segmented objects were extracted and preprocessed using Amira® visualization software. Due to the fact that these surfaces do not represent solid models needed for further investigations in COMSOL, the segmented compartments were subsequently transferred to SolidWorks® (Dassault Systemes SolidWorks Corp., MA, USA). Using this CAD program enabled to convert Amira surfaces to non-uniform rational basis spline (NURBS) objects, which were subsequently transferred to COMSOL used to calculate the distribution of the electrical potential within the virtualized structure. The extracellular potentials were extracted along the segmented nerve fiber pathways which were subsequently deployed as input variables for the compartment model. Further details are described in chapter 7.

Data Collection and Preparation

Since vital SGNs from the human auditory organ are not accessible for electrophysiological experiments, the electrical activity of auditory fibers can be studied with computer simulation that ameliorates our knowledge of action potential initiation and propagation along the neural pathway. The auditory neuron model which was used to analyze the natural spiking behavior as well as the response to extracellular stimulation is mainly based on its micro-anatomical structure, i.e. their geometrical parameters. As described in section 2.1 and 2.2, human auditory neurons possess unique features among other mammals which makes it impossible to generalize drawn conclusions from other species for the human case. To overcome these limitations, we investigated several human cochleae using various histological, imaging and data processing approaches which are outlined in this chapter.

3.1 Fixation and Sectioning of Specimens

The main purpose of fixation is to preserve all cellular and structural elements as nearly as in the natural living condition as possible. In other words, a good fixation changes the cell chemistry the least and preserves the cell structures the best (Yadav, 2003). The quality of fixation is determined by two factors:

- The time which elapses between the interruption of blood supply (death) and subsequent chemical fixation should be as short as possible (short post mortem time).
- The duration of tissue fixation by a chemical agent. Too long fixation ends up in tissue hardening and leads to shrinking artifacts that affect the geometrical properties of the tissue. Hyper fixation of tissue additionally causes the total loss or masking of antigenic properties.

Besides, the size of the specimen, the pH-value, the volume relation between the fixative and the specimen as well as the temperature at which the fixation process is undertaken affects the risk of morphological damages (Glueckert, 2013).

The specimens used in this thesis were extracted from temporal bones which were obtained during routine autopsy at the Institute of Pathology, Innsbruck Medical University. The post mortem time ranged from about 90 min to 12 hours with specimens showing excellent preservation of the auditory nerve tissue to some that did not meet the requirements for further analysis. Human specimens were fixed immediately after arriving in our lab with ice cold paraformaldehyde through the round and oval window accessing the fluid filled cavities followed by immersion for 24 hours. The fixation of tissue using aldehydes is most common for further analysis with biomarkers due to the very good conservation of the biological activity and the high preserved antigenicity. This is attributed to the small molecules of this fixative which diffuse very fast into the tissue. Additionally, the cross-linking between proteins is relatively slow and loose (Aeschl & Büchl-Zimmermann, 2010).

The analyzed cochleae were subsequently extracted from the temporal bones using forceps and small diamond-drills under a stereo microscope to mill off cochlea surrounding bone. In order to prepare thin sections of the specimens they were put into ethylenediaminetetraacetic acid (EDTA) for decalcification. This process takes about six weeks where calcium ions providing the rigidity of the bone are removed making the cochlea capable for cutting. The last critical step in the preparation of the specimens is their deep-freezing (-80°C) which has to take place quite fast which ensures to keep the evolved ice crystals as small as possible. Finally, the prepared cochleae were serially sectioned with a cryomicrotome with varying thicknesses ranging from 10 μm to 35 μm . Details about specimen fixation for further immunohistochemical analysis can be found in section 4.3.1, 5.3.1 and 6.3.1.

Two specimens have been scanned in high-resolution micro CTs which enabled to develop a FEM of the human cochlea and to trace nerve fiber bundles to extract the 3D-pathways of representative auditory neurons. To improve the contrast of the nerve tissue, cochleae were additionally post-fixed using osmium tetroxide (OsO_4) that covalently binds and crosslinks unsaturated fatty acids and thereby darkly stains lipids and membranes. This chemical compound reacts with the double bonds of myelin lipids and is subsequently reduced to metallic osmium which is deposited in the peripheral nerve tissue. Due to its quite high atomic number of 76, the stained myelinated fiber structures are clearly visible in micro-CT scans. Further details can be read in section 7.3.1.

3.2 Staining with Biomarker

Immunohistochemistry (IHC) was first published by Coons et al. (1941) describing a technique for the detection of cellular antigens in tissue sections. Nowadays, extremely sensitive methods are available to detect one or multiple antibodies simultaneously. IHC is based on the binding of antibodies to a specific receptor in tissue sections (Ramos-Vara, 2005). The principle of this binding is illustrated in Figure 3.1. Every cell in animals or plants possesses a set of different receptors which are located on the surface and/or inside the cell. To make the occurrence of one (or multiple) specific receptor(s) visible (an example is shown in Figure 3.1), the section is incubated with the primary antibody specific for receptor A. Subsequently, a secondary antibody is brought to the system which holds receptors to detect solely the primary antibody. Moreover, it is labeled with a fluorescent tag which is emitting light on a specific wavelength after excitation with light. Please see section 3.3 for further details concerning the detection of the emitting fluorescence signal.

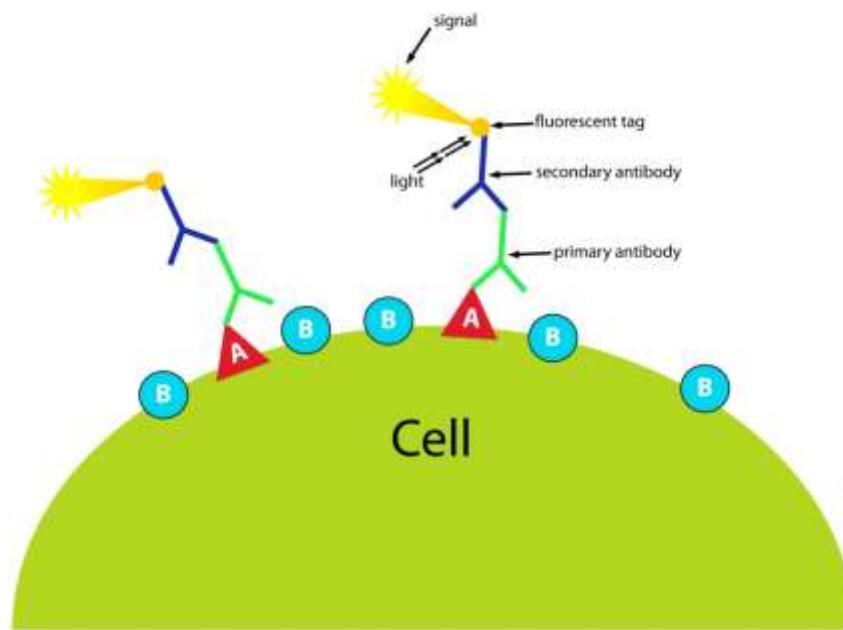


Figure 3.1: Illustration of the principle of immunohistochemical staining.

With this approach it was possible to detect and quantify various micro-anatomical structures of human SGNs which were subsequently incorporated in our computational cochlear neuron model (see section 2.5).

In chapter 4 we present the three dimensional acquisition of unmyelinated bipolar cell bodies which compose the main energy barrier for an auditory signal on its way to the auditory cortex.

As described previously, only a small percentage of human type I SGNs feature several isolating myelin layers surrounding their cell bodies. Using an antibody against anti-myelin basic protein (see chapter 5) enabled to quantify the number of these cochlear neurons within the spiral ganglion of three human specimens. Additionally, type II cochlear neurons which totally lack myelin were identified using an anti-peripherin antibody. This neuron-specific intermediate filament protein is well known to be expressed in mammalian (including human) type II SGNs enabling to determine also their frequency of occurrence in the studied human cochleae. With the simultaneous staining of these two antibodies we detected several cases of totally myelinated type II cochlear neurons. These data were implemented to the cochlea nerve model to develop a representative standard case for each detected characteristics.

Chapter 6 presents the quantification of commonness and the exemplary spatial reconstruction of auditory neurons which are arranged in cluster. Using antibodies against anti- β -III-tubuline, anti-S-100 and anti-myelin basic protein enabled to detect direct cell-to-cell contact of cell somata.

3.3 Acquisition of Data

Confocal Imaging

The geometrical parameters of investigated human and cat cochleae were acquired with a Confocal Laser-Scanning Microscope (CLSM). This microscopy technique is widely used in the biological and

medical sciences for investigating thin sections of living or fixed specimens. Compared to other imaging techniques like conventional widefield optical microscopy, confocal microscopy offers several advantages including (i) the ability to control depth of field, (ii) reduction or even elimination of background information away from the focal plane and (iii) the capability to scan sections in three dimensions. Modern CLSMs are equipped with several laser systems which enable to simultaneously detect multiple biomarkers labeled with fluorophores (Figure 3.1) of different wave length (Claxton et al., 2005) reaching a spatial resolutions in the submicrometer range.

The confocal principle is illustrated in Figure 3.2. A laser source (can have various wavelengths) sends light of a certain wavelength through the collimator and is then focused into the specimen via the beamsplitter. The subjacent scanning mirror moves the focused laser beam line by line over the specimen and excites distinctive fluorophores which consequently emit light (see Figure 3.1). These emitted signals are separated from the laser light by the main dichroic beamsplitter on their way to the confocal pinhole. This detection pinhole makes a CLSM really efficient since fluorescence signals originating from above and below the focal plane are rejected. The emitted photons are detected pixelwise and amplified by a photomultiplier.

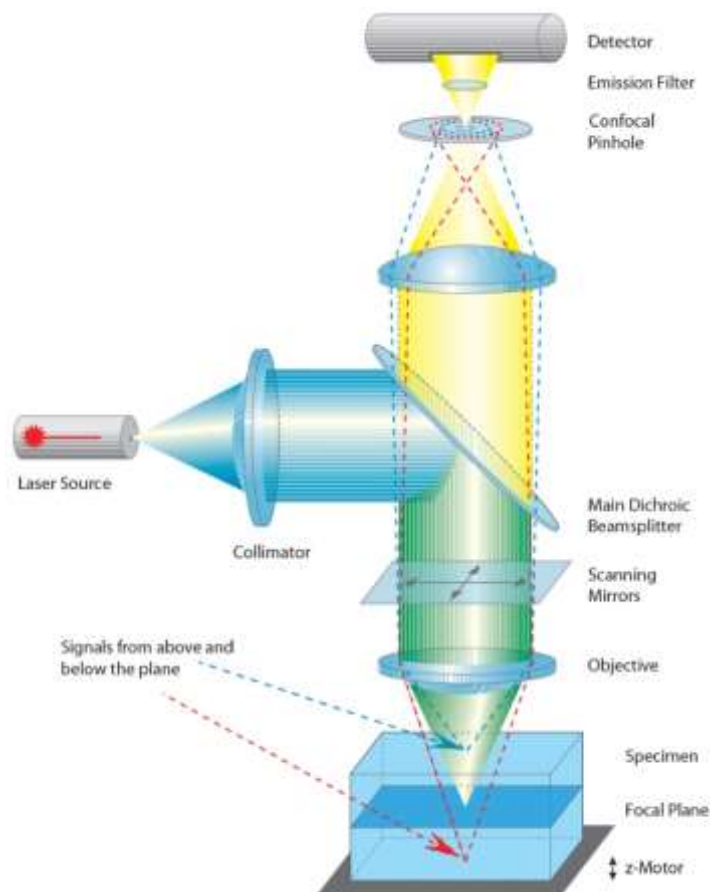


Figure 3.2: Principle of confocal microscopy (Simbürger et al., 2013)

As mentioned above, this imaging technology enables to acquire spatial details of fluorescence signals from biological tissue in the submicrometer range. To distinguish between such signals or to quantify geometrical and morphometrical parameters respectively, the sampling rate has to be chosen appropriately on the used imaging system. In general, sampling refers to the reduction of a continuous signal to a discrete signal (Pharr & Humphreys, 2010) which is also called analog-to-digital

conversion. The resolution in imaging is generally dependent on the sampling rate which describes how much information (pixels) is acquired in x- and y-direction. This factor must be preset and cannot be increased after image acquisition. Confocal microscopes detect the emission wavelength of numerous fluorophores and are mostly equipped with various objectives each with different numerical apertures (NA). The NA represents the range of angles an objective is able to capture light and is defined as

$$NA = n \cdot \sin \alpha \quad (3.1)$$

where n denotes the refractive index of the medium and α is the half angle of the maximum light cone that can enter the lens (Müller, 2006).

Consequently, the optical (hardware) setting determines the sampling rate which is necessary to capture all the information of your analyzed specimen to the image. This 'optimal' sampling rate is generally based on the Nyquist-Shannon sampling theorem which states that the minimal sampling frequency for accurate conversion from analog-to-digital information must be more than twice the frequency of the original signal. This relation reads as

$$f_{sampling} \approx 2 \cdot f_{original} + 1 \quad (3.2)$$

where $f_{sampling}$ is the sampling rate and $f_{original}$ denote the maximal frequency of the original signal.

Besides the NA of the used objective, the sampling rate is also affected by the emitted and captured wavelength of the used fluorescence microscope.

microCT imaging

As described in sections 3.1 and 3.2, using various antibodies in order to detect cell specific receptors and tissue respectively, requires sectioning of the specimen in very thin slices which additionally results in loss of information. This irrecoverable information can tremendously influence 3D-reconstruction and interpretation, especially for rather thin structures of several millimeters length like SGNs. Furthermore, time consuming acquisition of 3D image stacks and complex data merging restricts on the one hand quality of specimen reconstruction and influences productivity on the other.

Alternatively, non-destructive imaging methods like X-ray computed microtomography offers the possibility to analyze a complete isotropic data set of small biological structures. Consistent further development of X-ray cameras, diminution of the spot size and improvements of geometrical hardware inaccuracies allow a spatial resolution of few μm offered by commercialized systems. Chapter 7 is based on microCT imaging of two human cochleae which were subsequently used to

- trace and reconstruct nerve fiber bundles along the whole cochlea spiral (isotropic spatial resolution of 3 μm)
- develop a FEM completely based on human hearing organ anatomy (isotropic spatial resolution of 10 μm)

3.4 Data Processing

Confocal Data

The 3D-stacks acquired with the confocal microscope were divided into its component channels (each detected wavelength compose a distinctive channel) for subsequent image restoration. Image restoration is an objective method which reduces the blurring and noise of an image to recover pictured objects of interest (Petrou & Petrou, 2010). Subjecting confocal image data to image restoration is of prime importance when extracting geometrical and morphometrical data respectively, of immunohistochemical stained tissue because it ‘sharpens’ the picture which improves measurement accuracy.

The first step of this procedure is to determine the point spread function (PSF) of the used optical device which represents the aberrations determined by its non-ideal lenses. It describes how the objective distorts the image at each point (pixel) during the acquisition process. In general, there are two ways to define the PSF: (i) calculate theoretically or (ii) determine experimentally. Both approaches were evaluated for CLSM by Kozubek (2001) who published good agreement between the theoretical- and the empirical PSF in fluorescence microscopes. Consequently, the PSFs used for reducing out-of-focus fluorescence of the acquired image stacks studied in this thesis were calculated theoretically using Amira® visualization software (VSG – Visualization Science Group, Burlington, MA, USA).

After generating PSFs for every channel, these functions were used to subsequently deconvolute the image stack. In microscopy, deconvolution has the goal to reassign the optical blur to its original position and to reduce the statistical noise in the images (Sibarita, 2005). This can be realized using a direct- or iterative method, both showing advantages and disadvantages. In general, iterative methods incorporate some prior knowledge about data reducing the probability of occurring artifacts within the restored image solution (Maalouf, 2010). Consequently, the 3D confocal image stacks were deconvoluted using a non-blind maximum-likelihood image restoration algorithm (Holmes & Liu, 1989) over 40 iterations. A further advantage of this algorithm is the assumption that the reduced noise of the stacks underlies a poisson distribution which is a more realistic approach for the case of photons-limited imaging. More details concerning frequently used deconvolution algorithms can be found in van Kempen (1999) and Maalouf (2010).

microCT Data

The reconstructed DICOM stacks of the digitized cochleae (see section 7.3.3) were processed in a first step using a median smoothing filter (edge-preserving, 3x3x3) (Bartscher et al., 2012) for the purpose of enhancing the signal-to-noise ratio. In some stacks it was possible to define a region of interest within the acquired volume which was subsequently cropped in x-, y- and/or z-direction respectively, reducing the amount of data. This procedure improved its handling on the workstation used for further data analysis.

3.5 Data Visualization

The consistent development in hardware technology over the last decades which are used in science produce huge amount of abstract data. The exploration and analysis of this information becomes more and more challenging even though computational power increased steadily. Data is acquired by different methods in multiple fields which needs again different visualization methods. As a consequence, visualization can be divided in two categories: (i) information visualization and (ii) scientific visualization (Friendly, 2008). The common goal of all fields of visualization is to facilitate

existing scientific methods by seeing the unseen through various visual methods (Hansen, 2005). Data visualization provides a first and fast overview of the problem and subsequently assists to focus on qualitative and quantitative analysis and finally – is used for communicating the results.

Scientific visualization focuses on data acquired by scientific experiments that represent samples of continuous functions of space and time (ETH, 2010). It usually involves aspects from medicine, meteorology, biology, astronomy, etc. which are usually taking place in 3D space. The visual processing of data acquired by different imaging techniques such as confocal microscopy or microCT represent examples for scientific visualization. In this thesis, several visualization techniques were used analyze data and subsequently present results. Multiple geometrical parameters which were subsequently incorporated to the compartment model of a cochlear neuron (chapter 2.5) were segmented manually on three dimensional CLSM stacks (chapters 4 and 6) or on reconstructed DICOM files (chapter 7).

To visualize these structures, a geometrical contour representation of the reconstructed surface was created using a surface rendering approach. The contours of the segmented volume(s) are subsequently extracted with surface tiling techniques which are creating polygonal surfaces representing the segmented data. In general, surface rendering has the drawback that it requires segmentation to determine the structure to render. For that reason, potentially important information about structures inside or surrounding the rendered surface is lost (Kim et al., 2008).

Direct volume rendering visualizes every voxel belonging to a 3D scalar field not requiring any previous structure segmentation. This method assumes that every point in the data absorbs and emits light of distinct amounts which is determined from the scalar data by using a colormap (Amira, 2009). To visualize the complete volume data of a DICOM cochlea stack, a shaded and classical texture-based volume rendering technique was used which applies images as textures to geometric objects. The main idea of this method is to create parallel planes through the volume data which numbers are determined by the sampling rate during the data acquisition process. The planes are subsequently converted to polygons that are texture mapped with appropriate 3D texture coordinates derived from the volume data. Finally, the parallel planes are drawn in back-to-front order with blending of the voxel colors to result in a smooth surface. This visualization technique is quite frequently used in visualizing biomedical data due to its image quality and computational efficiency (Kim et al., 2008).

Within this thesis, surface- as well as volume rendering techniques was used to visualize different structures of the digitized human cochlea. The shape of segmented neural structures and their position along the cochlea spiral provided new insight to the micro-anatomical peculiarities and details of this highly sophisticated sensory organ.

3.6 Measurement of Distances within Medical Imaging Data and Extraction of xyz-Coordinates

In order to use the 3D pathways of the segmented human cochlear nerve fiber bundles for computer simulations, the respective xyz-coordinates were extracted. These coordinates were subsequently processed to calculate the length of the peripheral- and central processes as well as the length of the whole segmented fiber bundles originating from varying frequency regions. The evaluated coordinates were additionally used to determine the simulated electrical potentials along the fiber pathways within the developed FEM. Moreover, 3D data was implemented to the compartment model studying the effect of microstimulation to simulate the response of single SGNs.

The extraction of the xyz-coordinates of the manually traced cochlear fiber bundles was carried out using Fiji Win64bit image processing software (Schindelin et al., 2012) which offers the possibility to implement macros. The used macro enabled to highlight a single pixel and save its respective coordinates from every image of the analyzed stack. To calculate the distance (d), and therefore the line segment between such two given points (x_1, y_1, z_1) and (x_2, y_2, z_2) in 3D, the following formula was used

$$d = \sqrt{(x_2 - x_1)^2 + (y_2 - y_1)^2 + (z_2 - z_1)^2} \quad (3.3)$$

where (x_1, y_1, z_1) and (x_2, y_2, z_2) are any two points in the Cartesian plane.

The macro was subsequently used to measure the total length of specimen 1 and 2 and to position the electrodes of two different CIs in anatomical correct position. More application details are presented in section 7.3.6 and 7.3.7. The described method was also used in section 5 to determine the lengths of auditory neurons from the sensory epithelium to the cochlear nucleus located in the brainstem from man and cat.

3.7 Imaging and Data Processing Hardware

Immunostained sections of human as well as cat cochlea specimens were imaged using a Zeiss LSM 510 Meta confocal laser-scanning microscope equipped with a 20x/0.8 NA dry lens and a 63x/1.4 NA oil immersion lens. To simultaneously detect multiple tissue structures labeled with different fluorophores we used a 405 nm diode laser, a 488 nm line of an argon-krypton laser, a 543 nm and a 633 nm HeNe laser. Image capturing was performed using ZEN® software (Zeiss, Jena, Germany). All these experiments were performed in the Laboratory for Inner Ear Biology which is embedded in the Department of Otorhinolaryngology of the Innsbruck Medical University.

The developed FEM of a human cochlea and the reconstruction of 3D pathways of human cochlear nerve fibers (chapter 7) are based on microCT imaging achieved on two devices. The FEM is based on scans carried out on a SCANCO VivaCT 40 with an isotropic resolution of $\Delta x = \Delta y = \Delta z = 10 \mu\text{m}$. The average size of this image stack was 2048*2048*1200 voxels and was acquired using 16-bit grayscale value resolution. For this scan, the following hardware main settings were used: tube voltage was set to 45 kV, tube current to 177 μA , exposure time was 380 ms and 2000 projections were used. Scan time was about five hours for one specimen. Imaging was performed by Dipl. - Ing. Dr. med. Volker Kuhn of the Department of Trauma Surgery and Sports Medicine of the Innsbruck Medical University.

Tracing of 30 cochlea nerve fiber bundles along this sensory organ are based on scans acquired by an ultra-high resolution SCANCO VivaCT 100 micro-CT (Scanco Medical AG, Büttiselle, Switzerland) yielding an isotropic spatial resolution of $\Delta x = \Delta y = \Delta z = 3 \mu\text{m}$. The acquired image stack had a size of 5052*5052*2400 volume elements (voxels), again with 16-bit grayscale value resolution. The tube voltage was set at this scan to 70 kV, tube current to 182 μA and 2000 projections were used. Signal-to noise ratio was improved by averaging of 8 image frames each together with 1600 ms exposure time resulting in a scan time of ~20 hours. This scan was completed by Dr. Bruno Koller, CEO of Scanco Medical AG at Brüttisellen in Switzerland. From all scans, DICOM files were computed for further processing.

Confocal imaging data as well as microCT data were processed, analyzed and visualized on a Z800 high-performance workstation (Hewlett-Packard, Palo Alto, CA, USA) featuring 192 GB RAM, two six-

core Intel® Xeon® processors and a NVIDIA® Quadro 6000 graphic board located in the Laboratory for Inner Ear Biology, Innsbruck Medical University.

3.8 Statistics

Descriptive statistics provided a first overview concerning the distribution of collected parameter of cochlear neurons in all subsequent chapters. Prior to determining any significant differences between data along the cochlea spiral, quantile-quantile (qq) plots were calculated to estimate their normal distribution. A qq-plot represents a probability plot and is a powerful graphical tool to analyze and plot the empirical quantiles of the observed values as a function of the theoretical quantiles (Thode, 2002). This method features higher informative value compared to classical techniques by illustrates every single observation which facilitates the detection of outliers.

Statistical significance of data was calculated by one-way analysis of variance (ANOVA) which contemplates the ratio of two (or more) variances to compare the equality of their mean values (Randolph & Myers, 2013). After determining significance, post-hoc multiple mean comparison tests were conducted on relevant data using Fisher's least significant difference and the more conservative Bonferroni correction method. Furthermore, the actual power of some parameters presented in was calculated at a significance level = 0.01.

Besides standard statistical methods describing the distributions of various evaluated parameters and significant differences, the findings of four different groups of SGNs according their cell body volume are based on a hierarchical clustering. This method requires the user to specify a measure of dissimilarity between (disjoint) groups of observations, based on the pairwise dissimilarities among the observations in the two groups. As the name suggests, they produce hierarchical representations in which the clusters at each level of the hierarchy are created by merging clusters at the next lower level.

In order to calculate a measure of dissimilarity between samples of observations, an appropriate metric and a linkage criterion are necessary (Hastie et al., 2009). For the analyzed data, the best fitting metric was evaluated to be the Chebyshev distance D_{cheb} which is defined in 2D between two points' p and q in a Cartesian coordinate system (x_1, y_1) and (x_2, y_2) as (Cantrell, 2000)

$$D_{cheb} = \max(|x_2 - x_1|, |y_2 - y_1|) \quad (3.4)$$

Together with the Chebyshev distance function, the most appropriate linkage criterion was found to be the unweighted average distance algorithm which reads as

$$\frac{1}{|A| \cdot |B|} \sum_{x \in A} \sum_{y \in B} d(x, y) \quad (3.5)$$

The distance between any two clusters A and B is taken to be the average distances between pairs of objects x in A and y in B , that is the mean distance between elements of each cluster (Murtagh, 1984).

All statistical analysis in this thesis was conducted using Matlab® 2008 and 2011a (MathWorks, Natick, Ma, USA) respectively. Results were (partly) verified with OriginPro 8 (OriginLab, Northhampton, MA, USA) data analysis and graphing software.



Morphometric Classification and Spatial Organization of Spiral Ganglion Neurons in the Human Cochlea: Consequences for Single Fiber Response to Electrical Stimulation

4.1 Abstract

The unique, unmyelinated perikarya of spiral ganglion (SGN) in the human cochlea are often arranged in functional units covered by common satellite glial cells. This micro anatomical peculiarity presents a crucial barrier for an action potential (AP) travelling from the sensory receptors to the brain. Confocal microscopy was used to acquire systematically volumetric data on perikarya and corresponding nuclei in their full dimension along the cochlea of two individuals.

Four populations of SGNs within the human inner ear of two different specimens were identified using agglomerative hierarchical clustering, contrary to the present distinction of two groups of SGNs. Furthermore, we found evidence of a spatial arrangement of perikarya and their accordant nuclei along the cochlea spiral. In this arrangement, the most uniform sizes of cell bodies are located in the middle turn, which represents the majority of phonational frequencies.

Immunohistochemical staining combined with confocal laser scanning microscopy enabled to reconstruct perikarya and their corresponding cell nuclei from human SGNs for determining their volumes. Data were subsequently implemented to an adapted computational model of a human auditory neuron to systematically evaluate the volumetric impact in threshold and AP propagation stimulated by various electrodes with mono- and biphasic pulses.

Since single-cell recordings from other mammals may not be representative to humans and human SGNs are not accessible for physiological measurements, computer simulation has been used

to quantify the effect of varying soma size on single neuron response to electrical micro stimulation. Results show that temporal parameters of the spiking pattern are affected by the size of the cell body. Cathodic stimulation was found to induce stronger variations of spikes while also leading to the lowest thresholds and longest latencies. Therefore, anodic stimulation leads to a more uniform excitation profile among SGNs with different cell body size.

4.2 Introduction

Within the mammalian cochlea the existence of two different types of spiral ganglion cells (SGNs) based on morphological criteria is well described. A vast majority of 90 - 95% belong to 'large' type I cells while only 5 - 10% are assigned to 'small' type II SGNs (Ota & Kimura, 1980; Spoendlin, 1981). One significant feature of the human spiral ganglion cells is the lack of myelin layers around the majority of their perikarya. Only 5% of the neurons are surrounded by several loose myelin layers (Arnold, 1987; Ota & Kimura, 1980; Spoendlin & Schrott, 1989) often arranged in functional units covered by common satellite glial cells (Liu et al., 2012).

Prior research has led to speculation that the unique human morphology of SGN somata (Tylstedt & Rask-Andersen, 2001; Glueckert et al., 2005b) affects excitability and spiking pattern (Rattay et al., 2001a; Rusznák & Szucs, 2009) since these unmyelinated neuronal parts are the first energy barrier for an action potential travelling from the sensory epithelium to the auditory cortex (Rattay, 1995; Rattay et al., 2001a). Nevertheless, ever since Hodgkin & Huxley (1952) developed their model of a nonmyelinated squid axon, functional electrical stimulation has focused on myelinated nerve structures and nodes of Ranvier. Thus, in order to simulate the response of single SGNs to micro stimulation, some modelers have considered the soma to be myelinated (Frijns et al., 1994) or passive (Woo et al., 2009b), while others have completely neglected the presence of a soma (Mino et al., 2004). Since detailed data of this specific human feature is currently available, theoretical analysis concerning single neuron response shall incorporate fundamental anatomical data. These peculiarities of human SGNs are not considered so far while a growing amount of studies about cochlear implant strategies, electrode positioning within the cochlea, psychological measurements and recorded audiograms emerge. Nonetheless, the physiology of hearing is not yet fully understood, e.g., complex coding strategies as speech recognition and perception in noisy (Drennan et al., 2007), attenuation effects (Smit et al., 2009) and the temporal fine structure of the neural pattern.

In order to gain further knowledge of the shape, distribution and size of this unique human neuronal part, we acquired 3D morphometrics confocal stacks of normal human SGNs systematically and analyzed them using an agglomerative hierarchical cluster algorithm. Determination of neuronal classes based on micro-anatomic features of cochlea perikarya provides crucial geometric information from human spiral ganglion neurons.

Since vital human SGNs are not experimentally accessible, we used computer simulation to study possible changes in excitability with respect to varying soma sizes. To do this, we adapted the model of Rattay et al. (2001a), because it is the only cochlear nerve model which accounts for the poorly myelinated soma region in man. Based on our analysis of morphometric data, this paper sheds light on the difference in thresholds and action potential (AP) properties of single neurons stimulated by microelectrodes with mono- and biphasic pulses at different positions.

4.3 Materials and Methods

4.3.1 Specimens

The present study evaluated two temporal bones from individuals aged 74 (specimen 1, male) and 56 (specimen 2, male), respectively, without any known inner ear disease or hearing loss (audiograms not available). The temporal bones were obtained during routine autopsy at the Institute of Pathology, Innsbruck Medical University. Cochleae were fixed with ice cold 4% paraformaldehyde buffered with 0.1 M phosphate buffered saline (PBS, pH=7,4) within <5h post mortem via the round- and oval window and were immersed in the same fixative for 24h at 4°C. Small-sized diamond drills were used to mill off cochleae-surrounding bone. The cochleae were then dissected cochleae using a stereo microscope and forceps and subsequently cochleae were then decalcified using 20% Ethylenediaminetetraacetic acid at pH 7.4 for 6 weeks, after which they were and rinsed thoroughly in PBS. Inner ears were prepared for cryoembedding according to Coleman et al. (2009). Specimens were serially sectioned with a cryomicrotome perpendicularly and radially respectively, to the modiolus at 35 μ m thicknesses, thereby providing bipolar spiral ganglion somata in their full dimensions (Tylstedt et al., 1997; Tylstedt et al., 1997) on each cryosection.

4.3.2 Immunohistochemistry

In order to delineate perikarya from their surrounding satellite glial cells, antibodies against β -III-tubuline and the intermediate filament S-100 were used. After washing the sections in PBS (pH = 7.4; 3x10 min), non-unspecific sites were blocked with a dilution containing 0.1 M PBS, 30% normal donkey-serum and 0,3% Triton X-100 for 2 hours at room temperature. Cryosections were incubated overnight in a humid chamber at 4°C with a mixed solution of mouse-monoclonal anti- β -III-tubuline antibodies (1:500, Chemicon, Billerica, MA, USA) and rabbit-polyclonal anti-S-100 antibodies (raised against whole S-100 protein purified from bovine brain, 1:200, Sigma-Aldrich, St. Louis, MO, USA), followed by 75 minutes at 37°C.

After being rinsed with PBS (3x10 min), sections were incubated with secondary antibodies conjugated to Alexa Fluor 488 (donkey anti-mouse, 1:1000, Invitrogen, Carlsbad, CA, USA) and Alexa Fluor 633 (donkey anti-rabbit, 1:400, Invitrogen, Carlsbad, CA, USA), diluted in PBS for 2 hours at RT and mounted using Vectashield mounting medium with DAPI (Vector Laboratories, Burlingame, CA, USA) for additional nuclei-counterstaining. Figure 4.1 presents an example of immunolabeling of TuJ1 (green), S-100 (red) and DAPI (blue) staining of the human spiral ganglion. White arrows indicate cell-body candidates for volumetric reconstruction. Only perikarya completely surrounded by satellite glial cells without showing any shrinkage were chosen for three dimensional (3D) reconstructions.

4.3.3 Acquisition of confocal data

Sections were analyzed on a Zeiss LSM 510 Meta or a Leica SP5 confocal laser-scanning microscope equipped with a 63x/1.4 NA oil immersion lens. Simultaneous detection of perikarya and satellite glial cells involved excitation with the 488 nm line of an argon ion laser and a 633 nm HeNe laser. Cell nuclei were visualized using a 405 nm diode laser. Pixel sizes selected according to the Nyquist criterion were used for the acquisition of 3D-stacks, resulting in the following resolution: x=38 nm, y=38 nm, z=122 nm.

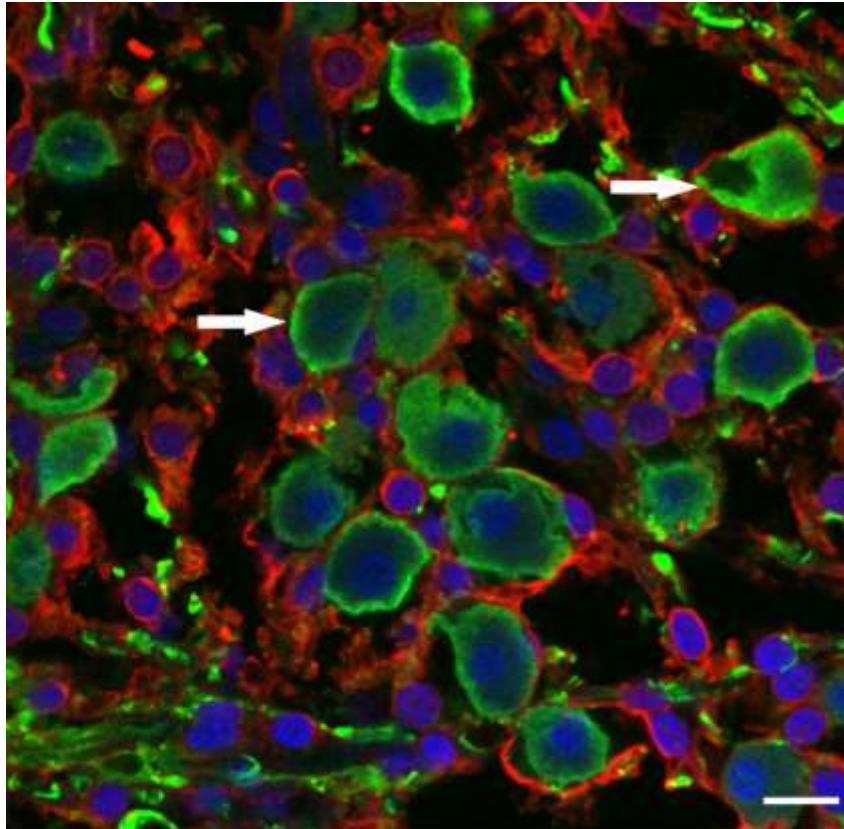


Figure 4.1: Immunolabeling forTuJ1 and S-100 in human spiral ganglion. SGNs are stained positively for TuJ1 (green). The satellite glial cells surrounding SGNs are strongly stained for S-100 (red). Nuclei of neurons and satellite cells are illustrated blue. White arrows indicate cell-body-candidates for volumetric reconstruction. Scale bar represents 20 μm .

4.3.4 Image processing

Confocal image stacks of the SGNs were processed with a high-performance workstation (Z800, Hewlett-Packard, Palo Alto, CA, USA, 32 GB RAM, a six-core Intel[®] Xeon[®] processor and a Quadro FX4600 graphical board) using Amira 5.3.3 (Mercury Computer Systems Inc., San Diego, CA, USA). Each stack was separated subsequently into its component channels to allow for image restoration via individual deconvolution. As a result, a theoretical point spread function was computed for each channel. The point spread functions were then used to deconvolute each channel using a non-blind maximum-likelihood image restoration algorithm (Holmes & Liu, 1989) over 40 iterations. To improve signal-to-noise-ratio a median filter was applied to the data prior to structure segmentation. Perikarya and nuclei were manually segmented using the Amira's 'Segmentation Editor'. Segmentation data were saved in a label field which was used to determine the volume of each structure using the 'MaterialStatistics' module from Amira. For visualization, data were smoothed by producing a surface from a resampled label field.

4.3.5 Statistical analysis

Statistical significance was calculated using one-way analysis of variance followed by Fisher's least significant difference (LSD) test and the Bonferroni correction. Normality of data was carried out using quantile-quantile plots. Hierarchical cluster analysis was performed on volumes of segmented SGN and corresponding nuclei in order to identify clusters with comparable similarities. In the

absence of an expectation as to the number of clusters present, we used an agglomerative (bottom-up) approach that starts with as many clusters as objects. Clusters are gradually merged in the following way until each object belongs to a cluster. All members of a cluster feature comparable similarities. For determining similarities between each pair of objects the distance matrix was calculated using the Chebyshev distance (maximum coordinate difference). This distance information was applied to ascertain the proximity of cell volumes to each other computed by the unweighted average distance algorithm.

To choose the best fitting distance metric and algorithm examining the present structures in the pairwise distance matrix of data, the cophenetic correlation coefficient was calculated systematically (data not shown). Both above mentioned algorithms reached the highest cophenetic correlation coefficient (0.84 ± 0.02).

To gain more information about the distribution of the volumes, the normalized eigenvalues of the correlation matrix were calculated and visualized in a scree plot (Cattell, 1966). These values indicate the percentage of variance explained. A linear fit (Nelson, 2005) calculated with the first 14 normalized eigenvalues was used to overcome reported problems of finding the distinctive sharp break (Costello & Osborne, 2005).

The 'sharp break' was defined at the number of populations where R^2 of fitting was ≥ 0.8 . Statistics were performed using MatLab[®] 2011a (MathWorks, Natick, MA, USA).

4.4 Computational model

In order to analyze the effect of the collected variations in soma size of human cochlear neurons, a detailed compartment model of one specific neuron was used. The two processes were split up into cylindrical compartments consisting of passive internodes (6 of varying size for the peripheral process with 40 layers of myelin, 5 central internodes with 80 layers of myelin) and active nodes of Ranvier. The spherical soma as well as the postsomatic and also the preceding presomatic region, consisting of three compartments, are assumed to be unmyelinated, i.e., only surrounded by 3 membrane layers (one SGN membrane, two satellite glial membranes) and modeled as active compartments with Hodgkin Huxley ion channel kinetics. Note that the original standard value of 30 μm for the diameter of the soma is certainly higher than the observed values, as discussed below. For details about geometric and electrical parameters see Rattay et al. (2001a).

For the simulations in this study all geometric and electrical model parameters are regarded to be constant, except the value of the soma diameter that was calculated from collected volumetric data of different human SGNs. By varying the diameter of the soma the influence on action potential (AP) properties and thresholds to micro stimulation was examined. Parameters like the AP height and AP width are explained in detail in Bean (2007). For the stimulation by a point electrode, thresholds for different electrode positions and four pulse shapes have been calculated (i.e., 0.1 ms long monophasic pulses for cathodic amplitudes and anodic pulses as well as biphasic pulses of equal amplitudes with 0.05ms/phase for leading cathodic phase or pulses with anodic phase first).

Four active electrode positions that correspond to cochlear implant situations in the basal turn have been examined and are illustrated in Figure 4.2. Two electrode positions (E1 and E2) simulate electrodes placed at the transition between bony columns housing nerve fiber bundles and osseous spiral lamina (E1) and at the distal end of the osseous spiral lamina (E2). E1 was previously introduced by Rattay et al. (2001a).

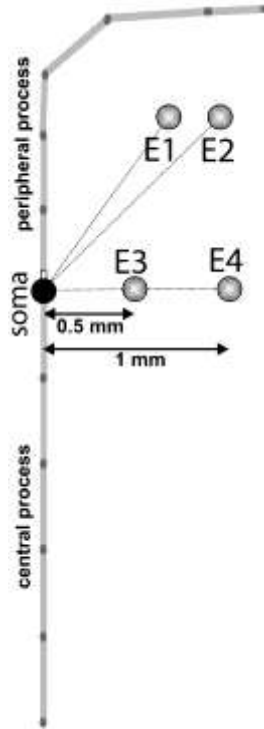


Figure 4.2: Electrode positions and spatial arrangement of the model neuron compartments. Peripheral and central processes are segmented in light grey internodes and black nodes of Ranvier. E1 and E2 simulate electrodes placed at the transition between bony columns and at the osseous spiral lamina. E3 and E4 are placed normal to the soma at two different distances.

E3 and E4 correspond to positions of a cochlear implant electrodes placed at the level of Rosenthal's canal that contain SGN somata orthogonal to the neural axis (Figure 4.2) in a distance of 0,5 mm (E3) and 1 mm (E4). Therefore E1 and E2 represent typical electrode positions with straight electrode arrays, whereas E3 and E4 illustrate perimodiolar electrode placement (Figure 4.2).

Additionally, the following parameters were acquired during simulation: the initiation site (IS), the corresponding time of the peak as well as the arrival time of the spike at the soma and the time at which the AP occurs at the end of the neuron as defined by the last compartment.

We assumed a spherical electrode in an infinite homogeneous extracellular medium with a resistivity of $\rho_e = 300 \text{ Ohm cm}$. Under quasi-static conditions the extracellular potentials V_e were calculated by

$$V_e = \frac{\rho_e * I_{electrode}}{4 \cdot \pi \cdot r} \quad (4.1)$$

where r is the distance from a compartment to the electrode and $I_{electrode}$ is the amplitude of the stimulating current pulse. The current to the center of the n-th compartment of the model neuron consists of the following components: capacitive current, ion currents across the membrane and ohmic currents to the left and right neighbors.

The following system of differential equations is deduced by introducing the transmembrane voltage

$$V^n = V_i^n - V_e^n$$

to compute the time course of V^n in every compartment. Applying Kirchhoff's law for compartment n results in

$$\frac{dV^n}{dt} = \left[-I_{ion}^n + \frac{V^{n-1} - V^n}{\frac{R^{n-1}}{2} + \frac{R^n}{2}} + \frac{V^{n+1} - V^n}{\frac{R^{n+1}}{2} + \frac{R^n}{2}} + \frac{V_e^{n-1} - V_e^n}{\frac{R^{n-1}}{2} + \frac{R^n}{2}} + \frac{V_e^{n+1} - V_e^n}{\frac{R^{n+1}}{2} + \frac{R^n}{2}} \right] / C_m^n \quad (4.2)$$

where V_i , R and C_m denote the intracellular potential, axial resistance and membrane capacity, respectively. In order to compute these parameters for each compartment, an intracellular specific resistivity of 150 Ohm cm and a specific membrane capacity of 1 $\mu\text{F}/\text{cm}^2$ (Rattay et al., 2001a) were used. Note that the resistance and capacitance of the somatic compartment will also change with varying diameter since the surface is also altered.

4.5 Results

4.5.1 Descriptive Statistics

To provide an overview of quantified volumetric data we quantitatively described the main features of spiral ganglion cell somata and their corresponding nuclei. For this purpose we discuss the median (M) in this section as it best describes the central tendency of the reconstructed perikarya.

4.5.2 Perikarya

A closer look at specimen 1 shows that the perikaryal size of the apical- and basal turn are comparable ($M_{\text{apical}}=4235 \mu\text{m}^3$, $M_{\text{basal}}=4011 \mu\text{m}^3$), varying only by 5.2%, with the largest cells located in the apex. The smallest SGNs from this inner ear are identified within the middle turn ($M=3379 \mu\text{m}^3$) representing a volumetric difference of 20.2% compared to the median apical value. There is no significant difference regarding the perikarya volumes determined in Specimen 1 (Figure 4.3 A).

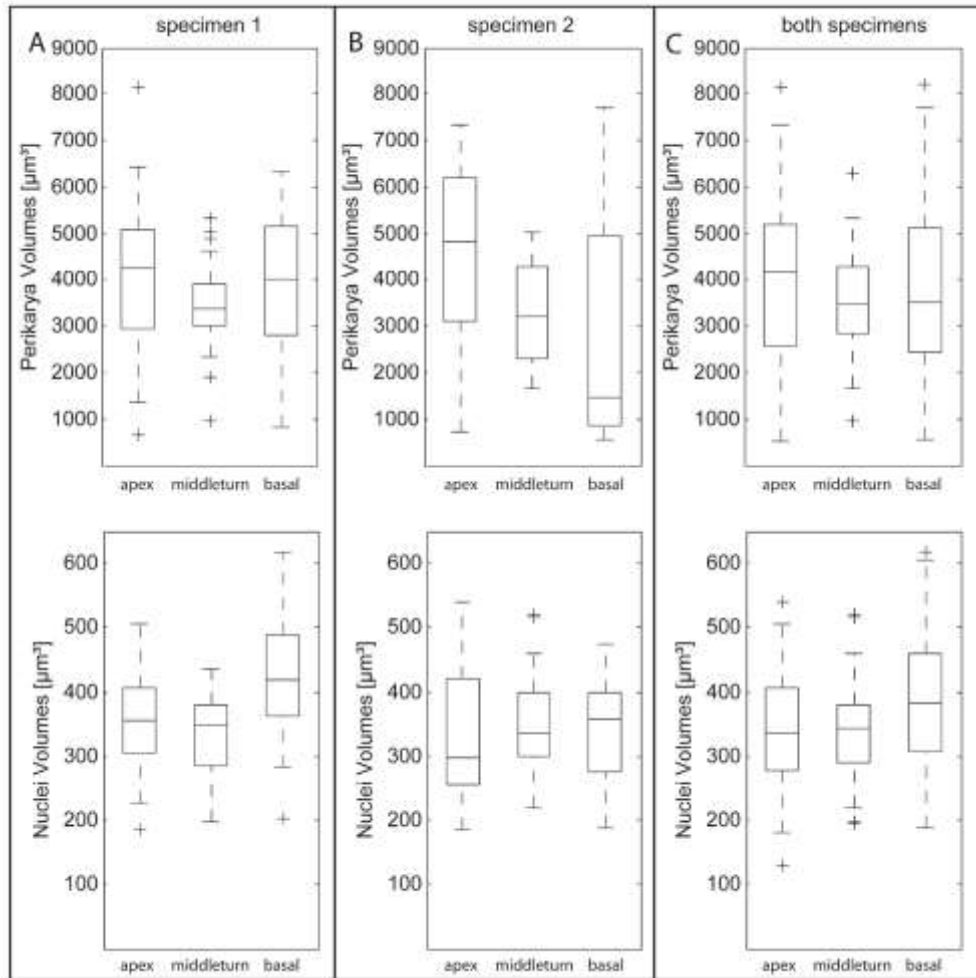


Figure 4.3: Box-Whisker-Plot depicts distributions of volumes from reconstructed perikarya and their nuclei. Data illustrates all acquired volumes of specimen 1 (column A, n=83), specimen 2 (column B, n=55) and both specimens (column C, n=138) according to their location within the human cochlea. The upper horizontal row illustrates perikaryal volumes; lower horizontal row represents the corresponding nuclei.

The SGNs in the apical turn of specimen 2 (Figure 4.3B) likewise reach the highest evaluated volumes ($M=4818 \mu\text{m}^3$). In addition, the smallest SGNs ($M=1474 \mu\text{m}^3$) in this specimen are also identified in the basal turn, reaching a volume 69.4% smaller than the perikarya in the low frequency region. The SGNs in the middle turn ($M=3208 \mu\text{m}^3$) show a 33.4% lower volume compared to cell bodies of the apical region. Significant difference in SGN volume is found in this specimen between the apical- and the basal turn ($p<0.1$, LSD).

The biggest SGNs in both specimens ($M=4197 \mu\text{m}^3$) are found in the apical turn (Figure 4.3A, Table 4.1). These SGNs show 17.3% higher volume compared to the perikarya measured in the middle turns ($M=3473 \mu\text{m}^3$). Reconstructed SGNs from the basal turn of both specimens reach an M of $3510 \mu\text{m}^3$, which is only 1.1% larger than the cells from the middle turn. No significant difference is found between perikaryal volumes of apical-, middle- and basal turn; however, the largest cells are observed in the low-frequency region (Figure 4.3 B and C).

An individual difference in SGN volume between specimen 1 and 2 is found in the basal region ($p < 0.1$, LSD). Perikarya of the basal region from specimen 1 are 63.3% bigger than neurons of the corresponding region in specimen 2.

Moreover, the difference in volume between the apical regions of the cochleae is 13.8%. Surprisingly, SGN volumes in the middle turn are rather uniform; the percentage difference between SGN volumes from the middle turns of both cochleae is found to be only 5.1%. Note the upper adjacent value (UAV) and lower adjacent value (LAV) of the middle turns presented on Table 4.1.

Perikarya	Region	Median	d	Q _L	Q _U	UAV	LAV
specimen 1	apical	4235	20.07	2948	5103	6436	1345
	middleturn	3379	18.62	2996	3928	4621	2321
	basal	4011	19.71	2789	5165	6325	825.9
specimen 2	apical	4818	20.96	3118	6190	7345	732
	middleturn	3208	18.30	2291	4298	5024	1659
	basal	1474	14.12	861.8	4962	7713	570.2
both specimens	apical	4197	20.01	2572	5184	7345	531,6
	middleturn	3473	18.79	2821	4298	5337	1659
	basal	3510	18.86	2439	5121	7713	570,2
Nuclei							
specimen 1	apical	355.1	8.79	303.3	407.2	506.5	226.3
	middleturn	346.9	8.72	284.8	380.3	434.9	196.5
	basal	419.4	9.29	361.7	489.8	617.8	282.8
specimen 2	apical	298.2	8.29	256.4	421.2	540	186.2
	middleturn	334.9	8.62	300.4	398.3	458.9	218.4
	basal	357.9	8.81	276.1	399.3	473	187
both specimens	apical	335.9	8.62	277	406.3	506.1	180.5
	middleturn	344	8.70	289.5	379.5	458.9	218.4
	basal	381.7	9.00	306.5	459.8	606.2	187

Table 4.1: Summary of the determined perikarya- and nuclei volumes and their diameters. Presented data were calculated from manually segmented data. The first part presents the evaluated perikarya volumes of both analyzed cochleae ($n=138$), specimen 1 ($n=83$) and specimen 2 ($n=55$) according to their location within the inner ear. Volumetric data of corresponding nuclei is shown in the lower part of the table in the same manner by the median (M [μm^3]), the lower quartile (Q_L [μm^3]), upper quartile (Q_U [μm^3]) as well as the lower adjacent value (LAV [μm^3]) and the upper adjacent value (UAV [μm^3]); d is shown as μm .

Remarkably, the absolute differences between these two values are $2300 \mu\text{m}^3$ ($n=25$) for specimen 1 and $3365 \mu\text{m}^3$ ($n=21$) for specimen 2, respectively. This absolute difference is only about 50% compared with other regions of specimen 1 (apical turn = $5091 \mu\text{m}^3$, basal turn = $5499 \mu\text{m}^3$) and specimen 2 (apical turn = $6613 \mu\text{m}^3$, basal turn = $7143 \mu\text{m}^3$).

SGN volumes of the middle turn in specimen 1 and the apical turn of Specimen 2 were calculated to be significantly different ($p < 0.1$, LSD).

4.5.3 Nuclei

Specimen 1 show slight differences between apical- ($M=355.1 \mu\text{m}^3$) and middle turn ($M=346.9 \mu\text{m}^3$) nuclei (-2.3%), whereas basal nuclei are 18.1% bigger ($M=419.4 \mu\text{m}^3$) compared to the apical turn (Figure 4.3A). Significant differences in the volume of nuclei are determined when comparing the apical- and middle turn with the basal region in specimen 1 ($p < 0.05$, Bonferroni).

SGN nuclei in specimen 2 are 12.3% bigger in the apical ($M=298.2 \mu\text{m}^3$) compared to the middle turn ($M=334.9 \mu\text{m}^3$) and 20% bigger compared to the basal ($M=357.9 \mu\text{m}^3$) SGN nuclei, respectively (Figure 4.3 B). However, nuclei volumes are not found to be significantly different along the cochlea spiral in specimen 2.

Analyzing data from both specimens (Figure 4.3C), we found the smallest nuclei of SGNs (Table 4.1) in the apical region of the cochleae ($M=335.9 \mu\text{m}^3$), slightly larger (+2.4%) nuclei in the middle turn reached a median of $344 \mu\text{m}^3$ and in the basal turn $381.9 \mu\text{m}^3$. This increase in volume (basal turn nuclei) corresponds to 13.7% bigger nuclei compared to the nuclei in the apical turn. A significant difference is found when comparing volumes of the apical- and middle turn with the nuclei of the basal turn ($p < 0.05$, Bonferroni).

Furthermore, between the basal turn of Specimen 1 and the apical-, middle- and basal turns of Specimen 2 the volumetric difference is calculated to be significant ($p < 0.05$, Bonferroni).

4.6 Hierarchical Clustering

Agglomerative hierarchical cluster analysis of volumetric data was used to identify similarities among reconstructed SGNs. The volume distribution was examined with scree plots of the percentage of variance explained which is described as a function of the amount of clusters.

4.6.1 Specimen 1

The applied algorithm of the cluster analysis identified four distinct populations of SGNs in specimen 1 ($n=83$). Figure 4.4A presents the results of this hierarchical clustering: The distinct groupings of the determined SGN-populations are color-coded in the scatterplot. These populations differ considerably in perikaryal size as well as in their incidence. The smallest identified population 1 of this cochlea is formed by 12% of reconstructed perikarya (Figure 4.4A, violet colored) with a mean volume of $1288 \pm 496 \mu\text{m}^3$. Interestingly, their corresponding nuclei are also found to be the smallest within the four populations ($228.2 \pm 60.4 \mu\text{m}^3$). The majority of measured cell bodies belonging to specimen 1 are classified as population 2 (80.7%) and have a mean volume of $3878 \pm 932.6 \mu\text{m}^3$ (green colored). Their nuclei are identified to be slightly larger ($372.8 \pm 80 \mu\text{m}^3$) compared to the nuclei from population 1. Cell population 3 is represented by 5.8% ($6297 \pm 140.7 \mu\text{m}^3$, red) of reconstructed perikarya (red colored). Their associated nuclei have a mean volume of $436.1 \pm 97.5 \mu\text{m}^3$ and represent the third-largest reconstructed group. The largest population 4 is represented by a single cell body with a mean volume of $8148 \mu\text{m}^3$ (cyan color). The volume of this perikaryon is 632.7% bigger compared to the mean volume calculated for population 1. Similarly, its nucleus measures $506.5 \mu\text{m}^3$, the largest reconstructed from this specimen. The volumetric difference compared with the corresponding value of the smallest population is 222%.

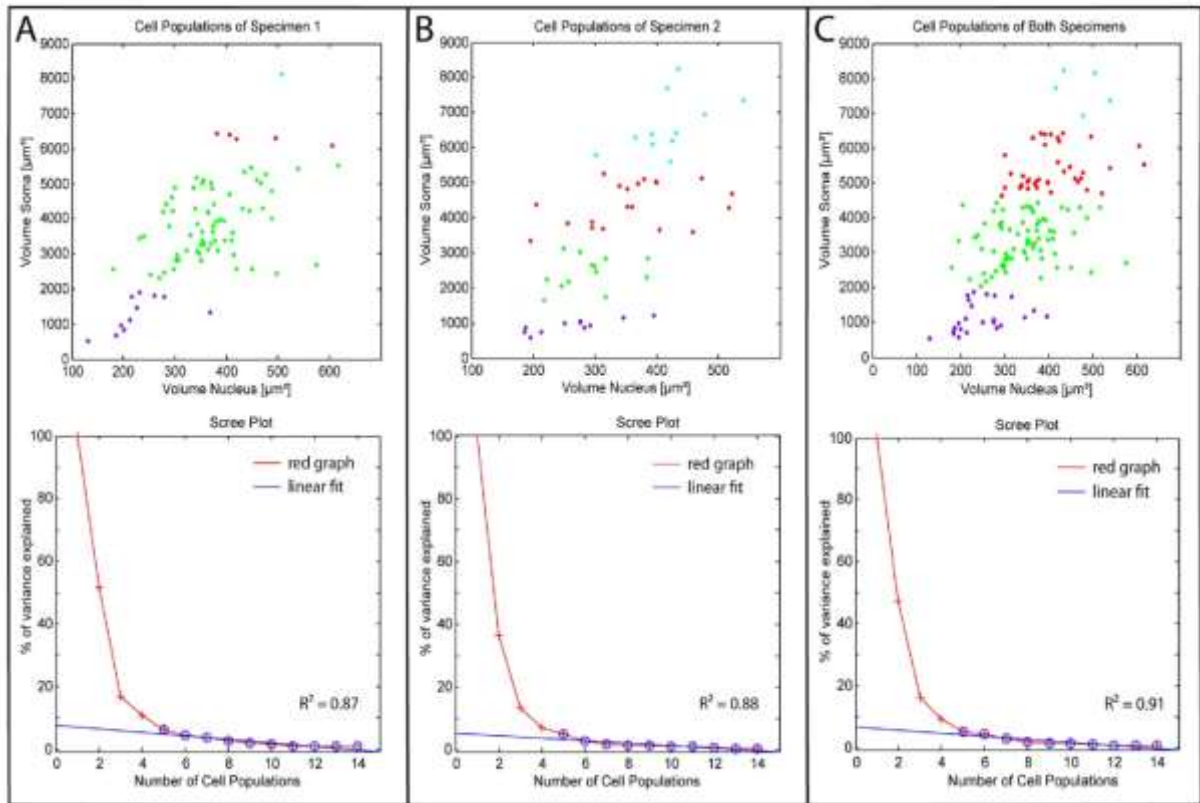


Figure 4.4: Result of the cluster analysis of reconstructed perikarya from specimen 1 (A, $n=83$), specimen 2 (B, $n=55$) and both specimens (C, $n=138$). The scatterplot illustrates arrangement of clusters in a color-coded manner, identified by the agglomerative hierarchical cluster algorithm applied on volumetric data. Purple dots represent the smallest cell population 1 while green and red colored dots illustrate population 2 and population 3 respectively. The biggest cell population 4 is visualized by cyan-colored dots. The screeplot strongly support the determined four cluster solution for each of the three data sets. The red graph presents the calculated percentage of variance explained. For determining the ‘sharp break’ in the scree plot a linear fit (blue line) of the percentage of variance explained was calculated. The “sharp break” was defined at the number of populations where R^2 of fitting was ≥ 0.8 .

The existence of 4 different populations among the analyzed SGNs of specimen 1 is strongly supported by the scree plot shown in Figure 4.4A, which shows a linear fit ($R^2 = 0.87$) of the percentage of variance explained. Furthermore, the volumes of the four identified perikaryal SGN populations and their corresponding nuclei are calculated to be significantly different from each other ($p < 0.001$ for perikarya and $p < 0.01$ for nuclei respectively, Bonferroni).

The determined classes of SGNs are also identified among cell bodies from the apical-, middle- and basal turn of the cochlea and show very large differences in the incidence of cells within the populations of distinct turns. Detailed data is given in Table 4.2.

4.6.2 Specimen 2

Figure 4.4B (same color-coded manner as used for specimen 1) presents the result of hierarchical cluster analysis of reconstructed perikarya of specimen 2. The evaluated SGNs of the four identified populations are much more homogeneously distributed, as seen in Table 4.2.

One-fifth of the cell bodies scanned in specimen 2 are classified to form population 1 ($919 \pm 192 \mu\text{m}^3$, violet colored). The appropriate nuclei of this smallest population are again the smallest reconstructed from specimen 2 ($264 \pm 67 \mu\text{m}^3$). The second population, illustrated in green contains 23.6% of all analyzed cell bodies within this specimen and has a mean volume of ($2441 \pm 461.3 \mu\text{m}^3$). Compared to population 1, their nuclei are found to be slightly larger ($290.2 \pm 53.4 \mu\text{m}^3$). Population 3 is composed of 36.4% of reconstructed perikarya with a mean volume of $4393 \pm 620.5 \mu\text{m}^3$ (red). Their corresponding nuclei have a mean volume of $359.9 \pm 89.9 \mu\text{m}^3$. Another fifth of all analyzed SGNs from specimen 2 are classified as the largest population 4 with a mean volume of $6636 \pm 826 \mu\text{m}^3$ (cyan). The reconstructed nuclei from the cells of this population represent the largest from this specimen with a mean volume of $418 \pm 60.6 \mu\text{m}^3$.

The scree plot ($R^2=0.88$) strongly supports the existence of the identified four population solution in specimen 2. Moreover, the reconstructed volumes of the four populations and their corresponding nuclei are shown to be significantly different from each other ($p < 0.001$ for perikarya and $p < 0.1$ for nuclei respectively, Bonferroni).

After dividing scanned cell bodies according to their origin along the cochlea spiral, the described four population solution is also determined for the apical-, middle- and basal region of this cochlea and strongly supported by the scree plot (for details see Table 4.2).

Cochlea Region	classification	specimen no. 1						specimen no. 2						both specimens						
		perikarya		nuclei		n =	Frequ. [%]	perikarya		nuclei		n =	Frequ. [%]	perikarya		nuclei		n =	Frequ. [%]	
Mean [μm^3]	SD [μm^3]	Mean [μm^3]	SD [μm^3]	Mean [μm^3]	SD [μm^3]			Mean [μm^3]	SD [μm^3]	Mean [μm^3]	SD [μm^3]			d [μm]	Mean [μm^3]	SD [μm^3]	Mean [μm^3]			SD [μm^3]
whole cochlea(e)	Population 1	1287.8	496	228.2	60.4	10	12.0	919.3	192	264	67	11	20	1153.8	13.01	429.7	247.9	64	24	17.4
	Population 2	3878.1	932.6	372.8	80	67	80.7	2440.6	461.3	290.2	53.4	13	23.6	3351.6	18.57	661.3	343.4	77.7	72	52.2
	Population 3	6297.4	140.7	436.1	97.5	5	5.8	4392.5	620.5	359.9	89.9	20	36.4	5407.1	21.78	592.5	409.6	74.7	37	26.8
	Population 4	8148.1	0	506.5	0	1	1.1	6635.6	826	418	60.6	11	20	7674.5	24.47	543.3	475.1	50.6	5	3.6
apical turn	Population 1	1859.5	829.1	254.3	69.8	12	37.5	874.4	201.6	231.4	63.9	2	14.3	1161.7	13.04	472.6	236.3	69.1	9	19.5
	Population 2	4416.4	558.3	373.7	58.7	17	53.1	3616.1	551.2	256.5	34.2	5	35.7	3599.3	19.01	642.6	323.5	78.3	20	43.5
	Population 3	6418.4	25	394.5	16.7	2	6.3	5843.7	453.8	370.7	59	5	35.7	5722.6	22.19	803.3	391	64.4	16	34.8
	Population 4	8148.1	0	506.5	0	1	3.1	7142.1	286.8	508.8	44	2	14.3	8148	24.97	0	506.5	0	1	2.2
middleturn	Population 1	970.9	0	196.5	0	1	4.2	2293.6	359.7	281	55.8	8	38.1	2048.7	15.76	450.7	258.3	53.1	10	21.7
	Population 2	2211	280.6	251.8	19.8	3	12.5	3621.3	222.6	315.4	108.6	4	19	3376.1	18.61	385.1	337.5	64.5	22	47.8
	Population 3	3513.3	480.8	343.4	54	17	70.8	4682.6	338.1	402.5	74.1	8	38.1	4739.3	20.84	352.6	383	68.9	13	28.3
	Population 4	5078.1	234.4	375	52.6	3	12.5	6293.2	0	364.7	0	1	4.8	6293.2	22.91	0	364.7	0	1	2.2
basal turn	Population 1	852.9	0	201.9	0	1	3.7	1011.7	322.5	275.9	66.8	10	50	1025.1	12.51	298.7	274.8	64.7	11	23.9
	Population 2	2942.4	438.6	402.4	81.8	13	48.2	3035.6	529.9	361.5	58.3	3	15	3034.8	17.96	446.5	388.9	73.2	16	34.8
	Population 3	4822.3	535.8	456	94.6	10	37	5519.1	688.9	413.5	39.9	5	25	5250	21.56	750.4	452.9	84.5	17	37
	Population 4	6227.2	132.7	507.9	93.2	3	11.1	7970.2	363.9	425.7	12.5	2	10	7970.2	24.78	363.9	425.7	12.5	2	4.3

Table 4.2: Summary of all determined perikarya- and nuclei volumes. Calculated mean \pm SD volumes [μm^3], diameter (d) [μm], number of cells (n) and frequency [%] of reconstructed perikarya and their corresponding nuclei of human cochleae are presented for pooled data of both cochleae as well as specimen-separated. Calculated volumes are additionally shown for apical-, middle- and basal turn of investigated specimen. Furthermore, evaluated values are presented for each population classified by the hierarchical cluster algorithm. The first horizontal row (whole cochlea(e)) presents data calculated from all reconstructed cell bodies and their nuclei from specimen 1, specimen 2 and pooled data of both specimens respectively. The following horizontal rows (apical-, middle- and basal turn) show calculated data of analyzed SGNs according to their origin along the cochlea spiral.

4.6.3 Individual differences

Comparing both analyzed specimens with respect to the distribution of SGN populations and incidence of cells within the populations in distinct turns offers striking individual variations (Table 4.2). As already stated, it is found that the majority of measured cell bodies belonging to specimen 1 are classified as population 2 (80.7%, n=83), whereas in specimen 2 some shifts of relative distribution in SGN populations are apparent. The corresponding group identified in specimen 2 contains 23.6% (n=55) with a mean volume that is 37.1% smaller compared to specimen 1.

Another example of individual differences is found within the middle turn. Only 4.2% (n=24) of SGNs are assigned to the smallest group in Specimen 1. However, no comparable 'small' population of cells is found in specimen 2.

The second biggest perikaryon is found in the apical turn of specimen 1, representing population 4 (3.1%, n=32). In contrast, the mean volume of the corresponding population of specimen 2 is 18.6% smaller while containing 20% (n=55) of the reconstructed somata.

Both the largest and smallest perikarya were found in specimen 2. 80% of the identified 'giant' neurons (n=5) were localized in specimen 2 within the apical- as well as the basal turn. In the basal turn, representing the high frequency region in cochleae, 50% (n=20) are classified as the smallest group (population 1), whereas only 3.7% (n=27) are classified as this population in specimen 1.

4.6.4 Pooled Data of Both Specimens

Hierarchical cluster analysis of the pooled volumetric data set demonstrates the distribution of reconstructed perikarya of both cochleae (n=138).

Figure 4.4C presents the results of this hierarchical clustering where the distinct grouping of the determined SGN-populations is shown in the same color-coded manner as was previously introduced. The existence of four classes of cell somata with respect to micro-anatomical features is found once again in pooled data of these two individual human cochleae.

17.4% of neurons could be assigned to the group with smallest cell bodies (population 1, violet) with a mean volume of $1154 \pm 429.7 \mu\text{m}^3$. Similarly, their corresponding nuclei are found to be the smallest within the identified populations with a mean volume of $247.9 \pm 64 \mu\text{m}^3$. Population 2 (green) contains the majority (52.2%) of all reconstructed SGNs with a mean soma volume of $3352 \pm 661.3 \mu\text{m}^3$. Interestingly, their corresponding nuclei range in volume from $180.4 \mu\text{m}^3$ (smallest) to $576 \mu\text{m}^3$ (largest), a volumetric difference of 314% within this determined population. This increase of size represents the largest variation of nuclei volume within all detected populations. The third identified population (population 3, red) of SGN covers 26.8% of all analyzed cells with a mean volume of $5407 \pm 592.5 \mu\text{m}^3$. Their corresponding nuclei have a mean volume of $409.6 \pm 74.7 \mu\text{m}^3$. The largest SGNs form population 4 (cyan). Only 3.6 % of all cells comprise this giant population of SGNs with a mean volume of $7675 \pm 543.3 \mu\text{m}^3$. The mean volume of these cells is 6.65 times larger than that of population 1. The volume of their nuclei is quantified as $475.1 \pm 50.6 \mu\text{m}^3$.

The existence of 4 different populations among the analyzed SGNs of both cochleae is strongly supported by the scree plot (Figure 4.4C) with a linear fit ($R^2 = 0.91$) of the normalized eigenvalues. Furthermore, the volumes of the four identified perikaryal SGN populations and their corresponding

nuclei are found to be significantly different from each other ($p < 0.001$ for perikarya and $p < 0.01$ for nuclei respectively, Bonferroni).

Likewise, the four classes of SGNs were individually examined in the apical-, middle- and basal turns of the cochleae presented in Table 4.2.

Within the apical- (population 4), middle- (population 1) and basal (population 1) turn of specimen 1, as well as in the middle turn region of specimen 2, only one cell body from each region is found to be an outlier. After removal of these four values, which represent 2.9% of all reconstructed SGNs, our hierarchical cluster algorithm was again applied to the data in order to determine the difference in cluster composition and the incidence of cells within the newly classified populations.

The specified four population solution supported by the scree plot is identified in both specimen 1 and 2. Furthermore, the four classes of neurons are determined among cell bodies separated according to their origin along the cochlea spiral (data not shown). It is observed that the newly determined mean volumes of the cell classes are 'shifted', resulting in more similar populations among the two cochleae. These shifts of populations are accompanied by a decrease in the standard deviation calculated from the reconstructed volumes among these subgroups. However, the incidence of cells within the four determined different populations remains unchanged representing huge individual variations.

The volumetric differences of the cell bodies and their corresponding nuclei are visualized in Figure 4.5 using a 3D rendering of a microscopic view comprising 3 distinct populations of SGNs. A small soma (population 1, green) of the apical turn of specimen 2 is shown alongside a 'giant' soma" (population 4, cyan) and medium sized SGNs of population 3 (red and yellow) which compose approximately one fourth of all scanned neurons.

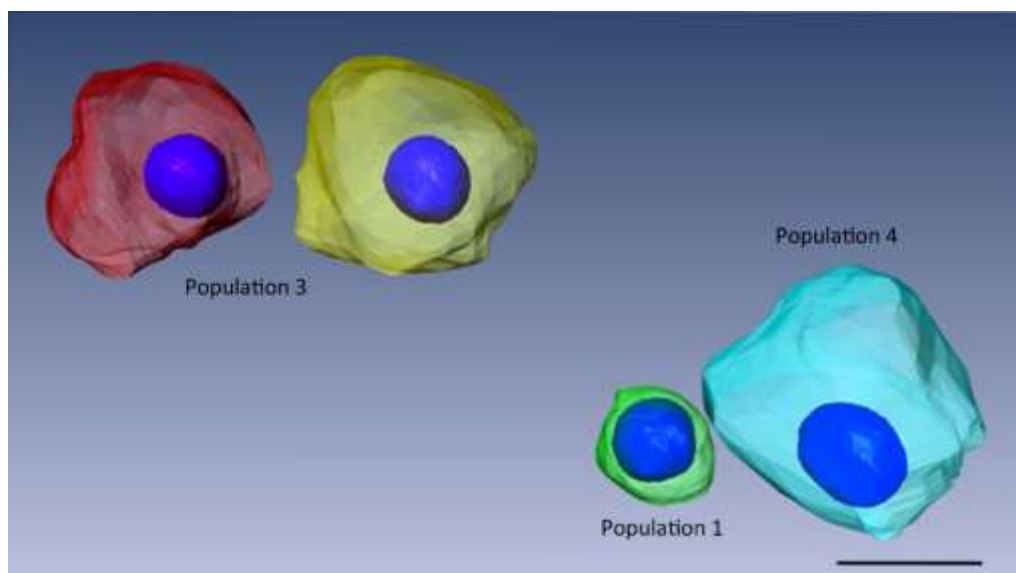


Figure 4.5: Surface rendering of manually segmented perikarya with their corresponding nuclei. The green-colored perikaryon represents a SGN from the apical turn of Specimen 2. It was one of the smallest scanned cell bodies and classified as population 1 by the cluster algorithm. On the other hand, the cyan-colored SGN represents one of the largest reconstructed perikaryon belonging to Population 4. Identified Population 3 is shown by the red- and yellow-colored soma. Scale bar represents 15 μm .

4.7 Computer Simulation

To quantify the effect of different soma volumes the model neuron has been analyzed during two different stimulation modes. The natural spiking behavior was examined with the injection of a current impulse into the first compartment (i.e., the distal end of the peripheral axon). Additionally, the stimulation by an extracellular point electrode simulates micro stimulation in the case of cochlear implants.

4.7.1 Intracellular Stimulation

Changes in soma diameter of the model neuron have insignificant influence on conduction velocity of an AP initiated in the first dendritic compartment. When the soma diameter is varied from minimum values of 10.05 μm to maximum values of 25.05 μm , the threshold amplitude for a 0.1 ms pulse is 60-70 pA. The traveling time of the spike for threshold current injection increases only slightly (i.e., 0.58 ms for the smallest cell to 0.65 ms for the largest one). The AP height at the soma shows a spread of only 2.3 mV. The AP width at the soma is always about 0.13 ms and its small variations do not correlate with soma diameter.

The unmyelinated soma region which is typical for human SGNs impedes spike traveling. Rattay et al. (2001) report sensitive model parameters for the signal transmission of a spike, e.g., the number of membrane layers at the soma, the length of the presomatic region or the diameter of the peripheral process. Even a small deviation from standard values can reduce the safety factor for successful spike conduction. The experiments performed (data not shown) demonstrate that this impediment to successful AP propagation is more pronounced for neurons with larger cell bodies.

4.7.2 Extracellular Stimulation with Electrodes E1 and E2

For both electrodes and all four stimulus configurations, the thresholds as well as initiation site (IS) did not change much within the range of all collected soma diameters. Temporal parameters of the spike were collected for threshold stimulation and additionally for pulses of doubled amplitude. We recorded the peak time of the AP at three different sites, namely the IS, the soma and compartment 27 which is the model neurons' end.

These temporal parameters are displayed in Figure 4.6 which demonstrates different spiking behavior when a selected model cell with $d=19.08 \mu\text{m}$ (which is the mean value of all evaluated diameters) is stimulated by electrode E1 with the four different pulse forms. The time courses of membrane potential of this cell are plotted for monophasic and biphasic threshold stimulations.

When stimulated with a 0.1 ms long cathodic pulse, the threshold value for E1 is about $-449 \mu\text{A}$ and $-186 \mu\text{A}$ for E2 regardless of the cell size. Note the difference in magnitude of the two values, although the electrodes are quite close (compare Figure 4.2). APs were generated in compartment 7 for E1 and in compartment 9 for E2, both pertaining to the peripheral axon. The IS for twice the threshold is changed to compartment 9 for E1 and remains the same for E2. Since for all cases the AP is initiated peripherally, the spike travels orthodromically over the soma to the central end of the neuron. This can be observed in the top left panel of Figure 4.6, where a threshold impulse initiates a spike after 0.445 ms at compartment 7, indicated by the blue line. The spike appears later at the yellow soma after 0.812 ms, and then reaches the axonal end 0.966 ms after stimulus onset, plotted as a red line.

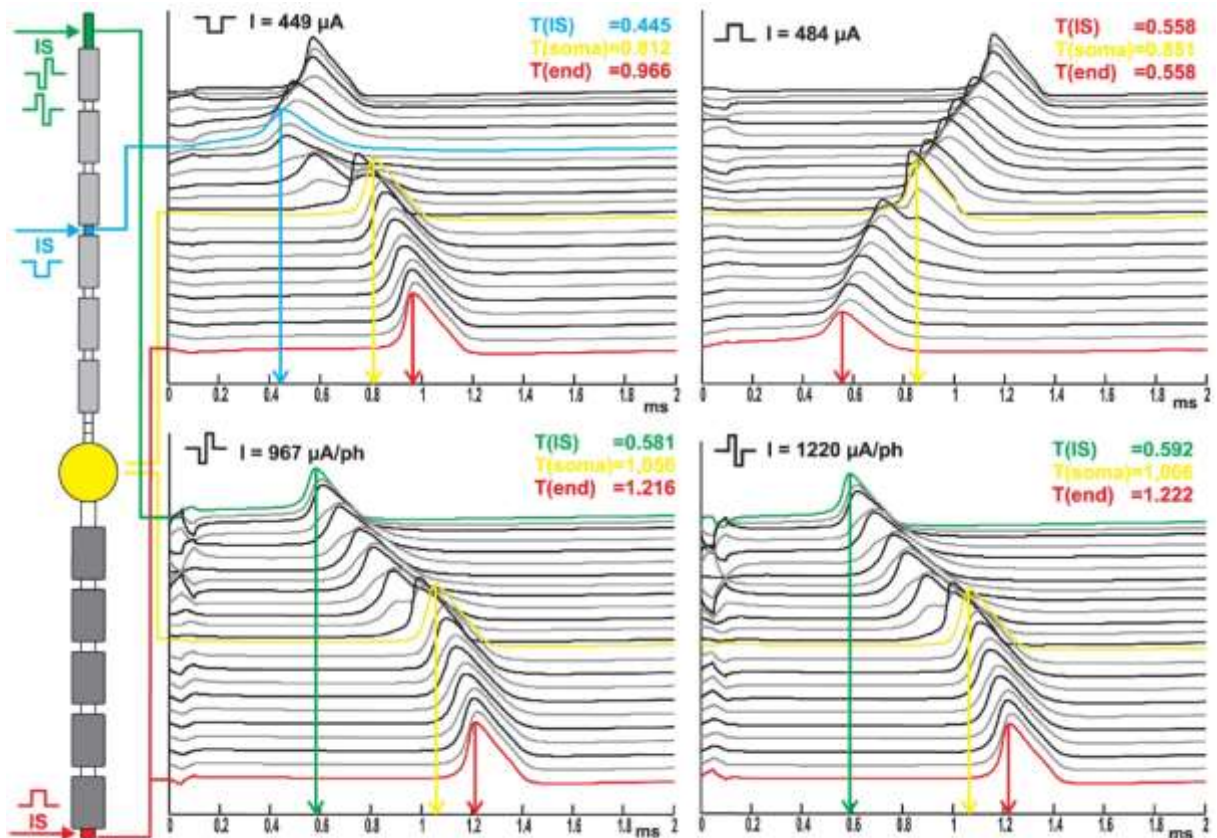


Figure 4.6: Spike initiation sites depend on stimulus pulse type. The left side illustrates the compartment model of a target neuron with spike origin (horizontal arrows) at threshold for four different pulses. Stimulating electrode E1. Traveling APs are plotted at the right. Each line represents the temporal change in transmembrane potential. The top line is the neurons peripheral end, the soma is always plotted in yellow. The values for the time at which the spike occurs at the IS, the soma and the end of the model neuron are given in ms and they are marked by vertical arrows.

Anodic thresholds slightly decrease with increasing soma size for E1 from 496 μA to 482 μA and cause the spike to start at the central end of the neuron at compartment 27. For E2 the threshold remains constant at 289 μA initiating the spike at the very peripheral end of the neuron in compartment 1. The IS stays the same for both electrodes and all cell sizes when stimulated with twice the threshold value. The spike travels orthodromically as it can be seen in the top right panel of Figure 4.6, where the AP at the soma (indicated by yellow line) appears later than the graph of the last compartment, indicated by the red line which represents both, the IS and the end of the neuron. Interestingly, the onset of the spike is delayed compared to the cathodic stimulation with a peak time value of 0.558 ms. Still, since it is also the end time of the spike, the delay of information processing is certainly reduced.

The thresholds for biphasic pulses from E1 remained constant at -967 μA for cathodic first and 1220 μA for anodic first pulses, both initiated the spike at compartment 1 for all cell sizes, indicated by the green lines in the bottom panels of Figure 4.6. Since the peak time values for both leading phases are quite similar, almost the same value of about 1.2 ms can be observed for the delay of spike transmission, which is certainly longer than for monophasic pulses.

No matter which cell size is observed, when the pulse amplitudes are doubled, the ISs are shifted to compartment 9 for biphasic cathodic first pulses and to multiple sites including compartment 27 and 3 for biphasic anodic first pulses. The corresponding threshold values for E2 are $-483 \mu\text{A}$ and $661 \mu\text{A}$, although it should be stated that the largest cell of the basal turn requires about $15 \mu\text{A}$ more threshold current amplitude compared to the constant values of all other possible cell diameters. Also, the IS is not constant for all cells, but rather switched between compartment 7 and 9 for both biphasic pulse forms of E2. When stimulated with twice the threshold value, the IS was constant for all cell sizes (i.e., compartment 9 for cathodic first and compartment 1 for anodic first biphasic pulses) This behavior demonstrates the overall trend that temporal fluctuations decrease for increased stimulus amplitudes.

Regardless of the electrode position and pulse form, and despite some fluctuations, it was observed that the peak time values of the spike increased with cell size. No matter which pulse form is chosen, changing the soma diameter alters the temporal spiking behavior and larger soma size delays information processing.

4.7.3 Extracellular Stimulation with Electrodes E3 and E4

These electrode positions were tested for all evaluated soma diameters. Both electrodes are placed normal to the soma at different distances, where E3 denotes the short distance case of 0.5 mm and E4 the longer, doubled distance of 1mm (Figure 4.2). Initially the individual monophasic and biphasic threshold currents have been determined for varying soma size. While analyzing all soma diameters, the spike is initiated either peripherally at compartment 13, which is the last node of Ranvier before the soma, or at the central end of the model neuron.

Due to the phase duration ratio of $100 \mu\text{s}$ to $50 \mu\text{s}$, the monophasic threshold currents for both electrode positions are approximately half the values of their biphasic counterparts, as can be seen in Figure 4.7.

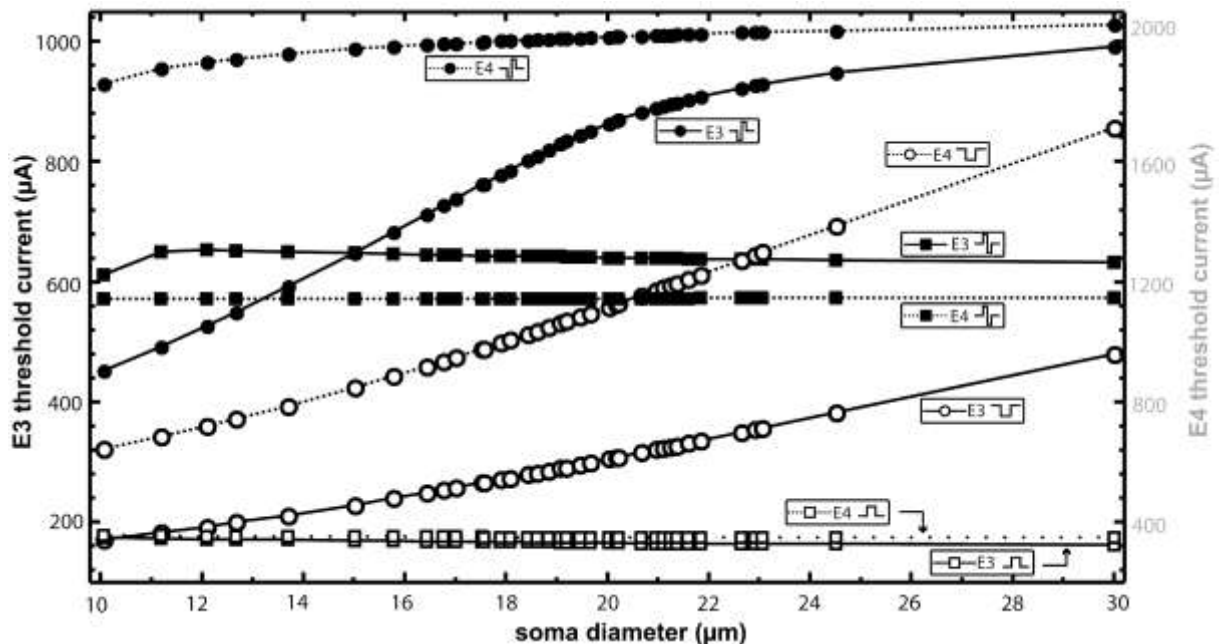


Figure 4.7: Threshold currents of E3 and E4 as function of soma diameter for all detected cells. The black E3 axis on the left is half of the grey E4 axis on the right. Corresponding threshold curves have the same color. For better visualization, the markers display a selection of evaluations.

When the soma-electrode distance is 0.5 mm, the cathodic threshold increases with soma diameter monotonically from $-171 \mu\text{A}$ to $-393 \mu\text{A}$, always initiating the AP at compartment 13. Contrarily, the anodic threshold decreases monotonically from $174 \mu\text{A}$ to $162 \mu\text{A}$ with a constant IS at compartment 27. For the biphasic pulses of E3, the thresholds as well as the IS changes with varying soma diameter. When stimulated with biphasic cathodic first pulses, the thresholds again increase with cell size. The values range from $-451 \mu\text{A}$ to $-954 \mu\text{A}$, although the slope of the curve decreases for diameters larger than $19.07 \mu\text{m}$ correlating with the change of IS from compartment 13 to 27 (compare top panel of Figure 4.8). For biphasic anodic first pulses, this change appears already for diameters above $11.64 \mu\text{m}$. As a result, the threshold values ascend steeply at first from $611 \mu\text{A}$ to $654 \mu\text{A}$, but then again decrease to $635 \mu\text{A}$ (compare bottom panel of Figure 4.8).

When the electrode is moved further away from the soma to a distance of 1 mm, the application of a cathodic pulse initiates the AP at compartment 13 for each soma diameter. For all other pulse forms and variations in diameter, the IS is the central end of the model neuron (i.e., compartment 27). The threshold values for both monophasic and biphasic cathodic pulses increase with cell size, although with a variation between $-643 \mu\text{A}$ to $-1420 \mu\text{A}$, the monophasic values show a steeper slope than those of biphasic pulses with values ranging from $-1858 \mu\text{A}$ to $-2040 \mu\text{A}$. For anodic stimulation, the threshold values remain virtually the same (i.e., for monophasic pulses the values decrease only slightly from $353 \mu\text{A}$ to $348 \mu\text{A}$, while the threshold values for biphasic stimulation fluctuate between $1142 \mu\text{A}$ and $1146 \mu\text{A}$, Figure 4.7).

While recording E3 and E4 threshold currents and ISs, we also collected temporal parameters of the spike, namely values of the AP peak time at the IS, the soma and the last model compartment. Corresponding values vary for different soma sizes when stimulated with the individual thresholds. For monophasic stimulation, the values for the spike onset, the AP peak time at the IS, seem to increase with broad distribution when the soma diameter is raised from its minimum of $10.05 \mu\text{m}$ to its maximum of $25.05 \mu\text{m}$.

The influence of the soma diameter for biphasic stimulation by E3 is illustrated in Figure 4.8. The shift in IS occurring for altering soma diameter is observed for the biphasic cathodic first pulses radiated by E3. The values jump from a lower level, around 0.25ms , to a peak time around 0.7ms at the IS for diameters larger than $19.07\mu\text{m}$ (compare top row of Figure 4.8). For anodic first pulses (bottom row) the latencies, the time at which the AP occurs at the end, are longest for small cells.

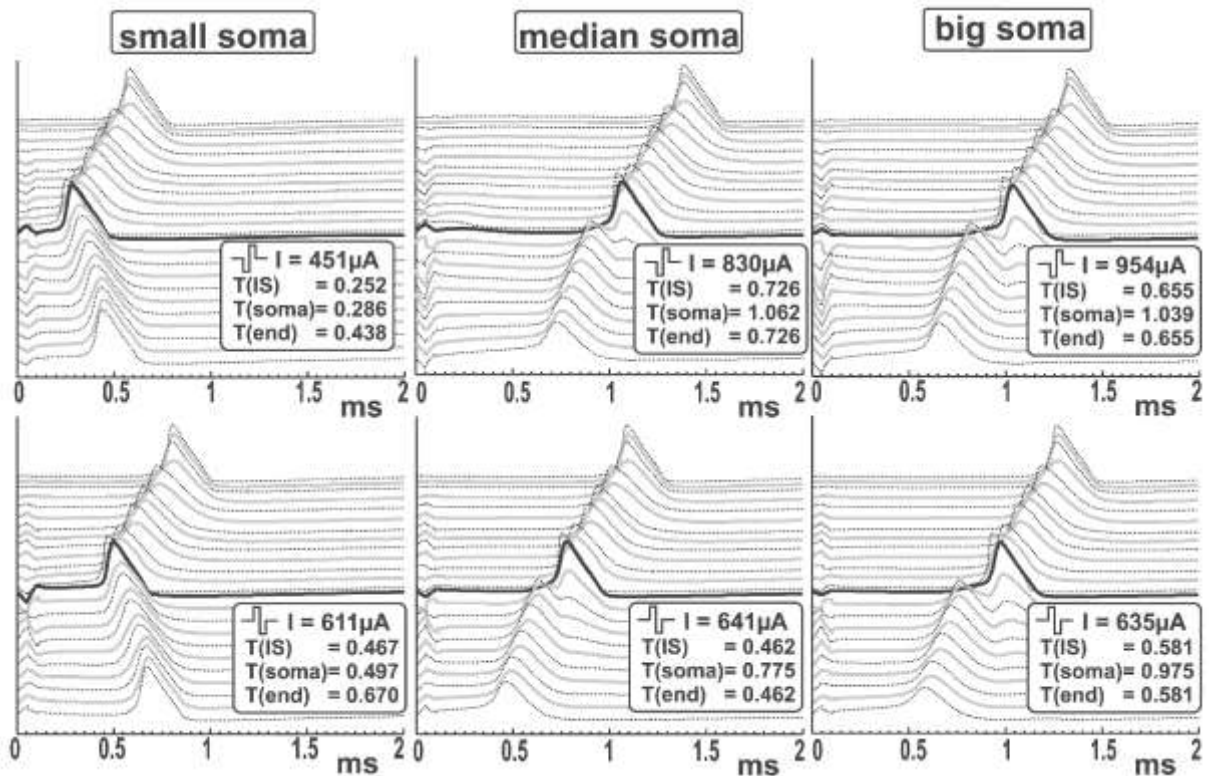


Figure 4.8: Biphasic threshold stimulation by E3 of three neurons with different soma size. The traveling APs (lines from top to bottom correspond to the transmembrane potential of every compartment from the peripheral to the central end) are simulated for the smallest ($d=10.05\mu\text{m}$), mean value ($d=19.08\mu\text{m}$) and biggest detected cell ($d=25.05\mu\text{m}$).

Table 4.3 summarizes the results of the whole set of soma diameters and compares different pulse forms for two different electrode-soma distances. Monophasic cathodic pulses lead to smaller E3 values of the AP peak time at the IS compared to their counterparts of E4 with doubled distance. Corresponding anodic values are higher, but the effect of increasing the electrode-soma distance is less pronounced. For biphasic pulses the values of E3 include spikes initiated at two different sites, compartment 13 and 27. Still, the mean value of E3 cathodic first pulses of 0.46ms is significantly higher than 0.583ms for E4. By contrast, anodic first pulses by E4 cause a slightly earlier onset. The fastest onset among all pulse forms of the two electrode positions appears for E3 stimulation with monophasic cathodic pulses.

Although changing the pulse shape or electrode position has the same consequences for the peak time at the soma, the variations among corresponding values are now higher. The influence of the soma size is most obvious for this temporal parameter, as the largest values of variance, standard deviation and overall range, appear in the middle part of Table 4.3. Moreover, the results predict that irrespective of the electrode-soma distance, the peak time values at the soma elevate with increasing diameter for each of the four pulse form (data not shown).

E3	peak time	min	0,332	0,464	0,252	0,458	E4	peak time	min	0,400	0,494	0,572	0,367	peak time	min	0,400	0,494	0,572	0,367
		max	0,360	0,486	0,668	0,467			max	0,445	0,551	0,594	0,508		max	0,445	0,551	0,594	0,508
		mean	0,346	0,475	0,460	0,462			mean	0,422	0,522	0,583	0,438		mean	0,422	0,522	0,583	0,438
	difference	0,027	0,022	0,416	0,009	difference		0,045	0,057	0,022	0,142	difference	0,045	0,057	0,022	0,142			
	var	0,000	0,000	0,087	0,000	var		0,001	0,002	0,000	0,010	var	0,001	0,002	0,000	0,010			
	svd	0,019	0,016	0,294	0,007	svd		0,032	0,040	0,015	0,100	svd	0,032	0,040	0,015	0,100			
E3	peak time soma	min	0,363	0,675	0,286	0,497	E4	peak time soma	min	0,476	0,747	0,816	0,572	peak time soma	min	0,476	0,747	0,816	0,572
		max	0,454	0,937	1,128	0,948			max	0,496	0,920	1,007	0,946		max	0,496	0,920	1,007	0,946
		mean	0,408	0,806	0,707	0,723			mean	0,486	0,834	0,912	0,759		mean	0,486	0,834	0,912	0,759
	difference	0,091	0,262	0,843	0,452	difference		0,020	0,174	0,190	0,374	difference	0,020	0,174	0,190	0,374			
	var	0,004	0,034	0,355	0,102	var		0,000	0,015	0,018	0,070	var	0,000	0,015	0,018	0,070			
	svd	0,065	0,185	0,596	0,319	svd		0,014	0,123	0,135	0,264	svd	0,014	0,123	0,135	0,264			
E3	end time	min	0,526	0,464	0,438	0,458	E4	end time	min	0,638	0,494	0,572	0,367	end time	min	0,638	0,494	0,572	0,367
		max	0,605	0,486	0,668	0,670			max	0,649	0,551	0,594	0,508		max	0,649	0,551	0,594	0,508
		mean	0,566	0,475	0,553	0,564			mean	0,643	0,522	0,583	0,438		mean	0,643	0,522	0,583	0,438
	difference	0,079	0,022	0,230	0,213	difference		0,011	0,057	0,022	0,142	difference	0,011	0,057	0,022	0,142			
	var	0,003	0,000	0,026	0,023	var		0,000	0,002	0,000	0,010	var	0,000	0,002	0,000	0,010			
	svd	0,056	0,016	0,162	0,150	svd		0,008	0,040	0,015	0,100	svd	0,008	0,040	0,015	0,100			

Table 4.3: Summary of temporal spike parameter values induced by E3 (left) and E4 (right). Values (in ms) for each pulse form are calculated from the whole set of soma diameters.

The bottom part of Table 4.3 represents the peak time at the end of the model neuron. Since in most cases the spike is initiated at compartment 27, the values of the peak time at the IS and at the end are equal. Spikes which are generated peripherally, as for monophasic cathodic stimulation, need to pass the delaying soma region and therefore have longer latencies than the other pulse forms. The shortest latency appears for E4 stimulation with biphasic anodic first stimulation with a minimum of 0.367 ms.

We not only acquired the volumetric data of a certain amount of SGNs, but also assigned cells to their site within the modiolus. We used this additional information to analyze the distribution of temporal spike parameters along the cochlear turns. Figure 4.9 shows boxplots of the peak time values of SGNs from the base, the apex and the middle turn which were collected for threshold stimulation of E3 and E4.

Biphasic cathodic first stimulation radiated by E3 leads to the widest variation in values of the peak time. Note that this electrode configuration also produces the lowest values of the peak time, although the mean value of apical neurons is certainly higher than those of middle turn and basal neurons. This is also visible for cathodic pulses of E3 and biphasic anodic first pulses of both electrodes, that confirms the trend of increasing values for increasing cell body diameter.

The results for the peak time at the soma are very similar. Since for cathodic pulses the AP is initiated peripherally, and therefore propagates orthodromically, the values of the peak time at the soma are higher than the peak time at the IS. The low outliers for biphasic anodic first pulses of E3 correspond to APs initiated in compartment 13.

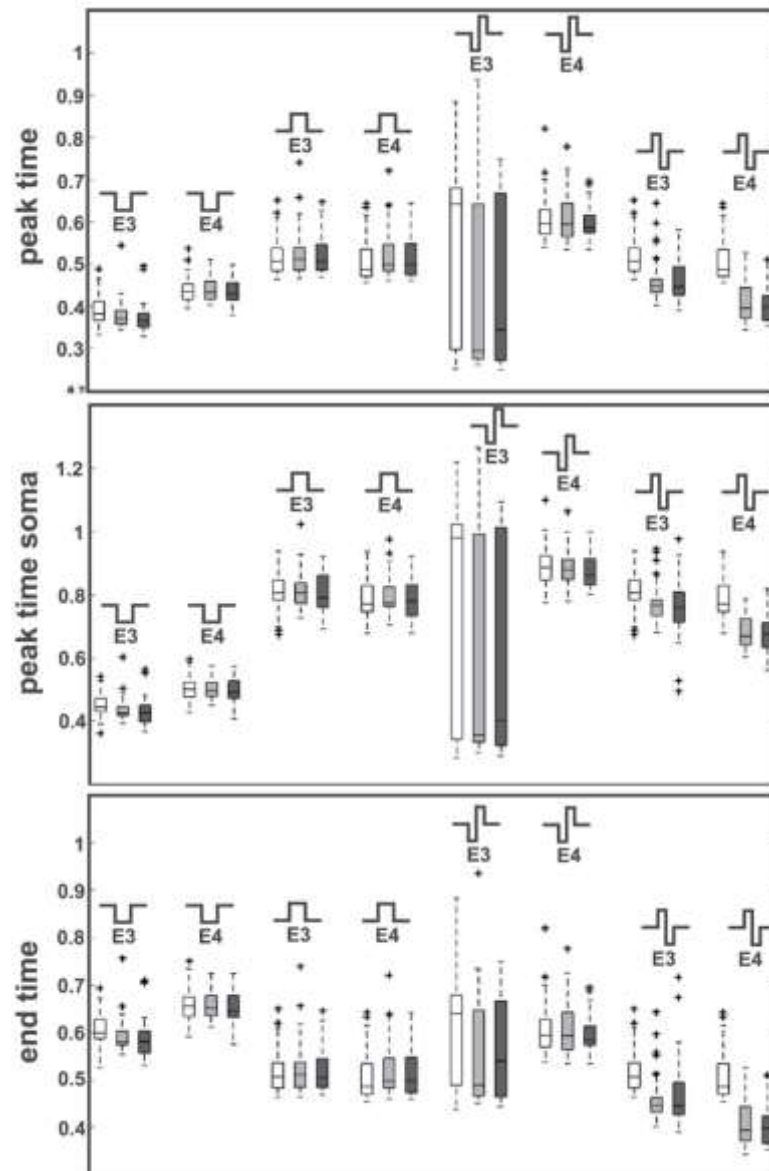


Figure 4.9: Comparison of temporal parameters in the three cochlear regions; Boxplot of temporal parameters of the spike induced by E3 and E4. The peak time at the IS (top) the peak time at the soma (middle) and the end time of the spike (bottom) are compared for apical (white boxes), middle turn (light grey boxes) and basal neurons (dark grey boxes).

Although neurons will respond earlier to cathodic pulses, the delay of information processing to the next cell is lowest for biphasic anodic first pulses (Figure 4.9, bottom panel), since the spike is initiated at the central end instead of propagating from peripheral sites over the soma. For monophasic and biphasic pulses, longer latencies appear for cathodic pulses. Surprisingly, E3 leads to smaller values than E4 when radiating cathodic pulses, although for biphasic anodic first pulses E4 shows shorter latencies.

4.8 Discussion

The unmyelinated perikarya of human cochlea neurons are the first energy dissipater for an AP on the way from the hair cells to the auditory cortex. To overcome this barrier the AP must load the membrane capacitance of the cell body, which is directly proportional to its surface (Rattay, 1995; Rattay et al., 2001a).

Since experimental investigations and electrical recordings of cat neurons do not account for this human characteristic, computer simulation which takes into account the volumetric nature of unmyelinated human SGNs is an important tool for enhancing the understanding of AP initiation and propagation triggered by micro stimulation. The mathematical models used for computer simulation are based on geometric parameters specified by the micro-anatomical characteristics of the simulated structures. Therefore, we systematically collected 3D-data of human SGNs and classified them according to these anatomical properties in order to acquire information about this critical parameter for cochlea neuron simulations.

Present knowledge concerning size of human SGN is based mainly on transmission electron microscopy studies taking morphological criteria into account. The main characteristics extracted from such studies include the maximum cross sectional diameter of perikarya and nuclei (Kiang et al., 1984) as well as their maximum circumference (Nadol et al., 1990; Rosbe et al., 1996). Analyzing these independent data, the authors suggest that there may be subgroups among large and small SGNs. Spoendlin (1984) analyzed cat cochleae at light- and electron microscope resolutions and distinguished three different types of spiral ganglion neurons. Another group (Jagger & Housley, 2003) studied 400 μm thick rat-cochlea slices but could not discern between type I and II cells based on morphological criteria. The diverging shapes of human SGN were also presented by Glueckert et al. (2005b). This group analyzed cochleae from normal-hearing subjects using scanning electron microscopy. The shapes of the SGNs range from spherical, elongated cylinder-like somata to (partly) squeezed lemon-like perikarya, which were also illustrated by Rusznák & Szucs (2009). We have seen in our study that this squeezing mainly results from perikarya-circumjacent, space-claiming satellite glial cells (especially their nuclei) and from myelinated nerve fibers surrounding the perikarya. Hence, the use of 2D-parameters such as the cross sectional area is not sufficient for obtaining information about non-uniform 3D-structures and reduces the possibility of drawing appropriate conclusions concerning their shape, and therefore, their actual size.

Sections used in ultrastructural studies have an average thickness of 90 nm. Assuming a SGN with a diameter of 20 μm , this section represents only about 0.45% from the whole available 3D-data of the structure. By scanning the evaluated perikarya and corresponding nuclei in their full dimension, our study overcomes the above mentioned morphological limitations and accounts for irregular shapes. In taking the whole available 3D-information of these two independent parameters into account, more precise data is available for statistical analyses.

For this analysis, we used an agglomerative hierarchical cluster algorithm to determine possible similarities. Using this approach we identified four different types of SGNs among all reconstructed SGNs. A closer look at scanned SGN from the apical-, middle- and basal turn representing different frequency-specific regions within this sensory organ shows the uniform existence of these four populations of cells in both investigated individuals.

The findings of small volumetric variation of SGNs in the middle turn may provide new insights into the adaption of speech. According to the Greenwood function (Greenwood, 1990; Loizou, 1999), this section of the cochlea is of prime importance for speech recognition (Hollien et al., 1971). The

greatest density of SGNs (Nadol, 1988a; Spoendlin & Schrott, 1988) as well as the maximum number of myelinated fibers and outer hair cells (Spoendlin & Schrott, 1989) per millimeter ensures that this region is at most sensitive within the human cochlea. In this region we identified, surprisingly, the smallest SGNs, which are boosting the chance that an arriving AP from the peripherals can load the membrane capacitance of the perikarya. These electric charging of the cell bodies ensure further signal transmission. Consequently, smaller cell bodies in this region should reduce the risk of information loss caused by 'stucked' AP within these important frequencies.

In contrast, we depict huge individual volumetric variations of SGNs in the apical and particularly in the basal turn of the analyzed cochleae. Such morphological differences and variations of SGNs along the cochlea spiral are also described by Nadol et al. (1990) and Thiers et al. (2000). A major problem imposed by the use of human material of heterogeneous genetic background and incomplete documentation of pre-mortem pathologic influence is that the observed morphology may reflect unknown pathology (Rosbe et al., 1996). Considerable variations in size as well as number of spiral ganglion neurons in the high frequency region are frequently reported and coincide with our own observations on human temporal bones (not published). In a recent large human temporal bone study by Makary et al. (2011), an SGN decline at a mean rate of 100 cells per year of life was found, with pronounced decline of neurons in the basal turn. This degeneration was evaluated from 100 normal hearing subjects and represents a 'normal' type of degeneration in our society. A pronounced loss of neurons in the basal turn results in an increased amount of slowly degenerating SGNs. Cochlear neuron deterioration often involves loss of peripheral processes and cell shrinkage that may explain the high variation of SGN size in the base of the cochlea. Middle and apical regions of the cochlea showed fewer declines of neurons in this study, reflecting a more stable population of nerve cells.

Furthermore we have identified a spatial organization of SGNs (Liberman & Oliver, 1984; Glueckert et al., 2005b) and their corresponding nuclei. Larger nuclei may be associated with higher metabolism. The identified volumetric variations of SGNs were incorporated into our model neuron to systematically test each collected diameter. Computer simulation of micro stimulation by electrodes E1-E4 demonstrates that changing the soma size affects the excitability of neurons in noticeably different degrees depending on electrode positions and stimulus shapes.

Although Miller et al. (2001) state interspecies difference in spiking behavior, the morphologically distinct soma region of human SGNs often remains unaccounted for. Goldwyn et al. (2010) suggest that the varying soma diameter may contribute to channel-to-channel variability of implants. With the acquired volumetric data of SGNs from different cochlea regions, these speculations can be tested systematically. Therefore, forthcoming studies should include varying soma sizes according to detected data, since thresholds and temporal parameters change significantly under certain circumstances (cathodic pulses for E3). Still, our threshold investigations for the four electrode positions support common findings of previous studies. They consider different electrode configurations concerning their position (Mino et al., 2004) and pulse forms, including monophasic (Miller et al., 1999), biphasic (Miller et al., 2001; van Wieringen et al., 2006) and triphasic pulses (Bierer, 2007; Goldwyn et al., 2010) as well as pulse trains (Miller et al., 1997; Woo et al., 2009a).

Greater latencies appear for cathodic stimulation (Miller et al., 1999; Shepherd & Javel, 1999) which also leads to lower thresholds compared to anodic pulses (Miller et al., 1999) and also to their biphasic counterparts (Shepherd & Javel, 1999; Miller et al., 2001). In accordance with our detected ISs, the results of Miller et al. (1999) also support the fact that neurons are mainly stimulated at central processes and that only a minority of fibers close to the electrode is excitable at the respective peripheral axons. This is of special interest for retrograde degeneration of peripheral

processes following loss of sensory cells reported in humans (Spoendlin, 1984; Glueckert et al., 2005b). Van Wieringen et al. (2006) also state that the trend of lower monophasic thresholds is also valuable for pulse trains and it will occur for different CI devices, different electrode configurations, and generally, for different phase duration.

Although recordings in cats may not be valid for humans, the neural response induced by micro stimulation can alternatively be studied with recordings of electrically evoked compound APs. Briaire and Frijns (2005) compared one model including a myelinated cell body with the unmyelinated cell body case. They also reported a delay caused by the lack of myelin layers and examined the difference in excitation by biphasic pulses of both leading phases. With the inclusion of our new morphological analysis, more precise results might be obtained. Macherey et al. (2008) not only studied the evoked compound AP, they also report that the human auditory system is more sensitive to anodic stimulation, yielding larger response at an equal stimulus level compared to cathodic pulses. Our results, which predict a quite uniform anodic threshold value for all soma diameters, are in accordance with this finding. Therefore, one anodic impulse might excite a larger number of SGNs compared to cathodic pulses with highly changing threshold current amplitude for varying soma size. Many more parameters which affect the neurons excitability vary along the length of the cochlea. For pending studies about electrode position and pulse configuration, three-dimensional data from a greater amount of traced cochlear neurons is crucial. Although the obtained results clearly show divergent single fiber response for different soma sizes, the model would certainly benefit from further adjustments.

In summary, we acquired volumetric data, reconstructed as well as analyzed soma size of human SGNs and identified four different populations of SGNs within the cochlea of humans. Moreover, we found evidence of a spatial arrangement of perikarya and their accordant nuclei from high- to low-frequency regions where the most uniform sizes of cell bodies are located in the middle turn representing the majority of phonational frequencies. This more accurate volume information of the unmyelinated human perikarya was used to analyze stimulation thresholds, initial sites and travel latencies of AP triggered by micro stimulation. Our results show that temporal parameters of the AP are affected by the size of the cell body with stronger variations for spikes induced by cathodic stimulation. Therefore, a more uniform excitation profile of the whole amount of cochlear neurons can be expected for anodic stimulation. Together with our morphometric findings, our results deliver new insight into the unique micro anatomical features of the human spiral ganglion and their impact on AP onset and propagation initiated by micro stimulation.



Impact of Morphometry, Myelination and Synaptic Current Strength on Spike Conduction in Human and Cat Spiral Ganglion Neurons

5.1 Abstract

Our knowledge about the neural code in the auditory nerve is based to a large extent on experiments on cats. Several anatomical differences between auditory neurons in human and cat are expected to lead to functional differences in speed and safety of spike conduction.

Confocal microscopy was used to systematically evaluate peripheral and central process diameters, commonness of myelination and morphology of spiral ganglion neurons (SGNs) along the cochlea of three human and three cats. Data was incorporated to an adapted biophysical model to study their impact on spike propagation.

Based on these morphometric data, model analysis reveals that spike conduction in SGNs is characterized by four phases: a postsynaptic delay, constant velocity in the peripheral process, a presomatic delay and constant velocity in the central process. The majority of SGNs are type I, connecting the inner hair cells with the brainstem. In contrast to those of humans, type I neurons of the cat are entirely myelinated. Biophysical model evaluation showed delayed and weak spikes in the human soma region as a consequence of a lack of myelin. The simulated spike conduction times are in accordance with normal interwave latencies from auditory brainstem response recordings from man and cat. Simulated 400 pA postsynaptic currents from inner hair cell ribbon synapses were 15

times above threshold. They enforced quick and synchronous spiking. Both of these properties were not present in type II cells as they receive fewer and much weaker ($\sim 26\text{pA}$) synaptic stimuli.

Wasting synaptic energy boosts spike initiation, which guarantees the rapid transmission of temporal fine structure of auditory signals. However, a lack of myelin in the soma regions of human type I neurons causes a large delay in spike conduction in comparison with cat neurons. The absent myelin, in combination with a longer peripheral process, causes quantitative differences of temporal parameters in the electrically stimulated human cochlea compared to the cat cochlea.

5.2 Introduction

The temporal characteristics of the spiking patterns of the auditory nerve are crucial in natural hearing (Wever & Bray, 1930; Young & Sachs, 1979; Shamma, 1985; Rattay & Lutter, 1997) and in its neuroprosthetic counterpart when action potentials (APs) are initiated via cochlear implants (van den Honert & Stypulkowski, 1987; Javel & Shepherd, 2000; Rattay et al., 2001a; Rattay et al., 2001b). Most of our knowledge on spike coding in the auditory nerve is based on single cell recordings in cats. As such recordings are not possible in man, findings from cats are often generalized to human due anatomical similarities. However, shorter total lengths of SGNs in cat, thinner processes, smaller cell bodies and fundamental differences in myelination are obvious reasons not to rely on a cat model when signaling in human auditory nerve is discussed as these differences between the species may lead to important differences in auditory nerve function.

In the cochlea, sensory hair cells convert sound into neural signals. These afferent signals are conducted along the auditory nerve by two types of SGNs. The vast majority of SGNs are bipolar type I cells with large cell bodies connecting inner hair cells (IHCs) with the cochlear nuclei, whereas smaller type II neurons transmit APs from the outer hair cells (OHCs) (Spoendlin, 1969; Spoendlin, 1985). Both types of cochlear neurons constitute the primary afferent input to the cochlear nucleus (Osen, 1970; Young, 1998) in the brainstem which represents the first central relay station in the ascending auditory pathway (Kandler & Friauf, 1993). Type II neurons are usually completely unmyelinated and have similar physiological properties in man and cat. However, standard type I cochlear neurons in humans are crucially different compared to that of other mammals as their cell bodies as well as the pre- and post-somatic segments lack myelin (Ota & Kimura, 1980; Nadol, 1988a; Liu et al., 2012)(Figure 5.1A). These human differences, together with varying diameters of the peripheral- and central processes (Liberman & Oliver, 1984; Felix et al., 1992) which determine AP velocities, suggest a diverse in auditory signal conduction times along SGNs between man and cat.

The high conduction velocities of myelinated axons are based on the electrical properties of the internode, which is the part between two nodes of Ranvier. Assuming a conducted AP in an idealized internode (membrane capacity $C=0$, membrane conductance $G_m=0$) would cause the same temporal characteristics in the transmembrane voltage profile at both ends, i.e. the conducted AP is reduced in amplitude by intracellular resistance but the maxima at the beginning and end of the internode appear at the same time. This phenomenon, known as saltatory conduction (Huxley & Stämpfli, 1949), requires only a very small capacitance. This is reached by many circumjacent myelin layers as C is inversely proportional to the number of myelin sheets covering the cells membranes (Rattay, 1990). A spike propagation problem may arise in SGNs when the small inneraxonal current of the thin peripheral process has to load the large capacitance of an unmyelinated soma (Hossain et al., 2005), which represents the main barrier for an AP along the neural tract.

A previously presented compartment model for cochlear neurons (Rattay et al., 2001a) was evaluated in this study in order to analyze the impact of myelination and morphometry on temporal features of signal conduction in cat and man. Important parameters for the velocity of spike conduction are the AP duration and its rise time. Different types of voltage-gated ion channels have been identified in SGN membranes based on rat and mouse data (Hossain et al., 2005; Yi et al., 2010), some with impact on the falling part of the spike or on accommodation and refractoriness (Negm & Bruce, 2008). However most ion channel models for non-myelinated neural membrane segments in warm blooded animals, including one of SGN type II of mouse (Hossain et al., 2005), show AP durations longer than 1 ms (Hu et al., 2009; Rattay & Wenger, 2010). An example for shorter APs is the octopus cell in the cochlear nucleus (Golding et al., 1999) whose spikes are still of double duration of a SGN.

In contrast to such membrane models, the original Hodgkin-Huxley model with a temperature fit to 27° C resulted in APs with a duration of 330 μ s and a short rise time that was consistent with intracochlearly recorded SGN spikes of cats (Hartmann et al., 1984; Motz & Rattay, 1986; Rattay et al., 2001a).

In this paper we present the first modeling study that analyzes the temporal features of spike conduction along afferent SGNs of man and cat. Immunohistochemistry and confocal microscopy imaging was performed to distinguish type I and II neurons and quantify process diameters of bipolar SGNs as well as myelination in cat and human cochleae. Major differences concerning the extent of myelination, morphometric characteristics and the length of the neural path between these two species were incorporated in our SGN model. In addition, computer simulation enables the analysis of functional effects of synaptic current strengths that differ essentially between type I and II neurons (Weisz et al., 2009; Grant et al., 2010).

5.3 Materials and Methods

5.3.1 Specimens

The study is based on three human temporal bones from individuals aged 56 to 74 without any diagnosed ear disease or hearing loss (audiograms were not available). Human temporal bones were obtained during routine autopsy at the Institute of Pathology, Innsbruck Medical University, Austria. These cochleae were fixed with 4% paraformaldehyde for 24h at 4°C, subsequently decalcified in 20% ethylenediaminetetraacetic acid at pH 7.4 for 6 weeks and prepared for cryoembedding according to Coleman et al. (2009). Details are described in chapter 4. Inner ears were serially sectioned with a cryomicrotome perpendicular and radial to the modiolus at 10 μ m and 35 μ m respectively.

Three young adult cats (8 - 10 months old, 3.5 – 4.5 kg weight sourced from the BRC located at Royal Victorian Eye and Ear Hospital Ethics Committee) were deeply anesthetized (sodium pentobarbitone; Nembutal; i.p., 60 mg/kg) and intracardially perfused with physiological saline (37°C) containing heparin (0.1% v/v) and sodium nitrate (0.025% v/v), followed by 10% neutral buffered formalin (NBF) at 4°C. The bullae were then removed and carefully opened to access the cochlea. Round and oval window were perforated with a microneedle and the cochleae were locally perfused with 10% NBF. Cochleae were post fixed with NBF for 1 hr at room temperature, then washed in PBS and stored in PBS (with 0.003% Sodium Azide). All procedures for animal tissue were approved by the Royal Victorian Eye and Ear Hospital Animal Research & Ethics Committee.

Measurements of unmyelinated peripheral- and central process diameters were carried out on three male, normal hearing human subjects (49 – 63 year old) without any diagnosed ear disease (audiograms not available) from archival material. Evaluation of cat process diameters are based on three inner ears from young female adult individuals, one year old, taken from archival material. Human as well as cat cochleae were fixed perilymphatically with ice-cold Karnovsky’s solution and prepared using a standard celloidin embedding technique (Spoendlin & Schrott, 1990). Specimens were serially sectioned perpendicularly to the modiolus at 25 µm thickness and stained with hematoxylin and eosin.

In order to quantify the length of a standard bipolar SGN used in our computational model, we analyzed CT/MR data acquired during daily clinical practice of three male human individuals (aged 14 to 46 years) and three adult domestic cats (2-3 years old).

5.3.2 Immunohistochemistry

Staining was performed after washing the sections in phosphate-buffered saline (PBS, pH=7.4, 6x5min) followed by blocking of unspecific reactions with PBS containing 5% bovine serum albumin (BSA, Serva, Germany), 15% non-immune normal donkey serum (NDS, Chemicon-Merck, Austria) and 0.3% Triton X-100 (Sigma, Germany) for 2h at room temperature (RT). Primary antibodies (Table 5.1) were diluted with a solution containing PBS, 1.67% BSA, 5% NDS and 0.1% Triton X-100. Cryosections were subsequently incubated for triple staining in a humid, darkened chamber at 4°C overnight followed by 1h 15min incubation at 37°C. After rinsing with PBS (6x5min) sections were incubated with secondary antibodies conjugated to Alexa Fluor™ 488 (donkey anti-rabbit, 1:1000, Invitrogen), Alexa Fluor™ 546 (donkey anti-mouse, 1:1000, Invitrogen) and Alexa Fluor™ 633 (goat anti-rat, 1:1000, Invitrogen) diluted with PBS for 2h at RT. After rinsing the stained sections with PBS (6x5min) cell nuclei were counterstained using 4’,6-diamidino-2-phenylindole, dihydrochloride (DAPI, 1:46000, Molecular Probes) for 35 min at RT. Sections were mounted after rinsing with PBS (6x5min) using Vectashield™ mounting medium for fluorescence microscopy.

Antibody	Dilution	Characteristics	Host	Source
anti-β-III-tubuline	1:500	monoclonal	mouse	Chemicon, MAB5544
Anti-myelin basic protein	1:100	monoclonal	rat	Sigma-Aldrich, M9434
anti-S-100	1:200	polyclonal	rabbit	Sigma-Aldrich, S2644
anti-peripherin	1:2500	polyclonal	rabbit	Millipore, AB1530
4’,6-diamidino-2-phenylindole, dihydrochloride	1:46000			Molecular Probes, D1306

Table 5.1: Primary antibodies for immunohistochemistry

5.3.3 Electron microscopy

Human specimens were prepared according the block surface technique described by Spoendlin and Brunn (1974) and Spoendlin and Schrott (1990). Subsequently, a Zeiss® Libra 120 (Zeiss®, Oberkochen, Germany) transmission electron microscope (University of Innsbruck, Institute of Zoology and CMBI) operating at 80kV with 500ms exposure time was used for examining ultra-thin sections at magnification of 200x. Digital images were captured using a TRS 2048 HSC High Quality camera.

5.3.4 Confocal imaging and processing

Immunostained sections were imaged using a Zeiss LSM 510 Meta confocal laser-scanning microscope equipped with a 20x/0.8 NA dry lens and a 63x/1.4 NA oil immersion lens. To simultaneously detect cell nuclei, type II neurons, cell bodies and SGN myelin we used a 405 nm diode laser, a 488 nm line of an argon-krypton laser, a 543 nm and a 633 nm HeNe laser. Image capturing was performed using ZEN® software (Zeiss, Jena, Germany).

To measure process diameters, three-dimensional image stacks were acquired from the celloidin embedded sections using a 63x/1.4 NA oil immersion lens and a 488 nm argon ion laser combined with a 505 nm long-pass filter. The emitted blue-green light was used to leverage the autofluorescence of the hematoxylin and eosin stained SGNs. Pixels sizes of the 3D-stacks were selected according to the Nyquist theorem resulting in the following resolution: x=43nm, y=43nm, z=130nm. In order to reduce the distortion created by the microscope and increase the quality of the quantitative analysis of the 3D-stacks, a theoretical point spread function was calculated for each image channel. These point spread functions were subsequently used to deconvolute the acquired image stacks using a non-blind maximum-likelihood image restoration algorithm (Holmes & Liu, 1989) over 40 iterations. Diameters were evaluated from the unmyelinated pre- and postsomatic segments of SGNs located in the Rosenthal's canal of the apical-, middle and basal regions of the samples.

5.3.5 Measurement of nerve length

Each CT/MR data pair was registered using normalized mutual information method (Veninga et al., 2004). Fused data was used to manually segment the brainstem and the cochlear nerve from the right and left cochlea (starting point for length measurement was defined in the middle of the cochlea at the height of the middle turn) via the internal auditory meatus to the cochlear nucleus of each individual. Visualizing the brainstem by surface rendering enabled us to determine the position of the VIIIth nerve entering the brainstem (endpoint for length measurement). This enabled the calculation of the total length of cochlear nerve fibers as cochlear nuclei are located next to this entry point.

In order to calculate the lengths of the manually segmented nerves, the xyz-coordinates of the highlighted pixels at each DICOM slice were extracted using Fiji Win64bit image processing software (Schindelin et al., 2012) using a macro to highlight a single pixel and save its respective coordinates from every image of the analyzed stack. Each line segment was considered as a vector. The sum of their lengths resulted in the total nerve length of the analyzed human and cat specimens.

Medical imaging data and acquired confocal image stacks were processed with a high-performance workstation (Z800, Hewlett-Packard, Palo Alto, CA, USA) using ImageJ v1.44 and Amira 5.4 (Mercury Computer Systems Inc., San Diego, CA, USA). 3D-data from celloidin embedded sections were processed as described previously in chapter 4.

5.3.6 Statistical analysis

Statistical significance was determined by one-way analysis of variance followed by Bonferroni correction. Quantile-quantile plots were calculated to assess normality of data. Descriptive statistics, significance of data as well as the actual power for the sample data (significance level < 0.01) were computed with MatLab® 2011a (MathWorks, Natick, MS, USA).

5.3.7 Computer simulation

We used the same compartment model, suited for human and cat, as described in detail in Rattay et al 2001, but changed geometrical parameters as well as the numbers of shielding myelin layers according to new morphometric and immunohistochemical evaluations. Accordingly, each neuron was split up into compartments, either with an active membrane with original Hodgkin Huxley ion channel kinetics at 27°C, or as passive internodes (Figure 5.1A). Transmembrane resistances r_m of internodes and myelinated somas were assumed to be constant and proportional to the number N of myelin layers ($r_m=N*1k\Omega/cm^2$) (Rattay et al., 2001a). The spiking of a target neuron was simulated by an electrical network, where the currents to the center of each compartment consist of a resistive and a capacitive current across the membrane as well as intracellular currents to the neighboring compartments (Figure 5.1B). The temporal profile of the transmembrane voltage of each compartment was computed by solving a system of four differential equations for compartments with an active membrane and by a single differential equation for the internode. Current injection into the first compartment of the model neuron, that is the peripheral terminal, simulated the synaptic activation by a hair cell.

The standard model for a human type I SGN consisted of a myelinated somatic region with few membrane layers that separate the heavily myelinated peripheral and central processes. This structure was modeled as the following sequence of compartments: an unmyelinated distal terminal, followed by an internode and 5 node-internode combinations, a presomatic region (segmented into three compartments for computational accuracy), soma, postsomatic region, internode-node combinations of the central process and finally an unmyelinated central terminal. The standard value used for the inner diameter of the peripheral process was 1 μm . According to our morphometric findings, the central process diameter was always of double size. Soma was assumed as a sphere with 20 μm in diameter, all other parameters as in Rattay et al. (Rattay et al., 2001a). The somatic region was assumed to be covered by three membrane layers. The standard model for a cat type I SGN differed from the human case in relation to fewer and shorter internodes, lack of pre- and postsomatic unmyelinated segments, smaller soma diameter (15 μm) with 13 shielding myelin sheets covering the soma (Figure 5.1A). The standard models for unmyelinated type II SGNs had the same process diameters as the myelinated ones for man and cat, but for computational accuracy more and shorter axonal compartments. For details about geometric and electrical parameters see Rattay et al (2001a) methodic and basic concepts are found in Rattay (1990; Rattay, 1999; Rattay, 2004).

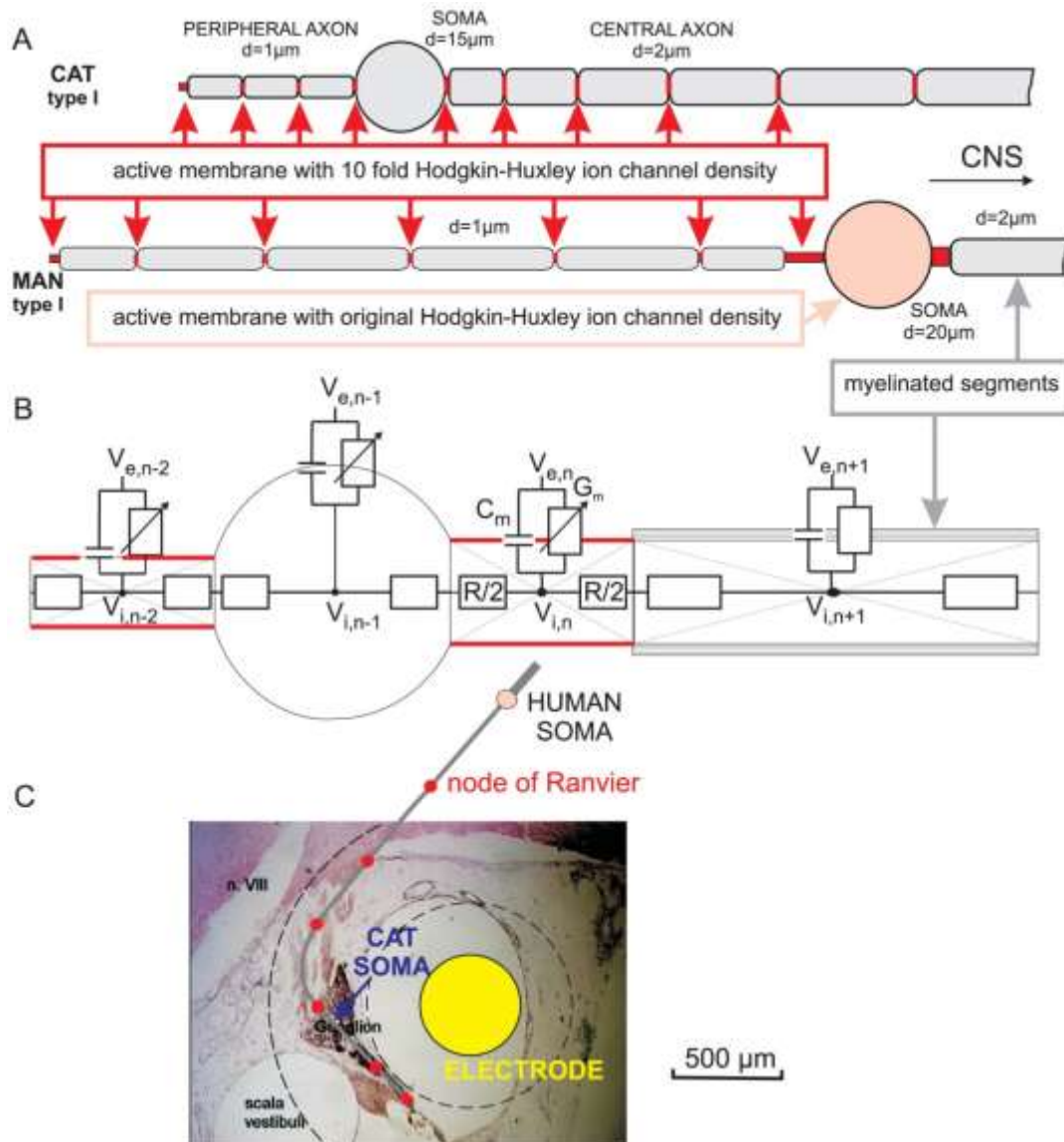


Figure 5.1: Compartment models for SGNs. (A) Type I cells, rectified: Myelinated segments are shown in gray. Excitable (active) membranes with high ion channel densities (red segments) in the peripheral terminal and in the nodes of Ranvier are needed for spike amplification. In contrast to feline cells, in man the pre- and postsomatic compartments are longer, the soma is larger and not myelinated and the peripheral as well as the central axons are longer. (B) According to Ohm's law the sum of all currents to the center of a compartment is zero. The currents are defined by extracellular potential V_e , intracellular potential V_i , membrane capacitance C_m , membrane conductance G_m and intracellular resistance R . Natural excitation by synaptic current from a hair cell ribbon synapse is simulated as current injection into the first compartment (peripheral terminal). In this case extracellular potentials V_e are assumed to be zero. For nonmyelinated type II cells the same modeling approach was used with uniform ion channel densities as in the original Hodgkin-Huxley model and with constant compartment lengths in the axons. (C) The same neural pathway of a human type I cell model as used in (Rattay et al., 2001a) is placed over a cross section of a feline cochlea demonstrating a possible position of a scala tympani electrode relative to a target cell. The length relations are the same as in the rectified versions in A. Extracellular potentials are calculated for a homogeneous infinite medium which causes spherical isopotentials, indicated by dashed lines. Note that the cat soma is much closer to the electrode than the human one.

5.4 Results

The first part of this work depicts the results of the immunohistochemical analysis of various geometrical parameters and the occurrence of myelination among human and cat SGNs. The collected data were subsequently incorporated in our cochlear neuron model to test their impact on spike excitation and signal conduction.

5.4.1 Myelination and soma sizes of SGNs in cat and man

Cat

In cat cochleae we found that in 95.54% of neurons (Table 5.2) examined both the soma and the processes of type I SGNs (n=3229) were surrounded by soma myelinating satellite glial cells (myelinating SGCs) within the spiral canal and myelinating Schwann cells within the osseous spiral lamina. Both types of glial cells were positive for myelin basic protein (MBP). The myelinating SGCs ensheath the entire cell body (Figure 5.2A and B, MBP) forming the distinct honeycomb structure in Rosenthal's canal sections where the cell bodies of the SGNs reside.

Type II cochlear neurons were identified using an anti-peripherin antibody. This neuron-specific intermediate filament protein is well known to be expressed in mammalian (including human) type II SGNs (Berglund & Ryugo, 1991; Kuijpers et al., 1991; Hafidi, 1998; Liu et al., 2009b; Liu et al., 2010) enabling the identification of these small cochlear neurons using confocal microscopy. The middle cochlear regions showed highest density of peripherin positive type II neurons (5.53% of n=995 analyzed neurons) followed by the apical (4.2% of n=1000) and basal (4.05% of n=1234 cells) regions. A total number of 147 cells (Table 5.2) were identified in cat cochleae as type II neurons, being positive for the peripherin protein (Figure 5.2A and B). This value represents 4.55% of all analyzed cat neurons. Moreover, type I and type II neurons of cats stained positive for TuJ1 protein (Figure 5.2A and B, TuJ1).

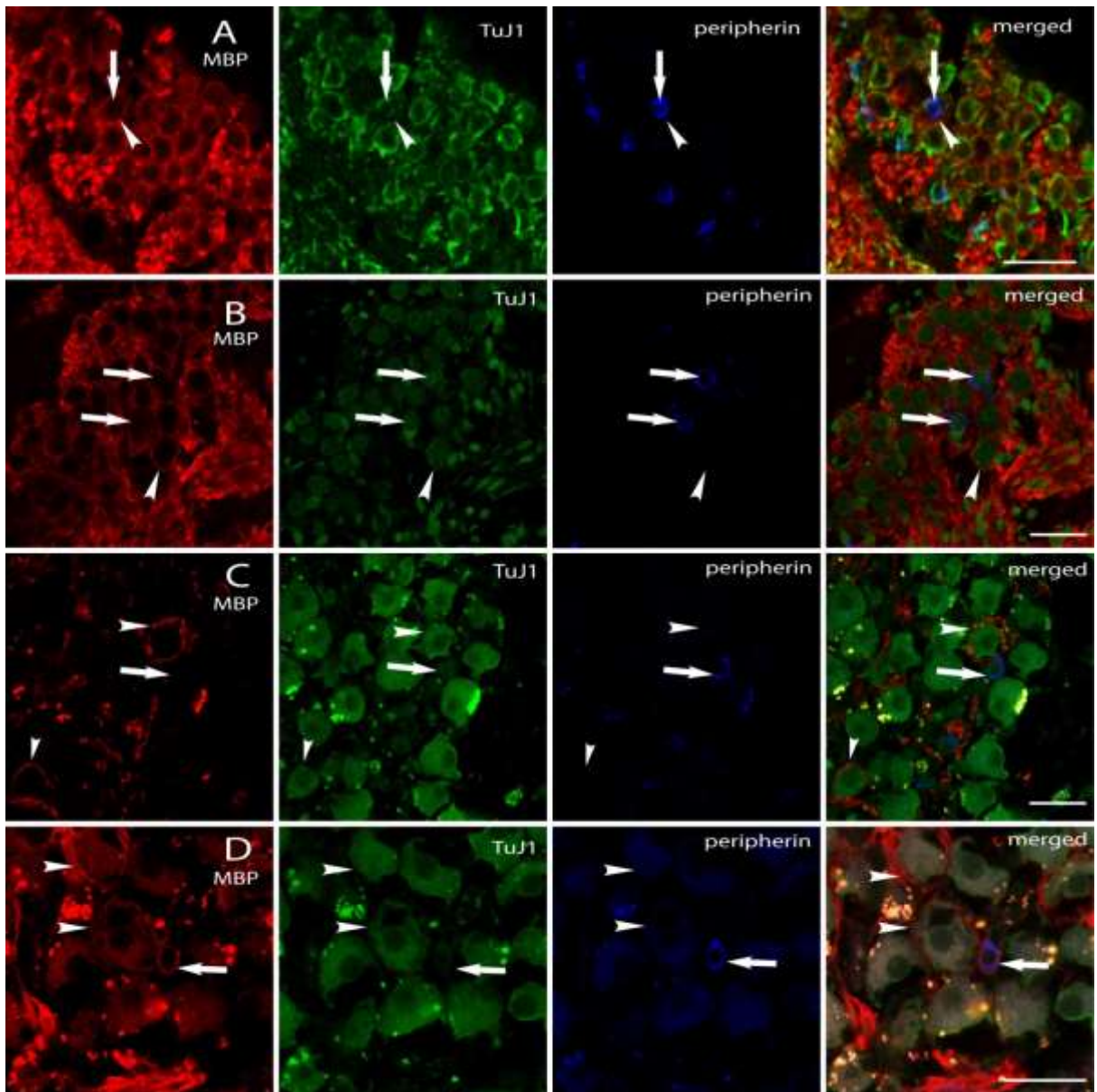


Figure 5.2: Immunofluorescence of MBP, TuJ1 and peripherin in cat (A, B) and human (C, D) spiral ganglion. (A, middle turn region) shows a myelinated type II neuron in a cat inner ear. The arrow highlights the peripherin positive cell body of a type II cochlear neuron; the arrow head depicts its isolating myelin. (B, basal region) illustrates two unmyelinated type II neurons (white arrows) which were (partly) surrounded by myelin of neighboring type I neurons. Additionally, the arrow head points to a type I SGN which was fully surrounded by myelin. Note the absence of these surrounding myelin layers at the depicted type II neurons. A myelinated type I neuron (white arrow head) and an unmyelinated type II neuron (white arrow) of the human spiral ganglion are shown in (C, basal turn). D (middle turn) presents a human type II cell body surrounded by myelin (white arrow) and type I neurons surrounded by myelin (white arrow heads). Scale bars 30 μm .

cochlea region	cat cochlea (n=3)				human cochlea (n=3)			
	n =	myel. cell	type II	d [μm]	n =	myel. cell	type II	d [μm]
basal	1234	1186	50	10.25 \pm 0.91	1109	36	16	9.36 \pm 0.70
percentage %		96.11	4.05			3.25	1.44	
middle	995	942	55	9.72 \pm 1.16	981	42	29	9.52 \pm 0.86
percentage %		94.67	5.53			4.28	2.96	
apical	1000	957	42	9.82 \pm 0.82	893	31	15	9.18 \pm 0.80
percentage %		95.70	4.20			3.47	1.68	
total	3229	3085	147	9.93 \pm 1.01	2983	109	60	9.39 \pm 0.82
percentage %		95.54	4.55			3.65	2.01	

Table 5.2: Summary of the detected myelinated and type II spiral ganglion cells. Presented are the total numbers of counted myelinated type I SGN and type II SGN somata from cat and human cochleae, their percentage as well as the evaluated soma diameters. In contrast to man, the vast majority of cell bodies analyzed from cat cochleae were found to be myelinated.

Four type II SGNs (2.72%, n=147) were found to have fully myelinated cell bodies (Figure 5.2A). However, the vast majority of peripherin protein positive type II cells (97.28%) feature unmyelinated cell bodies (Figure 5.2B) as well as unmyelinated peripheral and central processes. One 3D-image stack of such a standard type II neuron was acquired during data analysis. The measured peripheral- and central process diameter of this neuron was $d_1=0.73 \mu\text{m}$ and $d_2=1.3\mu\text{m}$ respectively, and was subsequently used in our computational model for further analysis.

The diameters of peripherin positive type II neurons were measured from deconvoluted 3D image stacks. Scrolling through the z-stack enabled the detection of the maximum diameter of the evaluated cell bodies, which was measured and used for statistical analysis. Type II neurons had a uniform soma diameter across all cochlear regions (Figure 5.3A) with a maximum in the basal region (median (M) = 10.29 μm), the smallest values with the largest variance (M=9.68 μm) in the middle turn and M= 9.92 μm in the apical region.

All three analyzed cat specimens showed the highest proportion of SGNs that are type II neurons within the middle turn region reaching 5.44% (n=515) in specimen 1, 6.61% (n=121) in specimen 2 and 5.29% (n=359) in specimen 3. The smallest percentages of type II cells were identified in the apical regions of specimen 1 and 3 (3.85%, n=182; 4.2%, n=262) whereas the minimum appeared in the basal region of specimen 2 (3.73%, n=322). Notable is the size distribution of type II SGNs, where the largest cell bodies were found in the high frequency region in all analyzed specimens.

The largest type I SGNs were identified in the basal regions (Figure 5.3C) of the analyzed cat specimens with a mean soma diameter of $15.81 \pm 2.03 \mu\text{m}$ (n=537). Type I SGNs located in the middle turn reached a mean diameter of $13.74\pm 3.25 \mu\text{m}$ (n=284). The apical regions of the investigated cat cochleae contained the smallest type I neurons with a measured mean diameter of $13.41 \pm 2.29 \mu\text{m}$ (n=427). Cell bodies of type I neurons located in the apical- and middle turn were found to be significantly smaller ($p < 0.01$, power=1) compared to those from the basal region. We used an average diameter of 15 μm of these types of SGNs in our computer simulations since the mean diameter of all analyzed somas was determined to be $14.52 \pm 2.69 \mu\text{m}$ (n=1248).

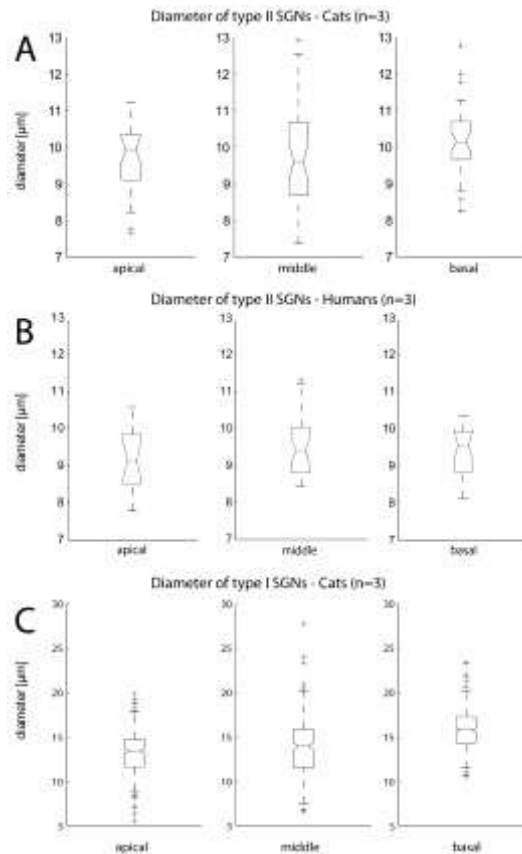


Figure 5.3: Box-Whisker-Plot depicting variations of type II SGN soma diameters for (A) cat and (B) man according to their specific region within the inner ear. (C) presents the evaluated diameters of type I SGN somata from the analyzed cat specimens located in the apical, middle and basal region of the cochleae.

Human

Analyzing data from three individual human cochleae, we found that 3.65% of $n=2983$ type I neurons (Table 5.2B) were surrounded by myelinating SGCs strongly positive for MBP (Figure 5.2 C, D). The acquired confocal stacks revealed that the isolating myelin layers fully wrap around the cell somas without any gaps. Furthermore, the pre- and postsomatic segments of SGNs were similarly surrounded by myelin comparable to these neuronal units of other mammals. The white arrowheads in Figure 5.2C highlight the MBP positive myelin layers of human type I SGNs. The merged image illustrates the myelinated cell bodies of human type I SGNs (TuJ1 positive) in contrast to the majority of unmyelinated SGNs.

The highest density of myelinated somas of $n=981$ type I SGNs (4.28%) were identified in the middle turn, the minimum in the basal turns (3.25% of $n=1109$ type I cells) and 3.47% of all analyzed cochlear type I neurons ($n=893$) in the low frequency regions. The standard case of a human type II neuron (Figure 5.2C) has a fully unmyelinated cell body. Confocal 3D-stacks also showed the complete absence of myelin at the peripheral and central neurite (data not shown). In contrast to type II cells of cat, human type II SGNs were not positive for TuJ1 – protein. Solely type I - SGNs are strongly positive for this neuron-specific class III beta-tubulin.

A total number of 60 peripherin positive SGNs (Table 5.2B) were identified representing 2.01% of all analyzed human neurons (n=2983). The highest incidence of type II cells was found in the middle turn (2.96%), followed by apical turns (1.68%) and the high frequency basal regions (1.44%). Interestingly, two type II neurons representing 3.34% (n=60) were found to be surrounded by myelinating SGCs (strongly MBP positive) wrapping myelin around the cell body as well as their processes. Again, the white arrow (Figure 5.2D) depicts a type II cell body positive for the peripherin protein. The merged image illustrates this cell and its surrounding myelin (red color). Additionally, white arrow heads point to myelinated type I cell bodies (Figure 5.2D). However, the standard type II neuron in the human inner ear completely lacks myelin. 3D image acquisition was performed on one type II cell with an unmyelinated cell body and processes. The evaluated process diameters used in our computational model are $d_1=0.65\ \mu\text{m}$ and $d_2=1.4\ \mu\text{m}$. The median diameters of human type II somata from all specimens (Figure 5.3B) were relatively constant with a maximum ($M=9.55\ \mu\text{m}$) found in the high frequency basal region, $M=9.39\ \mu\text{m}$ in the middle turn and the smallest value ($M=9.13\ \mu\text{m}$) in the apical region. The calculated mean values in Table 5.2B identifies the largest diameters of type II cells in the middle turns, a region of prime importance for speech recognition [48]. However, no significant differences were found comparing type II cell soma diameters between cats and humans ($p > 0.05$, power=0.82).

The myelination of human SGNs was additionally assessed on electron microscopy level (Figure 5.4A). White arrow heads depict the myelinated cell body of a type I SGN cell body and the myelinated process of a neurite. Note the continuous myelination of cell body and neurite. Figure 5.4B shows the standard case of a large unmyelinated type I cell body (white arrows) that is covered by non-myelinating SGCs. The part of the central neurite that connects directly to the cell body totally lacks myelin. Myelination of the neurite starts here after approximately $7\ \mu\text{m}$ (highlighted by the white arrow head) away from the soma.

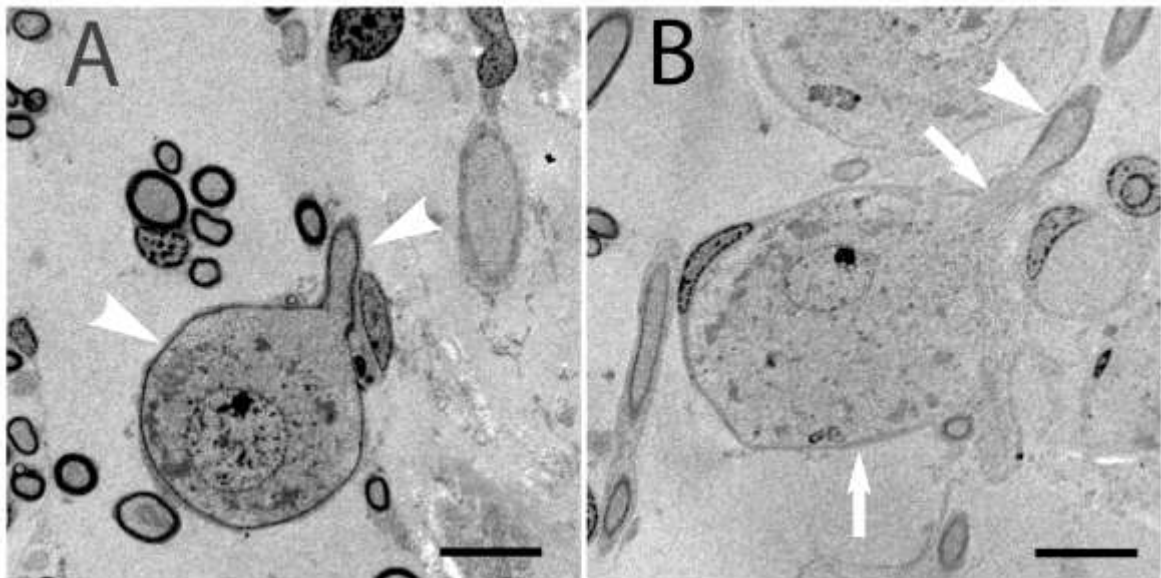


Figure 5.4: Transmission electron microscopy images of human SGNs. (A) Cell body of a putative type I SGN completely enwrapped with myelin. Additionally, the process of the SGN shows continuous myelination (white arrow heads). The standard human SGN is shown in B. White arrows highlight an unmyelinated cell body encircled by a satellite glial cell and the myelin lacking process of a SGN. The myelination of the central process starts after about $7\ \mu\text{m}$ pointed by the white arrow head. Scale bar $10\ \mu\text{m}$.

Individual differences in incidence, myelination, soma- and neurite diameter in type II neurons are summarized as followed (data not shown): The middle turn of specimen 1 and specimen 2 contain the highest densities of type II neurons (1.96% of n=255 and 1.46% of n=274 analyzed cells respectively) as well as myelinated SGNs (4.71% and 5.11% respectively). In specimen 3, the maximum density of type II cells (5.41% of n=148 evaluated neurons) and myelinated cells (5.41%) are both located within the apical regions. A surprising observation was the complete absence of type II neurons in the basal region of specimen 2 (n=351 cochlear neurons) and its rare appearance in the basal (0.77% of n=260 cells) and apical region (0.69% of n=433 analyzed bipolar neurons) of specimen 1.

5.4.2 SGN lengths in human and cat

In order to compute afferent spike conduction times with the cochlear neuron model, we needed the lengths of cochlear nerve processes. By analyzing clinical computer tomography data (one example is visualized in Figure 5.5) of three human individuals (n=6; right and left ear), we determined an average SGN length of 32.35 ± 1.45 mm. Evaluation of manually segmented right and left auditory nerves of three domestic cats (n=6) resulted in an average length of 15.81 ± 0.39 mm, which is half the length compared to human cochlear neurons. For better comparison of spike conduction times, the lengths of type I and II cochlear neurons were assumed to be the same.

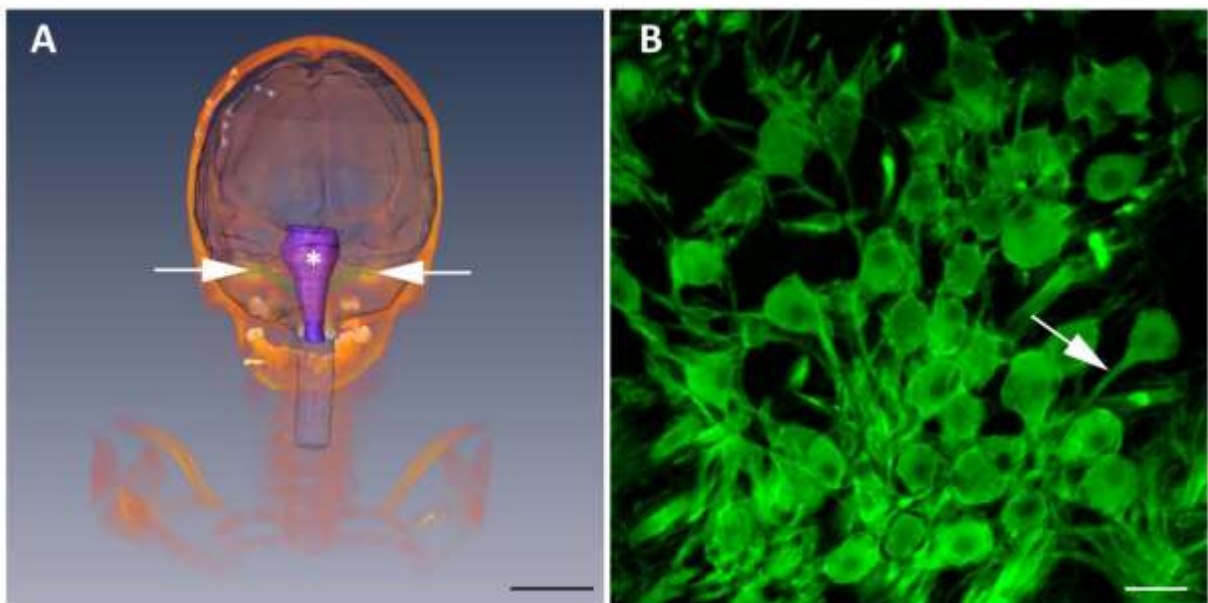


Figure 5.5: Visualization of SGN length measurement (A) and z-projection of a confocal image stack (B) of basal human cochlear neurons. (A) presents the volume rendered bone of an analyzed individual. The brain is illustrated in a transparent manner (blue) together with the manually segmented brainstem (white star). The starting points of the SGNs from the left and right cochleae are highlighted by the white arrows. The manually segmented Nervuli cochlearum are visualized using surface rendering (green colored). The white arrow in (B) highlights a central process connecting the cell body with the cochlear nucleus. The diameter of this neurite was measured to be $2.54 \mu\text{m}$. Scale bar in (A) indicates 5 cm; in (B) it indicates $20 \mu\text{m}$.

5.4.3 Type I process diameters of SGN in human and cat

Peripheral and central process diameters d1 and d2 were systematically evaluated within the Rosenthal's canal of three human specimens, which is illustrated in Figure 5.5. The mean diameter (Table 5.3) of the peripheral processes (n=212) was determined to be $1.32 \pm 0.15 \mu\text{m}$. The central process, which transmits the AP from the cell body to the cochlear nuclei, was measured to be $2.65 \pm 0.3 \mu\text{m}$ (n=236), which is double the size of the peripheral processes. Figure 5.6A illustrates the measured variations for d1 and d2 for human type I neurons. Note that deviations of about $\pm 32\%$ from the mean values for d1 and d2 were found. A closer evaluation of the different regions of the cochlea demonstrated no significant difference in process diameters comparing the basal-, middle- and apical region (Table 5.3, $p > 0.05$, power=1). Furthermore, each specimen was statistically analyzed according to these frequency specific regions as well as among themselves (data not shown). However, no significant differences regarding the diameters were found ($p > 0.05$, power = 1).

A	region	d1 [μm]	d2 [μm]	B	region	d1 [μm]	d2 [μm]
	basal	1.35 ± 0.15 (n=110)	2.67 ± 0.29 (n=125)		basal	1.03 ± 0.13 (n=55)	1.8 ± 0.2 (n=59)
middle	1.28 ± 0.13 (n=66)	2.63 ± 0.29 (n=71)	middle	0.99 ± 0.11 (n=22)	1.8 ± 0.17 (n=21)		
apical	1.32 ± 0.17 (n=36)	2.60 ± 0.34 (n=40)	apical	1.06 ± 0.1 (n=16)	1.88 ± 0.15 (n=13)		
total	1.32 ± 0.15 (n=212)	2.65 ± 0.30 (n=236)	total	1.02 ± 0.12 (n=93)	1.81 ± 0.19 (n=93)		

Table 5.3: Peripheral and central process diameters of type I neurons based on 3 human specimens (A) and 3 cat specimens (B). Data according their location along the cochlea spiral.

Table 5.3B illustrates the findings of process diameters d1 and d2 from three cat cochleae. Data is presented for SGN processes without a myelin sheet. For this purpose, the diameters of myelinated fibers were measured in a first step and recalculated using an inner/outer fiber diameter ratio $d/D = 0.7$. The thinner peripheral process (n=93) had a mean value of $1.02 \pm 0.12 \mu\text{m}$ whereas the mean diameter of the central process was $1.81 \pm 0.19 \mu\text{m}$. Deviations from the mean of about $\pm 30\%$ were observed for d1 and d2 in cats (Figure 5.6B). Analyzing the interspecies differences between d1 of human and cat as well as d2 between these two species reveal to be highly significant for both measures ($p < 0.001$, power = 1).

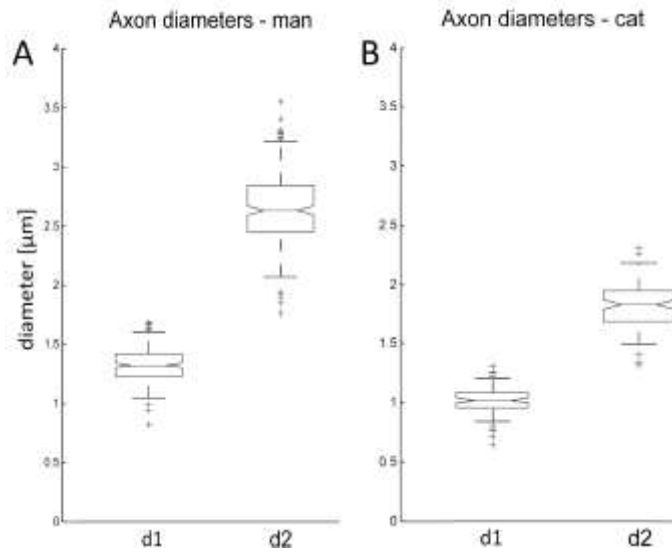


Figure 5.6: Box-Whisker-Plot illustrating measured peripheral- (=d1) and central (=d2) process diameters of type I SGN for man (A, n=3) and cat (B, n=3) within the inner ear.

5.4.4 Computer Simulation

In the first section, the temporal model features are evaluated with intracochlear recorded neural responses. Then, signal propagation in SGNs is shown to consist of four characteristic phases. Formulas for velocity-diameter relationships are found for the myelinated and unmyelinated axons of type I and type II cells. Systematic variations of model parameters show their impact on the total SGN signal conduction times for cat and man. In the last section consequences of strong postsynaptic IHC currents and weak postsynaptic OHC currents are analyzed.

AP duration

In a critical model evaluation the computed AP duration was compared with experimental data. Applying the original Hodgkin Huxley dynamics at 27° Celsius for all active membranes (Figure 5.7A and B) predicts quite short spikes in our SGN model. But are the APs in the human and cat cochlear nerve really three times shorter than spikes of comparable thick axons in the central nervous system (Bean, 2007; Kress & Mennerick, 2009; Hu et al., 2009; Rattay & Wenger, 2010)? As intracellular recordings are not available a positive answer to this question was found comparing simulated and recorded neural responses evoked by cochlear implant stimulation.

We simulated a cat SGN response to a cathodic 100 μ s, 300 μ A pulse from a spherical electrode (neural path and electrode position in the basal turn according to Figure 1C and Rattay et al. (2001a)). For this specific case, similar to natural excitation, a spike was initiated at the peripheral axon (Figure 5.7A). The spike is conducted with some delay before crossing the soma region. In the next step the transmembrane currents of the excited cell were modeled as local current sources and the sum of their contributions was computed for the position of the recording electrode which coincided with the stimulating electrode position (Rattay, 2004). The temporal characteristics of this voltage profile (Figure 5.7C) are similar to an intracochlear recording (Figure 5.7E) from Miller et al. (2004) (weakest cathodic stimulus in their Fig. 1). The recorded signal is broader as it represents the temporarily shifted contributions from many excited SGNs whereas the computed signal results from a single cell response (compare scale bars in Figure 5.7C and E). Spike conduction in the peripheral and central axon caused separate minima in the simulated extracellular voltage profile (Figure 5.7C).

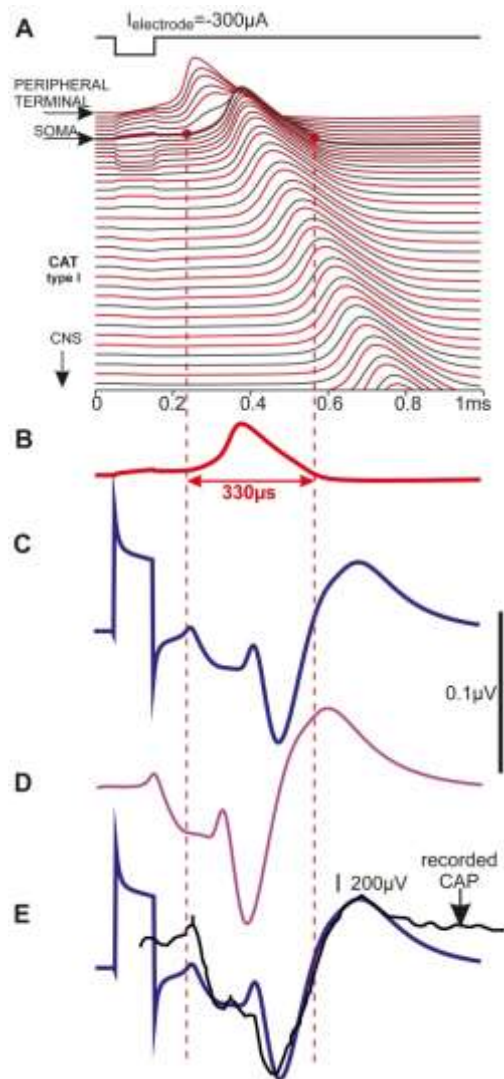


Figure 5.7: Temporal profiles of transmembrane voltages and extracellular potentials of an extracellularly stimulated feline type I cell. A small ball electrode simulates the situation of monopolar cathodic stimulation with a cochlear implant for a situation shown in Figure 5.1. (A) During application of the 100 μ s stimulus pulse the voltage across the membrane is influenced in each compartment. For this electrode placement the threshold is reached in the peripheral terminal and therefore the SGN excitation is similar to natural signaling. The transmembrane voltage lines, shifted vertically according to their distance along the neural path, show AP conductance; myelinated compartment responses in dark gray, compartments with voltage sensitive ion channels in red. (B) The short spike duration is demonstrated with the redrawn transmembrane voltage of the presomatic compartment. (C) Simulated extracellular potential for the position of the center of the stimulating electrode. (D) Simulated recorded signal for natural synaptic excitation, modeled as current injection into the first compartment (E) Simulated (blue, copy of C) and experimentally recorded (black) intracochlear voltage profiles generated with a cochlear implant show similar temporal characteristics although the simulated single cell activity is compared with a compound action potential recording. The black curve is redrawn from (Miller et al., 2004) (Figure 1, intracochlear recording, cathodic pulse -11.1dB rel. 1mA). Simulated situations correspond to scala tympani stimulation in the basal turn. Electrode position and neural path as in Figure 5.1C; homogeneous extracellular medium with extracellular resistivity of 300 Ohm.cm and other data as in (Rattay et al., 2001a).

Four phases in SGN signal transduction

Spike transduction along SGNs can be divided into four characteristic phases. (i) Spike initiation at the peripheral terminal caused by either natural synaptic activation or exogenous current injection resulting in a certain delay of excitation onset (postsynaptic delay t_1). (ii) Axial current flow causes AP conduction in the peripheral process with velocity v_1 . There is only a small deviation from a constant v_1 during the passage of the first node-internode segment. (iii) A considerable delay before the generation of the somatic spike is caused by the large soma capacitance that has to be loaded via axial current flow. Note the lower and long lasting voltage profiles in the presomatic compartments of Figure 5.8A indicated by vertical lines. (iv) Axial current flow from the soma into the central process again causes spike conduction with a velocity of v_2 .

The first characteristic phase, denoted as postsynaptic delay t_1 , is crucially influenced by the amplitude of an injected current pulse appropriate to simulate the synaptic SGN excitation by an IHC. For a 1 μm diameter myelinated peripheral process, a 100 pA square pulse caused a postsynaptic delay $t_1 = 133 \mu\text{s}$ for model data as illustrated in Figure 5.8A. Using a stimulus intensity comparable to recorded synaptic currents in rat, our simulations proposed a shorter postsynaptic delay in the order of 100 μs . The delay t_1 does not include the neurotransmitter release from the hair cell and the diffusion across the synaptic cleft. In man and cat simulations demonstrated nearly the same short postsynaptic delays for type I SGNs (Figure 5.8A and B). In contrast to the assumptions in Figure 5.8C essentially longer postsynaptic delays are expected in type II cells. This phenomenon is analyzed below.

The second and fourth phases denote the spike conduction times t_2 and t_4 in either the peripheral or the central process. A linear distance-time relationship is shown by each of the blue velocity vectors of the propagating APs in Figure 5.8, demonstrating constant propagation velocities v_1 and v_2 in the peripheral and central axons, respectively. By evaluation of the shifted blue velocity vectors in the left graph in Figure 5.8A we found that the AP requires 156 μs to travel 1 mm in the 1 μm thick peripheral process and almost half of this time, 75 μs , in the central axon that has double the diameter. Using the computed data of the longer central process of the human type I cell (Figure 5.8A, $d_2=2 \mu\text{m}$, $v_2=13.33 \text{ mm/ms}$), this quite linear velocity-diameter relationship for the well wrapped myelinated fibers is fitted by

$$v[\text{mm/ms}] = 6.66 \cdot d[\mu\text{m}]$$

wherein the factor 6.66 has the dimension $[1/\mu\text{s}]$ to match dimensional correctness.

The third phase, denoted by the presomatic delay t_3 , essentially depends on the axial current flow from the peripheral process required to load the somatic capacitance. Thus t_3 is influenced by the size and degree of myelination at the somatic region. Reducing the soma diameter in 5 μm steps resulted in a decreased delay of 22 μs per step.

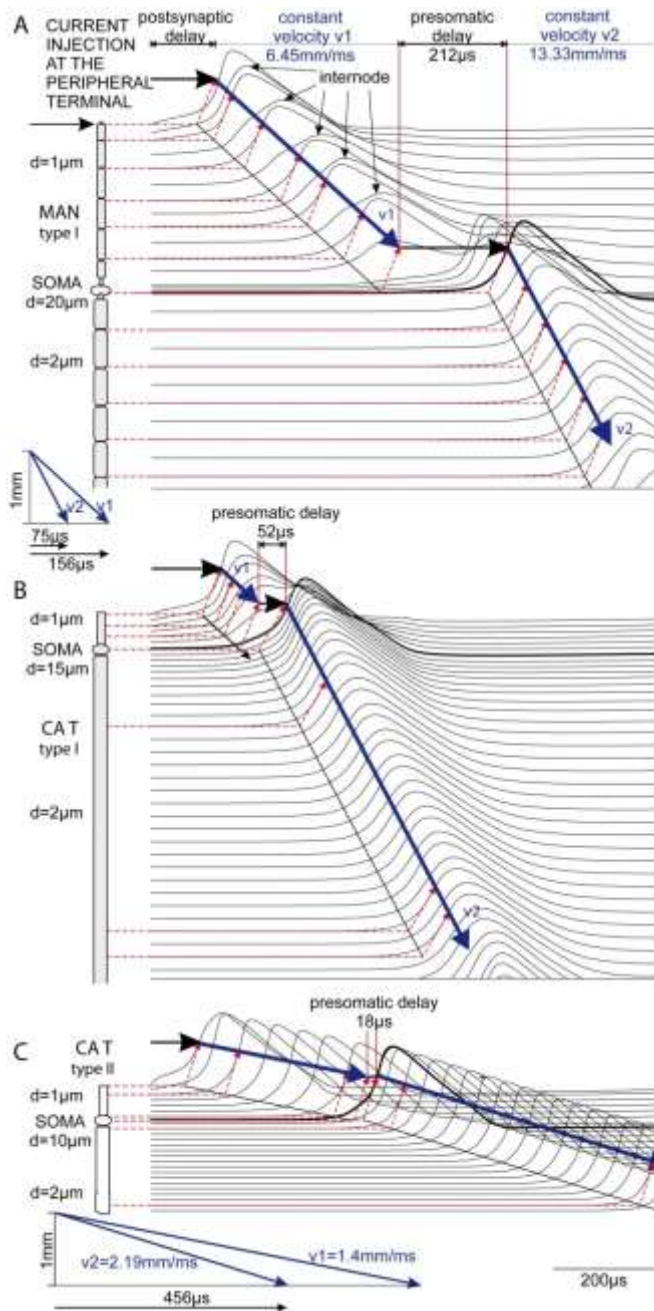


Figure 5.8: Simulated spike transduction in afferent cochlear neurons. Geometry of rectified SGNs (left, myelinated regions in gray) and transmembrane voltage profiles of the corresponding locations (right). For better comparison of phenomenological differences axon diameters and a peripheral terminal length of $10\mu\text{m}$ are chosen to be the same in A-C. Spike initiation by a 0.5ms pulse, 100pA (A and B) and 500pA for the non-myelinated case (C). Signal conduction with nearly constant velocities in the axons is indicated by the geometric construct with the broken red lines and thick blue velocity vectors. Note the attenuation of membrane voltage in the passive internodes and, most pronounced, in the presomatic region.

Type I SGNs

The presomatic delay of $212\mu\text{s}$ in human (Figure 5.8A) is shorter than previously reported by Rattay et al. (2001a). The reason is a reduction of surface and capacity at the soma by a factor $4/9$ when the

diameter is decreased from 30 μm (Rattay et al., 2001a) to an average value of 20 μm which is close to the average size of our morphometric data presented in chapter 4. The same effect occurs when the soma is further reduced to 15 μm which is the average value of cat type I cells. The higher number of myelin layers is even more influential since the somatic capacity decreases inversely with the number of covering membrane/myelin sheets. The human soma was simulated with 3 layers, and that of the cat with 13 layers. Thus the capacity of the myelinated cat soma is reduced by the factor $(3/13)*(9/16) = 0.13$. Further arguments for the vastly short 52 μs presomatic delay in cat (Figure 5.8B) are given below.

Simulated spike propagation along a type I SGN is shown for man and cat in Figure 5.8A and B. In Figure 5.8B the vertical distances of the voltage profiles are markedly shorter since the internodes are assumed to be shorter in cat than in man, although the model fiber diameters are the same. In spite of shortening the internodal lengths, the calculated conduction velocities are almost the same in both cases. Reduction of the internodal length of the central process from 500 μm in man to 350 μm in cat causes a v_2 increase $< 1\%$ from 13.33 to 13.44 mm/ms. Such small influences of the internodal length on the AP conduction velocity in homogeneous myelinated axons are also expected in other modeling work (Moore et al., 1978).

type I SGN										
d1	dsoma	d2 [μm]	nmsoma	t1	t2	t3	t4	t_total [ms]	$\Delta t _{dsoma+1\mu\text{m}}$	
1	20	2	1	0.1	0.339	0.286	2.255	2.981	7.2 μs	man
1	20	2	3	0.1	0.339	0.211	2.255	2.906	4.3 μs	man
1	20	2	7	0.1	0.339	0.178	2.255	2.873	2.7 μs	man
1	20	2	11	0.1	0.339	0.166	2.255	2.861	2.2 μs	man
1.3	20	2.6	3	0.1	0.261	0.186	1.735	2.282	3.5 μs	man
1.3	20	2.6	11	0.1	0.261	0.148	1.735	2.244	1.5 μs	man
1.4	20	2.8	3	0.1	0.242	0.178	1.611	2.131	3.5 μs	man
1.5	20	3	3	0.1	0.226	0.169	1.504	1.998	3.4 μs	man
2	20	4	3	0.1	0.170	0.125	1.128	1.522	3.2 μs	man
1	15	2	13	0.1	0.120	0.052	1.125	1.397		cat
nonmyelinated type II SGN										
d1	dsoma	d2 [μm]	nmsoma	t1	t2	t3	t4	t_total [ms]		
0.73	10	1.3	1	0.8	0.624	0.043	8.771	10.238	cat	
1	10	2	1	0.8	0.533	0.018	7.071	8.422	cat	
0.65	10	1.4	1	0.8	1.869	0.043	16.903	19.615	man	
1	10	2	1	0.8	1.507	0.018	14.142	16.467	man	
myelinated type II SGN										
0.73	10	1.3	13	0.8	0.166	0.035	1.748	2.749	cat	
0.65	10	1.4	11	0.8	0.497	0.083	3.061	4.441	man	

Table 5.4: Computed SGN spike conduction times with additional delay Δt per 1 μm soma diameter increase. d1 and d2 represent peripheral and central axon diameters; nmsoma denotes the number of surrounding single membrane layers in the soma region including the pre- and postsomatic segments. t1, t2, t3 and t4 denote postsynaptic delay, spike conduction time in the peripheral axon, presomatic delay and spike conduction time in the central axon, respectively. $t_{\text{total}} = t_1+t_2+t_3+t_4$, $\Delta t|_{dsoma+1\mu\text{m}}$ denotes the enlargement step of the presomatic delay when dsoma is 1 μm increased.

The velocities v_1 and v_2 are diameter dependent, and they are evaluated with the same equation (1) for cat and man. However, the cat peripheral process has only 3 nodes of Ranvier and evaluation of the velocity/diameter ratio is less precise in comparison to human because uniformity of signal conduction is disturbed at both ends of this short axonal segment.

Spike conduction times for several diameters and different numbers of myelin layers enwrapping the somatic region (n_{msoma}) are listed in the upper part of Table 5.4. Note that for the postsynaptic delay a constant value of $100 \mu s$ is assumed for all cases.

The presented values of the presomatic delay t_3 are computed for a soma diameter of $20 \mu m$ in man. When the number of membrane layers is increased to 11 we calculated a $0.12 ms$ reduction of this delay compared to the unmyelinated situation with 1 layer. Since this delay t_3 is also dependent on the diameter of the soma, the rising ratio of presomatic delay has been calculated for increasing the soma diameter with $1 \mu m$ steps. For standard type I neuron with 3 membrane layers around the soma (plasma membrane of SGN and 2 membranes of SGC) increasing the diameter to $21 \mu m$ resulted in a $4.3 \mu s$ increase of t_3 (compare right column in Table 5.4). These linear relations hold for human soma diameters ranging from 10 to $30 \mu m$ when the soma is connected with a peripheral myelinated process with $d_1=1 \mu m$ in diameter. Doubled diameter $d_1=2 \mu m$ causes stronger axial currents and the presomatic delay decreases from $211+4.3 \mu s$ to $125+3.2 \mu s$ for the $20 \mu m$ standard soma with 3 layers (t_3 column in the upper part of Table 5.4). The main results of Table 5.4 are summarized in Figure 5.9, demonstrating how model parameters accelerate signal conduction of type I cells. Beside the neuron's path length, axon diameter increase has the largest impact on shortening the arrival time, followed by the increase of n_{msoma} and the decrease of soma diameter.

Therefore the greatest advantage of fast signaling in myelinated cat SGNs (in comparison to the human case) results from the shorter auditory nerve ($15.81 mm$ in cat vs. $32.35 mm$ in man), followed by a smaller presomatic delay due to myelination and smaller soma surfaces. Another anatomical difference in typical type I SGN favors the fast signaling in cat. The pre- as well as the postsomatic region in human are unmyelinated segments whereas in cat the soma is assumed to be between two nodes of Ranvier (Rattay et al., 2001a), (Figure 5.1A). Spike conductance in the rather long unmyelinated presomatic segment in human is slow and causes an additional delay which is shown in t_3 (Table 5.4). This reduced velocity in unmyelinated axons explains why the $52 \mu s$ t_3 delay for cat (last row in upper part of Table 5.4 for $d_1=1 \mu m$, $n_{msoma}=13$, $d_{soma}=15$) is much shorter as expected by extrapolation of the $166 \mu s$ t_3 value for man (Table 5.4, row 4 for $d_1=1 \mu m$, $n_{msoma}=11$, $d_{soma}=20$) since a reduced soma diameter of $15 \mu m$ only causes a delay reduction of $5 \cdot 2.2 = 11 \mu s$.

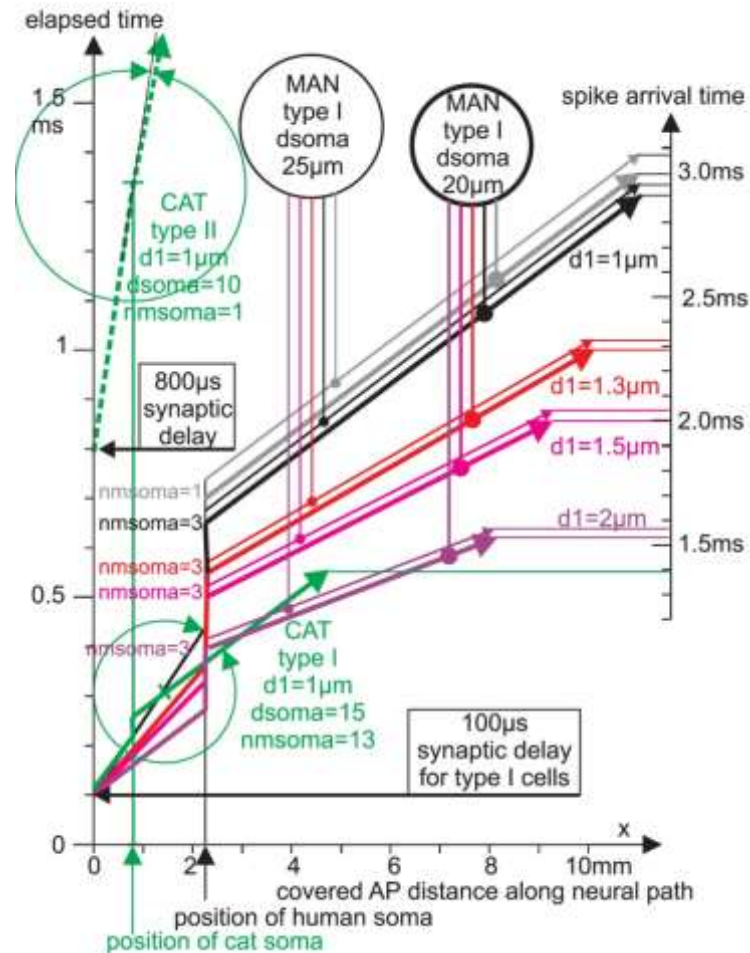


Figure 5.9: Main results of computed SGN conduction times. The diagram summarizes results from Table 5.4, indicating the impact of axon diameters, soma size and myelin on the arrival time under the assumption $d_2 = 2 \cdot d_1$ (central axon has doubled diameter of the peripheral process). The spike arrival time scale at the right side shows the total signal conduction time of type I cells for different axon diameters (marked by colors) for small somas ($d = 20 \mu\text{m}$, thick vectors) and large somas ($d = 25 \mu\text{m}$, thin vectors). All these cases are simulated with 3 sheets of membranes around the soma ($n_{\text{msoma}} = 3$) with the exception of the gray vectors ($n_{\text{msoma}} = 1$) which represent the slowest cases of type I cells. The fastest signal conduction in man (1.522 ms; $d_1 = 2 \mu\text{m}$, $d_{\text{soma}} = 20 \mu\text{m}$; purple thick vector) is topped by the shorter cat type I cell (green vector). The main part of the figure shows the four phases in SGN signal transduction as distance – time diagrams. All vectors for type I cells start with the same synaptic delay of $100 \mu\text{s}$. The lowest vector (purple, $d_1 = 2 \mu\text{m}$) is shifted vertically (according to the presomatic delay) and flattened (because velocity $v_2 = 2 \cdot v_1$) when the spike arrives at the soma (black vertical arrow). All other vectors have the same characteristic shapes with individual slopes and individual shifts at soma. Note that the vertical time shift at the soma increases when axon diameter decreases. Increase of soma diameter causes an additional delay indicated by the vertical distance between corresponding thin and thick vectors. The slow AP conductance of unmyelinated type II cells (green dashed vector) is obvious: the short presomatic delay (beyond graphical resolution) cannot compensate the $800 \mu\text{s}$ lasting synaptic delay. The process diameter enlargement at the soma position ($d_2 = 2 \cdot d_1$) is not as effective as in the myelinated cases. Angles between v_2 and v_1 slopes (green circle arrows) point out small velocity changes (small velocity ratio v_2/v_1) in unmyelinated type II neurons (upper green circle) compared to type I ganglion cells (lower green circle arrows).

Type II SGNs

Spike conduction in unmyelinated fibers requires larger intracellular current flow because of missing the isolating internodal segments of myelinated axons. The lack of myelin sheets causes vastly larger capacities of the fiber resulting in essentially slower conduction velocities. Comparing myelinated and unmyelinated SGNs in cat, the greater somatic capacity in Figure 5.8B is more than compensated by the much stronger axial current flow supplied by presomatic regions. This current increase results from the uniform active membrane of the peripheral unmyelinated process which is more efficient for loading the soma capacity compared to the contribution from sparsely distributed active nodes of Ranvier in myelinated fibers. Consequently a negligibly small presomatic delay of 18 μ s is predicted by our model evaluations (Figure 5.8C).

Still, in comparison with myelinated axons, conduction velocity is vastly slower. Spike conduction requires 456 μ s and 719 μ s for 1 mm in the peripheral and central process, respectively, resulting in $v_1=1.4$ mm/ms and $v_2=2.19$ mm/ms (blue vectors in Figure 5.8C, bottom). Theoretical investigations demand a quadratic velocity - diameter relationship for homogeneous fibers (Rattay, 1990).

The relationship

$$v[mm/ms] = 1.5 \cdot \sqrt{d[\mu m]}$$

with 1.5 of dimension $\sqrt{\mu m/\mu s}$ holds for the investigated non-myelinated fibers (Figure 5.8C) with a maximum deviation of 6%. This may be explained by irregularities in spike initiation at the beginning of each axonal section. Spike conduction times for the same process and soma diameters in cat and man are expected to differ only because of different process lengths (lower part of Table 5.4). Table 5.4 demonstrates that the slow afferent signaling from OHCs is based on a lack of myelin and, second, on an extreme long postsynaptic delay t_1 . Compare also myelinated vs. unmyelinated distance time diagrams in Figure 5.9.

As presented above, we have identified few myelinated type II cells in cat and man (Figure 5.2 A, D). In order to quantify the effect of myelination on type II cells the respective evaluated geometrical parameters were used to model a fully myelinated, OHC innervating neuron for cat and man. In cat, the myelinated type II neurons transmit an AP about 3.7 times faster compared to the unmyelinated standard case. In man, the corresponding neuronal structure transmits the electrical signal 4.5 times faster from the hair cell to the cochlear nucleus.

Jitter and AP delay t_1 are drastically reduced by high currents from ribbon synapses

The first 10 μ m long compartment of our model neuron simulates the short dendritic terminal that connects a type I SGN with an IHC (Spoendlin, 1985; Rattay et al., 2001a; Rattay et al., 2001b). In Figure 5.8 A,B current injection to this segment was a 100 pA, 0.5 ms pulse, which is a rather weak stimulus in comparison to currents from IHC ribbon synapses with an average amplitude I_0 of ~ 400 pA, 280 μ s for time to peak and a decay time constant τ of 370 μ s as recorded in adult P20 and P60 rats (Figure 3 in (Grant et al., 2010)). Applying stimuli of the recorded shape (Figure 5.10A) and intensity immediately initiated spikes for the standard human type I SGN geometry (Figure 5.10B). The fact that the spike in the first compartment almost returned to resting potential when the synaptic current reached its peak time (Figure 5.10A and B) is a consequence of the notably strong stimulus current which exceeds the threshold (Figure 5.10C) by a factor of at least 15. Note the increased spike amplitude of compartment 1 and even of compartment 3 in Figure 5.10B.

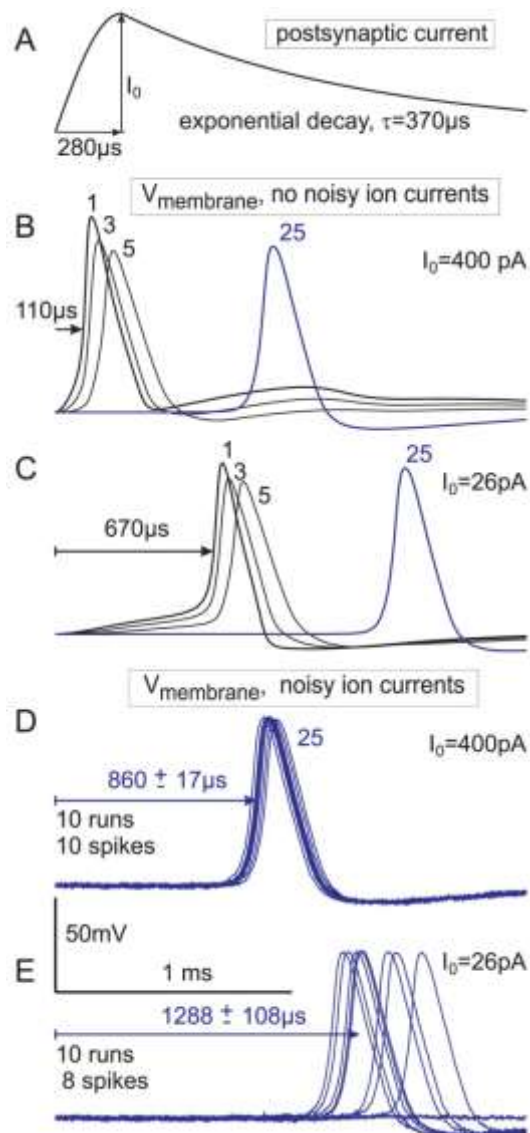


Figure 5.10: SGN response to strong and weak synaptic stimuli. (A) Postsynaptic currents from rat experiments are characterized by amplitude, time to peak and time constant for decay. (B-E) responses of a type I SGN with parameters from Figure 8A are shown for compartments # 1, 3, 5 and 25. Reduction from a typical synaptic current amplitude (B) to threshold (C) caused an essentially longer delay. Including ion current fluctuations (noisy membrane current model, (Rattay et al., 2001a)) in all compartments with active channels resulted in sharply synchronized responses for strong stimulation (D) and in late responses with large jitter (E). Compartment 25 is the fifth postsomatic node of Ranvier in the central process and represents the main part of the expected jitter at the proximal axon ending.

Synchrony in spiking is disturbed by ion current fluctuations in every active compartment with an intensity that was assumed to be proportional to the square root of the number of sodium channels involved (Rattay et al., 2001a). This noisy ion current approach demonstrated a small jitter for strong stimuli (Figure 5.10D) but a large disturbance of synchrony for stimuli in the lower suprathreshold regime (Figure 5.10E). Beside loss of spikes in the order of 20% (Figure 5.10E) an increase of signal transduction time of about 500 μ s can be expected when type I neurons would be stimulated with $I_0=26$ pA.

In contrast to type I cells, the weak stimulus current $I_0=26$ pA seems to be typical for afferents from OHCs (Weisz et al., 2009; Weisz et al., 2012). Whereas type I cells contact single IHCs, type II terminals arborize extensively among OHCs. Seven or even much more synaptic OHC contacts in a region of several hundred micrometers are assumed to be the average for a type II cell (Simmons & Liberman, 1988; Weisz et al., 2012). Because of a lack of data we have not simulated one of the various geometries of the distal terminals of type II cells. The large length constant in the order of 1 mm as reported by Weisz et al. (2009) supported our assumption to simulate this structure again as a single compartment and to use for a rough approach the same excitation characteristics as for the type I cell in Figure 5.10.

Despite their greater pool of synaptic inputs, the frequency of synaptic events in type II afferents is assumed to be about one tenth that observed in type I cells (Weisz et al., 2012). The spatial distribution of synaptic contacts within the terminal causes an additional irregular delay component in t_1 for the signal propagation within this segment. Three new components of t_1 for type II cells should be involved in the model approach: (i) an additional delay of 428 μ s corresponding to the time difference for the spike arrival times in compartment 25 according to cases D and E of Figure 5.10, (ii) a large jitter and (iii) a further delay component by an increased loss of effective synaptic current as consequence of larger axial currents in unmyelinated axons (larger stimulus in Figure 5.8C than in Figure 5.8B). The total t_1 delay can be estimated with 600-1000 μ s. A t_1 value of 800 μ s is used in Table 5.4 for all type II SGNs.

5.5 Discussion

A vast majority of human SGNs (96.35%) are embedded in a continuous, honeycomb structure formed by satellite glial cells (Liu et al., 2012) representing the standard case of type I cells. Thus, each unmyelinated type I cell body is encapsulated by at least one cellular layer of a satellite glial cell [14] resulting in two additional membranes. This micro-anatomical peculiarity is interpreted as $nmsoma=3$ for our standard cochlear type I neuron. The assumed $nmsoma=11$ for the myelinated case is based on 4 and 17 (mean=10.5) myelin layers enwrapping the cell bodies (Ota & Kimura, 1980). This group and Arnold (Arnold, 1987) report that the myelin sheaths were observed to be compact, loose or semicompact, although the loose form was most common.

The process diameter relationship $d_2 = 2 * d_1$ precisely holds for each analyzed human specimen ($n=3$) everywhere along the cochlea spiral. This relationship may also be valid for type II neurons even though the respective diameters (of only one cell) were determined to be half the size compared to type I neurons. Interestingly, the highest density of type II neurons was found within the middle turn of the analyzed specimens where the majority of phonational frequencies are situated (Loizou, 1999; Hollien et al., 1971).

Based on morphometric data, degree of myelination and postsynaptic hair cell currents, we used a biophysical model to simulate and compare excitation profiles and spike propagation in human and feline SGNs.

5.5.1 Spike duration

In contrast to long lasting spikes of a SGN mouse model (Hossain et al., 2005) the AP duration of 1/3 ms of our model was shown to be in agreement with temporal properties of intracochlear recordings (Figure 5.7E). Such short APs are known from peripheral nerve models for myelinated axons in frog, rat and rabbit (Chiu et al., 1979; Schwarz & Eikhof, 1987; Sweeney et al., 1987; Rattay, 1990; Rattay &

Aberham, 1993; Rattay et al., 2003). AP durations longer than 1 ms are typical for excitable membranes in the central nervous systems (Bean, 2007; Kress & Mennerick, 2009; Hu et al., 2009; Rattay & Wenger, 2010). Shorter spikes are reported from octopus cells in the ventral cochlear nucleus (Golding et al., 1999), but the SGN spikes are even shorter. The time to peak and the duration of an AP depend on the types of ion channels, their kinetics and densities, the membrane capacitance and other parameters. Although many relevant details are known for mammalian SGN membranes, as yet there is no accurate cable model available which matches the AP shape of type I cells. An appropriate short and rapidly increasing AP as simulated with our model is a key element for the quick signal conduction in the afferent part of the auditory nerve. The short spikes and the fit of the formula for axon conduction velocity of type I cells (Eq. 1) to experimental findings on peripheral myelinated axons (see below) underlines closer electrophysiological affinity of SGNs to the peripheral nerve system than to the central one.

5.5.2 Simulated conduction times correlate with ABR

The simulated spike conduction times for afferent signal transmission can be evaluated with auditory brainstem response (ABR) data as time difference between the peaks of wave I and wave III. Esteves et al. (2009) reported corresponding ABR interpeak times of 2.13 ± 0.14 ms ($n=120$ ears) in normal hearing human subjects. Van den Honert and Stypulkowski (1986) analyzed ABR recordings of 10 normal hearing cats and reported a mean signal latency between waves I and III of 1.41 ± 0.1 ms. According to our model, the corresponding values in Table 5.4 are 2.13 ms for a peripheral process diameter $d_1=1.4$ μm (man) and 1.40 ms for $d_1=1$ μm (cat). Whereas the cat data fit was almost perfect, our systematic morphometric evaluation from human specimens rely on the $d_1=1.3$ μm case which predicts a 150 μs longer conduction time of 2.28 ms.

Closer examination of the cat data (Table 5.3) shows that the systematic diameter evaluation in cat deviates from the $d_2/d_1=2$ relation used in Table 5.4. Reducing d_2 from 2 μm to 1.8 μm demands for a 10% reduction of velocity v_2 (Eq. 2) and a 10% increase of t_4 according to Table 5.4, leading to an additional delay of 112 μs . A possible explanation to this discrepancy between spike conduction times and ABR interpeak times may be found with the help of Figure 5.7 where the conducted spike is recorded within the cochlea. Although the recording electrode is close to the thin peripheral process (Figure 5.1C) the main contribution in the recorded signal appears when the spike passes the soma region (Figure 5.7). This activity should contribute more to the peak I in ABR recordings than the excitation of the peripheral axon. ABR peak III should be generated when the spike arrives at the increased surface of excited membranes in the branching central SGN terminals causing synaptic activation in the cochlear nuclei.

Electrically evoked ABRs from cochlear implantees were analyzed recently (Undurraga et al., 2013). Poststimulus latencies of peak III were shorter for anodic pulses and they clustered at about 2 ms. In most of the reported cases spike initiation can be assumed within the central axon at a site close to the soma. This 2 ms delay which is similar to the interpeak time III - I recorded in healthy people (Esteves et al., 2009) supports a hypothesis derived from Figure 5.7E where it is seen that the second peak exceeds the contribution of the thin peripheral process. This effect is assumed to be more pronounced in human type I cells because of the higher current flux across the active membrane in the larger presomatic compartment. Therefore, peak I in healthy people may represent the large sodium current influx when the spike enters the nonmyelinated presomatic region.

5.5.3 How myelin accelerates signaling

The examples in Figure 5.8 and Table 5.4 suggest two types of acceleration of signal conduction by myelin, namely at the axons and in the soma region. The values t_2 and t_4 in the upper and lower part of Table 5.4 demonstrate the rapid conduction of myelinated fibers compared to the non-myelinated. The factor 6.66 for the linear relation between axon diameter and simulated velocity (Eq. 2) is quite close to 6.57, which is the corresponding scaling factor for small diameter myelinated axons as reported by Boyd and Kalu (1979), who found an average value of 4.6 for v/D . Incorporating an inner/outer fiber diameter ratio $d/D = 0.7$, the equivalent scaling factor is $4.6/0.7=6.57$.

Reduction of myelin layers and the markedly bigger diameter of the soma are the reason for a notable capacity enlargement resulting in a distinct presomatic delay for bipolar neurons in man. This delay is smallest for non-myelinated cells with a small diameter ratio of soma / peripheral process, e.g. 18 μs for type II cells (t_3 in the lower part of Table 5.4 and Figure 5.8C) but increases for human type I cells to 286 μs ($d_1=1 \mu\text{m}$, $d_{\text{soma}}= 20 \mu\text{m}$, $n_{\text{soma}}=1$; Table 5.4) and even higher delays are expected for large somata (Figure 5.9) (Rattay et al., 2001a). According to observations of Spoendlin (Spoendlin, 1985) there is a single node of Ranvier in the vicinity of the cat soma, whereas biophysical modeling demonstrates the need for a considerably longer active membrane length of the presomatic segment in cases of poorly myelinated somata (Figure 4B) in order to provide enough inneraxonal current to load the capacity of the cell membrane. The length of this presomatic nonmyelinated segment was not systematically determined, but it is always considerably longer than a node of Ranvier, e.g. Ota and Kimura (1980) measured 5-26 μm long presomatic segments in human type I cells.

The signal accelerating effect of myelin is imposingly demonstrated by type II cells (Table 5.4, lower part and Figure 5.9). A fully myelinated small cochlear neuron transmits an AP in about one-fifth of the time over its neuronal structure which influences the spatial- as well as temporal pattern of spiking. These changes show probably the highest effect in elderly people as a consequence of reported increase of myelination with age not favoring any type of neurons (Ota & Kimura, 1980). As Table 5.4 presents, myelination alters the temporal pattern of APs on their way to the cochlear nucleus which may additionally influence temporal processing throughout the auditory pathway. This could be a problem for the elderly with reduced brain plasticity and, thus, reduced ability to resolve that temporal changes.

Our auditory nerve model confirmed that the conduction velocity of a uniform myelinated axon is proportional to the diameter but it is rather independent from the internodal length. However, signal amplitude is smaller in the internode than in the voltage amplifying node. This phenomenon is especially evident in human type I cells at the last internode before the presomatic section and, in contrast to the myelinated cat soma, the weak inneraxonal current causes a remarkable presomatic delay and endangers signal propagation. Two or more cell bodies of human SGNs sometimes comprise a common insulation by glial cells. Within such a cluster a close contact of somatic cell membranes is evident. Tylstedt and Rask-Andersen (Tylstedt & Rask-Andersen, 2001) speculate whether unique formations between such human spiral ganglion cells may constitute interactive electrotonic or ephaptic transmission pathways. These may increase neural synchrony and signal acuity related to the coding of speech. This hypothesis will be tested in a forthcoming paper as well as our suggestion that clusters could also work as filters in order to suppress spontaneous spikes without acoustic signal information.

5.5.4 Synaptic hair cell currents

Another surprising fact predicted by the biophysical model can be deduced from the large stimulus of $\sim 400\text{pA}$ recently recorded from the inner hair cell ribbon synapse (Grant et al., 2010) which is in accordance with our simulations of about 15 times the threshold current of typical type I SGNs. Such strong stimuli cause an accelerated spike propagation in the peripheral terminal via increased axial current leading to an extremely short postsynaptic delay t_1 of $\sim 100\ \mu\text{s}$. Weak synaptic stimulation, e.g. $26\ \text{pA}$, as found in type II cells (Weisz et al., 2009; Weisz et al., 2012) causes a longer delay t_1 in the order of $1\ \text{ms}$ but also a large AP jitter that disturbs synchrony of the firing SGNs. This excess of stimulus energy is obviously important for quick and precise signaling in type I cells.

5.5.5 Significance for natural hearing and cochlear implants

The quite constant diameter ratio of $1/2$ for peripheral/central processes and the similarity in distinctive myelination of human type I SGN guarantees constant spike conduction times in each frequency region of the cochlea. Taking into account the coiled symmetry of the cochlea, uniform signal conduction times are most likely for APs triggered within the basal turn as well as for signals originating from the middle portion. In the low frequency region, increasing conduction times can be expected (Shamma, 1985; Rattay & Lutter, 1997) due to varying lengths of the peripheral processes. However, this continuously rising time delay for signals from the apical region can be assumed to have insignificant effects due to rather constant length of SGNs responsible for frequencies of one octave. This neural architecture maintains most of the temporal information of acoustic signals and allows phase locking up to $4\ \text{kHz}$ in the spiking patterns of higher auditory centers of the brain ((Shamma, 1985; Rattay & Lutter, 1997) Figure 4B). Contrary to natural hearing, cochlea implants initiate spikes at different sites along SGN (Javel & Shepherd, 2000; Rattay et al., 2001a; Rattay et al., 2001b) which depends on the degree of preservation of cochlear neurons (Nadol, 1997; Nadol et al., 2001; Glueckert et al., 2005b). The resulting temporal mismatch within a population of excited cells is mainly caused by simultaneous AP initiations in peripheral and central axons. As an example, the presented biophysical model predicts the lower threshold in cat for cathodic pulses but in man for anodic ones (Rattay et al., 2001a), which was assumed to be the same in both species but model results have been confirmed by implantees (Macherey et al., 2008). This study has shown that due to several differences between the cat and human SGNs, for example a considerably longer human presomatic delay, these differences should be incorporated into auditory nerve models that rely on the data from the cat when investigating speech processing strategies for cochlea implant recipients.

Clustering of Human Spiral Ganglion Neurons: An Morphometrical Analysis and Computational Model Study of Ephaptic Coupling Effects to Intra- and Extracellular Stimulation

6.1 Abstract

The unmyelinated cell bodies of human auditory neurons are the most specific peculiarity and represent the first crucial barrier for an action potential (AP) on the way from the hair cells to the auditory cortex. The vast majority of these cell bodies are embedded in a honeycomb-like structure formed by satellite glial cells (SGC). Sometimes, two or three cell bodies are positioned so close to each other that their cell membranes feature direct-cell-to-cell contact, not separated by any branches of SGC between them. This unique arrangement of spiral ganglion neurons (SGN) give rise to numerous speculations concerning possible interaction pathways that may increase plasticity and signal acuity related to the coding of speech.

Immunohistochemical staining in combination with confocal microscopy was used to systematically study three human specimens to determine in a first step the frequency of occurrence of cluster-arranged neurons along the cochlea spiral. Three dimensional confocal image stacks enabled to reconstruct such clusters comprising two or three cell bodies of SGN. In order to analyze these bi- and tricellular arrangement on potential ephaptic interactions, a biophysical model of a SGN was adapted. Therefore, a new model approach was developed that includes ephaptic coupling between cell bodies of SGNs. The ephaptic interaction and the resulting coupling effects were studied when single pulses or pulse trains of different frequencies were offered by intra- as well as extracellular stimulation.

Analysis of the occurrence of clustering cell soma based on three individual cochleae reveal a spatial organization along the cochlea spiral with a distinct maximum in the low-frequency regions. In contrast, the middle turn region which is of prime importance for speech understanding houses quite the same amount of bicellular clusters in all three investigated cochleae. The subsequent conducted computer simulations with the aim to study ephaptic coupling effects between clustering SGNs predict two different consequences: (i) a spike that is generated by ephaptic coupling get synchronized with the triggering AP of the adjacent neuron, and (ii) when the ephaptic conductivity between two cells is beyond a certain range, inhibiting effects occur due to somatic current loss and the APs break down at the soma.

The presented biophysical model enables to study ephaptic coupling effects between adjacent cell bodies of human SGNs. It is shown that electric and ephaptic interaction has powerful impact on signal transmission in the normal hearing cochlea. Even adjoining cells that send APs at different frequencies to the central nervous system can be synchronized which influences the temporal pattern of such neurons. Together with our immunohistochemical findings concerning the maximum occurrence of clustering SGNs, clustering in humans may represent adaptedness to verbal communication compared to other mammals.

6.2 Introduction

Cell bodies of type I cochlear neurons in mammals are isolated by numerous layers of myelin which ensure efficient spike propagation but reduces the ability of physical and/or chemical interactions between individual perikarya of cochlear neurons or between cell bodies and their circumjacent SGC. The unique, unmyelinated cell body of human auditory neurons (Ota & Kimura, 1980; Arnold, 1987; Spoendlin & Schrott, 1989) which are mostly covered by common SGCs (Liu et al., 2012) boosts the capability to form a structural and functional neuron-glia unit featuring two-way exchange of information.

Absence of insulating myelin forms the basis of the second outstanding peculiarity among human afferent cochlear neurons. Kellerhals et al. (1967) was the first group which reported in an ultrastructural study that human SGNs can form structural groups or cell clusters. A more detailed analysis of these unit-like structures (Tylstedt et al., 1997) using a transmission electron microscope (TEM) suggests that within the cochlea region of maximal innervation density, the cell bodies of neurons were frequently ensheathed by the same SGC so that they are gathered to clusters with 2-4 neurons. These clustered SGNs showed signs of physical interaction as the membranes of adjacent somata were in direct apposition. In addition, the addressed frequency region within the human cochlea is of prime importance for speech understanding (Hollien et al., 1971; Loizou, 1999). In another study Tylstedt and Rask-Andersen (2001) investigated distinct membrane specializations of these 'gaps'. They speculate whether unique formations of SGCs may constitute interactive electrotonic or electronic transmission pathways. These would be more frequently in the low frequency region due to reported higher cluster density (Tylstedt et al., 1997) and may increase plasticity and signal acuity related to the coding of speech.

Some modeling studies did comprehend with ephaptic coupling between neural elements although most theoretical studies of ephaptic interactions have been performed for parallel axons (Binczak et al., 2001) due to the simple geometry as summarized in Holt and Koch (Holt & Koch, 1999).

Within a more recent immunohistochemical study, Liu et al. (2009a) identified several connexin proteins within various regions of the human hearing organ. Based on their results, the group suggests that some neurons may encode their incoming sound information using nerve signal synchronization with closely adjacent neurons. This would be quite efficient due to much faster responses of electrical- compared to chemical synapses and was also reported to happen within the central nervous system (Bennett & Zukin, 2004). Moreover, this much quicker information exchange may play a crucial role in encoding the quite complex and unique human speech. Connexins were also identified to be expressed by SGCs located in the spiral ganglion (Liu et al., 2009a) forming the distinct honeycomb alignment that houses the somata of SGNs (Liu et al., 2012). Liu et al. (2012) additionally discusses the hypothesis that this unique micro-anatomical setting facilitate the possibility that electric currents from a cell soma may spread over the surrounding SGCs to activate a small population of adjoined neurons simultaneously resulting in synchronization of transmitted encoded auditory signals.

In this paper we present a new modeling approach that enables to study ephaptic interactions in cell clusters which are uniquely formed by human type I SGNs. Immunohistochemistry including confocal microscopy was performed to (i) determine the morphometrical composition of clusters within the human spiral ganglion and to (ii) identify the frequency of occurrence of these arrangements along the cochlea spiral of three human individuals. Confocal microscopy was deployed to acquire three-dimensional image data of clustering neurons which were manually reconstructed to calculate the volume and the surface of involved cell bodies. Data was subsequently used to quantify the shared contact areas of clustering bipolar cell bodies of four representative clusters. For the conducted computer simulations, a biophysical model of an auditory neuron (Rattay et al., 2001a) was extended by incorporation of morphometrical cluster data. This adapted computational model was used to study the ephaptic excitation profiles of clustering neurons to various intra- as well as extracellular stimulation frequencies.

6.3 Material and Methods

6.3.1 Specimens

The current study investigated three inner ears from male individuals aged 56 to 74 years without any diagnosed ear disease or hearing loss (audiograms not available). The cochleae were obtained during routine autopsy at the Institute of Pathology, Innsbruck Medical University. Human cochleae were prepared, fixed and embedded as described in chapter 4. Briefly, after opening the round- and oval window, cochleae were immersion fixed in 4% paraformaldehyde for 24h at 4°C. Afterwards, specimens were decalcified using 20% ethylenediaminetetraacetic acid at pH 7.4 for 6 weeks and prepared for cryoembedding according to Coleman et al. (2009).

6.3.2 Immunohistochemistry

After washing with PBS (pH=7.4, 6x5 min) sections were incubated with a solution containing PBS, 5% bovine serum albumin (BSA), 15% non-immune normal donkey serum (NDS) and 0.3% Triton X-100 for 2h at room temperature to block unspecific reactions. Cryosections were treated using a mixed solution of mouse-monoclonal anti- β -III-tubuline antibodies (1:500, Chemicon, Billerica, MA, USA), rabbit-polyclonal anti-S-100 antibodies (1:200) and rat-monoclonal anti-myelin basic protein (1:100, both Sigma-Aldrich, St. Louis, MO, USA) in a humid and darkened chamber overnight at 4°C followed by 75 min at 37°C. Primary antibodies were diluted in a solution containing PBS, 1.67% BSA, 5% NDS and 0.1% Triton X-100. After rinsing sections with PBS (6x5 min) they were incubated with secondary antibodies conjugated to Alexa Fluor 488 (donkey anti-rabbit, 1:1000), Alexa Fluor 546 (donkey anti-

mouse, 1:1000) and Alexa Flour 633 (goat anti-rat, 1:1000, all Invitrogen, Carlsbad, CA, USA) diluted in PBS for 2h at RT under dark conditions. After a last washing step with PBS (6x5 min), sections were subsequently mounted using Vectashield mounting medium with DAPI (Vector Laboratories, Burlingame, CA, USA) for complemental nuclei-counterstaining.

6.3.3 Confocal Imaging and Processing

A Zeiss LSM 510 Meta confocal laser-scanning microscope equipped with a 20x/0.8 NA dry lens and a 63x/1.4 NA oil immersion lens was used to analyze immunohistochemistry stained sections. To detect cell nuclei, cell bodies, SGCs and myelination of cochlea neurons simultaneously, we used for excitation a 405 nm diode laser, a 488 nm line of an argon ion laser, a 543 nm and a 633 nm HeNe laser. Images and 3D-stacks were captured using ZEN software (Zeiss, Jena, Germany). The pixel-sizes of the acquired 3D-stacks were chosen and calculated according the Nyquist-Shannon sampling theorem resulting in the following resolutions: $x=38$ nm, $y=38$ nm, $z=122$ nm. Subsequently, the acquired 3D - Confocal image stacks of the SGC clusters were processed with Amira 5.4 (Visage Imaging, Carlsbad, CA, USA). Each stack was separated subsequently in its single channels allowing individual deconvolution for image restoration. Therefore, a theoretical point spread function was computed for each channel. The point spread functions were then used to deconvolute each channel using a non-blind maximum-likelihood image restoration algorithm for 40 iterations. To enhance Signal-to-Noise-Ratio a median filter was applied to data prior to segmentation. Perikarya, their corresponding nuclei as well as their direct contact area within a cluster were manually segmented using Amira's 'Segmentation Editor'. Segmentation data were saved in a label field which was used to quantify the volume of each mentioned structure as well as the contact area between cell somata. For visualization data were smoothed by producing a surface from a resampled label field.

6.3.4 Statistical Analysis

One-way analysis of variance followed by Bonferroni correction was used to determine statistical significance. Normality of data was assessed by quantile-quantile plots. Statistical significance as well as descriptive statistics was computed using MatLab[®] 2011a (MathWorks, Natick, MS, USA).

6.3.5 Computational Model

Each neuron of a modeled cluster was split up into cylindrical compartments with passive internodes (40 myelin layers for the peripheral process, 80 layers for the central process) and active nodes. These nodes as well as the unmyelinated soma, the postsomatic region and the presomatic segment (consists of three compartments) were with modified Hodgkin Huxley ion channel kinetics at 37°C. The spherical soma diameter of 20 μ m was taken from chapter 4 and represents a mean value for human cochlear perikarya along the spiral organ. To create the human standard type I SGN, the compartments of the peripheral process were modeled with a diameter $d_1=1.3\mu$ m whereas the diameter of the central process was set to $d_2=2.6\mu$ m (chapter 5). The unmyelinated somatic region is enwrapped by three membrane layers (chapter 5) representing the standard case in the human cochlea (Rattay et al., 2001a).

In order to analyze the effect of possible ephaptic coupling between human cochlear neurons, the biophysical model has to be extended at the soma compartment where neurons are in direct contact on a certain area. The adapted circuit for a two cell cluster is presented in Figure 6.1 where V denotes the potential of the first cell and W denotes that of the second cell. The red arrows correspond to the electrical currents of the soma compartment of the first cell, whereas the blue ones indicate those of cell 2. This representation shall help to derive the equations for the two and three neuron cluster.

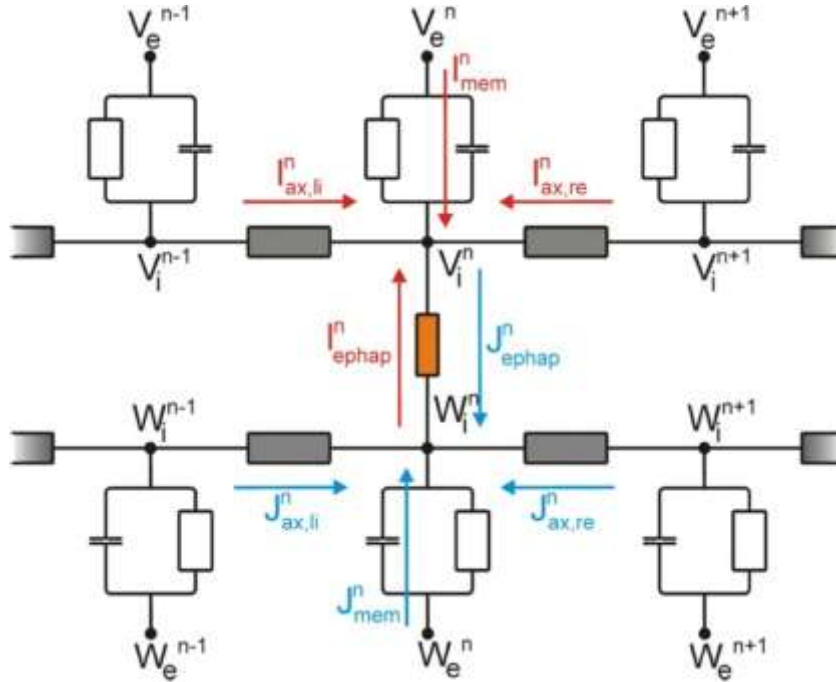


Figure 6.1: Electrical circuit model of the adapted biophysical model. The cell somas of two neurons are surrounded by one common sheet of myelin. I currents denote to cell 1 of the bicellular cluster, J currents correspond those of cell2.

Thus, the equations for the soma compartments will be deviated by applying Kirchhoff's Law. This time the ephaptic current has to be included, i.e. I_{ephap}^n denotes the current from the inside of the first cell with an internal potential denoted as V_i^n . The corresponding current of the second cell is denoted as J_{ephap}^n . The extended equation therefore can be written as

$$I_{ephap}^n + I_{ax,r}^n + I_{ax,l}^n + I_{mem}^n = 0 \quad (6.1)$$

$$J_{ephap}^n + J_{ax,r}^n + J_{ax,l}^n + J_{mem}^n = 0 \quad (6.2)$$

If ephaptic connections are considered to allow electrical current flow through a resistor from one intracellular soma compartment to the other intracellular soma compartment it follows

$$I_{ephap}^n = G_E^n \cdot (V_i^n - W_i^n), \quad (6.3)$$

$$J_{ephap}^n = G_E^n \cdot (W_i^n - V_i^n) = -I_{ephap}^n. \quad (6.4)$$

Critical assumptions have to be made for the parameter $G_E^n = g_E^n \cdot A_{contact}^n [mS/cm^2] \cdot [cm^2]$. One layer of membrane is assumed to have a conductance of $g_E = 1 mS/cm^2$ (Rattay et al., 2001) If two cells have direct contact one could assume two layers of membrane (summing up to $g_E = 0.5 mS/cm^2$) or also consider possible ionic flow through certain membrane specializations which might increase the value of g_E .

Our immunohistochemical analysis detected besides bicellular clusters also the occurrence of tricellular neuron arrangements where one soma in the middle of the cluster is in between two outer

somata. Therefore, each outer neuron share a certain contact area with the middle neuron that has direct cell-to-cell contact to the outer neurons.

For this configuration, three transmembrane potentials in the cluster are assumed that vary with time: V_n^1 describes the transmembrane potential of the n-th compartment of cell 1, V_n^2 of cell 2 and V_n^3 of cell 3. Since we investigate ephaptic coupling effects between cell somata, n denotes the soma compartment of each cell. Additionally, the ephaptic currents are described in the same manner so that $I_{ephap,n}^1$ denotes the ephaptic current of soma 1, $I_{ephap,n}^2$ of soma 2 and $I_{ephap,n}^3$ that of soma 3. Hence, the ephaptic currents of the tricellular cluster reads as

$$I_{ephap,n}^1 = G_{E,n}^1 \cdot (V_{i,n}^1 - V_{i,n}^2) \quad (6.5)$$

$$I_{ephap,n}^2 = G_{E,n}^1 \cdot (V_{i,n}^2 - V_{i,n}^1) + G_{E,n}^2 \cdot (V_{i,n}^3 - V_{i,n}^2) \quad (6.6)$$

$$I_{ephap,n}^3 = G_{E,n}^2 \cdot (V_{i,n}^3 - V_{i,n}^2) \quad (6.7)$$

This time, the differential equations have to be adapted according to

$$I_{ephap,n}^1 + I_{ax,R,n}^1 + I_{ax,L,n}^1 + I_{mem,n}^1 = 0 \quad (6.8)$$

$$I_{ephap,n}^2 + I_{ax,R,n}^2 + I_{ax,L,n}^2 + I_{mem,n}^2 = 0 \quad (6.9)$$

$$I_{ephap,n}^3 + I_{ax,R,n}^3 + I_{ax,L,n}^3 + I_{mem,n}^3 = 0 \quad (6.10)$$

Intracellular stimulation

The synaptic activation of a type I cell by an inner hair cell was mimicked by an injected current pulse (0.1nA, 0.1ms) to the first unmyelinated compartment. This model neuron was stimulated by single pulses as well as pulse trains at frequencies of $f_{stim}=200\text{Hz}$ and $f_{stim}=333\text{Hz}$.

Extracellular stimulation

One active electrode position was used to mimic a firing cochlear implant in the basal turn. The electrode was virtually placed in scala tympani close to the distal end of the bony spiral lamina. The electrode position was introduced previously as E1 in chapter 4, Figure 4.2.

Threshold currents for four different pulse shapes were evaluated: monophasic cathodic (CAT) and anodic (ANO) pulses with a length of 0.1ms as well as biphasic pulses of equal amplitudes for leading cathodic (BIC) or anodic (BIA) phase both with 0.1ms/phase. During the simulations, parameters like the initiation site (IS) of APs and the corresponding peak time (PT) as well as the time when the AP reaches the last compartment of the model neuron (ET). Single pulses as well as pulse trains of different frequencies (200Hz, 333Hz and 2000Hz) are delivered by a spherical electrode. Details concerning further geometric and electrical model parameters are described in Rattay et al. (2001a).

6.4 Results

Since we want to analyze the effect of direct cell-to-cell contact on the excitation profiles of such closely spaced neurons, a new definition of these structures was introduced:

'A cluster consists of two or more perikarya which show direct cell-to-cell contact without any (branches of) satellite glial cells in between which would act as separative elements electrically isolating one neuronal structure from the other'

6.4.1 Clusters along the Cochlear Spiral

According to this definition, the use of anti-S-100 antibodies against SGCs (among others) enabled to detect such neuron separating cells on confocal microscopy level. In order to not overlook any SGC branches between perikarya, we acquired 3D-stacks and analyzed them individually. The results regarding their frequency of occurrence are presented in Table 6.1 for each specimen as well as their origin along the cochlea spiral.

We did not identify any cluster according our definition within the high frequency region of specimen 1 (n=184 cell bodies). Within the middle turn, 10 cell bodies were arranged in 2-neuron-clusters representing 3.2% of all analyzed perikarya of this region (n=315). The majority of clusters are identified in the apical region of specimen 1 where 24 cells (\pm 8.2%) are forming 2-neuron-clusters. Furthermore, another 6 cell bodies were found to compose 3-neuron-clusters representing 2% of all analyzed perikarya (n=294) within the low-frequency region of this inner ear.

Neuron-clusters were again completely absent within the basal turn of specimen 2 where 293 cells bodies were evaluated (Table 6.1). A total number of 12 perikarya were identified in the middle turn of this cochlea (n=410) to form 2-neuron-clusters representing 2.9% of all scanned neurons within this region. Contrary to analyzed specimen 1 and 3, one 3-neuron-cluster (\pm 0.7%) comprised of three perikarya with direct cell-to-cell contact were found in the middle turn. Again the highest density of cluster-forming was identified within the apical region. Analyzing 479 cell bodies depict that 28 neurons (\pm 5.8%) constitute 2-neuron-clusters while one 3-neuron-cluster was detected which represents 0.6% of apical cell somata.

As it was shown in the other inner ears, the basal turn of specimen 3 once again lacks neuron-clusters according our definition (n=527). In the middle turn region (n=301), 8 cochlea neurons were found to form 2-neuron-clusters (\pm 2.7%) while one 3-neuron-cluster (\pm 3.4%) and four 2-neuron-clusters (\pm 1.3%) were identified in the apical region (n=236) of this specimen.

Analyzing data of all three inner ears we did not identify any two- or three-neuron cluster within the basal turns representing the high-frequency regions (Table 6.1). From this region, we examined a total number of 1004 cell bodies. Within the middle turns (n=1026) we found 30 cell bodies forming 2-neuron-clusters (\pm 2.9%) and 3 cell bodies aligning one 3-neuron-cluster representing 0.3% of all analyzed middle turn neurons. The majority of clusters were identified in the apical region of the analyzed specimens. 62 neurons (\pm 6.1%) of all scanned perikarya of this region (n=1009) appear as 2-neuron clusters while 12 cell bodies formed 4 individual 3-neuron-clusters (\pm 1.2%). In summary, we examined 3039 cell bodies of three independent human cochleae and identified 92 perikarya aligned to 2-neuron-clusters (\pm 3% of all evaluated neurons) and 15 cells composing 3-neuron-clusters (0.5% of all scanned cell bodies).

Cochlea	Region	n=	Bicellular Cluster	Tricellular Cluster
Specimen 1	basal	184	0	0
	percentage [%]			
	middle	315	5	0
	percentage [%]		3,2	
	apical	294	12	2
	percentage [%]		8,2	2
Specimen 2	basal	293	0	0
	percentage [%]			
	middle	410	6	1
	percentage [%]		2,9	0,7
	apical	479	14	1
	percentage [%]		5,8	0,6
Specimen 3	basal	527	0	0
	percentage [%]			
	middle	301	4	0
	percentage [%]		2,7	
	apical	236	4	1
	percentage [%]		3,4	1,3
Total	basal	1004	0,0	0,0
	percentage [%]			
	middle	1026	15	1
	percentage [%]		2,9	0,3
	apical	1009	31	4
	percentage [%]		6,1	1,2

Table 6.1: Summary of identified direct cell-to-cell contact clusters. Data is presented for each analyzed specimen along distinctive regions along the cochlea spiral.

6.4.2 Cluster Arrangements

In order to study possible ephaptic coupling effects between cell somata of cochlea neurons, we reconstructed four representative neuron-clusters from 3D confocal stacks for further analysis. Figure 6.2 illustrates three clusters consisting of 2-neurons while reconstructed cluster 4 represents a 3-neuron-cluster featuring direct cell-to-cell contact.

Cluster 1 (see Figure 6.2) was acquired in the apical region of specimen 2 and consists of two perikarya of cochlear neurons. The green colored somata represents cell 1 and has a diameter of 17 μm whereas larger cell 2 is presented in yellow reaching 21.4 μm in diameter (Table 6.2). The corresponding cell nuclei are illustrated in blue. The reconstructed, direct contact area between these two cell bodies (visualized in red) was calculated to be 113.7 μm^2 representing 12.5% of the total area of cell 1 and 7.9% of the determined surface of cell 2. According to our previous work (see chapter 4) where we classified perikarya of human SGNs according to their volume along the cochlear spiral, green-colored cell 1 belongs to population 2 ($18.6 \pm 5.4 \mu\text{m}$) and cell 2 represents population 3 ($21.8 \pm 5.2 \mu\text{m}$).

	Cell Body	Volume [μm^3]	d [μm]	Surface [μm^2]	Contact Area [μm^2]	percentage of total area [%]
CLUSTER 1	cell 1	2571,5	17,0	3630,8	113,7	12,5
	cell 2	5125,1	21,4	5750,2		7,9
CLUSTER 2	cell 1	909,4	12,0	1815,7	74,8	16,5
	cell 2	1029,8	12,5	1972,6		15,2
CLUSTER 3	cell 1	3207,8	18,3	4207,4	83,4	7,9
	cell 2	3237,2	18,4	4233,1		7,9
CLUSTER 4	cell 1	3664,7	19,1	4598,0	135,6	11,8
	cell 2	2213,6	16,2	3285,5		16,5
	cell 2	2213,6	16,2	3285,5	76,3	9,3
	cell 3	1728,6	14,9	2786,1		11,0

Table 6.2: Summary of reconstructed neuron-clusters featuring direct cell-to-cell contacts. Given are the calculated volumes of cluster-involved cell somata, their diameter and total surface area as well as segmented cell-to-cell contact area and the respective percentage of the total area.

The second cluster was reconstructed from the middle turn of specimen 3. Both neurons are almost similar sized and belong to the smallest identified population 1 ($13 \pm 4.7 \mu\text{m}$) among human cochlear neurons. The diameter of the green-colored soma was measured to be $12 \mu\text{m}$; cell 2 (illustrated in yellow) is slightly larger reaching $12.5 \mu\text{m}$ (Table 6.2). The direct cell-to-cell contact area was assessed at $74.8 \mu\text{m}^2$. Due to their closely spaced positions, this contact surface results in quite high percentages in respect of the total area of each cell (16.5% for cell 1 and 15.2% for cell 2).

The third presented cluster was scanned in the apical region of specimen 1 and shows again quite uniform diameters. Reaching $18.3 \mu\text{m}$ and $18.4 \mu\text{m}$ for cell 1 (green) and cell 2 (yellow) respectively, these two neurons are assigned to be members of population 2. The direct contact area was determined to be $83.4 \mu\text{m}^2$ which represents 7.9% of the total area of both neurons. Note that contrary to the other presented 2-neuron-clusters, the influence of the cell bodies on each other is equal. Furthermore, cluster 3 shows the smallest contact area in respect to the total area of both perikarya (Table 6.2).

Cluster 4 represents a 3-neuron-cluster reconstructed from the apical region of specimen 1 (Figure 6.2). The green-colored cell 1 is the biggest cell (diameter = $19.1 \mu\text{m}$) within this triple-arrangement followed by the central-positioned yellow cell 2 (diameter = $16.2 \mu\text{m}$). Both neurons are belonging to the second largest population 3 of SGNs within the human cochlea. The diameter of cell 3 (population 1, red colored) was calculated to be $14.9 \mu\text{m}$. It seems that cell 1 somehow entangles centered cell 2 resulting in a direct contact surface of $135.6 \mu\text{m}^2$ between them (Table 6.2). This value corresponds to 11.8% of the total soma-surface of cell 1 whereas 16.5% of the reconstructed surface of cell 2 is in distinctive contact with cell 1. In this 3-neuron-configuration there is a second contact area among cell 2 and cell 3 which was calculated to be $76.3 \mu\text{m}^2$. This second contact surface claims additional 9.3% of the total area of cell 2 and represents 11% of the total surface of cell 3. Note that a quarter of the total surface of the central-positioned cell 2 is in direct contact to its neighboring somata.

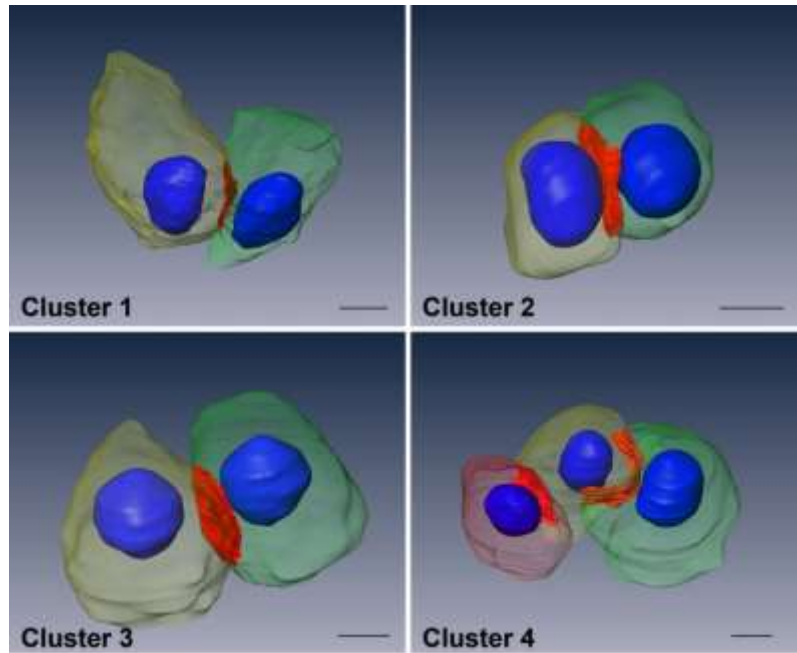


Figure 6.2: Arrangement of reconstructed clusters featuring direct cell-to-cell contacts. Cluster 1 to 3 represents detected 2-neuron-clusters; Cluster 4 represents identified 3-neuron-clusters. Cell 1 (of each cluster) is illustrated in green, yellow color feature cell 2 and the red colored somata of cluster 4 represents cell 3. The reconstructed cell bodies are visualized in a transparent manner. Cell nuclei are blue colored and direct cell-to-cell contacts between perikarya are visualized in red. Scale bars indicate 5 μm .

6.4.3 Satellite Glial Cells

In the following, our findings concerning different types of glial cells within distinct anatomical regions of the human cochlea are presented.

Spiral Ganglion

Using antibodies against S-100 and MBP amongst others enabled to identify three different subgroups of glial cells within the human cochlea. Figure 6.3A displays two different glial cells. The white arrow heads highlight SGCs surrounding sensory neurons where the cytoplasm is positive for S-100 protein which compose the distinct honeycomb network which can be seen in Figure 6.3B (S-100 channel). A second subgroup within the human spiral ganglion is depicted by the yellow arrow head. The nucleus of a soma-myelinating SGC is situated next to a Type I SGN (TuJ1 positive) enveloping the cell body with myelin (note white arrow). There is also a branch of the upper SGC visible which seems to embrace the myelinated type I neuron.

A third identified subgroup of SGCs in the human spiral ganglion is pointed out by the white arrow head in Figure 6.3B. The cytoplasm surrounding this SGC nucleus is positive for S-100 protein and also slightly positive for MBP. As a consequence, this type I neuron is fully isolated by myelin which is additionally positive for S-100 protein. However, the majority of human type I SGNs possesses unmyelinated perikarya which are surrounded by SGCs forming the distinct honeycomb pattern (Figure 6.3B, S-100) embedding cochlear neurons. A further Schwann cell (SC) which is just positive for MBP (as described above) is highlighted by the yellow arrow in Figure 6.3B. This cell is located in close proximity to a fiber myelinating its axon. Note that the expression of S-100 is completely absent.

Lamina Spiralis

The axons of the nerve fibers in the human lamina spiralis (Figure 6.3C) were found to be encircled by MBP positive myelin layers (white arrow) provided by myelinating SCs. Such a myelinating SC is highlighted by the yellow arrow head. The cytoplasm surrounding the nucleus is only positive for MBP. Note the absence of S-100 protein at the vast majority of myelinated fibers.

Cochlear Nerve

Similarly to the spiral ganglion we found evidence of parallel existence of three subtypes of glial cells within the cochlear nerve. The white arrows head in Figure 6.3D highlights an S-100 protein positive stained unmyelinating SC. A myelinating SC which is positive for MBP is highlighted by the yellow arrow head. Note the absence of S-100 protein expression in the cytoplasm of this cell. The third identified subtype is depicted by the white arrow. The cytoplasm of this glial cell is positive for S-100 and MBP. However, both antibodies were found all over the NC.

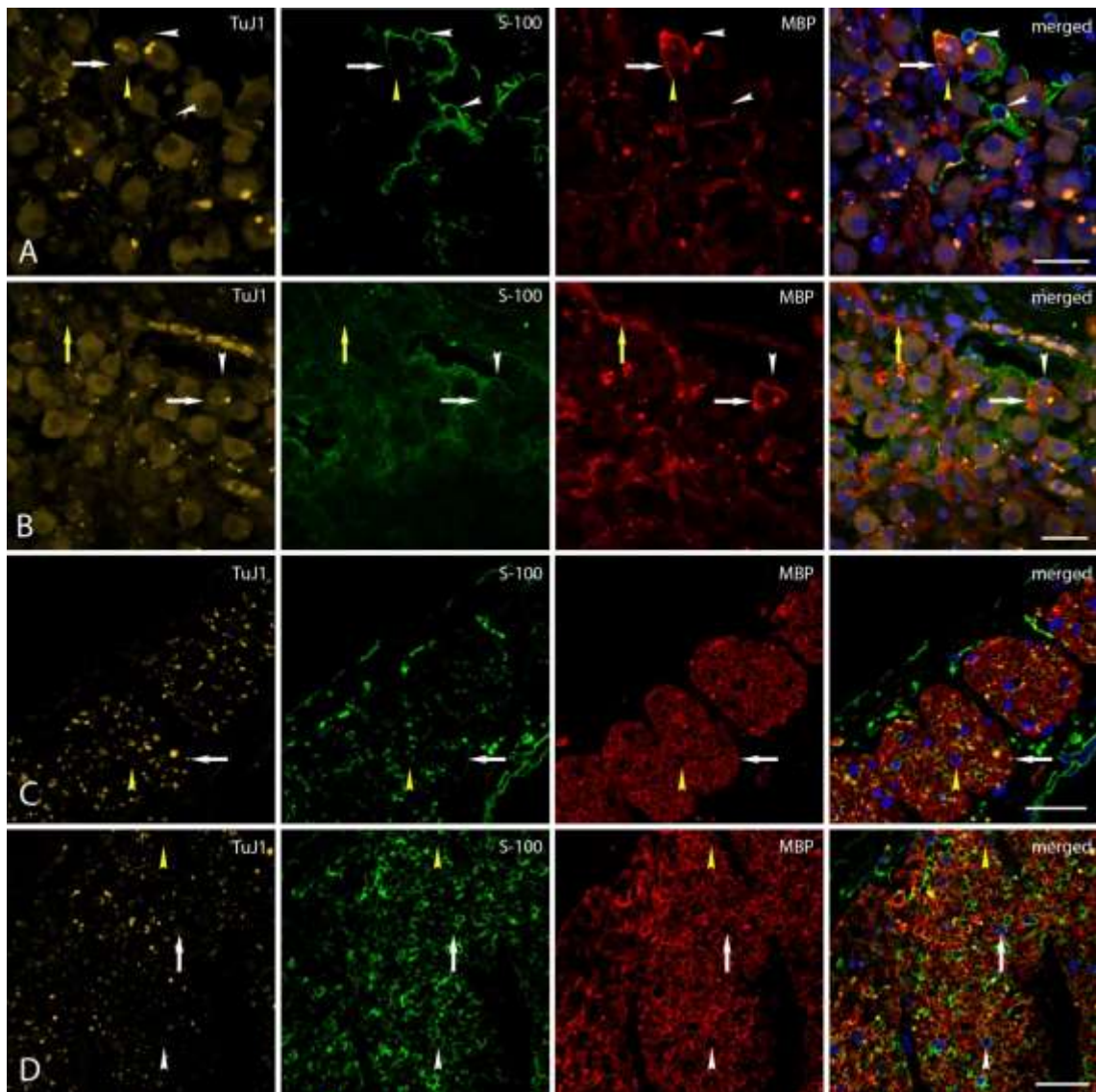


Figure 6.3: Immunofluorescence of DAPI, TuJ1, S-100 and MBP in human spiral ganglion (A,B), lamina spiralis (C) and the cochlea nerve (D). The majority of human SGNs are surrounded by satellite glial cells (B, S-100 channel, basal turn). White arrow heads (A, middle turn) highlight SGCs strongly positive for S-100 protein. In human inner ears myelinating SGCs surrounding type I neurons positive

for MBP were identified as shown in A by the yellow arrow head. B presents a soma-myelinating SGC enwrapping a human Type I SGN positive for S-100 and MBP. The peripheral processes in the human osseous spiral lamina are myelinated and positive for MBP lacking the expression of S-100 protein (C, white arrow). The yellow arrow head points to a Schwann cell which cytoplasm is positive for MBP. Scale bars represent 30 μm .

6.4.4 Computer Simulation

All four detected clusters have been systematically tested in a first trial with two different lengths of the presomatic compartment in order to examine critical values of the ephaptic conductance g_E that represents a measure of possible ephaptic interaction. This was done by stepwise increasing of neuron connecting conductance, starting at $g_E = 0 \text{ mS/cm}^2$.

6.4.4.1 Bicellular Clusters

Three of the four reconstructed clusters (Figure 6.2) contain two neurons with direct cell-to-cell contact of a certain area (Table 6.2). Both neurons of each cluster were investigated with varying length of the presomatic compartment (50 μm and 100 μm). The ephaptic excitation of the bicellular clusters was tested with current injection ($I_{\text{stim}} = 0.1 \text{ nA}$) into the peripheral terminal of one cell for increasing values of g_E .

The resulting critical values of g_E for cluster neurons featuring a short presomatic segment of 50 μm are presented in Table 6.3 (left column). The stimulated cell only triggers an AP in the second non-stimulated cell when g_E is within the displayed range. For higher values of the ephaptic conductance, the AP breaks down for both cells due to current loss on the soma region. However, one irregularity was observed when analyzing cluster 1. A current injection into the peripheral terminal of cell 2 does not generate a successful AP that arrives at the central model end. The AP is initiated and travels over the peripheral process but breaks down at the somatic region. The reason is that for large cells the most sensitive parameter is the length of the presomatic compartment which has to be larger than a certain minimum. Is this not the case, the arriving AP at the soma is not able to fully load the capacitance of its soma which causes the collapse of the AP. Since cell 2 of cluster 1 is with a diameter of 21.4 μm quite large, a presomatic region with 50 μm is too short for successful electrical signal transmission over the whole model neuron. A second surprising observation was the high theoretical values of g_E determined for cluster 2. This is may be a result of the quite high contact areas of both involved cells. An example of such an inhibiting cluster effect is presented by Figure 6.4 which visualizes the temporal pattern of interconnected neurons of cluster 2.

When the length of the unmyelinated presomatic compartment was increased to 100 μm , the ephaptic excitation of the second cell was successful in all trials resulting in robust AP conduction when g_E is chosen beyond the displayed values (Table 6.3, right column). Increasing the ephaptic conductance leads generally to synchronization of transmitted APs, i.e. the triggered AP at the soma of the unstimulated cell adapts to the temporal pattern of the intracellular stimulated neuron. This behavior is illustrated in Figure 6.5 where the temporal patterns of both neurons composing cluster 3 are visualized at different increasing values of g_E .

		$l_{pre} = 50 \mu\text{m}$			$l_{pre} = 100 \mu\text{m}$		
		$I_{stim} [\text{nA}]$ cell 1	$I_{stim} [\text{nA}]$ cell 2	g_E [mS/cm ²]	$I_{stim} [\text{nA}]$ cell 1	$I_{stim} [\text{nA}]$ cell 2	g_E [mS/cm ²]
Cluster 1	nm=3	0,1	0	$5 \leq g_e \leq 13$	0,1	0	$g_e \geq 5$
		0	0,1	failure	0	0,1	$g_e \geq 4$
Cluster 2	nm=3	0,1	0	$3.5 \leq g_e \leq 96$	0,1	0	$g_e \geq 4$
		0	0,1	$4 \leq g_e \leq 97$	0	0,1	$g_e \geq 4$
Cluster 3	nm=3	0,1	0	$5.5 \leq g_e \leq 12$	0,1	0	$g_e \geq 5.5$
		0	0,1	$5.5 \leq g_e \leq 11.5$	0	0,1	$g_e \geq 5.5$

Table 6.3: Critical values of the ephaptic conductance g_E for the reconstructed bicellular clusters. The ephaptic excitation of the neurons was studied in cluster 1 to 3 for varying presomatic lengths and alternating artificial cell excitation.

Ephaptic Coupling

The effect of ephaptic coupling and spike inhibiting is shown in Figure 6.4. The activating current was injected into the first peripheral compartment of cell 2 at $t = 0$ ms that causes the generation of an AP after 0.246ms. The signal reaches the central model end 0.804 ms after spike onset. When g_E is assumed to be 0 which represents no connection between the cells (first row), cell 2 stays in resting state and the transmembrane potentials are steady over time. When g_E is increased to the critical value of 4 mS/cm², the electrical signal of cell 2 triggers an AP at cell 1 at the somatic region where the incoming AP can fully load the capacitance of cell soma 1. This process requires 0.352 ms which corresponds to the time delay of the signals at their respective model end. The described effect is observable until $g_E = 97$ mS/cm² (Figure 6.4, third row) which was found to be the upper limit of possible g_E . The increasing ephaptic conductance causes the synchronization of both APs so that the resulting delay at the central end of the neurons shrinks to only 0.025 ms. Interestingly, when comparing the transmembrane potentials at the soma compartment of both neurons (Figure 6.4, third column) it can be seen that the APs are synchronized to the triggered AP of cell 1. Cell 2 delays the spike as long as cell 1 starts to propagate the spike in both directions. Even the peripheral process of cell 2 starts to slightly depolarize again. Compared to the initial situation (Figure 6.4, first row), the AP of cell 2 arrives 0.394 ms later at the central terminal when considering $g_E = 97$ mS/cm². Further increase of $g_E \geq 98$ leads to inhibition of the artificially generated AP in cell 2 at the somatic region. Consequently, the somatic region of cell 1 starts slightly to depolarize but both cells are unable to initiate or propagate respectively, a successful spike to the last central compartment.

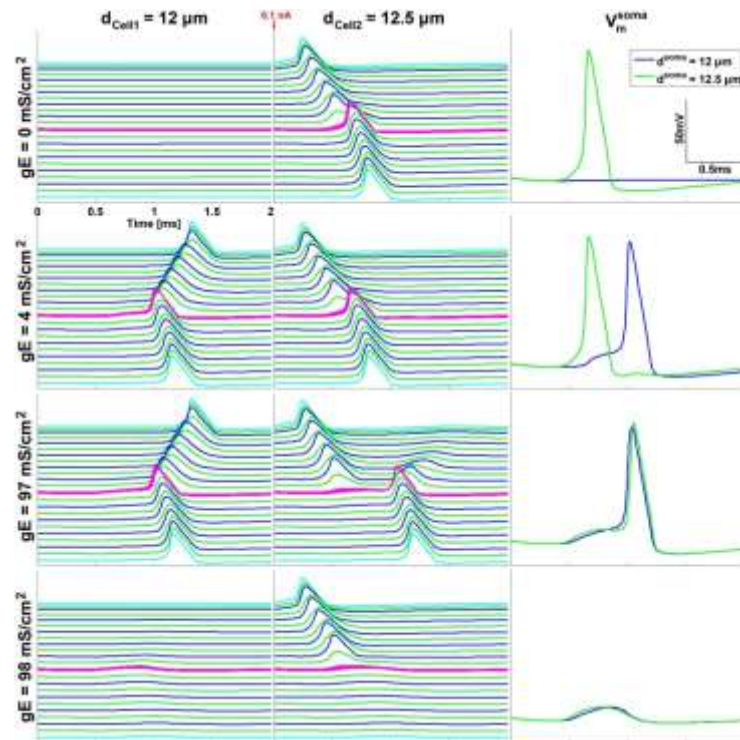


Figure 6.4: Neuron 2 of cluster 2 receives a current injection of 0.1nA to the peripheral terminal. Both interconnected neurons featured a short presomatic region ($length_pre = 50\mu m$) and three membrane layers surrounding the somatic region. Each line of the plots of the left (cell 1) and the middle (cell 2) panel represents the temporal change of the transmembrane potential along the model neurons. Blue lines depict nodes while green lines illustrate internodes. The unmyelinated peripheral- and central terminal are presented in cyan while the somatic region is visualized in pink color. Right panel shows the corresponding transmembrane potentials at the soma compartment of both neurons as a function of time. When g_E is within the range of $4 \leq g_E \leq 97$ mS/cm² both cells successfully conduct the generated APs to their central model end. In contrast, higher values of g_E show inhibiting effects on the AP transmission.

The effect of ephaptic coupling and robust AP conduction with long presomatic compartments ($pre_length = 100 \mu m$) is presented by cluster 3 in Figure 6.5. Both neurons were modeled with three membrane layers surrounding the somatic region ($nm=3$) and g_E was successively increased. Cell 1 was excited by a current injection of 0.1nA at the peripheral terminal. Spike onset occurs in the intracellular stimulated cell 1 after 0.245 ms. The generated AP reaches the central terminal 0.838 ms after current injection. When g_E is assumed to be 0 (first row), cell 2 remain in resting state and the transmembrane potentials are steady over time. This behavior is unchanged until the ephaptic conductance is increased to 5 mS/cm². At this value, the transmembrane potential at the soma of cell 2 (Figure 6.5, right panels) starts slightly to depolarize which is caused by the somatic current flow from the connected cell 2. When g_E is further increased to the critical value of 5.5 mS/cm² (see Table 6.3) the artificially induced AP of cell 1 is able to fully load the somatic capacitance of adjacent cell 2. This triggers an AP which is conducted in both directions (Figure 6.5, third row) along the model neuron. The activation process needs 0.398 ms which again represents the delay of both signals when reaching the respective central model end. Further increase of g_E causes more and more synchronized APs so that both generated signals reach the central terminal at quite the same time. A theoretical g_E of 30 mS/cm² reduces the time needed to activate cell 2 to 0.076 ms (Figure 6.5, last row) which is also directly connected to the earlier arrival times of both APs.

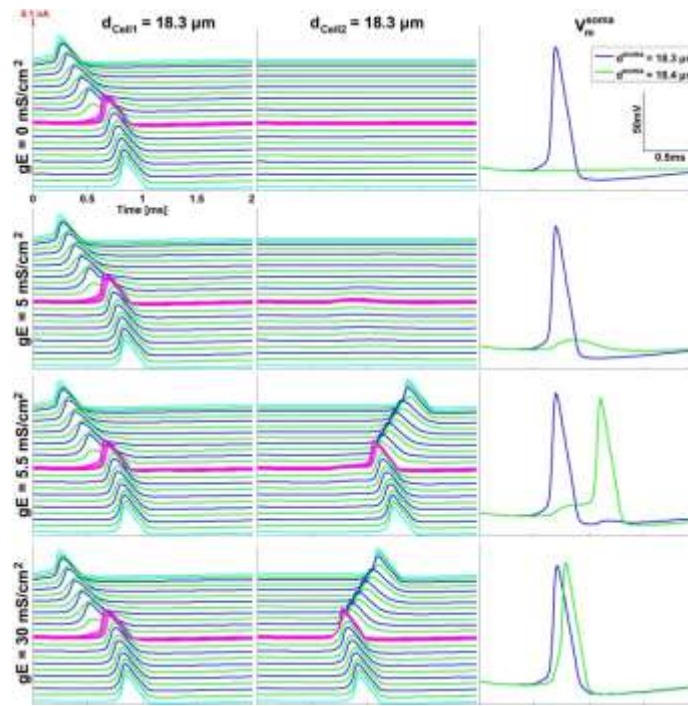


Figure 6.5: Neuron 1 of cluster 3 is stimulated by 0.1nA injected into the peripheral terminal. Both neurons featured a long presomatic region ($\text{length_pre} = 100\mu\text{m}$) and three membrane layers surrounding the somatic region. The transmembrane potentials along the neurons are illustrated in the same manner as in Figure 6.4. If the ephaptic conductance is high enough ($\geq 5.5\text{mS}/\text{cm}^2$) a spike is triggered at the soma of neuron 2. Both spikes are further synchronized for increasing values of g_E .

Synchronization

The effect of signal synchronization was further analyzed with cluster 2. For this trial, both neurons were modeled with $\text{nm} = 3$ and a long presomatic length of $100\mu\text{m}$. The neurons received a current injection of 100nA in their peripheral terminal but at different times. In all trials, cell 1 was intracellular stimulated at $t = 0\text{ms}$, cell 2 received its stimulus after 0.5ms (first row), 1ms (middle row) or 2ms (third row) for varying values of g_E in the range of 0 and $20\text{mS}/\text{cm}^2$.

Figure 6.6 presents the resulting transmembrane potential of the soma of cell 1 (blue) and cell 2 (green) as a function of time. The first row (

Figure 6.6) illustrates the resulting potentials for a small delay of 0.5ms . For the first two cases, the ephaptic conductance is too low to cause a coupling effect. Therefore, the initiated APs arrive at their central model end with a delay of $500\mu\text{s}$ (cell 1 after 0.765ms ; cell 2 after 1.265ms after spike onset). When g_E is increased to $4\text{mS}/\text{cm}^2$, the ephaptic conductance is high enough that the arriving AP at the soma of cell 1 can load the capacitance of cell 2 which successfully triggers a spike. In this case, the artificially initiated AP in cell 1 reach the central terminal again after 0.765ms but the triggered signal of cell 2 reach the model end after 1.038ms which represents an earlier arrival of signal 2 of 45.4% compared to the $g_E \leq 2\text{mS}/\text{cm}^2$ case. This effect of signal synchronization is more distinct for higher values of the ephaptic conductance, e.g. to $20\text{mS}/\text{cm}^2$. In this case, both signals arrive at the central terminal with a delay of 0.078ms that represents a difference of 84.4% compared to the initial arrival time. Signal synchronization in the analyzed cluster starts at $g_E = 4\text{mS}/\text{cm}^2$ and is independent of the stimulation delay of cell 2.

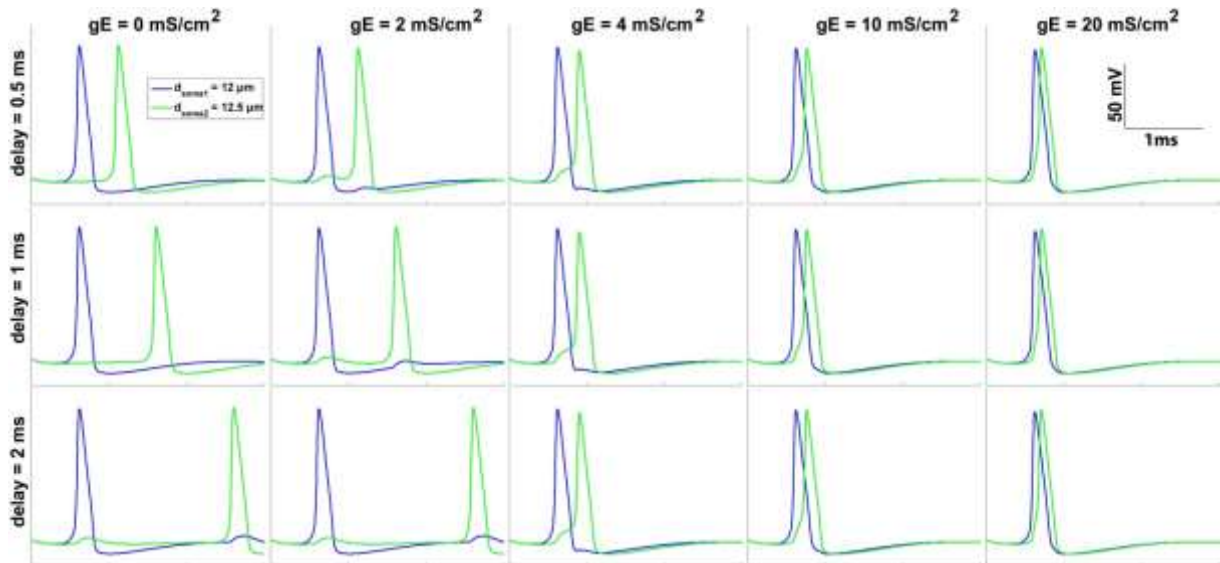


Figure 6.6: AP synchronization in cluster 2 due to ephaptic coupling. A current of 0.1 nA was injected in the peripheral terminal of both neurons but at different times. The transmembrane potentials at the soma of cell 1 (blue) and cell 2 (green) are presented as a function of time. Cell 1 was always stimulated at $t = 0$ ms whereas cell 2 received the current injection with a delay of 0.5 ms (first row), 1ms (middle row) or 2 ms (third row) for increasing values of g_E . When the ephaptic conductance is high enough ($g_E \geq 5$ mS/cm²), the spikes are always synchronized. Both neurons featured $nm_soma = 3$ and $length_pre = 100$ μ m.

6.4.4.2 Tricellular Cluster

Cluster 4 represents a three-neuron arrangement (Figure 6.2) and was systematically tested to detect ephaptic coupling effects with. Both neurons showed the same parameters as the studied neurons of the bicellular clusters. Since this cluster is composed by three neurons, two different contact areas g_{E1} and g_{E2} have to be considered. As before, the ephaptic conductances were increased step-by-step starting with $g_{E1} = 0$ and $g_{E2} = 0$ until the first ephaptic coupling effect occurred, i.e. the adjacent cell was activated successfully. This value was fixed and the second conductance was increased or decreased until the remaining third cell was activated at the soma to determine the lower limit. In a last step, both conductances were individually increased to detect their upper limits.

Ephaptic coupling

The ephaptic excitation of the tricellular clusters was tested as previously with current injection ($I_{stim} = 0.1$ nA) into the peripheral terminal of one cell while the other two receive ephaptic excitation or two cells receive stimulus current and one remains unstimulated. Table 6.4 presents the determined critical values of g_{E1} and g_{E2} for neurons with a short pre somatic compartment (50 μ m). Ephaptic excitation only occurs when both ephaptic conductances are in the presented range, i.e. if cell 1 is stimulated and $g_{E1} \geq 3.5$ & $g_{E2} \geq 4.5$ (Table 6.4, first trial). With this setting, APs were generated in all three neurons and transmitted to the central model end. Increasing the values until the displayed upper limit leads to synchronization of all three signals as illustrated for the bicellular case in Figure 6.5. When one of the ephaptic conductances is exceeded, inhibiting effects as visualized in Figure 6.4 are provoked and the artificially generated AP breaks down at the soma. Consequently, no electrical signal is further transmitted by the cells to the central model end.

		$l_{pre} = 50 \mu\text{m}$				
		I_{stim} [nA] cell 1	I_{stim} [nA] cell 2	I_{stim} [nA] cell 3	g_{E1} [mS/cm ²]	g_{E2} [mS/cm ²]
Cluster 4	nm = 3	0,1	0	0	$3.5 \leq g_{e1} \leq 26$	$4,5 \leq g_{e2} \leq 11$
		0	0,1	0	$g_{e1} \geq 3.5$	$g_{e2} \geq 5$
		0	0	0,1	$3.5 \leq g_{e1} \leq 7$	$g_{e2} \geq 6$
		0,1	0	0,1	$g_{e1} \geq 3$	$g_{e2} \geq 5.5$
		$l_{pre} = 100 \mu\text{m}$				
		0,1	0	0	$g_{e1} \geq 3.5$	$5 \leq g_{e2} \leq 21$
		0	0,1	0	$g_{e1} \geq 4$	$g_{e2} \geq 6$
		0	0	0,1	$3.5 \leq g_{e1} \leq 6$	$g_{e2} \geq 6.5$
		0,1	0	0,1	$g_{e1} \geq 2$	$g_{e2} \geq 2$

Table 6.4: Critical values of g_{E1} and g_{E2} for tricellular neuron arrangements. The ephaptic excitation was studied for two different lengths of the presomatic compartment and varying cell excitation patterns. The ephaptic behavior of the black colored trials are the same as visualized for bicellular cluster. Red colored trials are represented by Figure 6.6.

For the two investigated cases, (i) the middle-positioned cell 2 or (ii) the outer two cells cell 1 and 3 receive a current injection, APs at the adjacent cells were found to be always initiated by ephaptic excitation when g_{E1} and g_{E2} are higher than the displayed lower limits. As described before, higher values of the ephaptic conductance between two cells increase AP synchrony for these cases. This behavior of the cluster neurons hold for short- as well as long presomatic compartments.

When analyzing the red colored settings from Table 6.4, we observed a new ephaptic excitation pattern that is visualized in Figure 6.7. For the first trial, both ephaptic conductances were set to 0 (first row) and a current of 0.1 nA was injected to the peripheral process of cell 3 with a presomatic length of 50 μm . Since there is no ephaptic connection between the cells, only cell 1 transmits an AP which reaches the central model end 0.783 ms after spike onset. Afterwards, both conductances were increased to their critical values, i.e. $g_{E1} = 3.5 \text{ mS/cm}^2$ and $g_{E2} = 6 \text{ mS/cm}^2$. As demonstrated in the second row of Figure 6.7, the somatic current flow from the soma of cell 3 to cell 2 and between cell 2 and cell 1 is high enough to ephaptically generate APs in both adjacent neurons. The intracellular generated AP of cell 3 arrives at the model end 0.786 ms after spike generation. With a delay of 0.342 ms, the ephaptic excited signal transmitted by cell 2 the central end. It took another 0.33 ms until the second ephaptic excited electrical signal reaches the central terminal of cell 1. In a next trial, g_{E2} was unchanged but the ephaptic conductance of the contact area between cell 1 and 2 was increased slightly beyond its upper limit to $g_{E1} = 8 \text{ mS/cm}^2$ (Figure 6.7, third row). This increase of g_{E1} and the accompanied higher current flow between cell 2 and 1 acts suppressively on ephaptic interaction and no AP is generated at the somatic region of cell 2 or 1. Only the transmembrane voltage profile of cell 2 shows that its somatic region is slightly depolarizing but too weak for generating an AP. The last row in Figure 6.7 visualizes the tricellular activity when both ephaptic conductances are further increased ($g_{E1} = g_{E2} = 20 \text{ mS/cm}^2$). The high ephaptic conductances enable that cell 2 and 1 successfully initiate spikes at their somatic regions. As demonstrated in previous cases, higher values of g_E results in synchronization of the generated APs. In this case, the ephaptic triggered AP of cell 2 and cell 1 arrive 0.105 ms and 0.174 ms respectively, after the artificial generated signal of cell 3.

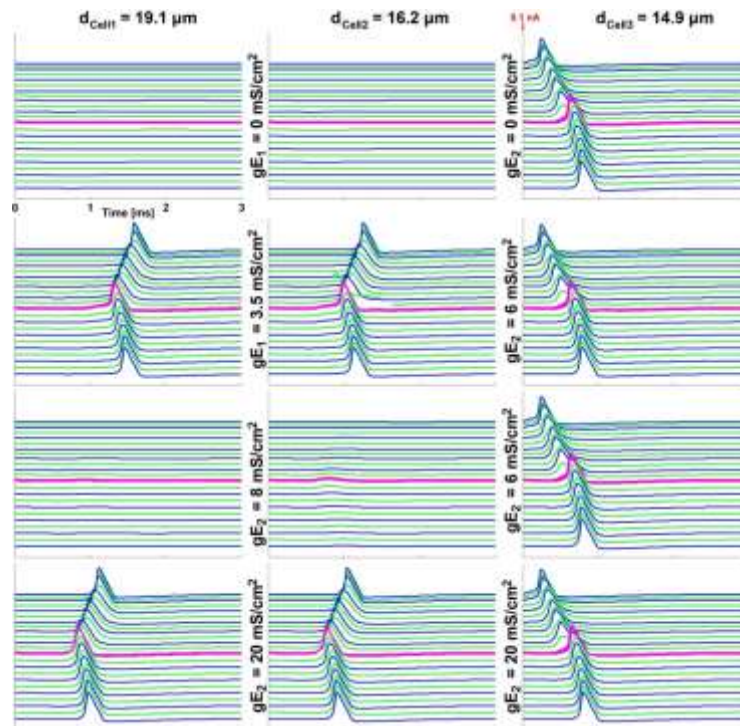


Figure 6.7: Cell 3 of the reconstructed tricellular cluster is stimulated by 0.1nA current injection to the peripheral terminal. The involved neurons feature a short presomatic compartment ($50\mu\text{m}$) and their somatic region is surrounded by three membrane layers. The transmembrane potential profiles along the cells are illustrated in the same manner as in Figure 6.4. Ephaptic conductances of $g_{E1} = 3.5 \text{ mS/cm}^2$ and $g_{E2} = 6 \text{ mS/cm}^2$ ensure aphaptic interaction and consequently, successful AP generation at the soma of cell 2 and 1 (second row). Further increase of g_{E2} beyond the critical value displayed in Table 6.4 acts suppressively on ephaptic interaction and no AP is generated in both cells. As presented in previous cases, further increase of g_E secure ephaptic AP initiation and synchronization of transmitted signals.

6.4.4.3 Intracellular Spike Trains

In order to analyze the ephaptic behavior of the clusters when pulse trains at different frequencies are injected, neurons belonging to our standard cluster 3 were modeled with the following parameters, i.e. $\text{length_pre} = 100 \mu\text{m}$, $\text{nm} = 3$ for a human cochlear neuron. Figure 6.8 shows the temporal answer of the transmembrane potentials along the modeled neurons with stimuli injected into the peripheral terminal of cell 1 every 5 ms (Figure 6.8A) and every 3ms (Figure 6.8B). When $g_E = 0 \text{ mS/cm}^2$ in both cases, APs are periodically initiated in cell 1. The first AP in cell 1 is initiated 0.245ms after spike onset ($t=0$) and reach the model end at $t= 0.832 \text{ ms}$. Comparable times were recorded for the first AP of cell 2. Increasing the ephaptic conductance slightly below the crucial value ($g_E = 4 \text{ mS/cm}^2$) causes again weak depolarization of the transmembrane potentials along cell 2 (Figure 6.8, second row). It can be observed at the crucial value of $g_E = 5 \text{ mS/cm}^2$ for both cases (third row) that the expected first AP of cell 2 is not generated. The neuron slightly depolarizes in this time slot but no spike arises. However, the second and subsequent expected AP were initialized at the somatic region and successfully propagated to the model end with delays of about 0.354 ms in both cases. When the ephaptic conductance is further increased (Figure 6.8, fourth row), also the

first AP of cell 2 is generated and the induced APs are again more and more synchronized reaching the model end slightly delayed with 0.094 ms time difference.

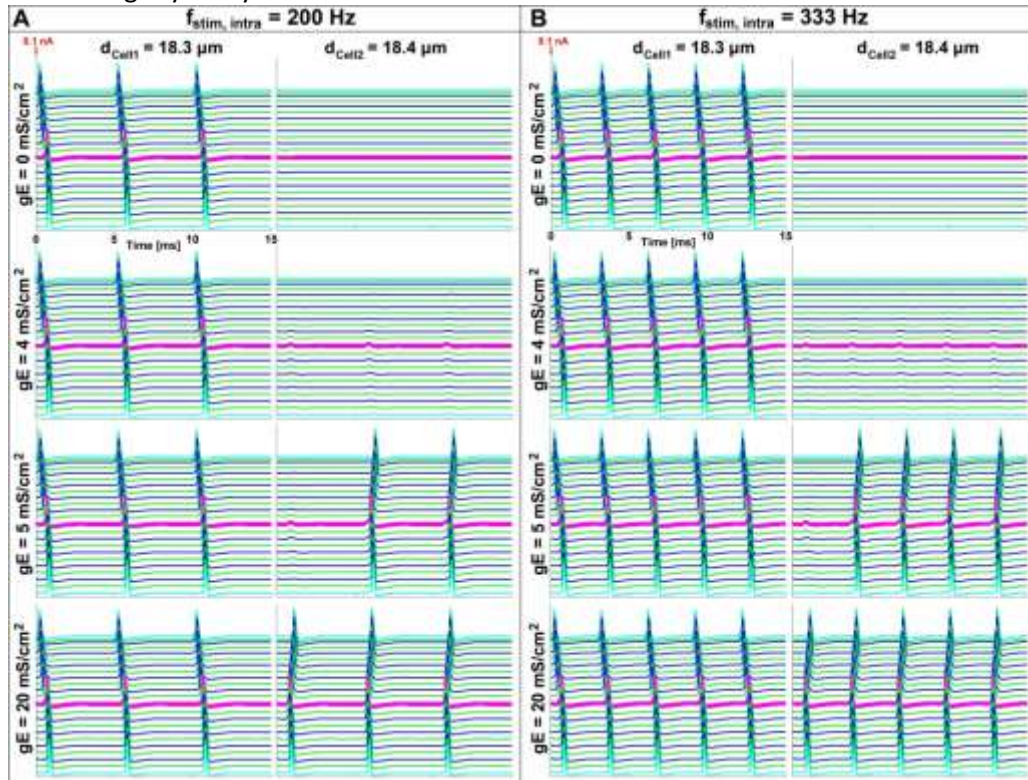


Figure 6.8: Ephaptic coupling of cluster 3 stimulated with spike trains of 200 Hz (A) and 333 Hz (B). The transmembrane potentials along the neurons are illustrated in the same manner as described in Figure 6.4. For both frequencies, an assumed $g_E \geq 5$ leads to ephaptic coupling between the neurons and APs are generated in the non-stimulated cell. As illustrated previously, a higher g_E value leads to robust AP propagation and synchronization of both signals.

In a second trial we analyzed the neuronal behavior when both cells are stimulated simultaneously, but at different frequencies. Again, cluster 3 was chosen: this time, cell 1 receives current injections of 0.1nA in the peripheral terminal every 3 ms; cell 2 every 5 ms. When the cells are stimulated without any contact between them ($g_E = 0$ mS/cm²) both neurons transmit successfully the generated APs at their distinct stimulation rate to the model end (Figure 6.9, first row). The expected firing rates remain constant for $g_E \leq 4$. However, the transmembrane voltage profile of cell 2 slightly starts to depolarize when a potential spike crosses the somatic region of cell 1. However, both cells are firing constantly at their input frequency. The spiking pattern of cell 2 changes completely when g_E is increased to the critical value of 5 mS/cm². The very first spikes of both cells are initiated as usual (Figure 6.9, third row). But this time, the ephaptic conductance is high enough so that the second generated spike of cell 1 loads the somatic capacity of cell 2 and the resulting AP travels in both directions reaching the central terminal 0.383 ms after the triggering signal of cell 1. Moreover, all the following spikes of cell 1 initiate synchronized spikes in cell 2 which is consequently adapting the firing rate of cell 1. The intracellular stimuli of cell 2 are all non-effective. The reason for this can be found in the membrane potentials of cell2. At the times when the current is injected to the peripheral terminal cell 2 is not fully repolarized and therefore unable to fire again. Besides this total firing adaption, further increases of g_E result in more synchronized spikes (Figure 6.9, fourth row). For $g_E = 20$ mS/cm² the delay between a spike of cell 1 and its triggered AP on cell 2 is reduced to 0.096ms.

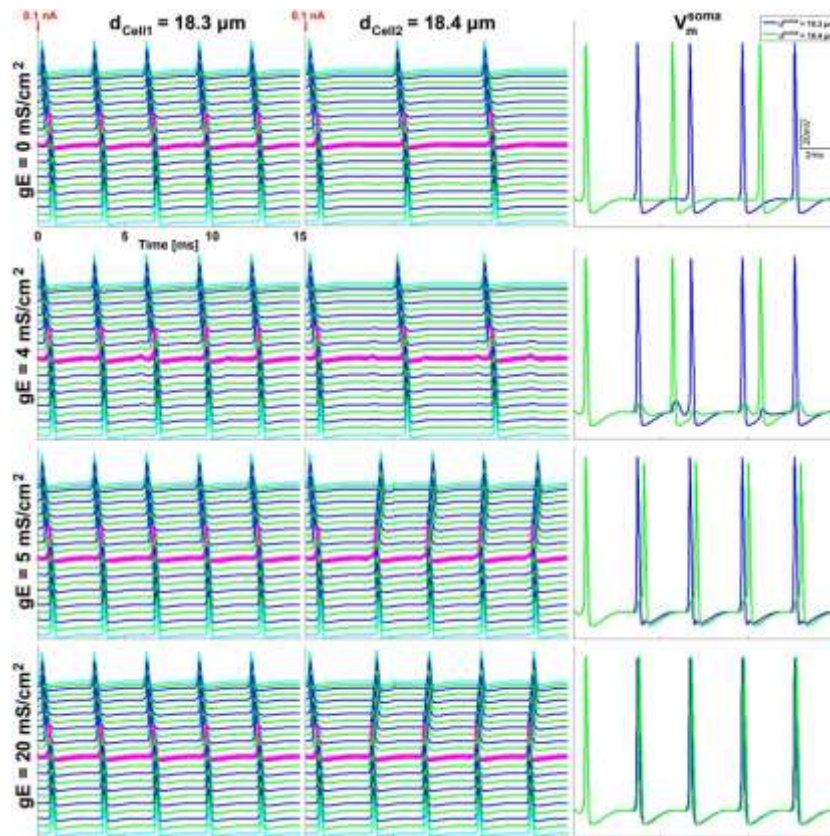


Figure 6.9: Frequency adaption and synchronization due to ephaptic coupling. Both neurons composing cluster 3 received simultaneously current injection of 0.01 nA to the peripheral terminal at certain frequencies. Cell 1 received input every 3ms whereas cell 2 was stimulated every 5ms with different values of the soma connecting ephaptic conductance g_E . $g_E \geq 5$ leads to frequency adaption of cell 2 and synchronization effects occur.

6.4.4.4 Extracellular stimulation

In order to test the ephaptic behavior of clusters to extracellular stimulation, we have chosen bicellular cluster 3 featuring our standard configuration (length_pre=100, nm=3). Subsequently, the cluster was stimulated by (i) single stimulus and (ii) pulse trains at different frequencies and the transmembrane excitation profiles were again simulated as functions of time.

Single Pulses

In a first run, the ephaptic conductance was set to $g_E=0\text{mS/cm}^2$ and the required threshold currents necessary to successfully generate an AP were determined: stimulation with a 0.1 ms long monophasic cathodic pulse needs -449 μA for AP initiation at the peripheral terminal of both neurons 0.621 ms after spike onset and reach the central model end after 0.666ms travelling time at $t=1.287\text{ms}$. The evaluated threshold for a BIC pulse requires slightly more current at -491 μA . APs are again initiated simultaneously in both neurons at the first dendritic compartment, 0.518 ms after firing. This time, the spike needs 0.6ms to reach the model end at $t=1.118$ ms which is 13% earlier compared to a CAT stimulus. Monophasic anodic stimulation generates a spike 0.617 ms after firing and needs 0.518 ms to travel to the peripheral terminal which is reached at $t = 1.135$. Threshold current for successful stimulation with this pulse is 491 μA . The highest current requires a biphasic

stimulus with a leading anodic pulse with 680 μA . Spikes are generated again in the first compartments of both neurons though after 0.709 ms which represents the longest time between firing and AP generation. Consequently, the AP arrives latest of all other applied pulses at $t = 1.311$ ms and needed 0.631 ms for travelling over the 27 compartments. In a second run, the ephaptic conductance of the cluster contact area between the two neurons was increased to $g_E = 5 \text{ mS/cm}^2$ and $g_E = 20 \text{ mS/cm}^2$ to evaluate the influence on threshold current level and possible ephaptic coupling effects. However, no deviations concerning the evaluated threshold currents, PT, ET or the IS of spike generation in any of the investigated pulse forms were detected.

Pulse Trains at Threshold Current

After evaluating the threshold current for single pulses, the responses to 15ms pulse trains were investigated with frequencies of 200Hz, 333Hz and 2000Hz. A CAT pulse with a duration of 0.1ms at threshold current ($= -449 \mu\text{A}$) was used, the ephaptic current conductivity was again set to $g_E = 0 \text{ mS/cm}^2$. Figure 6.10 presents the results of this trial. The first row presents the neuronal answer of cell 1 and 2 stimulated by a single pulse at threshold current where both neurons transmit the signal successfully and simultaneously to the central terminals. When the cluster is stimulated by the electrode every 5ms (second row), only the first spike is initiated in the first compartment at both cells and is again successfully propagated to the central ends. However, the delivered threshold currents at $t=5\text{ms}$ and $t=10\text{ms}$ do not initiate APs along both neurons. The transmembrane potentials along the peripheral processes are slightly depolarizing but they are too weak to generate APs. The same behavior was observed when the frequency was further increased to 2000Hz. Again, the first expected AP is successfully generated and propagated to the model ends. As previously, no further stimulus can activate the neuron; only weak but periodic depolarizing effects are illustrated as a reaction to the applied pulse trains (fifth row). When the cluster was stimulated every 3ms (Figure 6.10, third row) the threshold current was sufficient to generate APs in a periodic manner (see peripheral terminals). A closer look to the transmembrane profiles of both neurons on the central terminal region suggests an irregular arrival pattern of the APs at the last compartments. The first and second spike arrives periodically, between the second and third signal seems to be more time and again, the third and fourth AP arrives as expected. The reason for this behavior was found in the initiation sites of the generated APs along the different APs. Figure 6.10 illustrates in the fourth row in the transmembrane voltage profiles of spike 2, 3 and 4 when stimulated every 3 ms but with changed time units of the x-axis. The third spike is initiated at the first compartment of both neurons about 0.534 ms after the electrode fired as it is the case when the bicellular cluster is stimulated by a single pulse (first row). Spike 3 needs 0.641 ms to travel from the first to the last compartment. The second spike is initiated at compartment 9 in cell 1 and 2 belonging to the peripheral process and is much closer to the cell soma. AP initiation occurs with 0.398 ms about 37.9% earlier in this case, compared to the previous spike. Due to the much shorter distance the AP has to travel, it arrives already after 0.349ms at the central end. Displayed spike 4 is again generated in compartment 9 and arrive the central end of both cells after about 0.337 ms which is 47% earlier compared to the required travel time of the third spike. A possible reason for spike generation at compartment 9 can be the position of the electrode close to that IS. However, this does not explain the described inequality concerning the jumping IS from one stimulus to the next. Afterwards, the same trials were repeated but with an increased ephaptic conductance of $g_E = 5\text{mS/cm}^2$ and $g_E = 20\text{mS/cm}^2$. However, no difference in the neuronal answer was found when repeating with the same stimulation settings as described above.

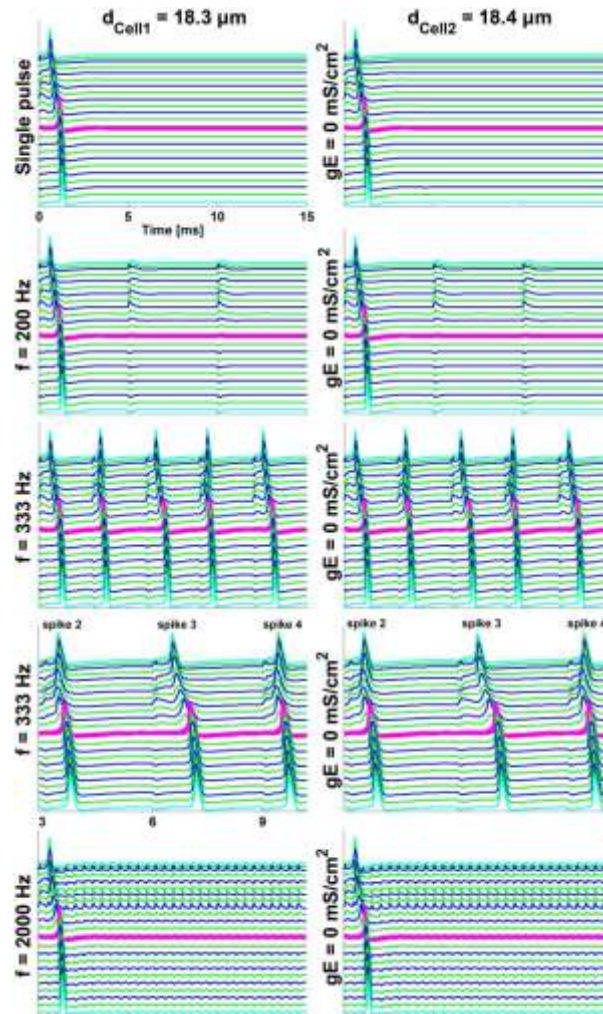


Figure 6.10: Neuronal answer of cluster 3 stimulated with pulse trains of various frequencies. The first row presents the resulting changes of the transmembrane voltage along the neurons when stimulated with a single monophasic cathodic pulse at threshold current. When the firing frequency of the electrode is increased to 200 Hz (second row) or 2000 Hz (last row), only the first AP is successfully generated while the following spikes produce only weak depolarization of both neurons, especially in the peripheral processes. On the other hand, if the electrode is firing every 3 ms (third row), every pulse initiates an AP but at different sites along the neurons (fourth row).

Pulse Trains at 1.5 * Threshold Current

Since stimulation with threshold current is not efficient for pulse trains, bicellular cluster 3 was stimulated with 50% increased currents ($= -673.5 \mu\text{A}$). As previously, the ephaptic conductance between the neurons was set to $g_E = 0\text{mS}/\text{cm}^2$ and pulse trains of 200 Hz, 333 Hz and 2000 Hz were applied for 15ms. The first row in Figure 6.11 illustrates the neuronal answer to a single CAT pulse with raised stimulation current for cell 1, cell 2 and a detailed view of the generated spike with a changed x-axis time range. As this third plot in the first row of Figure 6.11 suggests, the AP is generated at $IS = 9$ of the peripheral process and travels in both directions. Due to the higher stimulation current, the spike is initiated 80.4% earlier compared to neuron activation at threshold level which corresponds to 0.122 ms after stimulus pulse onset. Since the AP was induced along the peripheral process, the signal needs only 0.443 ms for travelling to the central end (arrives at $t = 0.565$ ms) which is 56.1% earlier compared to the evaluated threshold case.

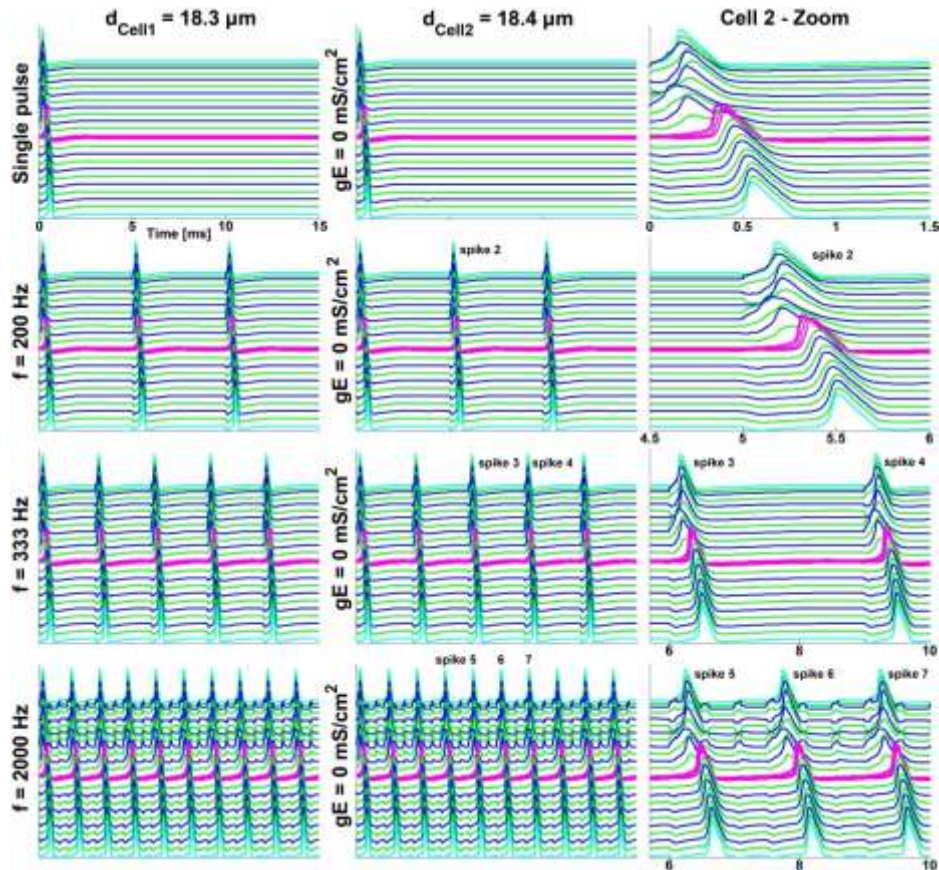


Figure 6.11: Cluster 3 stimulated with pulse trains of various frequencies and increased threshold (+50%). Monophasic cathodic pulses were offered at different frequencies. The ephaptic conductance was decreased to $g_E=0\text{mS/cm}^2$. The first and second column present the resulting transmembrane profiles of cell 1 and 2 respectively, while the third column visualizes selected APs induced at cell 2 at appropriate time ranges.

The second row in Figure 6.11 presents the neuronal answer of cluster number 3 to 200 Hz stimulation. Contrary to threshold stimulation, a current increase of 50% is sufficient to periodically generate APs which are successfully transmitted by both neurons to the central end. The third plot in this row enables a closer look of the second generated spike which shows a similar profile compared with the single pulse case. This time, the AP is generated 0.136 ms after the electrode applied the second pulse at IS=9. The model end is reached by the electrical signal after 0.366 ms at $t = 5.502\text{ms}$. As it was the case with CAT threshold stimulation, every applied electrical pulse at $f_{\text{stim}} = 333\text{Hz}$ successfully generate APs in both cells of the bicellular cluster. In contrast to threshold stimulation (Figure 6.10, third and fourth row), the simulated APs arrive at the central model end at the expected times without any delays. This is demonstrated by the third plot of this row which shows the temporal pattern of spike 3 and 4 of cell 2. Both APs are generated again in compartment 9 belonging to the peripheral process after 0.137 ms (spike 3) and 0.14 ms (spike 4) after the electrode fired the CAT pulse. Both signals need quite the same time to travel to the central model end (spike3: 0.362 ms; spike 4: 0.355 ms) compared to the presented threshold case. The fourth row in Figure 6.11 visualizes the excitation pattern of both neurons when extracellular stimuli are offered at $f_{\text{stim}} = 2000\text{Hz}$. Due to the position of the electrode, all simulated spikes are again induced at compartment 9. As an example, spike 6 is generated 0.255 ms after the electrode fired at $t = 7.5\text{ms}$. For the distance between IS and the central model end, the spike needed 0.403ms arriving at $t = 8.158\text{ms}$.

Stimulation of the bicellular cluster with such a high stimulation rate results in AP initiation every 1.501 ± 0.006 ms. The presented simulations were again conducted with increased ephaptic conductance of $g_E = 5$ mS/cm² and $g_E = 20$ mS/cm². However, neither the excitation profiles nor the temporal patterns of the cluster composing neurons 1 and 2 showed any significant changes compared to the $g_E = 0$ mS/cm² case as presented.

6.5 Discussion

The unshielded perikarya of auditory neurons are the most specific feature within the human cochlea and represent crucial obstacles for electrical signals on the way from the sensory receptors to the nucleus cochlearis. In other mammals, these neural units are fairly enwrapped by compact myelin sheath reducing the somatic capacitance which is inversely proportional to the number of isolating myelin layers. Consequently, this dielectric material ensures fast and safe signal transmission from the auditory sensory organ to the central nervous system. One of the most interesting peculiarities of unmyelinated perikarya is the previously reported 'clustering' of two or more cell bodies featuring direct physical contact based on ultrastructural findings (Kellerhals et al., 1967; Tylstedt et al., 1997; Tylstedt & Rask-Andersen, 2001). The delicate handling of electron microscopes and the time-consuming preparation of the specimens mostly results in a rather small amount of analyzed spiral ganglion cells. However, immunohistochemical analysis combined with confocal laser scanning microscopy allow for fast, systematic evaluation of this distinctive feature along the cochlear spiral as presented in a first part within this study.

The identified occurrence of cochlear neurons featuring direct cell-to-cell contact reveals a spatial organization along the cochlea spiral in each of the investigated inner ears ($n=3$, Table 1), showing a distinct maximum in the apical portion. These highest cluster densities in the low-frequency regions of all analyzed specimens are consistent with earlier findings by Tylstedt and Rask-Andersen (2001) who analyzed one human cochlea. In contrast to the varying percentage rates of 2-neuron-clusters identified within the apical sections (Table 1), the middle turn regions comprise quite the same amount of neurons with direct cell-to-cell contacts in all investigated three cochleae. The addressed section within the human hearing organ comprises the majority of phonational frequencies (Hollien et al., 1971; Loizou, 1999) and shelters moreover the highest density of spiral ganglion cells (Nadol, 1988a; Spendlin & Schrott, 1988) emphasizing it of prime importance for human communication. Interestingly, we identified a quite constant percentage of bicellular neuron clusters within this specific region of the inner ear in each specimen ($2.9 \pm 0.25\%$) compared to the apical turn ($5.8 \pm 2.4\%$). This quite constant value of clustering SGNs provide a small amount of synchronized APs or inhibit little number of transmitting signals from the middle turn but are may be essential to optimize signal acuity within this most sensitive region. More information about the e.g., frequency responsibility of the cluster sharing cells are crucial for understanding their role in human hearing sense.

The unmyelinated cell bodies of human cochlear neurons can demonstrate a consequence of higher evolutionary adaptedness to verbal communication compared to these myelinated neural units of other mammals. Perikaryal myelination of cochlear neurons secures safe and quick AP propagation by electrical isolation but reduces conversely the ability of chemical signaling between a neuron and its circumjacent SGC. Within the human inner ear, an unmyelinated soma together with its surrounding SGC constitutes a structural and functional neuron-glia unit facilitating bidirectional exchange of information. This improved communication and facilitated trophic support can be a hint for the observed much longer survival rates of human SGNs after deafness or cochlear insults compared to other mammals. A study on a human inner ear has shown that SGNs can be still alive in individuals suffering up to 50 years from deafness (Glueckert et al., 2005b). In contrast,

degeneration and loss of fully myelinated SGNs starts in other mammals shortly after cochlear insults was induced (Liberian & Kiang, 1978; Miller et al., 1997; McFadden et al., 2004; Gillespie & Shepherd, 2005) leading to a massive decrease in absolute quantity. Popa et al. (2001) detected nitric oxide synthase in human SGNs which catalyzes the production of nitric oxide (NO). NO stimulates SGCs to produce growth factors that have neuroprotective influence (Hanani, 2010) on cochlear neurons. These findings together with the results of Liu et al. (2009, 2012) suggest high dynamic interconnection between human SGNs with their embracing SGCs which should be further investigated in future studies.

The observed parallel occurrence of three groups of SGCs within the human cochlea was identified by immunohistochemical analysis. However, more investigations using various subtypes of S-100 protein are necessary to draw conclusions about possible functional diversities.

In order to analyze the ephaptic coupling effect at the adjacent soma of clustering cochlear neurons, a new model approach was developed where the introduced ephaptic conductance g_E shall represent a measure of possible electric and ephaptic interaction. The ephaptic impact of closely-spaced soma on each other was tested by altering g_E . Two basic consequences were determined during analysis of reconstructed bi- and tricellular clusters: (i) successful ephaptic stimulation causes spike synchronization of adjacent neurons; (ii) inhibiting effects on spike transmission occurs when the ephaptic conductance is beyond an upper limit due to large current loss on the sensitive human soma region and (iii) complete adaption of firing rate of both clustered neurons when initially stimulated at different frequencies.

The first two mentioned effects of ephaptic interaction have been described in previous studies. Binczak et al. (2001) studied the ephaptic coupling on parallel running axons and determined synchronized spike patterns. They additionally compared the spike conduction velocities of ephaptically induced electrical signals to normal (uncoupled) ones and reported disagreements in the onset of failure. Also Anastassiou et al. (2011) support the notion that ephaptic potentials serve to synchronize neuronal activity with little regard to whether excitatory or inhibitory. They further suggest that such synchronization may have a substantial effect on neural information processing and plasticity. The study of Holt and Koch (1999) on extracellular potentials near cell bodies reports that in extreme cases an AP can be induced in an inactive axon by a nearby one, whereas the investigations of Anastassiou et al. (2011) from pyramidal neurons suggest that ephaptically induced changes in V_m under physiological conditions cannot give rise to APs when V_m is around rest. However, based on the narrow cell contacts, the presented modeling approach suggests strong interactions between adjacent SGCs which is why the ephaptic excitation of a neuron at rest can be observed, i.e. an inactive SGC will initiate a spike at its soma when enough current is supplied by a passing AP of the other cell for single pulses as well as injected pulse trains (Figure 5 and 8). But raising the ephaptic conductance can on the other hand cause inhibiting effects where clusters show more an AP filtering function instead of a supporting or frequency focusing one. Since healthy human SGNs are not accessible for electrophysiological measurement, the tested values for g_E are supposed to be hypothetical and were raised quite high for causing signal inhibition.

The determined frequency adaption of neurons (Figure 9) alters not only the frequency pattern delivered to the auditory cortex, but also the temporal fine structure of the neural code due to AP initiation at the soma of the electrified neuron. This behavior may have impact on the generation of noise which could influence sound and speech perception especially in the elderly. Systematic morphological studies that investigate the occurrence of clustering in humans at different age would be quite helpful to clarify this question.

In this paper we present a new model approach that enables to study ephaptic coupling interaction between human SGNs. Based on immunohistochemical analysis and 3D reconstruction, bicellular and tricellular cluster arrangements were incorporated to the extended biophysical model. Ephaptic coupling can have synchronization or inhibiting effect on transmitted APs. Furthermore, clustering SGNs that fire at different frequencies show adaption of their firing rate which alters the frequency profile transmitted to the auditory cortex. However, ephaptic coupling do not impact the activation pattern of clustering neurons when extracellular stimulated with pulse trains but can have substantial influence on the temporal fine structure around threshold stimulation.

Finite Element Analysis and Three-Dimensional Reconstruction of Tonotopically Aligned Human Auditory Fiber Pathways: A Computational Environment for Modeling Electrical Stimulation by a Cochlear Implant based on micro-CT

7.1 Abstract

Faithful computer simulations that consider the influence of human cochlea geometry to microstimulation to analyze the resulting excitation profiles and the temporal fine structure of the transmitted neural code of cochlear neurons require (i) detailed anatomical numerical representation of the cochlea and (ii) three dimensional information about neuronal pathways of auditory neurons from the organ of Corti (OC) through the cochlea-volume.

Ultra-high resolution microCT imaging allowed digitalizing a human cochlea which was used to develop an anatomically correct Finite Element Model (FEM) to calculate the spreading of intracochlear electrical potentials induced by distinct electrodes. The isotropic data set ($\Delta x = \Delta y = \Delta z = 3\mu\text{m}$) was subsequently used to reconstruct 30 tonotopically organized nerve fiber pathways, distributed over eight octaves (11500 – 40 Hz). The resulting extracellular potentials induced by microstimulation along these neurons were implemented to an adapted compartment model of a human auditory neuron to study their responses to stimulation pulses from varying electrode positions.

Computer simulations show that extracellular stimuli configurations but especially the positions of the stimulating electrode remarkably influence the temporal spiking pattern of stimulated human auditory neurons. Particularly electrodes located in the narrowing middle- and apical turn cause the infringement of the tonotopical principle even at threshold currents. Moreover, biophysical model evaluation predicts variations in the temporal fine structure of the neural code when comparing normal- with degenerated neurons: The action potential (AP) of successfully stimulated degenerated human cochlear neurons reaches the central model end significantly earlier ($p < 0.05$) compared to the normal case.

The presented models enable to mimic the complex processes in the electrically stimulated human cochlea and to analyze the resulting temporal parameters to various stimuli configurations in an anatomical correct computational environment. It is shown that the auditory cortex receives partially wrong auditory spectral input due to infringement of the tonotopical principle. Furthermore, the parallel existence of normal and degenerated neurons within a pathological and artificially stimulated human cochlea confuses the temporal fine structure of the auditory neural code transmitted to the central nervous system (CNS) which may influence speech understanding and the general perception of sound.

7.2 Introduction

The first systematic histological analysis of the human hearing organ was published by Retzius (1884). Based on light-microscopy, his drawings delivered the first detailed insight into the quite complex (micro) anatomical structure of the human bony labyrinth and the auditory nerve. The vast majority of biological imaging methods require sectioning of the specimens that corresponds with loss of information and effects disruptive to three dimensional relations (Hardie et al., 2004). This irrecoverable information caused by the preparation of thin sections can tremendously influence 3D-reconstruction and subsequent quantitative parameter evaluation (Weinstein & Castleman, 1971; Song et al., 2013). It is particularly a problem to trace and reconstruct quite thin structures over several millimeters length (Liberman et al., 1990; Sato et al., 1999) through a volume with these techniques as it is the case with auditory neurons. Furthermore, time consuming acquisition of image stacks and complex data merging are required when analyzing bigger samples restricts additionally quality (Berthold et al., 1982; Deverell et al., 1989; Schormann et al., 1995) and productivity (Lu et al., 2009).

Non-destructive imaging methods like X-ray computed microtomography (Elliott & Dover, 1982) offers the possibility to analyze a complete isotropic data set of small biological structures (Metscher, 2009). Consistent further development of X-ray cameras, diminution of the spot size and improvements of geometrical hardware inaccuracies allow a spatial resolution of a few μm offered by commercialized systems. Due to the inherent radio opacity of the bony labyrinth, microCT is eminently suitable to efficiently scan, visualize and conduct anatomical measurements on inner ears (Van Spaendonck et al., 2000; Shibata et al., 2009; Schnabl et al., 2012; Braun et al., 2012; Malherbe et al., 2013; Shin et al., 2013). The additional use of contrast agents (de Crespigny et al., 2008) deposited in the dielectrically myelin sheath of cochlear neurons (Poznyakovskiy et al., 2008; Lareida et al., 2009) enabled to visualize, segment and reconstruct auditory signal transmitting nerve structures originating from varying frequency regions. This three dimensional pathway information of the neurons enable to predict their excitation profiles to microstimulation in a much more realistic way.

Electrically evoked spiking patterns are essentially determined by the distribution of the electrical potential through cochlea tissues which feature varying conductivities. This heterogeneous environment can be mimicked by creating a FEM representing its entire sophisticated anatomical structure. Due to the anatomical complexity of the snail-shaped organ, the spiral form was not considered in early modeling studies and was assumed to be fully uncoiled (Spelman et al., 1980; Black et al., 1983; Finley et al., 1990; Suesserman & Spelman, 1993). However, most numerical models of the cochlea available to date are restricted on simplifying assumptions by using 2D histological sections for geometry construction. Frijns et al. (1995, 1996) developed a rotationally symmetric model of a guinea pig cochlea using the boundary element method. Their model was later refined by Braire and Frijns (2000) to feature a more spiral constructed cochlea geometry virtually embedded in hard bone but still representing a guinea pig' cochlea. Both models were based on a 2D cross section from the second turn. They also interpolated several neurons along the whole cochlea spiral of the model but neither spiral pathways nor varying lengths of the peripheral processes were taken into account. Hanekom (2001) developed a simplified FEM of a human cochlea by combining two cross sections. The geometry was modeled around the axis of the modiolus though only for one and a half turn (Hanekom, 2001), Figure 2 and 3) which restricts in analysis of the very important upper middle- and apical turn. Rattay et al. (2001b) used for geometry development a microphotograph of a midmodiolar section of a human cochlea. This model includes its dimensions, spiral shape as well as the complex helicotrema. However, the group further concluded that a refined model should include the natural pathways of auditory neurons of different frequency regions due to reported geometry-based differences in neuronal excitation (Rattay et al., 2001a). These data can be used for subsequent analysis of the temporal spiking behavior in normal and degenerated modeled auditory neurons to get insight to the temporal fine structure along the tonotopically organized cochlea spiral. The 3D pathway variations may cause variation in the temporal fine structure of the neural code that influences the understanding of speech and the general perception of sound (Ghitza, 1994; Rattay & Lutter, 1997; Füllgrabe et al., 2006; Moore, 2008).

To overcome this limitation, we present in this paper the digitalization of a human cochlea using ultra-high resolution microCT imaging. Based on the acquired isotropic data set ($\Delta x = \Delta y = \Delta z = 3 \mu\text{m}$), this is according to our knowledge the first study that presents the manually segmented and reconstructed pathways of 30 tonotopically organized cochlear nerve fiber bundles along the human hearing organ representing frequencies between 11.5 kHz and 42 Hz. Imaging data was subsequently used to develop an anatomical correct finite element model of the snail-like hearing organ containing five compartments. This model was used to calculate the arising distribution of the electrical potential along the traced nerve fiber bundles induced by distinct electrodes of two CIs. Implementation of data to an adapted electrical circuit model of an auditory neuron (Rattay et al., 2001a) enabled to analyze neuronal behavior to microstimulation and to quantify the temporal- and spiking pattern of these neural parts on several stimuli configurations. Evaluation of the computational environment predicts the infringement of the tonotopical principle when stimulated with varying pulses and intensities at different positions. Especially within the apical region, this phenomenon is most distinct and is primarily based on the spiraling nature of neurons originating from the low-frequency region.

7.3 Methods

7.3.1 Human Cochleae Preparation and Fixation

The current study is based on two male individuals aged 40 (specimen 1) and 54 (specimen 2) years without any known ear disease or hearing loss (audiograms not available) from our archival material.

The investigated specimens were obtained during routine autopsy at the Institute of Pathology, Innsbruck Medical University. After manual opening of the round- and oval window, the inner ears were both fixed via these accesses using 4% paraformaldehyde with 0.1% glutaraldehyde in 0.1 M cacodylate buffer (pH=7.4) at 4°C for 24 hours within 90 and 60 minutes respectively, post mortem. After fixation, diamond drills of varying sizes were used to mill off cochlea surrounding bone to reduce the size of the specimen for later micro-CT imaging to a minimum. In order to remove the hard mineral components from bone in specimen 2, this inner ear was subsequently immersed into a solution of 0.1 M phosphate-buffered saline containing 20% ethylenediaminetetraacetic acid at pH 7.4 for 6 weeks at 37°C.

To improve the contrast of the cochlear nerve tissue structures in both specimens for further ultra-high resolution computer tomography, inner ears were post-fixed using 1% osmium tetroxide (OsO₄), that covalently binds and crosslinks unsaturated fatty acids and thereby darkly stains lipids and membranes. OsO₄ was dissolved and incubated in 0.05 M cacodylate buffer (pH=7.4) at 4°C for 48 hours (Lareida et al., 2009) and reacts with the double bonds of myelin lipids and is subsequently reduced to metallic osmium which is deposited in the peripheral nerve tissue. Due to its quite high atomic number of 76, the stained myelinated fiber structures are clearly visible in micro-CT scans. Afterwards, human cochleae were dehydrated through ascending series of ethyl alcohols from 70 to 100%. Subsequently, the prepared specimen 1 was embedded in epoxy resin and specimen 2 was stored in 80% alcohol for micro-CT imaging.

7.3.2 Micro-CT Imaging

Specimen 1

One human cochlea (specimen 1) was imaged using an ultra-high resolution SCANCO VivaCT 100 micro-CT (Scanco Medical AG, Büttiselle, Switzerland) yielding an isotropic spatial resolution of 3 µm. The acquired image stack had a size of 5052*5052*2400 volume elements (voxels) with 16-bit grayscale value resolution. The tube voltage was set to 70 kV, tube current to 182 µAs and 2000 projections were used. Signal-to noise ratio was improved by averaging of 8 image frames each together with 1600 ms exposure time.

Both Specimens

Micro CT imaging of the decalcified human sensory organ (specimen 2) was performed using a SCANCO VivaCT 40 reaching an isotropic resolution of 10 µm. The average size of this image stack was 2048*2048*1200 voxels, again featuring 16-bit grayscale value resolution. For this scan, the following hardware main settings were used: tube voltage was set to 45 kV, tube current to 177 µA, exposure time was 380 ms and 2000 projections were used. Furthermore, specimen 2 was additionally scanned using the VivaCT 40 micro-CT which constituted the basis for the development of a finite element model of the human cochlea for further numerical analysis. From all imaged data, DICOM files were computed for further processing from both scanned cochleae.

7.3.3 Data Processing

Calculated DICOM images of all three scans were further processed with a high-performance workstation (Z800, Hewlett-Packard, Palo Alto, CA, USA, 32 GB RAM, two six-core Intel® Xeon processor and a Quadro FX6000 graphical board) using Amira® 5.4.2 (Visage Imaging Inc., San Diego, CA, USA) visualization software. Due to the immense size of the acquired image stacks (especially for specimen 1), a region of interest was manually defined in a first step for each image stack.

Redundant voxels without any usable information of the specimens were cropped in xyz-direction reducing the imaged stack to a more easy-to-handle size. However, another problem concerning the size of data and the limited RAM used in our workstation arose: Amira® uses data objects of type *LabelField* to store the result of e.g, manual segmentation applied to a 3D image volume. This data object is a regular cubic grid which needs to use the same dimensions as the underlying image volume. As a consequence, the image stack of specimen 1 was separated in z-direction at the upper middle turn region (~500 Hz) resulting in two data sets manageable for further processing.

In order to reduce the amount of noise in data, an edge-preserving smoothing filter (Median filter, 3x3x3) was applied prior to segmentation of nerve-fiber bundles to each image stack. In a next step, the high resolution DICOM data of specimen 1 was newly adjusted in a more convenient plane using multi-planar reconstruction. The *ObliqueSlice* module of Amira enabled to manually position a non-orthogonal plane in a way that the resulting image stack is orientated in xy-direction from the most apical region to the basal turn. This direction allows to start with the segmentation of nerve fiber bundles from the lowest frequency region of the cochlea following down the spiral architecture of this sensory organ.

7.3.4 Segmentation and Visualization

Segmentation

Fiber bundles of the auditory nerve with a diameter of 15 µm were manually segmented from specimen 1 using Amira's '*Segmentation Editor*'. Segmentation allows dividing an image into different sub-regions of interest for further analysis. The starting point for all segmented structures was the habenula perforate, where the myelination of the peripheral process starts. This anatomical landmark was clearly visible due to the staining with OsO₄, corresponds to the level of the inner hair cell and defined furthermore the origin for length measurement of the peripheral process as well as the whole fiber bundle length for all segmented structures. The pathway of the fiber bundles was reconstructed following along the osseous spiral lamina (Figure 7.1B and C) to the Rosenthal's canal (RC) where the cell bodies of the bipolar cochlear neurons are located (Figure 7.1D). Due to the fact that cochlear SGNs are often arranged in functional units containing several neurons (Liu et al, 2012), the resolution of the Viva CT100 was sufficient to detect these grape-like arrangements of perikarya for the reconstructed nerve fiber bundles along the cochlea spiral.

Neurons belonging to the apical portion of the specimen were reconstructed down the modiolus taking its helical nature into account. The central processes of the more basal auditory neurons have to cross the highly-fenestrated bony column connecting the spiral canal of the cochlea with the modiolus. Bundles of nerve fibers were segmented as far as the fundus region that is located at the base of the inner ear. Unfortunately, the whole N. cochlearis acusticus was cut away during specimen preparation without the possibility of further segmentation in direction of the cochlea axis. To overcome this limitation, segmentation data of specimen 1 was merged with the DICOM stack of specimen 2 which enabled extrapolation of fiber bundles (Figure 7.4).

As mentioned previously, segmentation data were saved in a *LabelField* containing defined 'Materials' which represent the nerve bundles from low- to high frequency regions in a color-coded manner. After manual segmentation of the possible 3D pathways in both image stacks of specimen 1, the two resulting *LabelFields* containing segmentation data were merged using the *Merge* module of Amira®. This module works on any 3-dimensional field on rectilinear coordinates and merges the input data by interpolation. Taking *LabelFields* as input data, nearest-neighbor interpolation is preset by the software.

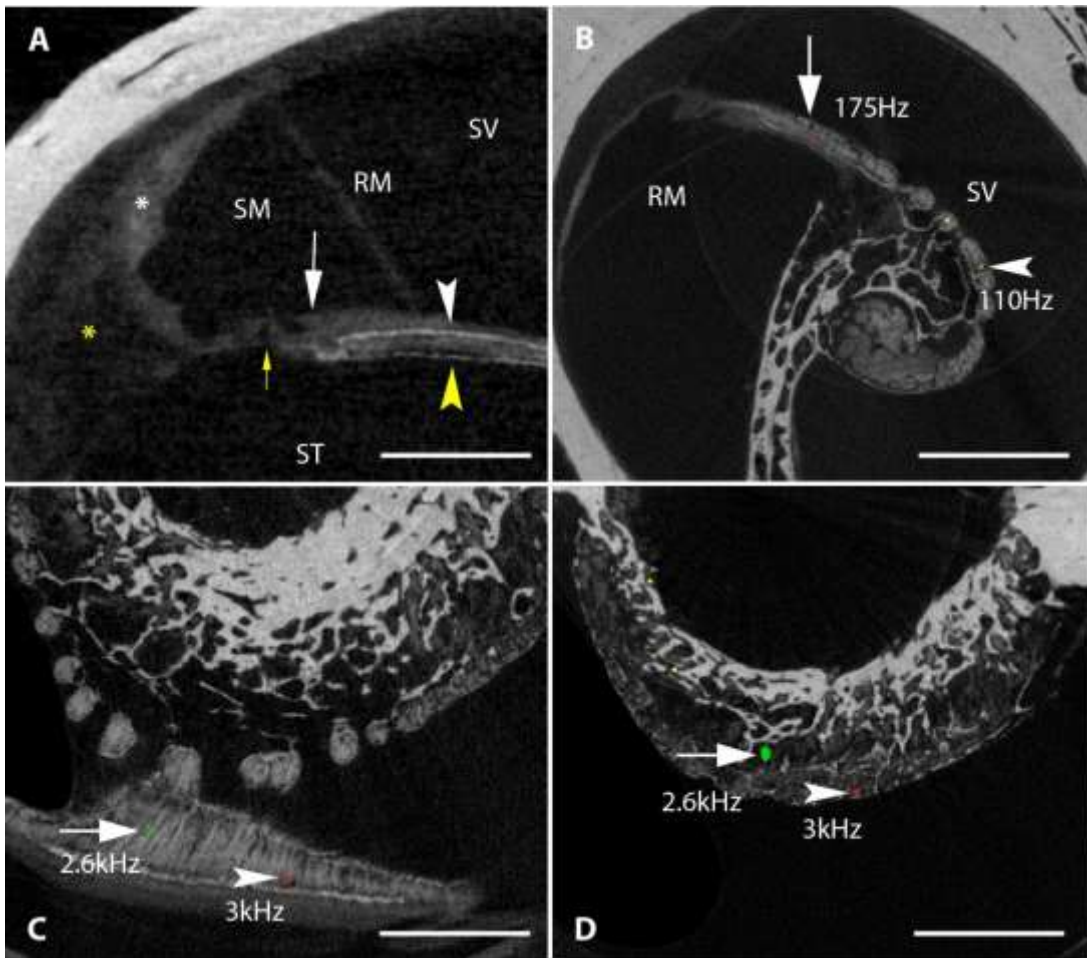


Figure 7.1: Micro-CT images of specimen 1 used for nerve fiber bundle reconstruction along the whole cochlea spiral. (A) illustrates the sensory epithelium with adjacent scales (ST=Scala tympani, SM= S. media, SV=S. vestibuli) of the basal turn at the 4 kHz region. Furthermore, the Reissner's membrane (RM) is clearly visible along the whole length of the inner ear. At the organ of Corti, some details are observable. The yellow arrow highlights the tunnel of Corti. Moreover, the white arrow highlights the spiral limbus which ends externally in the sulcus spiralis internus. The bony sheets of the osseous spiral lamina reaching as far as the habenula perforata are marked by the white and yellow arrow head which are clearly distinguishable from the inside located peripheral nerve tissue. On the lateral end of the inner ear cavity, the stria vascularis (white star) differs obviously in their grayvalues from the loosely arranged cells of the spiral ligament (yellow star) making these two structures additionally distinguishable. (B) presents single manually segmented 'areas' of auditory nerve fiber bundles belonging to the apical portion. The green area (white arrow head) marks one section of nerve bundle apical 4 originating at about 110 Hz within the spiral lamina. Another example of the low frequency region is highlighted by the white arrow (red area) representing the sixth traced apical nerve bundle (175 Hz). Again, the Reissner's membrane is clearly imaged in the apex. (C) shows single manually segmented areas of peripheral processes located within the osseous spiral lamina of nerve bundle basal 5 (green, white arrow) and basal 6 (red, white arrow head). They represent about 2.6 kHz and 3 kHz respectively. Note the clearly visible fiber bundles constituting the basis for tracing. The appropriate perikarya of that fiber bundles are illustrated in (D) highlighted by the white arrow (green colored). The peripheral neurite of nerve bundle basal 6 just enters the Rosenthal's canal while the yellow colored examples (basal 3 \cong 2 kHz and basal 4 \cong 2.3 kHz; left) enter and already passed respectively, the bony labyrinth. Scale bars indicate 1 mm.

Data Visualization

Data sets of the scanned specimens were resampled and illustrated using digitally reconstructed radiograph method which simulates a radiograph display from arbitrary views. Furthermore, bones and nerve fibers of the inner ears were displayed using classical texture-based volume rendering using different shadow effects. The radius of the segmented nerve fiber bundles was expanded to $d=30\ \mu\text{m}$ for improved visualization. Additionally, segmentation data from the *LabelField* were resampled for visualization and smoothed by producing a surface.

7.3.5 Data Merging and Nerve Fiber Extrapolation

Due to preparation technique of specimen 1, it was not possible to trace nerve fiber bundles beyond the bony labyrinth which represents the border of the cochlear fundus. To overcome this limitation, segmentation data of specimen 1 was manually registered to the scanned stack of specimen 2. With this approach, it was possible to extrapolate fiber bundles for about 5 mm in direction of the cochlear axis taking additionally the spatial orientation of the central processes on their way to the cochlear nucleus into account. However, several data processing steps must be considered: For a first step, one has to ensure that the matrix dimensions and voxel sizes of the image data and the *LabelField* are identical. Thus, the voxel sizes of the *LabelField* were resampled to an isotropic resolution of $10\ \mu\text{m}$ and the dimension of its data matrix was adjusted. Additionally, the data type of the *LabelField* was changed to 'unsigned char (8 bit)' data type which enabled to get the required transformation matrix via manually registering. This was done using the 'Multi-Planar Viewer' of Amira®. Subsequently, the proper transformation matrix was copied to the original *LabelField*. The attached 'ApplyTransform' module created a new field corresponding to the position in space of the imaging data of specimen 2. Again, nearest-neighbor interpolation method was used which avoids creating fractions of the label field indices. Now, the created registered label field can be used in the 'Segmentation Editor' together with the image stack of the second cochlea for further processing. The already segmented 30 nerve fiber bundles along the cochlea spiral were then extrapolated onwards the N. cochlearis acusticus for several millimeters.

7.3.6 xyz-Coordinates Extraction and Length Measurements of Traced Nerve Fibers

In order to use the 3D pathways of the segmented human cochlear nerve fiber bundles for computer simulations, the respective xyz-coordinates were extracted. These coordinates were subsequently used to calculate the length of the peripheral- and central processes as well as the length of the whole segmented fiber bundles originating from varying frequency regions. This was carried out using Fiji Win64bit image processing software (Schindelin et al. 2012) offering the possibility to implement macros. The used macro enabled to highlight a single pixel and save its respective coordinates from every image of the analyzed stack. To calculate the distance (d), and therefore the line segment between such two given points (x_1, y_1, z_1) and (x_2, y_2, z_2) in 3D, the following formula was used

$$d = \sqrt{(x_2 - x_1)^2 + (y_2 - y_1)^2 + (z_2 - z_1)^2} \quad (7.1)$$

where (x_1, y_1, z_1) and (x_2, y_2, z_2) are any two points in the Cartesian plane.

7.3.7 Length Measurements of Cochleae and Neuron Frequency

The macro was subsequently used to measure the total length of specimen 1 and 2 at the level of the OC. This was done by manually following the tunnel of Corti (Figure 7.1A, yellow arrow) along the cochlea spiral starting at the most apical point towards the most basal point near the round window membrane, where the highest frequencies are located. Again, the respective xyz-coordinates of the highlighted pixel at each DICOM slice were extracted and the total length was calculated by summing up the length of the single line segments. The evaluated length of specimen 1 was subsequently used in the Greenwood function (Greenwood 1961, 1990) to calculate the appropriate frequency domain for each segmented fiber bundle and reconstructed electrode position along the spiraling cochlea.

Greenwood (1961, 1990) estimated the frequencies of different cochlear regions along the OC which is not valid and applicable for the human cochlear spiral ganglion (SG). To overcome this limitation, we used a mathematical function developed by Stakhovskaya et al. (2007) matching frequencies along the OC with the corresponding frequencies along the SG as the cochlear neurons enter RC. For this purpose, we measured the length of the SG at the medial wall of ST in the middle of RC of specimen 1 representing the neurons' entry point. The percentage distance of the measured SG length was used to calculate the corresponding percentage distance along the OC. These values were used subsequently to recalculate the appropriate frequency domain for every virtually positioned electrode of the perimodiolar CI using the standard Greenwood function (Greenwood 1961, 1990).

7.3.8 Electrode Positions based on routinely implanted CIs

In order to establish the possibility to perform realistic simulations of the auditory response induced by cochlear implant (CI) stimulation, the geometrical parameters of two routinely used electrode arrays were incorporated in our model. To cover a preferably broad range of clinically used CIs, we mimicked a deep-insertion array (FLEX^{SOFT}, MED-EL, Innsbruck, Austria and a perimodiolar located CI (CI24RE Contour Advance, Cochlear, Sydney, Australia). For better reproducibility, subtended electrodes on analyzed electrode configurations were neglected and hence only 12 electrodes were modeled from the MED-EL CI. Moreover, all electrodes were modeled as a sphere made of platinum with a diameter of 0.2 mm.

Deep Insertion

MED-EL FLEX^{SOFT} CI (Med-El, 2012) has a total length of 31.5 mm each with a 2.4 mm gap between the electrodes resulting in an active stimulation range of 26.4 mm. The gap from the entry point of the CI into the Scala tympani (round membrane) to the first active, most basal electrode was taken into account for electrode-position-determination and was measured to be 3.55 mm. At this point, the xyz-coordinates of the first electrode were determined once again using Fiji imaging software. For a standardized identification of the 12 electrode positions along the inner ear, two additional criteria were considered: (i) the electrode is located in the scala tympani and (ii) is close to the lateral wall which represents the expected positioning after successful implantation. Using these criterias together with the geometrical design of this CI, the 12 electrodes were virtually positioned along the cochlea spiral.

Perimodiolar CI

The Contour Advance CI (Cochlear, 2012) contains a slightly bent electrode array arranging 22 electrodes on a length of 14 mm. For this mimicked electrode array, the distance from the cochlea entry point (round window niche) to the most basal electrode was determined to be 5 mm. The distances between the electrodes connected in series decreases (mostly) progressively ranging from 0.92 mm (between basal electrode 1 and 2) to 0.45 mm (between apical electrode 21 and 22). Due to

the perimodiolar position of this investigated CI electrode array, a new second criterion for virtual positioning of the electrodes was formulated: (ii) electrodes are modeled in close proximity to the medial wall of the ST, in the middle of the RC which houses the cell bodies of the SGNs. Again, the 22 electrodes were virtually positioned along the RC of the model.

7.3.9 Finite Element Model

Segmentation of Compartments

In order to develop an anatomically accurate model of the spiraling human cochlea (Figure 7.2) used to analyze the distribution of electrical potentials around distinct electrodes, we used the high-resolution dataset of specimen 1 (spatial resolution = 10 μm , Figure 7.3A). Data was loaded to the 'Segmentation Editor' of Amira® and five materials representing the cavities within this sensory organ, the cochlea-surrounding bone and the centrally located modiolus (including osseous spiral lamina) were created. Subsequently, the Scala tympani, media and vestibuli were segmented manually along the spiral geometry and saved to the created LabelField (Figure 7.3B). At regions where the structure of interest did not change a lot in z-direction, data was interpolated. However, each interpolation step was inspected manually by scrolling back and forth. This original *LabelField* was used to determine the volume of each structure using the '*MaterialStatistics*' module of Amira®. For further processing, the three segmented structures were separated and saved to individual *LabelFields*. From these data objects, triangular surfaces were computed using the '*SurfaceGen*' module.

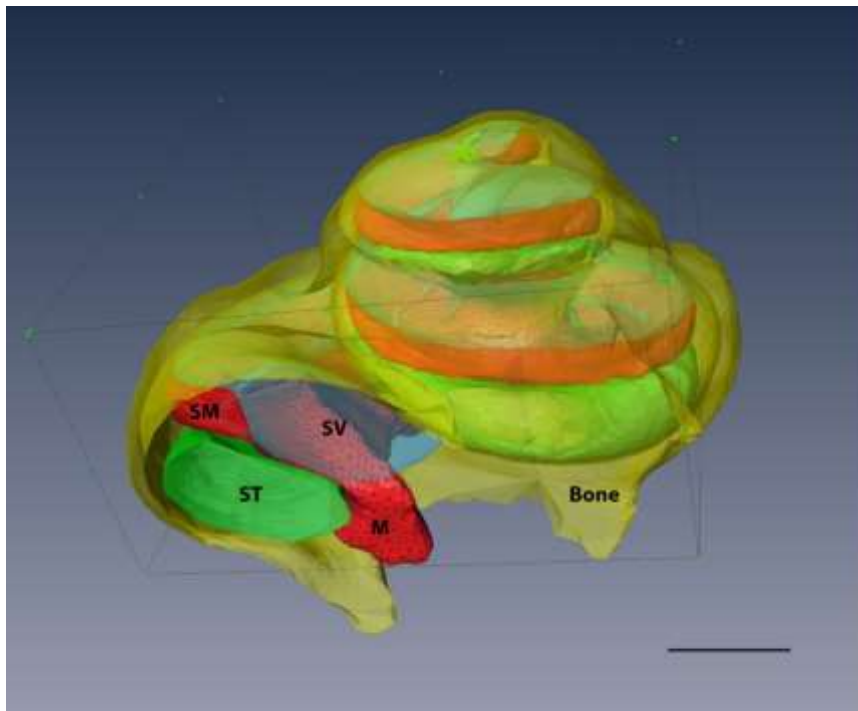


Figure 7.2: Visualization of the segmented compartments of the developed FEM. The image illustrates the three fluid filled cavities of the human cochlea in a transparent manner. Scala vestibuli (SV) is shown in cyan; S. tympani (ST) in green and S. media (SM) in red. The centrally located modiolus (M) with the osseous spiral lamina is illustrated with its triangularized surface. Yellow-colored, again in a transparent manner, represents the cochlea surrounding compact bone. Scale bar represents 2 mm.

In humans, the sensory organ for hearing is surrounded by the mastoid portion of the temporal bone which is known to be the hardest in the body. To mimic the anatomical conditions as adequately as possible, a fourth compartment – the bone encapsulating the cochlear cavity – was added to the model. For this purpose, the appropriate voxels were selected by threshold segmentation. After specifying the minimal and maximal image intensity for display and masking of data, the operation was performed in the whole volume which was assigned to a *LabelField*. Segmentation data also contained the central spindle or modiolus with various cavities like a sponge. However, further processing and preparation of data to generate a tetrahedral model (procedure explained later) was not possible due to the highly porous micro-anatomical characteristics of this part of the cochlea. Consequently, the part representing the modiolus was removed manually and a triangular surface of the residual bone data was computed.

As mentioned, separating the modiolus in two single compartments representing the spongy bony structure and the nerve tissue respectively is not possible. However, this part of the cochlea together with the osseous spiral lamina, which comprises the peripheral processes of the neurons within a bony shelf, contains the pathways of all traced nerve fiber bundles. Consequently, these structures play important roles when analyzing electrical potential distribution along these neural structures. To overcome this limitation, the bony and the nerve tissue portion of the analyzed specimen were assigned together in a *LabelField* using threshold segmentation after appropriate masking. To eliminate the hard, cochlea-surrounding bone from this compartment, a binary image stack of the bone compartment was created first (pixels representing bone were assigned to be 0). In a second step, the fifth compartment was multiplied with the binary image and the surrounding compact bone was eliminated. Remaining segmentation data was controlled manually, smoothed and holes within the modiolus were filled to get a compact, closed 3D-model. Finally, a triangular surface of the modiolus and the spiral lamina was computed for further processing.

Data Processing

Due to import limitations of triangle surfaces to SolidWorks® 2012 (Dassault Systemes SolidWorks Corp., MA, USA), which is needed in the data processing pipeline, the total number of faces representing each of the four compartments were reduced to 15000 in a surface simplification step. Now, the four surfaces were ready for further editing using Amira's '*SurfaceEditor*'. This editor contains five useful tests for increasing the quality of the surfaces before tetrahedralization. Each test identifies inaccurate triangles that do not meet criteria. Depending on the test, triangles can be repaired manually and/or using an automatic tool. Tests mandatory for further tetrahedralization are the (i) intersection test which identifies triangles intersecting with its neighbors and the (ii) orientation test seeking for partial overlapping of triangles. The third and fourth test include the (iii) aspect ratio (should be <10) identifying badly-shaped triangles and (iv) the dihedral angle (should be >10) which influences the speed and accuracy of the numerical analysis. The last applied test checks (v) the tetra quality (should be <25) by computing the aspect ratio of the tetrahedron probably created for each triangle. After succeeding above mentioned tests on each single compartment, the generated surfaces were individually saved as STL-files which enabled further processing using the 3D computer-aided design (CAD) program SolidWorks.

Why using the CAD program SolidWorks? The triangular surfaces which were processed and optimized in Amira®, can be saved in mesh or point cloud files. One major drawback of these files is that they cannot be used directly for finite element analysis. A point cloud file has to be processed to a mesh file first. An STL-file, which is a mesh file, represents only the surface geometry of a 3D object without any texture information or other CAD model attributes (Burns, 1993). In other words: these files are not representing solid models. Furthermore, finite element analysis software, like COMSOL

Multiphysics® (COMSOL, Inc., Palo Alto, CA, USA) which is used in this work, need non-uniform rational B-splines (NURBS) describing the surface of an model. NURBS are mathematical models widely-used in computer graphics and most CAD design software's and represents smooth surfaces using only few vertices. The construction of the basic functions of NURBS surfaces used for surface reconstruction is described in Piegl and Tiller (1997). Due to the missing NURBS model implementation in Amira, an additional processing step of the segmented compartments was performed using SolidWorks.

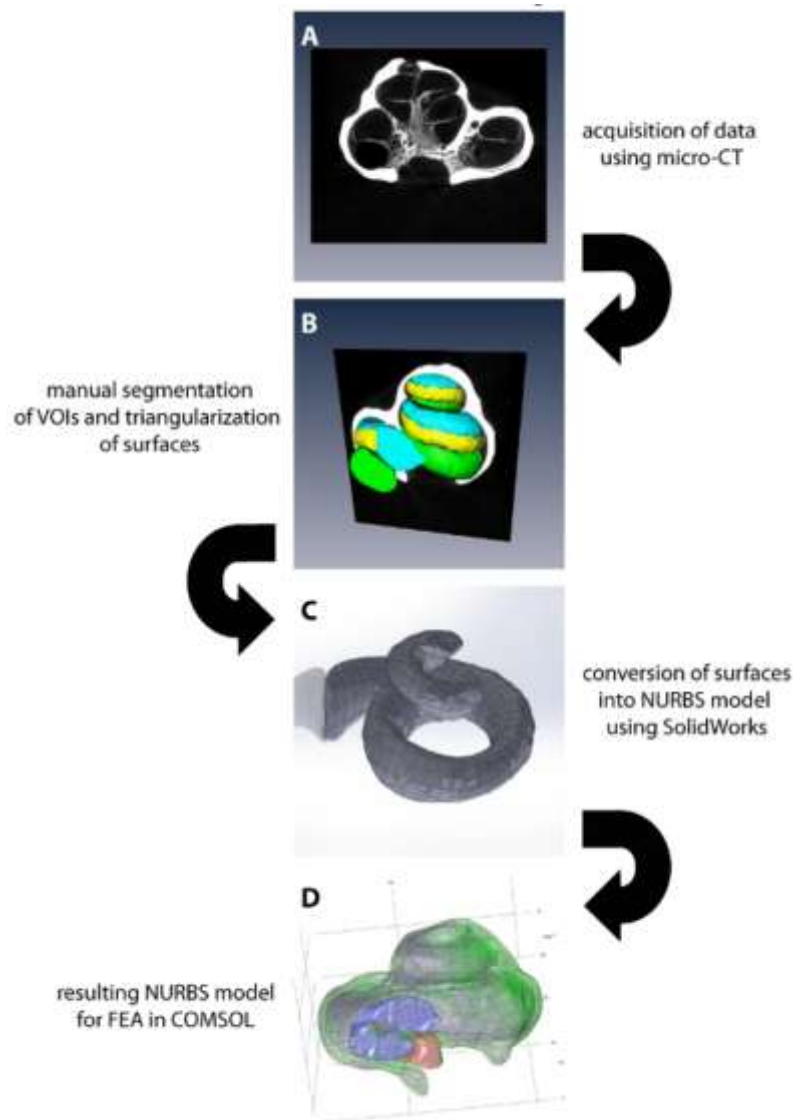


Figure 7.3: Illustration of workflow of data processing. The graphic presents the necessary steps to generate a solid NURBS model from segmented data of a human cochlea micro-CT scan. In a first step (A, mid-modiolar view), a human cochlea was digitized using an ultra-high-resolution micro-CT reaching an isotropic resolution of $3 \mu\text{m}$. Afterwards, data (B, green=S. tympani, cyan=S. vestibuli, yellow=S. media) was preprocessed and the inner ear cavities as well as the surrounding bone were segmented manually. The surfaces were optimized, represented by triangles and saved as STL-mesh file. Single compartments were subsequently imported to SolidWorks (C, e.g. S. vestibuli) and prepared to export a volume model represented by NURBS. Finally, SolidWorks was synchronized with COMSOL (D, all five compartments) to enable finite element analysis.

SolidWorks software's 'ScanTo3D' option allows data importing, in the presented case, a STL-file, prepare the data and subsequently convert it into a solid model used for finite element analysis (Figure 7.3C). In a first step, the mesh saved as a STL-file is cleaned up and a mesh feature is produced from which it is possible to create the final solid model. The cleaning option includes possibilities for, e.g. smoothing, mesh simplification or correction of wrongly orientated triangles. However, proper surface preparation using Amira[®] according to the criteria as described above reduces preparation effort in SolidWorks. The resulting mesh feature is then converted into a manual definable number of surfaces which represents the desired surface detail. The created surfaces are made-up of numerous patches forming regions on the surface. Their boundaries are represented by so-called feature lines which can be moved, added or deleted. Editing the feature lines can cause surfaces with self-intersections which must be repaired to guarantee a homogeneous model surface. When no more errors are displayed, the created surfaces are knitted together and a solid model is generated.

7.3.10 COMSOL

The generated solid model (Figure 7.3D) was subsequently transferred to COMSOL Multiphysics[®] 4.2 engineering simulation software via the LiveLink[™] for SolidWorks[®] which offers the possibility to synchronize both software programs. Using this bidirectional connection, the five compartments were transferred individually taking their original orientation in space into account. In order to calculate the electric field in the human cochlea model, the five compartments were set up in the AC/DC module and individual conductivities were assigned to each segmented cochlea structure (Table 7.1). Afterwards, the cochlear structures were meshed using the physics-controlled approach with 'fine' element size. A total number of 520768 tetrahedral elements were calculated describing the segmented compartments (individual split-up is presented in Table 7.1).

The five cochlear structures were enclosed by a cuboid (featuring bone conductivity) which outer boundaries were set to electric ground simulating the return electrode for monopolar stimulation. The human cochlea model was placed just beyond (0.4 mm) the upper surface and in the middle of the cuboid (7 mm to adjacent surfaces). At the base of the cochlea model, the cuboid was extended for 30 mm to mimic the anatomical direction of the traced nerve pathways.

Four different models were calculated analyzing the electrical potentials induced in the basal- and middle turn (by both electrode arrays) which corresponds to realistic CI situations. The active electrodes of both CIs were assumed to be spherical with a diameter of 0.2 mm. The distribution of the electrical potential was studied under quasi-static conditions for a fixed potential of ± 1 V at the surface of selected active electrodes (Rattay et al, 2001b) of the two analyzed CIs. Therefore, COMSOL calculated the potential distribution of each model using the iterative 'Conjugate Gradients' linear solver together with the preconditioner SOR (Successive Over-Relaxation) which speeds up convergence. The electric potentials were subsequently evaluated for various segmented nerve fiber pathways within the defined cochlear geometry.

To determine the applied current by the electrode, the current density norm on the electrode surface was integrated in COMSOL after model calculation under quasi-static conditions (1V). A standard value of 215 μ A was determined and used for further calculations.

FEM Compartments	Conductivity [S/m]	Tetrahedral elements
Scala tympani	1.43	131939
Scala vestibuli	1.43	109430
Scala media	1.67	64489
Modiolus (Bone + Nerve tissue)	0.0334	86961
Bone	0.016	127949
Electrode	1000	70

Table 7.1: Conductivities of cochlear compartments according to Rattay et al. (2001b) and number of tetrahedral elements for each cochlear structure.

7.3.11 Compartment Model

In order to analyze the influence of different positions of active CI electrodes within the S. tympani, we used the calculated extracellular potentials (V_e) along traced human cochlear nerve fibers as input for the compartment model to analyze the response of cochlear neurons to microstimulation.

Since we have manually traced and reconstructed 30 AP transmitting pathways along the cochlea spiral we are aware of morphometrical and geometrical characteristics respectively, like (i) the length of the peripheral- and central processes and (ii) the position of the soma along each SGN. Consequently, the processes were split up in varying numbers of passive internodes (peripheral process with 40 myelin layers, central process with 80 myelin layers) and interjacent active nodes of Ranvier. To model the unmyelinated somatic region of human cochlear neurons, these neural subunits were modeled as active compartments with temperature compensated (37°C) Hodgkin Huxley ion channel kinetics surrounded by three membrane layers (one bipolar cell membrane and two satellite glial cell membranes). The diameter of our standard soma was set to 20 μm as investigated in chapter 4. The model neurons additionally feature an unmyelinated peripheral terminal (first compartment) and an unshielded central terminal (last compartment). Further details concerning the geometrical and electrical parameters of the used compartment model are described in Rattay et al. (2001a). Since the extracellular potentials along the most excitable neuron calculated by the FEM is compared with the homogeneous extracellular medium case (Rattay et al., 2001a; Rattay et al., 2001b), the assumed spherical electrode (again $d_{electrode} = 0.2 \text{ mm}$) and the analyzed neuron are arranged within an infinite medium with constant resistivity of $\rho_e = 300 \Omega \text{ cm}$. For this case, the calculation of V_e reads as

$$V_e = \frac{\rho_e \cdot I_{EL}}{4 \cdot \pi \cdot r} \quad (7.2)$$

where I_{EL} is the amplitude of the stimulating current pulse and r denotes the center-center distance from a neural compartment to the active electrode.

In order to analyze the temporal excitation profiles of selected neurons, four different pulse shapes were tested to calculate their individual (i) activation threshold, (ii) spike initiation site (IS), (iii) peak time at which the AP occurs in the IS after spike onset (PT) and (iv) the peak time at which the AP reaches the central end of the model neuron (ET). The four pulse shapes were monophasic pulses of both polarities with a duration of 0.1 ms (CAT describes cathodic; ANO stands for anodic pulse) and biphasic pulses with a duration of 0.1 ms/phase for leading CAT phase (BIC) or ANO pulse (BIA) first.

7.3.12 Statistical Analysis

One-way analysis of variance followed by Bonferroni correction (Dunn, 1961) was used to determine statistical significance. Normality of data was assessed by quantile-quantile plots. Statistical significance as well as descriptive statistics was computed using OriginPro 9.0 (OriginLab, Northampton, MA, USA) and Matlab® 2011a (MathWorks, Natick, MS, USA).

7.4 Results

7.4.1 Cochleae length, width and height – 3D merging and comparison of different individuals

The determined OC length of specimen 1 was 40.28mm; the SG possesses an average length of 17.6mm within the cochlea. The volume of *S. tympani* where CIs are located after successful implantation, was determined to be 37.9mm³ followed by *S. vestibule* with 33.9mm³. This decline corresponds to about 10.5%. The endolymph filled *S. media* was determined to be smallest reaching a volume of 8.3mm³.

The length of the second scanned cochlea (specimen 2) used for fiber bundle extrapolation, was found to be 5.5% shorter at the OC-level compared to specimen 1 (38.1 mm) and features a 3.2% shorter SG (17 mm). While registering the *LabelField* containing the segmentation data with specimen 2, a quite good analogy of the particularly geometry in the basal turn between these two cochleae was found by visual inspection. The terminal ends of the reconstructed basal fiber bundles from specimen 1 corresponded very well to the position of the sensory epithelium of specimen 2 which is visualized in Figure 7.4A. This indicates that the basal turns of the analyzed samples feature similar geometrical dimensions.

In order to verify this similarity, the width of the basal turn of both specimens was measured in a mid-modiolar plane from the lateral wall of the Scala tympani at ~11 kHz to the respective opposite side corresponding to the ~2 kHz region. Comparison of the measured values depicts a difference of 5.2% between the cochleae (6.53 mm for specimen 1 and 6.19 mm for specimen 2). Note the percentage-correlation to the cochlea lengths! Furthermore, the difference in height between the two inner ears was about 10% (4.24 mm for specimen 1 and 3.87 mm for specimen 2) as measured from the cochlea fundus where the cochlear nerve exits into the inner acoustic meatus to the most apical limit of the cavity along the cochlea axis. This difference can be seen in Figure 7.4B where the segmented fiber bundles from the upper middle- and apical turn of specimen 1 exceed the geometrical conditions of specimen 2.

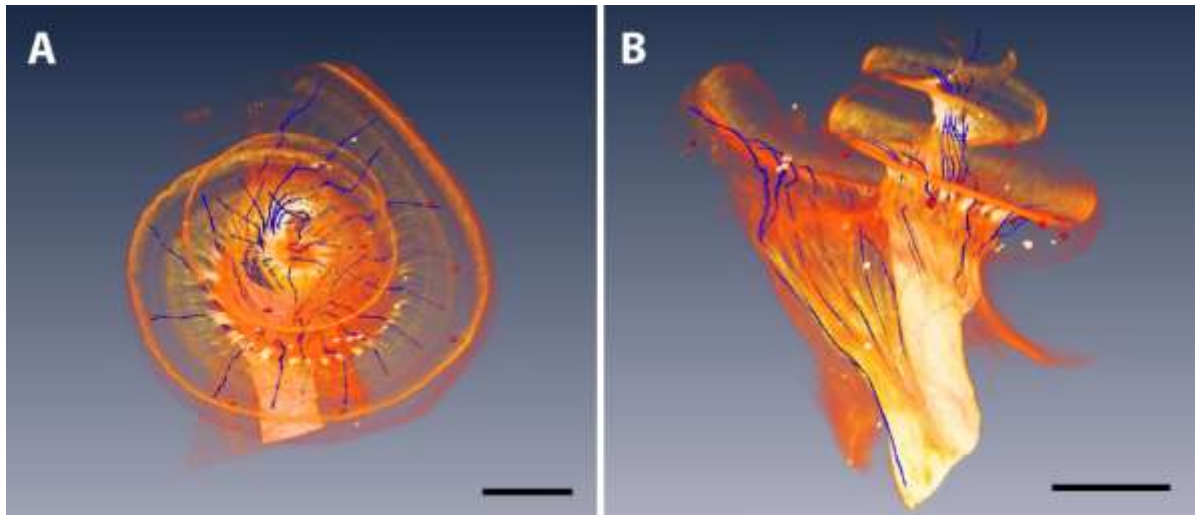


Figure 7.4: Visualization of specimen 2 and registered segmentation data. (A) offers a view from above to the surface rendered segmentation data (segmented nerve fiber bundles are blue-colored; electrode positions red) of specimen 1 and the volume rendered image data of specimen 2. Due to decalcification and OsO_4 staining of specimen 2, the nerve tissue is excellently visible (note the cochlea fiber bundles within the spiral lamina in A). It illustrates additionally that the basal geometry of specimen 1 (segmented nerve fiber bundles) and 2 (volume-rendered cochlea) look similar featuring comparable dimensions. A lateral view of the same structures is presented in (B) clearly visualizing the basal- middle and apical portion of specimen 2. Note that the central processes of fiber bundles from the first 180° of the basal turn join the pathways of the other reconstructed examples in the *N. cochlearis acusticus* as far as 4 mm after the fundus region. Scale bars indicate 2 mm.

7.4.2 Cochlea Details and Fiber Bundle Tracing

The small-sized structure of the cochlea can be effectively imaged in micro-CTs due to the inherent radio opacity of its bony microstructure. Furthermore, the deposited metallic osmium in the myelin sheets of the cochlear neurons increases its tissue density which enabled to visualize the auditory nerve tissue besides the bone. Exemplary details of the acquired X-ray computed tomographies are displayed in Figure 7.1. The sensory epithelium with its adjacent scalae (ST=Scala tympani, SM= S. media, SV=S. vestibuli) of the basal turn at the 4 kHz region is presented in Figure 7.1A and Figure 7.5E. Clearly visible is the Reissner's membrane (in Figure 7.1A and B) which is composed of two cell layers separating the endolymph filled Scala media (SM) with the perilymphatic Scala vestibuli (SV). Even at the OC some details are observable as presented in Figure 7.1: The white arrow highlights the spiral limbus which ends externally in the sulcus spiralis internus. Moreover, the tunnel of Corti (yellow arrow) dividing the outer- and the inner hair cells is clearly visualized along the cochlea spiral. Another detail can be seen in the bony sheaths of the osseous spiral lamina. The upper layer (white arrowhead) is displayed more compact and connected in a steady manner. On the contrary, the lower layer (yellow arrow head) is thinner and features gaps indicating a highly porous microstructure. Furthermore, on the lateral end of the inner ear cavity, the compact and highly vascularized stria vascularis (white star) differs obviously in its' grayvalues from the loose connective tissue of the spiral ligament (yellow star) making these two structures additionally distinguishable.

Due to the OsO_4 staining, the nerve fiber tissue in the spiral lamina enclosed by the bony sheaths was obviously visible (Figure 7.1B and C) which enabled to manually segment the passing bundles of nerve fibers along the osseous spiral lamina. Examples are presented of such fiber bundles with a

diameter of 15 μm and are highlighted by white arrows and arrow heads in Figure 7.1B (from apical portion) and C (belonging to basal turn). In (B), the green area marks one section of nerve bundle apical 4 originating at about 110 Hz, the red area highlights the sixth traced apical nerve bundle (175 Hz). Further examples of traced fiber bundles are illustrated in Figure 7.1C by the segmented fiber bundle basal 5 (green, white arrow) and basal 6 (red, white arrow head) representing 2.6 kHz and 3 kHz respectively. Their appropriate perikarya are illustrated in (Figure 7.1D) highlighted by the white arrow (green colored). The peripheral neurite of nerve bundle basal 6 just enters the RC while the yellow colored examples (basal 3 \cong 2 kHz and basal 4 \cong 2.3 kHz; left) are on their way through the highly porous bony column.

7.4.3 Nerve Bundle Lengths

Apical turn

Seven fiber bundles from the auditory nerve were reconstructed located at the apical portion (Figure 7.5A) of specimen 1 covering a frequency range of 42 – 228 Hz over a distance of 5.7 mm (Table 7.2).

Region		total segmented length [mm]	length peripheral process [mm]	length central process [mm]	distance apex to bundle [mm]	representing frequency [Hz]
apical_1		11,484	2,892	8,592	1,050	42
apical_2		10,946	2,757	8,189	1,512	53
apical_3		10,492	2,317	8,175	3,009	92
apical_4		10,671	2,187	8,484	3,590	109
apical_5		10,120	2,058	8,062	4,335	133
apical_6		9,845	1,837	8,008	5,474	174
apical_7		9,514	1,950	7,564	6,780	228
	mean	10,439	2,285	8,153		
	SD	0,623	0,372	0,312		
middle_1		9,12	1,549	7,571	7,588	266
middle_2		9,321	1,487	7,834	8,422	309
middle_3		9,284	1,57	7,714	10,100	411
middle_4		8,832	1,411	7,421	10,929	469
middle_5		7,995	1,345	6,65	11,667	526
middle_6		8,092	1,484	6,608	13,157	657
middle_7		7,654	1,528	6,126	14,045	747
middle_8		7,951	1,231	6,72	14,566	805
Middle_9		8,115	1,358	6,757	15,940	976
	mean	8,485	1,440	7,045		
	SD	0,612	0,106	0,565		
basal_1		7,745	1,959	5,786	17,249	1166
basal_2		7,512	1,916	5,596	19,233	1519
basal_3		8,039	1,797	6,242	21,255	1977
basal_4		7,623	1,861	5,762	22,385	2285
basal_5		8,008	1,962	6,046	23,420	2607
basal_6		7,75	1,732	6,018	24,472	2977
basal_7		7,971	1,712	6,259	25,460	3371
basal_8		8,32	1,929	6,391	26,515	3845
basal_9		9,007	1,897	7,11	27,700	4455
basal_10		8,269	1,719	6,55	30,165	6040
basal_11		9,077	2,075	7,002	31,921	7492
basal_12		9,108	1,929	7,179	32,660	8200
basal_13		11,019	2,055	8,964	33,924	9568
basal_14		10,812	1,941	8,871	35,452	11524
	mean	8,59	1,89	6,70		
	SD	1,08	0,11	1,02		

Table 7.2: Summary of the determined nerve fiber bundle length along the cochlea spiral. Furthermore, their corresponding frequency region was calculated using the Greenwood function (Greenwood 1961, 1990).

This frequency range correlates to the first 360° of the spiraling inner ear from the apex towards the basal turn. Within this first turn, the mean length of the peripheral process was determined at 2.29 ± 0.37 mm which is significant different to correspondent values evaluated from the middle- ($p < 0.001$) and basal region ($p < 0.05$). However, the length of the peripheral process ranges from 2.9 mm (Figure 7.5A, highlighted by the white arrow, apical bundle 1) to 1.87 mm (apical 6, white arrow head) which corresponds to about 57%. Their appending central processes had a uniform length (8.15 ± 0.31 mm) due to the position of their cell bodies which were located at quite comparable positions within about half a millimeter (Figure 7.5A, yellow star). The length of the central neurite was found to be significant different compared to the middle turn ($p < 0.05$) and the basal region ($p < 0.05$). All reconstructed neurons were extrapolated to the same plane for better comparability (Figure 7.5A-D). Note the spiraling pathway of the central processes down the cochlea axis which lengthens the AP transmitting structures. This physical spiral-lengthening-effect is additionally shown by the most apical fiber bundles. Based on the coiled geometry of the inner ear, the reconstruction depicts that the length of the peripheral processes of auditory SGNs is significant longer ($p < 0.05$) until the ~90 Hz region compared to the remaining fiber bundles from the low frequency region (around 100 Hz – 230 Hz). The determined difference in length within this portion is with 33% remarkable. No such significant difference in peripheral process length was calculated analyzing the reconstructed fiber bundles from the middle- of basal turn respectively.

Middle turn

The reconstructed peripheral processes from auditory neurons originating from the middle turn ($n = 9$, Figure 7.5B) were the shortest (Table 7.2). Their length was quite uniform (1.44 ± 0.11 mm) reflected by the small calculated standard deviation. However, the absolute difference between the longest (Figure 7.5B, white arrow, middle 1) and shortest (Figure 7.5B, white arrow head, middle 8) was much lower (27.5%) compared to the apical turn. Furthermore, a significant difference turned out when comparing middle turn fibers with the apical ($p < 0.05$) and basal region ($p < 0.05$) in this specimen. The length of the peripheral neurite of the bipolar SGNs is determined by the position in space of their appropriate perikarya. For fiber bundles originating from the apical turn, these neuronal subunits were located within the distal end of the RC, known as the bulge region, within 1.2 mm in z-direction. Note the ascending pathway of the peripheral processes of the upper three fiber bundles (~260 – 410 Hz) based on cochlea geometry. In this upper middle turn region, the coiled and snail-like geometry of the inner ear results in narrowing scalae which causes more and more steepening fiber bundles.

The reconstructed nine fiber bundles originating from the middle turn region cover an acoustic spectrum ranging from 266 – 976 Hz along 8.35 mm of OC. This represents the second half turn starting from the apex. The thicker, central processes were about 16% shorter compared to matching structures in the low frequency regions which results from the geometric nature of the cochlea. However, central processes from the apical region were found to be significantly longer ($p < 0.05$) while no statistical difference was found compared to the basal turn. Note that only the central processes run spiral around an axis through the modiolar spindle; peripheral processes travel quite linear from their peripheral terminal to their SGN cell bodies.

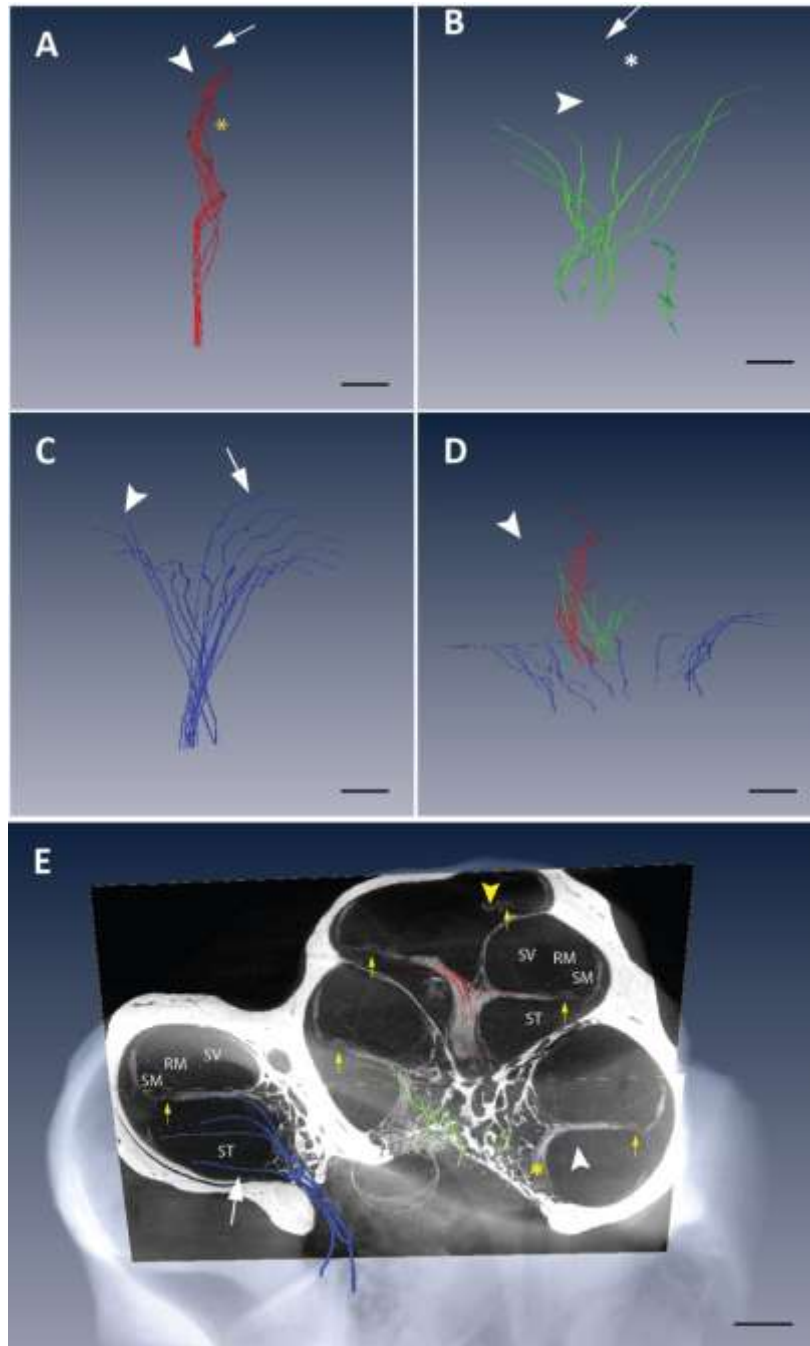


Figure 7.5: Overview of reconstructed auditory nerve fiber bundles along the cochlea spiral. The segmented examples from the apical portion ($n=7$) are presented in (A) where the longest nerve bundle (apical 1) is highlighted by the white arrow and the shortest (apical 6) by the white arrow head. The region where their appropriate cell bodies are located is marked by the yellow star. The shorter reconstructed fiber bundles originating from the middle turn ($n=9$) are illustrated in (B). Likewise, the white arrow depicts the longest bundle (middle 1) and the white arrow head the shortest one (middle 8). The white star labels the ascending and more steepening fiber bundles belonging to the upper middle turn. The most uniform cochlear neurons are located in the basal portion of the analyzed specimen ($n=14$) and are presented in (C). The most basal reconstructed fiber bundle (basal 14) is highlighted by the white arrow while basal 1, located at the transition of basal- to middle turn, is marked by the white arrow head. A view of all 30 reconstructed human fiber bundles

from the human inner ear is illustrated in (D). The white arrow head depicts fiber bundle basal 1 (about 1150 Hz) which is located at the transition from the upper basal region to the middle turn. Here, cochlea geometry and therefore the pathways of fiber bundles change essentially. A view of the imaged cochlea in a mid-modiolar plane combined with all 30 reconstructed fiber bundles is presented in (E). Clearly visible along the whole cochlea length is the sensory epithelium (yellow arrow) and the Reissner's membrane (RM). Additionally, the adjacent scalae are labeled exemplarily (ST=S. tympani, SM= S. media, SV=S. vestibuli). The segmented fibers from the basal- (blue colored), middle- (green) and apical (red) turn are displayed using surface rendering. As above, the white arrow highlights the first, most basal fiber bundle; the white arrow head depicts the last nerve bundle from the basal turn (basal 14). The appropriate position of perikarya within the Rosenthal's canal is labeled by the yellow star. In the apical portion, the yellow arrow head highlights the terminal end of the most apical reconstructed fiber (apical 1). Scale bars indicate 1 mm.

Basal turn

The length of the segmented peripheral processes (Figure 7.5C) originating at the basal turn ($n = 14$) of the investigated human cochlea show significant differences compared to the middle- ($p < 0.001$) and apical turn ($p < 0.05$). They represent frequencies ranging from 1166 – 11524 Hz which corresponds to a length of 18.2 mm (Table 7.2). Adding the missing ~ 3.5 mm (due to specimen preparation) of the basal turn to get the total length of this specimen, the basal turn covers about 54% of the whole cochlea length measured at OC level. This value matches exactly reported mean values for human cochleae (Erixon et al., 2009). Due to the spiraling geometry of the cochlea, the basal portion comprises the most uniform length of the peripheral processes reaching 1.89 ± 0.11 mm. Consequently, the difference between the longest and shortest measured peripheral process is about 21% representing the smallest difference of the three analyzed specific regions within this specimen. Moreover, the peripheral neurites of SGNs from the most distal 5 mm of the lower basal end follow a steeper pathway from the sensory epithelium to the RC due to cochlea geometry in that particular region. This characteristic is illustrated by the segmented fiber bundle basal 14 (Figure 7.5C and E white arrow) representing about 11.5 kHz and located 4.8 mm after cochlea entrance. However, the geometrical courses of fiber bundles basal 13 (~ 9.5 kHz) to basal 2 (~ 1.5 kHz) are quite similar due to the relatively constant geometry of the cochlea cavity. The steady and comparable pathways go as far as the ~ 1.2 kHz region represented by reconstructed example basal 1 (Figure 7.5C, white arrow head). From this region onwards, the snail-shaped geometry of the inner ear causes a steeper course of the peripheral processes. These changes are additionally visualized in Figure 7.5D and E. Here, fiber bundle basal 1 is highlighted by the white arrow head while all 30 reconstructed structures are displayed in the same color-coded manner as before (blue $\hat{=}$ basal turn, green $\hat{=}$ middle turn, red $\hat{=}$ apical region). Basal 1 nerve fiber bundle which sits at this geometrical transition between basal- and middle turn is visualized in Figure 7.5E highlighted by the white arrow head. Segmented perikarya within RC are labeled with a yellow star. The central processes revealed shortest mean length but the highest standard deviation (6.7 ± 1.02 mm) with a significant difference compared to the apical turn ($p < 0.05$).

7.4.4 Spiral Pathways of Cochlear Neurons

Apical Turn

Bipolar SGNs belonging to the apical portion of the cochlea indicate spiral characteristics in both, the peripheral- as well as the central process. The most apical traced nerve fiber bundle (apical 1) rotates overall about 900° on its own axis. 360° of the whole rotation are assigned to the shorter, peripheral neurite. The residual 1.5 rotations are completed by the central process located in the modiolus of the analyzed specimen. Spirality of the peripheral process decreases systematically as far as 45° for

fiber bundle apical 7. Interestingly, the described rotation of about 540° by the central processes was found in all traced apical samples which is due to the helical nature of the nerve fibers in the modiolus until they leave the fundus region.

Middle Turn

Only the peripheral processes of fiber bundles middle 1 and 2 show slightly rotational character of about 45° and 30° respectively. The peripheral neurites of the remaining samples (middle 3 – 9) run quite linear from the sensory epithelium to the RC. However, all their central processes show again spiraling pathways of about 270° - 360° about their own axis before leaving the fundus region.

Basal Turn

All segmented nerve fiber bundles belonging to the basal turn run linear from the OC following the lamina spiralis to their perikarya located in the RC. Traced samples basal 1 – 6 show spiral characteristics of the central processes of about 180°. By contrast, fiber bundles basal 7 – 14 show fan-shaped pathways on their way from the RC to the N. cochlearis acusticus.

7.4.5 Cochlear Implant Electrodes

FLEX^{SOFT}

The first, most basal electrode of this routinely implanted CI stimulates SGNs located at 13.5 kHz (

Table 7.3). Eight out of twelve electrodes are located within the basal region of this cochlea. The eighth electrode (counted from shaft to electrode tip) stimulates cochlear neurons that are excited at around 1.5 kHz (

Table 7.3). The remaining four electrodes of the array stimulate frequency regions in the middle turn ranging from about 1.1 kHz down to 355 Hz within a sensory epithelia length of 7.5 mm representing about 18.5% of total cochlear length. Considering additionally the basal turn, the entire electrode array covers about 68% of the whole length of this inner ear by direct stimulation which means that every electrode on the array is responsible for stimulating its specific frequency band. However,

Table 7.3 reveal that the apical seven as well as the first two reconstructed fiber bundles from the upper middle turn are not stimulated using this direct, spatially and temporally-coded approach (compare with Table 7.2). Consequently, no electrode is located within the apical portion and for frequencies <430 Hz respectively (Figure 7.6), of this analyzed sensory organ.

Contour Advance

This CI has its first, most basal electrode positioned at a frequency of ~7260 Hz (Table 7.3) which roughly corresponds to electrode number three and four of the FLEX^{SOFT} array. The distance from this point, back to the beginning of the RC housing cell bodies of SGNs was measured to be 1.35 mm. The following 21 electrodes stimulate frequencies up to about 300 Hz which corresponds to the most upper middle turn region of reconstructed specimen 1 (Figure 7.6). The distance of this most apical electrode to the end of the RC was measured to be 2.03 mm. Note the high number and closely spaced electrode positions stimulating the upper basal- and middle turn region!

Electrode number	FLEX ^{SOFT}		Electrode number	Contour Advance	
	distance apex to electrode [mm]	stimulation frequency [Hz]		distance apex to electrode [mm]	stimulation frequency [Hz]
12	10,375	429	22	2,480	297
11	12,775	621	21	2,945	320
10	15,175	877	20	3,500	350
9	17,575	1219	19	4,018	382
8	19,975	1674	18	4,577	420
7	22,375	2282	17	5,157	468
6	24,775	3093	16	5,742	520
5	27,175	4174	15	6,330	583
4	29,575	5617	14	6,975	658
3	31,975	7542	13	7,636	748
2	34,375	10109	12	8,297	854
1	36,775	13533	11	8,972	990
			10	9,613	1127
			9	10,281	1318
			8	11,008	1543
			7	11,681	1820
			6	12,405	2155
			5	13,128	2586
			4	13,838	3171
			3	14,561	3936
			2	15,335	5065
			1	16,254	7261

Table 7.3: Summary of the electrode positions along the cochlea spiral of both investigated CIs. The corresponding frequency positions for the FLEX^{SOFT} array were calculated using the Greenwood function (Greenwood 1961, 1990) whereas the frequencies for the perimodiolar located Contour Advance CI was determined by an mathematical formula developed by Stakhovskaya et al. (2007).

In order to analyze the effect on neuron excitability of both CIs, two comparable active electrode positions of each array were selected from the basal turn and the middle turn region which represents the apical end of both devices. Figure 7.6 illustrates the investigated electrodes in blue color. Both basal electrodes (electrode 4 of FLEX^{SOFT} and electrode 5 of the Contour Advance CI) are in close proximity to traced fiber bundle basal 11 (highlighted by the white arrow head) which represents the 7.5 kHz region. The apical end of the active electrode arrays of both CIs is represented by of electrode 21 of the perimodiolar and electrode 11 of the deep insertion bionic implant which are located in the immediate vicinity of traced fiber middle 5 (yellow arrow head). This neuron belonging to the middle turn region transmits APs from about 520 Hz. Together with its basal counterpart, these neurons are expected to obtain the maximum voltage of the active electrodes.

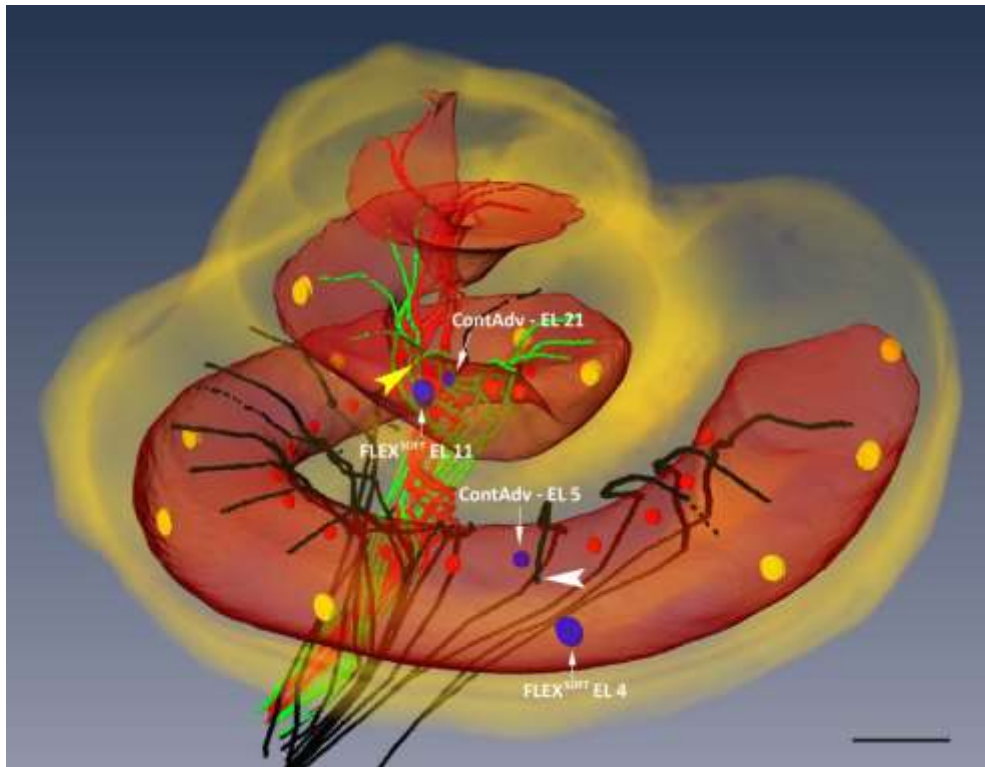


Figure 7.6: Visualization of the modeled electrode positions along the cochlea spiral. Image presents the manually segmented *S. tympani* (transparent red), the traced apical (red), middle (green) and basal (black) turn nerve fiber bundles. Yellow-colored and located within the *S. tympani* are the electrodes of the mimicked deep insertion CI FLEX^{SOFT} while electrodes belonging to the Contour Advance array are illustrated in red. The analyzed electrodes from the basal- and the middle turn of both arrays are presented in blue. Basal fiber bundle number 11 (white arrow head) which represents the 7.5 kHz region was determined to be the closest to analyzed basal electrode positions of both arrays. Its respective counterpart is represented by middle turn fiber number 5 which transmits electrical signals from about 520 Hz. Scale bar = 1 mm.

7.4.6 Distribution of the electrical potential based on FE-Analysis

In a first step, the electrical potential distribution within the developed human cochlea model was calculated for monopolar stimulation with four different active electrode positions as visualized blue-colored in Figure 7.6 (marked by white arrows). Each model was computed in consideration of the defined boundary conditions, i.e. (i) the surface potential of the bony cuboid enclosing the cochlea was set to 0V and (ii) the active electrode was set to 1V.

Basal turn

The potential distribution of the analyzed basal electrode 4 of the deep insertion CI is visualized in Figure 7.7A together with the surface grids of the modeled compartments. This stimulating electrode is situated on the lateral wall of *S. tympani* which facilitates electrical potential spreading due to its highly conducting fluid content in apical- and basal direction. Besides, the lower conductivity of the modiolus compartment which comprises the lamina spiralis restrains the electrical potential to spread further into above located *S. vestibuli* and *media* respectively. Since the electrode is modeled just beyond the OC at the lateral wall of ST, the nearest neuron (basal 11) is the most influenced and feels the maximum electrode voltage (EV) of 704 mV at the peripheral terminal which is only 0.6 mm away. The distribution of the electrical potential along this reconstructed nerve fiber bundle as well

as for other selected neurons is shown as a function of neuron length in Figure 7.7B. Traced fiber bundles basal 11 as well as its adjacent neighboring basal neurons show a second voltage peak around their somatic region (note the varying length of the peripheral processes) or even their maximum at regions where they enter the RC close to the medial wall of ST. Neurons at the opposite represented by the lower middle turn region are exposed to a maximum of about 40% EV. This value decreases to about 33% reaching the peripheral terminal of neuron apical 1. Apical 1, the most apical traced neuron, receives the maximum EV (436mV) at its central process after about 7.2 mm which correlates with the minimum distance to the active electrode (3.54 mm). The reason for the peak EV quite far from the somatic region of this neuron can be found in the spiral character of apical SGNs.

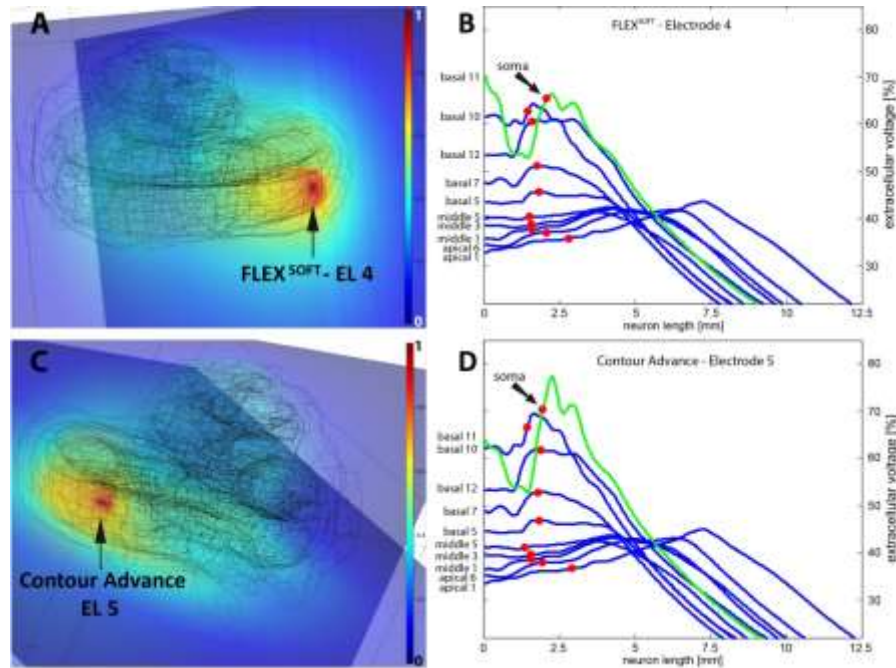


Figure 7.7: Visualization of the electrical potential distribution of active CI electrodes located in the basal turn computed with the Finite Element Method. Electrode 4 of the deep insertion CI (A) is placed on the lateral wall of ST. The resulting distribution of the extracellular voltage along selected manually traced SGN pathways is shown in (B) as a function of neuron length. The fourth electrode is located just beneath the peripheral terminal of fiber bundle basal 11. Electrode of the perimodiolar CI is close to the medial wall of S. tympani (A) where fiber bundle basal 11 is again closest (D) which is illustrated by the resulting voltage distribution along reconstructed fibers. Green lines (B,D) represent the neuron which feels the maximum of the electrode voltage; Colorbars (A,C) represents calculated voltages by finite element analysis.

Figure 7.7C presents the calculated distribution of the electrical potential induced by the fifth electrode of the perimodiolar electrode array. This electrode is again situated within ST which is a good voltage conductor due to its high conductivity. Since this electrode is modeled at the medial wall of this fluid filled cavity, right next to the RC, traced fiber bundle basal 11 (Figure 7.7D) shows its highest felt EV of 772 mV at the central process about 300 μ m next to the unmyelinated cell soma. The distance between this point along the neuron and the electrode was determined at 0.41 mm. The farther apical a neuron is located the lower the EV along the traced neuronal pathways. Again, the first traced apical fiber shows its maximum extracellular potential (445 mV) in the central process with a distance of 2.19 mm to electrode 5 of the perimodiolar CI. However, the voltage profiles of the vast majority of the analyzed fiber bundles (except basal 11 and basal 10) are not significantly influenced by the different electrode positions in the basal turn of the two CIs.

Middle turn

To analyze the consequences of electrical stimulation within the middle turn we calculated two FE-models each with the penultimate electrode of the deep insertion- and the perimodiolar electrode array respectively. The resulting voltage distribution of electrode 11 of the FLEX^{SOFT} CI is visualized in (Figure 7.8). As in the basal turn, this electrode is also located close to the lateral wall of S. tympani beyond the OC. As a result, the distance to the peripheral terminals of the surrounding basal neurons is smallest resulting in the maximum extracellular potential at this first unmyelinated compartment. As described in the basal turn, the fluid filled ST ensure again that the voltage spreads further in apical- and basal direction whereas the voltage propagation is restricted by the lamina spiralis to the other fluid filled cavities. The resulting voltage profiles along selected reconstructed neurons are again presented as a function of neuron length in Figure 7.8B. Due to the position of the electrode, the closest neuron (middle 5) is only 0.22 mm away and receives the maximum EV at its peripheral terminal (809 mV). Interestingly, the more apical situated neuron middle 3 feels the maximum of the applied electrical potential (618 mV) in a distance of 2.87 mm from the peripheral terminal. The reason for this can be explained by the spiraling pathway of middle- and apical turn neurons towards the central spindle. This spiral characteristics brings the neuron quite close to the active electrode (0.79 mm) ensuring the maximum extracellular voltage of neuron middle 3 at the level of the electrode. Least effected by the middle turn electrode are the basal fibers which get maxima around 40% on their central process.

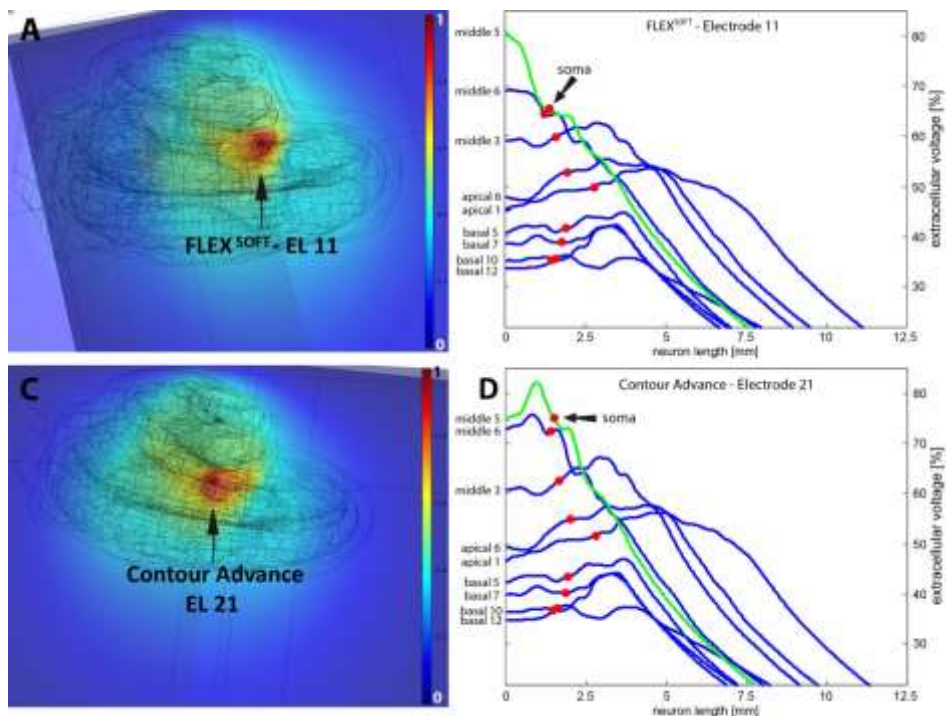


Figure 7.8: Visualization of the electrical potential distribution of active CI electrodes located in the middle turn. The electrically stimulated cochlea induced by Electrode 11 of the FLEX^{SOFT} deep insertion CI is presented in (A). The resulting voltage profiles of selected neurons along the cochlea spiral are illustrated in (B) as a function of neuron length. The potential distribution within the cochlea provoked by electrode 21 from the perimodiolar electrode array is presented in (C). For this electrode, the extracellular potentials along traced nerve fiber bundles are plotted in (D). Green lines (B and D) represent the neuron which feels the maximum of the electrode voltage; Colorbars (A,C) represents calculated voltages by finite element analysis.

The same situation is visualized for the second last electrode of the perimodiolar electrode array. Located close to the medial wall of the perilymph filled ST the applied voltages are higher at the lateral wall of the RC compared to the peripheral terminal. As a consequence, reconstructed fiber bundle middle 5 gets the maximum extracellular voltage of 819 mV after 0.82 mm on the peripheral process. At this point, the distance to the active electrode was evaluated to be only 0.25 mm. As stimulated by electrode 11 of the deep insertion CI, neuron middle 3 shows the same voltage profile but has a higher maximum of about 9% (671 mV) at the same location. As it was the case in the basal turn, the voltage profiles of the majority of neurons induced by the two analyzed electrode positions (Figure 7.8A and B) in the middle turn are quite the same without any considerable difference.

7.4.7 Finite Element Solution vs. Homogenous Medium Solution

Figure 7.9 presents the resulting extracellular potentials (V_e) calculated with the FEM and for the homogeneous case along the most excitable neurons stimulated by four different electrode positions (see Figure 7.6) within ST. The top graph in Figure 7.9A presents V_e of basal neuron 11 calculated with the FEM which takes five different compartments each with varying conductivity into account. The neuron is stimulated by electrode 4 of the deep insertion CI resulting in a maximum EV of 704 mV at the peripheral terminal which is located in closest distance. A second voltage peak appears 80 μm after the soma center representing the unmyelinated presomatic compartment featuring a total length of 100 μm . Yet another peak arises again at the central process in both calculated solutions 760 μm after the somatic center. At these regions, the fiber bundle proceeds in close proximity to the lateral wall of the RC resulting in higher EVs at these parts due to lesser attenuation of the applied voltage spreading in the perilymph filled ST. The subjacent plot illustrates the calculated voltage profile of the same neuron though it is located within a homogeneous medium possessing constant resistivity. In this assumption, the resulting electrode voltage along the neuron is inverse proportional to the distance to the electrode. Hence, the peripheral terminal of basal neuron 11 feels the maximum voltage of 401 mV which is 43% smaller than determined by the finite element solution. Contrary to the inhomogeneous case, the extracellular potential along the peripheral process decreases rapidly until the neuron enters the RC. The second peak in this profile appears where the neural pathway slightly turns closer to the electrode.

V_e of the same basal electrode but stimulated with the fifth electrode of the perimodiolar located electrode array is illustrated in Figure 7.9B. Due to the electrode position close to the medial wall of ST, the closest point along the reconstructed neuron is about 230 μm after the cell soma on the central process where the maximum voltage was determined by the FEM (772 mV) as well as for the homogeneous medium assumption (622 mV). However, the resulting maximum value calculated with constant resistivity is 19.4% below the computed finite element solution. Again, a second peak appears along the central process 966 μm after the soma where the neuron comes a little closer to the electrode.

The most excitable neuron stimulated each with the second to last electrode of both simulated CIs, is the middle turn neuron number 5. Stimulation with the FLEX^{SOFT} electrode 11 (Figure 7.9C) results in a maximal EV of 809 mV for the finite element solution, while 678 mV were determined for the homogeneous case. This represents a difference of 16%. The peripheral terminal of this traced cochlear neuron is closest to the voltage source and therefore obtains most of the electrical potential in both cases. Due to the electrode location close to the lateral wall of ST, the computed extracellular potential at the basis of the homogeneous assumption decreases continuously until a second peak appears 844 μm after the soma center.

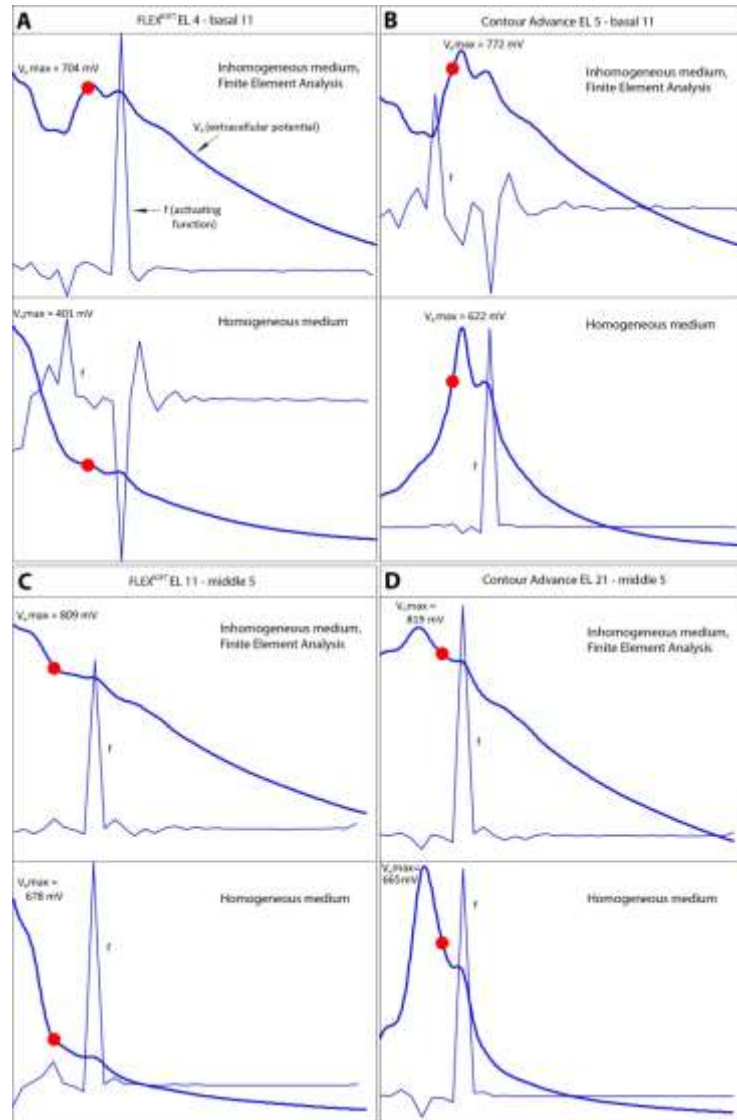


Figure 7.9: Comparison of the extracellular potential (V_e) at neuron basal 11 and middle 5 under different assumptions. The finite element solution for the most excitable neuron basal 11 stimulated by electrode 4 ($V_{\text{electrode}} = 1V$) of the FLEX^{SOFT} CI is presented in the graph on the top of (A). Subjacent plot illustrates the extracellular potential along the same neuron but within a homogeneous medium with constant electrical resistivity ($\rho_e = 300 \Omega \text{ cm}$). The comparison of the solutions regarding the most excitable neuron is presented for the FLEX^{SOFT} electrode 11 and neuron middle 5 in (B), (C) shows the reaction of basal neuron 11 stimulated by the perimodiolar located Contour Advance electrode 5 while (D) illustrates the excitation profiles of neuron middle 5 stimulated by the Contour Advance CI electrode 21. All illustrated cases include pictures of the calculated activating function (f). Red spheres indicate the position of the cell soma along the neurons in all plots.

Excitation of the same neuron with electrode 21 of the perimodiolar situated electrode array (Figure 7.9D) results in quite different voltage profiles in both assumptions compared to the respective electrode of the deep insertion CI (Figure 7.9C). The FEM predicts the maximum electrode voltage (819 mV) along the peripheral process about 525 μm before the middle of the cell soma. As before, a second peak appears for the in- as well as the homogeneous cases 200 μm after the somatic center on the central process due to the reconstructed neural pathway through the RC. At the same position

along the peripheral process of the neuron, 665 mV were predicted based on the homogeneous assumption representing a 17.8% lower value compared to the finite element solution. Based on the electrode – V_e max distance relation, the homogeneous solution shows generally a steeper decreasing profile in both, peripheral- and central directions.

7.4.8 Compartment Model Analysis

In order to study the influence of both CIs pursuing different implantation strategies on selected human cochlear neurons, the 3D data of the target neurons which received the maximum of the EV were implemented in our adapted compartment model. Their neuronal answer to microstimulation was tested with four stimulus signals. Parameters like the activation threshold, the spike IS and various temporal parameters were determined and recorded.

Normal Fibers

Basal Turn

As presented in Figure 7.7B and D, traced cochlear neuron basal 11 which is located at the 7.5 kHz region receives the maximum EV from both CIs. The peripheral process of this neuron has a length of 2.075 mm (see Table 7.2) which was modeled with an unmyelinated peripheral terminal (Figure 7.10A and C, cyan colored), ten active nodes (green spheres) and ten passive internodes (red lines) followed by the unmyelinated somatic (yellow colored) which consists of three active compartments (pre- and post somatic region and the cell somata). Note that the soma has constant diameter ($d_{\text{soma}} = 20 \mu\text{m}$) in all conducted simulation trials. The central process with a reconstructed length of 7 mm was, together with all other traced neurons, extrapolated in running directions to a common plane which ensures better comparison of the determined ETs.

All four stimulus pulses generated by electrode 4 of the deep insertion electrode array initiate the spike in the unmyelinated peripheral terminal (distance EL to IS = 0.6 mm) of the analyzed target neuron basal 11 (Figure 7.10A). The temporal changes of the membrane potential along the reconstructed neuron are presented in (Figure 7.10B). The activation threshold for stimulation with a 100 μs long cathodic pulse requires a current of -24.1 μA (Table 7.4) which causes the spike onset 0.386 ms after firing. Stimulation of the basal neuron using a BIC stimulus accelerates spike initiation of 9.3% (after 0.36 ms) at the same IS. The threshold for monophasic anodic stimulation was determined with a current of 38.3 μA which is 55% higher compared to CAT stimulus. Compared to the monophasic CAT pulse, AP initiation needs 1.55 times longer with ANO pulses resulting in a recorded PT of 0.596 ms. The corresponding biphasic pulse (anodic first) requires a minimum current of 24.9 μA to generate a AP and possesses the same PT as stimulated with a monophasic anodic pulse. The AP was initiated at the first compartment with both stimulation pulses (ANO & BIA, Table 7.4).

Extracellular stimulation of the target neuron by the fifth electrode of the perimodiolar CI cause AP initiation at compartment 11 (=postsomatic compartment) for CAT (distance to EL = 0.48 mm) and compartment 1 for ANO, BIC and BIA pulses (distance to EL = 1.38 mm) which are all located peripherally (Figure 7.10C). Contrary to the deep insertion case, the threshold for CAT, BIC and BIA configurations increase highly significant ($p < 0.001$) with the perimodiolar approach even though its close location to the medial wall of ST. Furthermore, the recorded PTs of these three stimuli configurations tend to be additionally increased. However, no significant difference was determined ($p > 0.05$). The temporal changes of the membrane potential induced by four different stimuli configurations which were subsequently applied via the stimulating electrode along the reconstructed neuron are presented in Figure 7.10D.

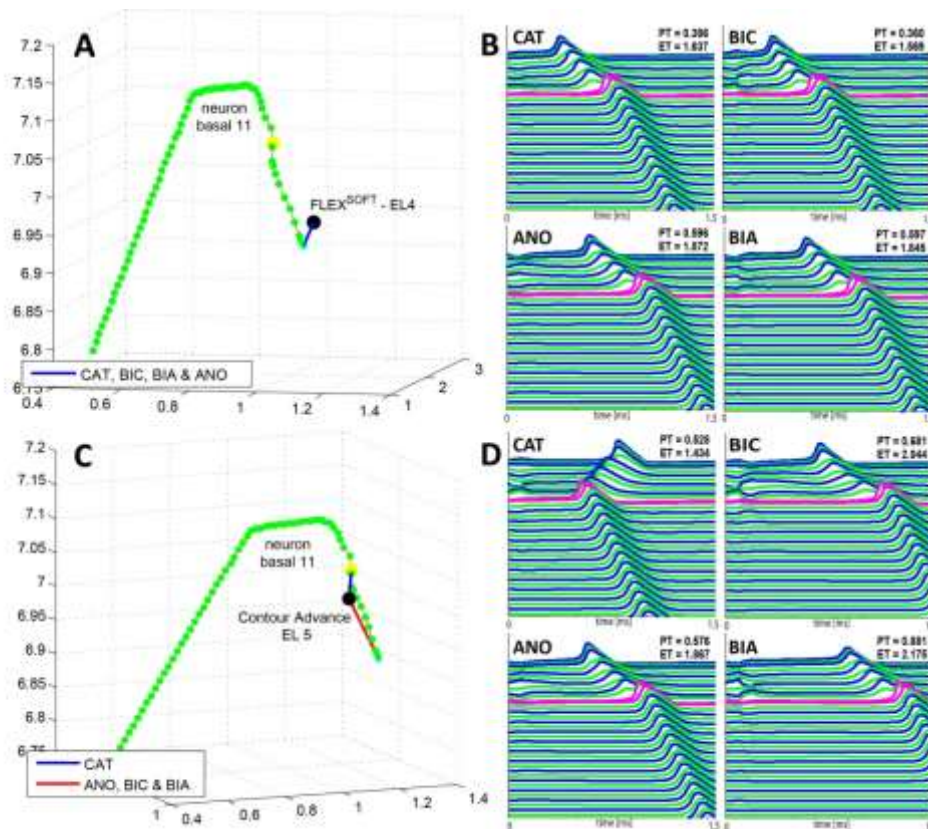


Figure 7.10: Compartment model of neuron basal 11 and temporal parameters of its answer after microstimulation. (A) and (C) visualize the partitioning of the target neuron in active nodes (green spheres), passive internodes (red lines) and the unmyelinated cell soma. The peripheral terminal (cyan colored) is modeled active with a length of 10 μm . Black spheres illustrate the active electrodes from where the blue and red lines depict the IS induced by varying stimulus configurations. (B) and (D) present the travelling APs induced by the tested four different pulses triggered by a deep insertion and a perimodiolar located CI. Each line of the plots represents the temporal change of the transmembrane potential along the reconstructed neuron. Blue lines illustrate nodes while green lines visualize the temporal answer of the internodes. The unmyelinated somatic region is presented in pink color.

To activate the target neuron via CAT pulse requires 65% more electric current ($-39.7 \mu\text{A}$, Table 7.4) compared to EL4 of the deep insertion CI although the distance between the electrode and IS is 0.12 mm (-20%) shorter with the perimodiolar approach. Spike onset was also delayed resulting in a +39% (PT = 0.529 ms) increase. The corresponding current thresholds for BIC and BIA impulses were elevated for 25% ($-36.7 \mu\text{A}$) and 40% ($34.9 \mu\text{A}$) respectively. Their recorded PT was additionally delayed compared to the deep insertion case. The AP triggered by the BIC pulse was initiated after 0.681 ms which represent an increase of 89%. For the BIA configuration, the PT at the first compartment was recorded 0.881 ms (+48%) after the electrode fired. Stimulating the target neuron with a monophasic anodic pulse requires a current of $33.9 \mu\text{A}$ which is 11% less compared to EL4 of the deep insertion CI. Also the PT slightly decreased to 0.576 ms which results in a 3.5% earlier spike onset with the perimodiolar CI.

For all simulated cases within the basal turn, the initiated spikes travelled orthodromically over the soma to the central end of the traced cochlear neuron basal 11 which is visualized by the plots in Figure 7.10B and D.

Middle turn

Figure 7.8B and D illustrates that the reconstructed neuron middle 5 feels the maximum of EV from both electrode positions. The length of the peripheral process of this neuron representing a frequency of about 530 Hz along the cochlea spiral was determined to be 1.345 mm (see Table 7.2). The unmyelinated peripheral terminal (cyan color) is followed by six passive internodes (red lines) and six active nodes (green spheres). The unmyelinated cell soma of this middle turn neuron is again shown in yellow (Figure 7.10A and C). The central process was also extrapolated to the same plane as done with neuron basal 11.

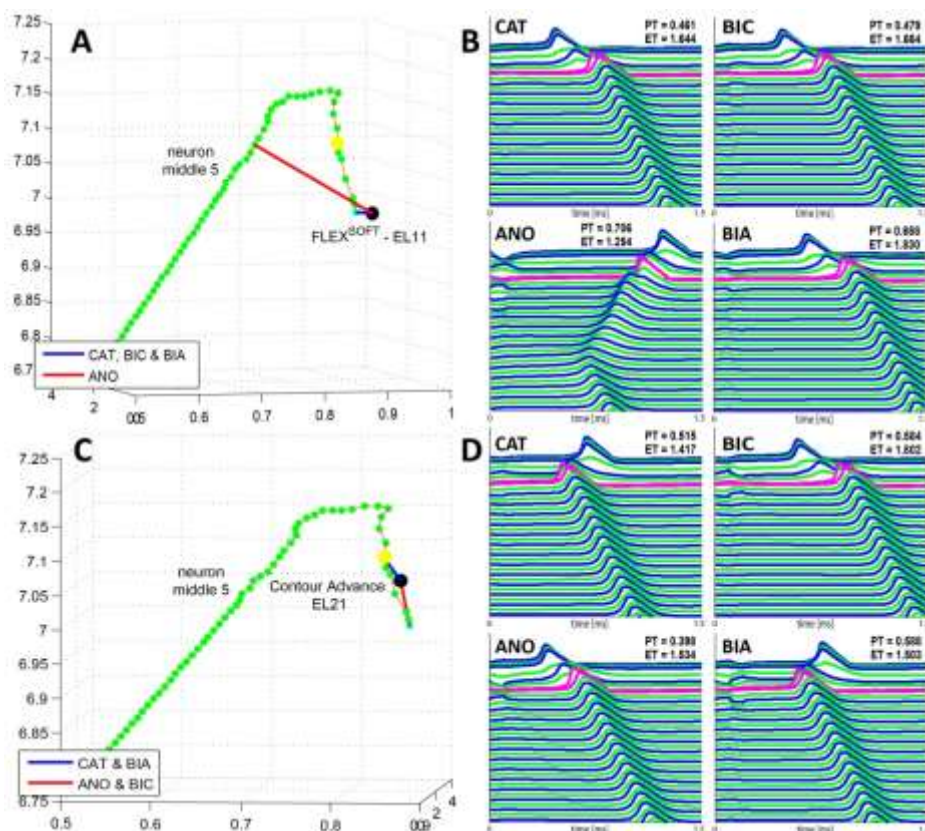


Figure 7.11: Reconstructed neuron middle 5 and its answer to four different stimuli pulses after microstimulation. (A) and (C) illustrate the neuron which is split up in active nodes (green spheres), passive internodes (red lines) and the unmyelinated soma (yellow sphere). The active electrodes of both CIs are represented by the black spheres where the blue and red lines depict the IS induced by varying stimulus configurations. (B) and (D) present the travelling APs along the neuron induced by different four different pulses triggered by a deep insertion and a perimodiolar located CI. Each line of the plots represents the temporal change of the transmembrane potential along the reconstructed neuron. Blue lines illustrate nodes while green lines visualize the temporal answer of the internodes. The unmyelinated somatic region is presented in pink color.

When stimulating the neuron via electrode 11 of the deep insertion CI with CAT, BIC or BIA configuration, the AP at threshold level is induced at the peripheral terminal of the neuron while an

ANO pulse triggers the AP at compartment number 27 (=central node 18) of the neuron (Figure 7.10A). The distance between the active EL11 and IS were 0.352 mm to the first compartment and 3.94 mm to compartment 27 located at the central process.

The activation threshold for a monophasic cathodic pulse was evaluated at $-37.7 \mu\text{A}$ (Table 7.4) with AP generation after 0.461 ms of firing (Figure 7.10B). Biphasic stimuli configurations BIC (PT = 0.479 ms) and BIA (PT = 0.658 ms) required with $-50.6 \mu\text{A}$ and $59.8 \mu\text{A}$ higher currents to generate an AP at the first compartment of the neuron. The by far highest current of all trials were needed to successfully generate an AP with monophasic anodic stimulation. $210.1 \mu\text{A}$ were necessary for its generation at the central process. Note that the corresponding PT was with 0.706 ms also quite long (second longest of all trials).

Stimulating the target neuron belonging to the middle turn with monophasic CAT and biphasic BIA pulses cause AP generation at compartment 7 (Figure 7.10D) which represent the unmyelinated postsomatic process. The necessary threshold current for the CAT stimulus was determined at $-43 \mu\text{A}$ which corresponds to an increase of nearly 14% compared to the second evaluated electrode position. Additionally, the time which elapses between electrode firing and AP initializing was determined to be 11.7% longer (PT = 0.515 ms) with the perimodiolar electrode. For a BIA pulse, the threshold was determined at $61.3 \mu\text{A}$ which is slightly more (+2.4%) compared to the other CI. With this stimulus pattern, the resulting AP is initiated 10.6% earlier (PT = 0.588 ms) compared to the deep insertion CI.

The active electrode in perimodiolar position needs only 42.2% ($88.6 \mu\text{A}$) of the current required by the second CI for AP initiation with an ANO stimulus. Due to the much closer position of the IS, the AP is generated 43.6% earlier (PT = 0.389 ms). With $-51.6 \mu\text{A}$, the threshold for BIC pulse is quite similar (+1.9%) to that necessary for initializing an AP via the deep insertion electrode array. Its PT was recorded at 0.584 ms which is 21.8% longer compared to EL4 of the deep insertion CI. As for the investigated basal region, the initiated spikes travelled orthodromically to the central end of the traced cochlear neuron middle 5 in all trials.

In general, slightly more current is needed to stimulate healthy cochlea neurons with electrodes in perimodiolar position using CAT, BIC and BIA configuration (Table 7.4). However, there was no significant difference found in current strength between the two electrodes positions located within the middle turn.

7.4.9 Comparison with Degenerated Neurons

In order to quantify the difference on activation currents, resulting IS and recorded temporal parameters between normal healthy and degenerated neurons, the most excitable neurons basal 11 and middle 5 were modeled without their peripheral process. Therefore, both neurons started with the unmyelinated soma, followed by the postsomatic compartment and the thick central process leading to their central terminal which ends in the same plane as in the normal healthy case. This enabled to record comparable ETs for both microanatomical conditions which illustrate changings in the temporal fine structure between these naturally occurring cases. Table 7.4 presents the results for both simulated cases:

Besides one case (EL11 – mid5, ANO), much more current is needed with all studied stimuli pulses to activate the correspondent nearest degenerated fiber. This is in particular the case for the investigated FLEX^{SOFT} electrode 4 located in the basal region. Due to the increased distance to the first compartment, a CAT pulse needs about 145% more current to generate an AP initiated at the soma (Table 7.4, IS=1=soma) compared to the healthy case. The maximum increase in all trials was

determined for neuron activation with a BIA pulse which requires more than five times the current compared to the normal neuron. The second most increase of all trials denotes stimulation of the degenerated fiber basal 11 with monophasic anodic current. In this configuration, an increase of 400% is needed to generate an AP at the soma which constitutes the first compartment. Activation of the neuron by a BIC pulse needs 215% more current compared to the normal case.

Stimulation of the same tested neuron though using the perimodiolar approach offered by the Contour Advance CI needs significantly lower currents ($p < 0.001$) for neural activation compared to the deep insertion CI. However, currents of all four stimuli configurations must be increased to activate the target neuron compared to a healthy auditory neuron. A monophasic cathodic pulse needs 26% higher current and a BIC pulse a 90% increase to successfully excite the neuron. As observed with electrode 4 of the deep insertion CI, AP generation by an anodic-involved pulse (ANO: 272%, BIA: 192%) requires again the highest increases in this setting.

Due to the narrowing scalae until the middle turn region, increasing a monophasic cathodic pulse for 56% is sufficient to activate the target neuron middle 5 by electrode 11 of the FLEX^{SOFT} CI. As already pointed out above, the ANO pulse is the only one in all settings where a reduction of the current (-19%) is sufficient to ensure that an AP is transmitted to the CNS. Interestingly, a biphasic pulse with a leading anodic phase needs a proportionally high increase of 162% followed by a BIC pulse that requires an increase of 88% for threshold activation of the analyzed neuron.

The position of electrode 21 close to the RC of the Contour Advance CI ensures the lowest average increase of the investigated positions. Only a 13% higher stimulus is required to activate the degenerated neuron middle 5 by a CAT pulse followed by an ANO and BIC pulse each with an increase of 27% compared to the normal healthy case. A biphasic pulse with an anodic leading phase requires 56% more current for threshold stimulation.

In addition, analysis of the recorded ETs suggests significant variations ($p < 0.05$) in the temporal fine structure of the transmitted neural code between normal- and degenerated neurons (Table 7.4). This is especially the case in the basal region stimulated by electrode 5 of the perimodiolar CI where the generated signals arrive by an average of 30.9%, which corresponds to 0.572ms, earlier compared to a stimulated normal neuron. Interestingly, this behavior was also observed in the middle turn which is stimulated by the 21st electrode. The position of the electrode is quite close to both modeled neurons though in the investigated degenerated case, an induced electrical signal with threshold current arrives 16.8% earlier the central end. The corresponding value for the degenerated fiber basal 11 stimulated by electrode 4 of the deep insertion array was determined only slightly lower at 15.4% which represents a 0.267ms earlier arrival. Activation of the degenerated fiber middle 5 by electrode 11 of the same array located in the middle turn, which features generally shorter electrode-to-neuron distances, ensures that the AP reach 11% earlier the central terminal compared to the normal auditory neuron. Generally speaking, an AP induced in an analyzed degenerated neuron arrive the central end $18.4 \pm 8.4\%$ earlier compared to auditory neurons with an intact peripheral process

electrode array	active electrode	nerve fiber	fiber pathology	Stim. pulse	Threshold Current [μ A]	IS	PT [ms]	PS [ms]	ET [ms]	
FLEXSOFT	EL 4	bas 11	norm	CAT	-24,06	1	0,386	0,772	1,637	
			degen	CAT	-59,14	1	0,729	0,729	1,572	
			norm	ANO	38,28	1	0,597	1,004	1,872	
			degen	ANO	191,61	1	0,548	0,548	1,391	
			norm	BIC	-29,35	1	0,360	0,706	1,569	
			degen	BIC	-92,36	1	0,442	0,442	1,196	
			norm	BIA	24,88	1	0,597	0,980	1,845	
			degen	BIA	150,26	1	0,842	0,842	1,696	
	EL 11	mid 5	norm	CAT	-37,739	1	0,461	0,785	1,644	
			degen	CAT	-59,040	1	0,903	0,903	1,758	
			norm	ANO	210,085	27	0,706	1,081	1,254	
			degen	ANO	170,660	20	0,528	0,849	1,008	
			norm	BIC	-50,608	1	0,479	0,801	1,664	
			degen	BIC	-94,96	4	0,447	0,452	1,200	
			norm	BIA	59,825	1	0,658	0,965	1,830	
			degen	BIA	156,90	1	0,869	0,869	1,721	
	Contour Advance	EL 5	bas 11	norm	CAT	-39,68	11	0,529	0,581	1,434
				degen	CAT	-50,13	1	0,495	0,495	1,334
norm				ANO	33,87	1	0,576	1,002	1,867	
degen				ANO	126,09	10	0,384	0,552	1,073	
norm				BIC	-36,69	1	0,681	1,180	2,044	
degen				BIC	-69,88	4	0,392	0,449	1,155	
norm				BIA	34,85	1	0,881	1,311	2,175	
degen				BIA	101,79	1	0,817	0,817	1,669	
EL 21		mid 5	norm	CAT	-42,96	7	0,515	0,563	1,417	
			degen	CAT	-48,52	1	0,528	0,528	1,364	
			norm	ANO	88,56	1	0,398	0,644	1,534	
			degen	ANO	112,69	10	0,422	0,575	1,124	
			norm	BIC	-51,59	1	0,584	0,939	1,802	
			degen	BIC	-65,74	6	0,406	0,464	1,167	
			norm	BIA	61,27	7	0,588	0,641	1,503	
			degen	BIA	95,47	1	0,699	0,699	1,553	

Table 7.4: Threshold currents [μ A] and temporal parameters of most excitable neurons. Parameters are given for investigated electrode positions, varying stimuli configurations as well as for normal and degenerated human auditory neurons.

7.4.10 Excitation pattern of normal neuron population

In order to compare the neuronal answer of the traced auditory neurons to different stimulation pulses and intensities, all four analyzed electrodes (see Figure 7.6) were firing (i) a monophasic cathodic pulse with threshold current 1CAT, (ii) a monophasic anodic stimulus with 2*threshold 2ANO and (iii) again a monophasic cathodic pulse but this time with 3*threshold 3CAT.

Figure 7.12 illustrates the behavior of all reconstructed nerve fiber bundles (red spheres indicate soma position along the neuron) excited by basal-located electrodes of both mimicked CIs. The first row in Figure 7.12A allows for comparison of the membrane voltages V_m induced by electrode 4 of the deep insertion electrode array as a function of reconstructed auditory neuron length. As described above, neuron basal 11 is closest to the stimulating electrode and is the only one that is activated by a 1CAT as well as a 2ANO stimulus (Figure 7.12A middle). This neuron is most excitable at the peripheral process and its first compartments of the central process for both cases. However, excitation of the neuron steadily decreases in the central process with increasing distance to the electrode. Note that several other reconstructed basal neurons show subthreshold V_m reactions. Raising the stimulating pulse to 3-fold CAT threshold (Figure 7.12A, right plot) will activate several additional neighboring neurons from the basal turn (basal 14 - 9). All these neurons, which represent about 11.5 kHz – 4.5 kHz, send an AP initiated at the peripheral terminal of the peripheral process (data not shown) to the central nervous system. These six excited neurons show different excitation profiles and are most sensitive at the first about 3.5 cm length including the peripheral process, the unmyelinated somatic region and the first 3 - 4 passive compartments of the thicker central process.

The same situation is visualized by the three graphs in Figure 7.12B though the stimulating electrode was changed to electrode 5 of the Contour Advance CI pursuing perimodiolar-located electrodes. Compared to the deep-insertion FLEX^{SOFT} CI, a 1CAT stimulus is sufficient to activate two neurons (basal 11 and 10) simultaneously. The distance between them is about 1 mm and in both neurons, an AP is triggered at the unmyelinated somatic region (compare Figure 7.10D, CAT). If the electrode is firing a 2ANO strong stimulus, only the closest fiber basal 11 is triggered although several other basal neurons show again subthreshold reactions in their resulting membrane voltages V_m .

The infringement of the tonotopical principle was observed when stimulating auditory neurons with a monophasic 3CAT pulse induced by the perimodiolar-located electrode. Besides neuron basal 11, all traced fiber bundles situated between neuron basal 14 (~11.5 kHz) and basal 7 (~3.35 kHz) are excited to send APs to the auditory cortex. Due to the three dimensional pathways of middle turn neurons number 2 and 6, these two frequency regions are also activated by the 3-fold CAT threshold at the central process. However, all other reconstructed fiber bundles from the middle turn as well as basal fibers 1 to 6 are not firing (Figure 7.12B left) due to quite long distances between the electrode and the fibers and additionally because of the interjacent located modiolus compartment featuring lower conductivity that impedes the electrical potential in further spreading. Interestingly, all reconstructed apical fibers (representing frequencies ≤ 228 Hz) are successfully stimulated by the basal electrode with 3CAT current intensity. These neurons send electrical signals generated at their central processes (data not shown) to the auditory cortex. In total, 17 out of 30 neurons are activated by this evaluated configuration. However, neurons originating from the upper basal turn as well as the middle turn region remain unaffected and stay in resting state.

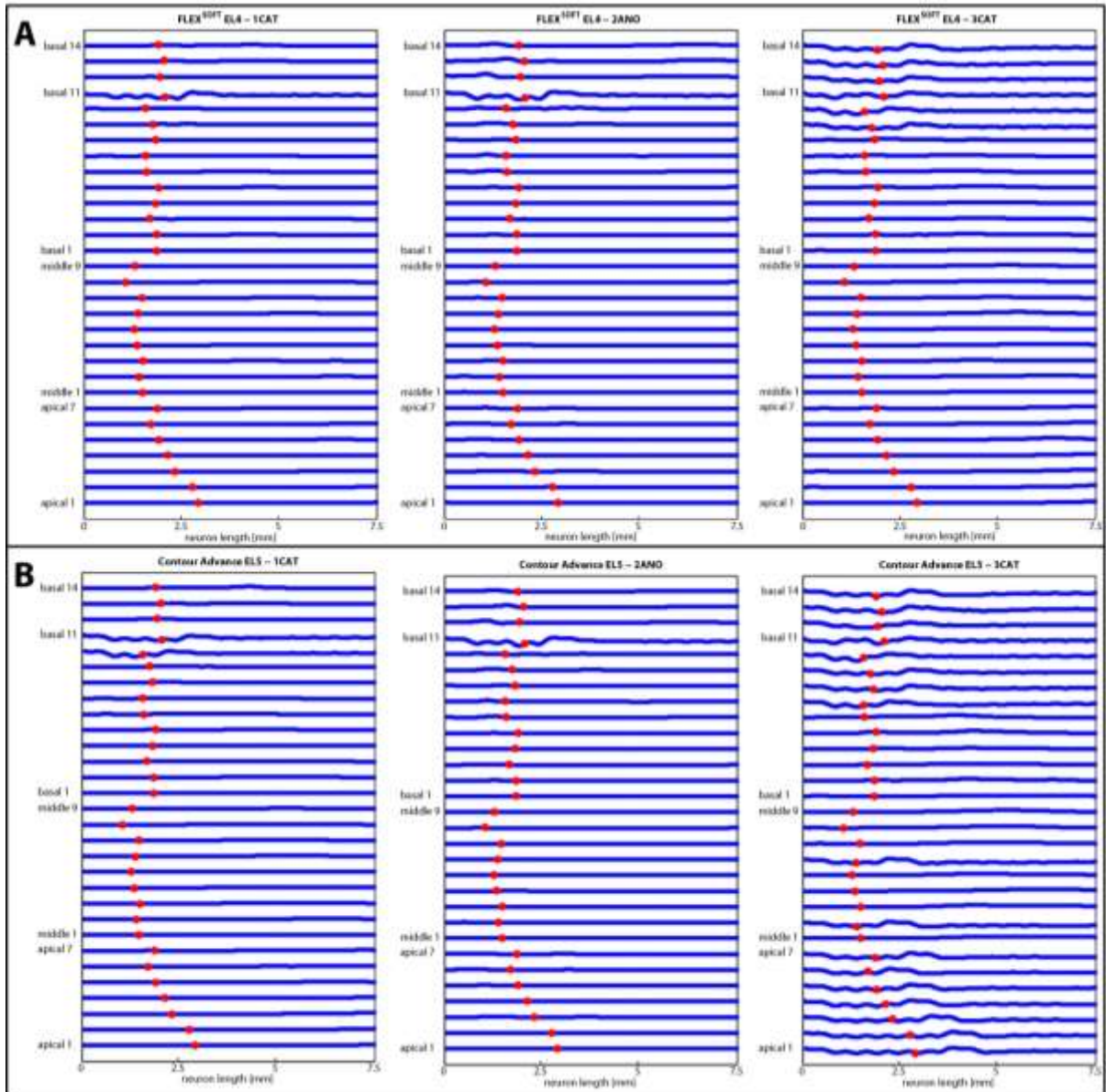


Figure 7.12: Membrane voltage V_m characteristics induced by middle turn electrodes. V_m is presented as a function of neuron length considering different stimuli pulses and current levels as well as varying electrode positions within the basal turn. The first row (A) illustrates the neuronal answer of all 30 traced neurons stimulated by basal located electrode 4 of the deep insertion electrode array excited by CAT threshold, 2-fold ANO threshold and 3-fold CAT threshold level. The second row (B) enables to compare the V_m of the same neurons but initiated by electrode 5 of the perimodiolar-located electrode array. Red spheres indicate the position of the soma along the reconstructed neurons.

The impact of varying but comparable electrode positions within the middle turn region is illustrated in Figure 7.13 in the same manner. Again, V_m is plotted as a function of neuron length for every of the 30 traced auditory nerve fiber bundles stimulated with different pulses and intensities by two different electrodes. Since electrode 11 of the FLEX^{SOFT} CI was determined in closest proximity to the traced middle turn neuron 5, only this neural structure is activated when the electrode is firing a monophasic CAT pulse at threshold level (Figure 7.13A, left). The AP is initiated in the peripheral

terminal which is in closest to the electrode (see Figure 7.10B, CAT). All other neurons are unaffected by this stimulus configuration. The very high determined threshold level (210.1 μA) needed to activate a neuron using a monophasic anodic approach is the reason why all traced neurons were activated using a 2ANO intensity level (Figure 7.13A, middle). All neurons were activated breaching the tonotopical principle at compartments belonging to the thicker central process which may be explained by closer proximity to the electrode.

The infringement of the tonotopical principle was additionally determined when stimulating the neurons with a 3-fold CAT pulse (Figure 7.13A, right plot). 21 out of 30 nerve fibers originating along all frequency regions are generating spikes for the central nervous system. Due to their long and spiral pathways, APs were generated in the central process of all activated apical fibers (number 2 and 4 – 7) while the vast majority of middle turn fibers (all except middle 9) were activated at the peripheral terminal. This was also the case for fibers basal 3 and 5 – 11 which are more or less subjacent-positioned from electrode 11 (see Figure 7.6). A 3CAT strong current was found to be sufficient to activate these neurons even through the modiolus compartment.

When stimulating the cochlea with the perimodiolar-located electrode within the middle turn using a single monophasic cathodic current level (Figure 7.13B, left plot), again, only the closest fiber middle 5 is successfully activated at the unmyelinated somatic region (Figure 7.10D, CAT). Increasing the stimulus current and changing the pulse to a monophasic 2ANO or a 3CAT configuration respectively, induces again the infringement of the tonotopical principle. At 2ANO (Figure 7.13B, middle) current level, one third of all analyzed neuronal pathways were activated mostly dominated by fiber bundles originating from the upper middle- and the lower apical turn (middle 5 and 1-3; apical 5 – 7) which are quite close to the current applying electrode. Due to its spiraling pathway, the central process of fiber apical 1 comes quite close to the electrode resulting in AP generation in the central process. Also fibers basal 9 and 10 which are located at a subjacent position in respect of the electrode are both successfully generating an electrical signal.

Increasing the stimulus to a 3CAT (Figure 7.13B, right plot) configuration, the vast majority of neurons (except neurons middle 9, basal 1, 2 and 14) is excited and spiking representing all frequency regions ≤ 9.5 kHz. Due to the close proximity to the electrode, the APs were all generated at the unmyelinated somatic region or on the central process (especially apical fibers) of the neurons.

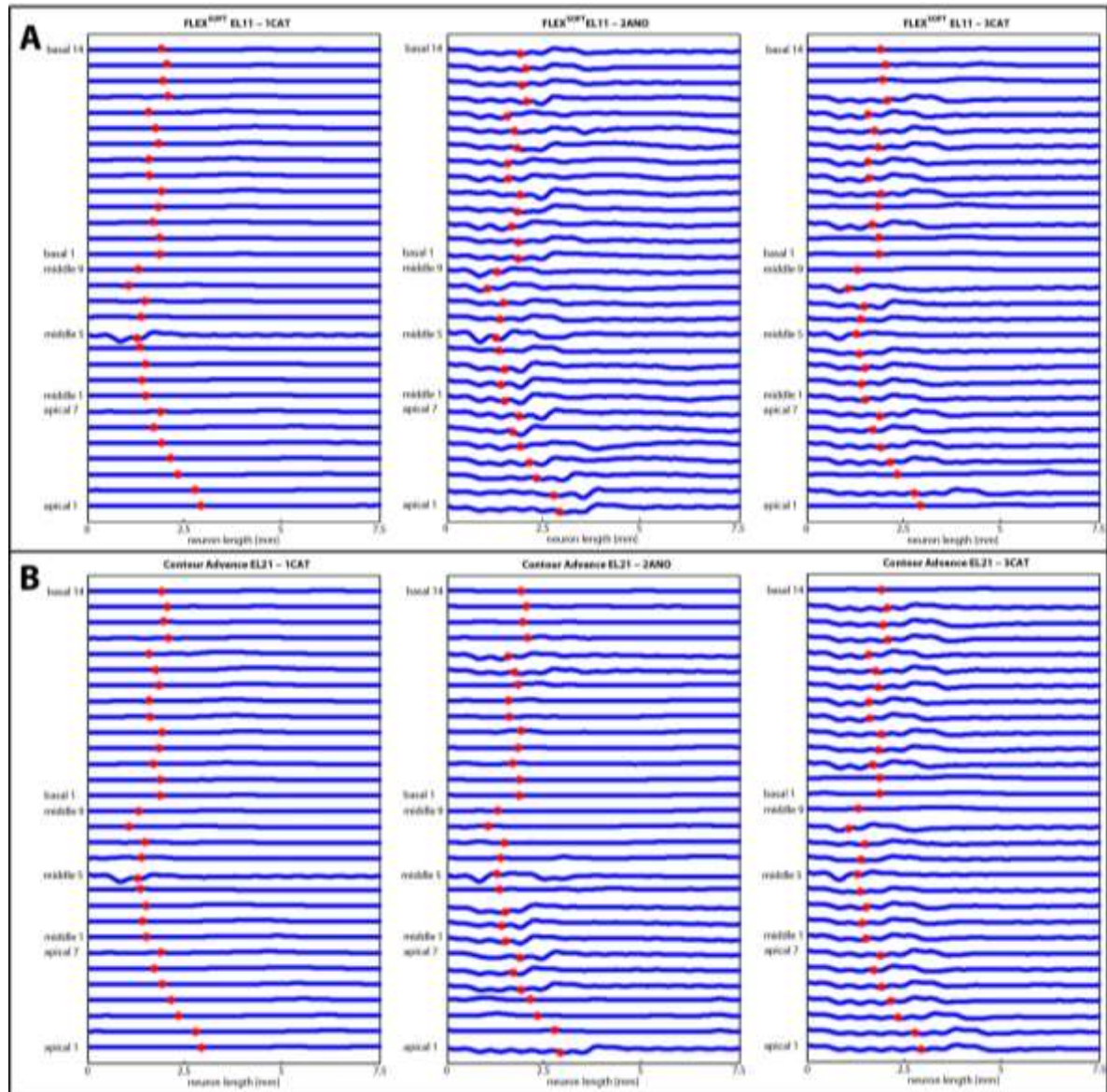


Figure 7.13: Membrane voltage V_m variations induced by middle turn electrodes. V_m is presented as a function of neuron length considering different stimuli pulses and current levels as well as varying electrode positions within the middle turn. The first row (A) illustrates the neuronal answer of all 30 traced neurons stimulated by middle turn located electrode 11 of the deep insertion electrode array excited by CAT threshold, 2-fold ANO threshold and 3-fold CAT threshold level. The second row (B) enables to compare the V_m of the same neurons but initiated by electrode 21 of the perimodiolar-located electrode array. Red spheres indicate the position of the soma along the reconstructed neurons.

7.4.11 Analysis of the normal apical turn

As described previously in the results section, especially the nerve fiber bundles reconstructed from the apical turn deviate from the usual quite linear pathways of SGNs belonging to the middle- and basal turn. The spiraled peculiarity in the thinner peripheral processes is most distinct with regard to reconstructed fiber bundles apical 1 and 2 (Figure 7.14A and compare Figure 7.5A - C).

In order to study the consequences of this spiraling characteristic, eleven electrodes were virtually positioned in the apical region of ST between 870° and 570° in respect of cochlea beginning (Figure 7.14A). Note that these assumed positions were not reached by one of the investigated electrode arrays. Afterwards, the electrodes applied various stimuli (again CAT, ANO, BIC and BIA) with fixed pulse duration of 0.1 ms but variable pulse amplitude. The evaluated thresholds needed to activate a fiber or a subpopulation respectively, is displayed in Table 5.4.

Electrode	CAT activates	Threshold [μA]	ANO activates	Threshold [μA]	BIC activates	Threshold [μA]	BIA activates	Threshold [μA]
el 1	apical 1	30	apical 1	30	apical 1	30	apical 1	35
el 2	apical 1	30	apical 1	35	apical 1	40	apical 1 apical 3	45
el 3	apical 1	50	apical 1	45	apical 5	55	apical 1	60
el 4	apical 1	40	apical 1 apical 5	55	apical 1 apical 5	50	apical 1	50
el 5	apical 1	40	apical 5	45	apical 5	40	apical 5	45
el 6	apical 1 apical 4 apical 5	45	apical 5	45	apical 5	45	apical 5	50
el 7	apical 4 apical 5 apical 6 apical 7	45	apical 7	45	apical 7	40	apical 5 apical 7	50
el 8	apical 5	40	apical 7	45	apical 7	40	apical 7	45
el 9	apical 5 apical 7	45	apical 7	45	apical 7	40	apical 7	45
el 10	apical 6 apical 7	40	middle 1	40	apical 6 middle 1	40	apical 6	45
el 11	apical 6	35	middle 1	45	apical 6	40	apical 6	40

Table 7.5: Most sensitive fibers in apical region. Presented are the determined thresholds [μA] necessary to excite apical fibers by electrodes at varying positions with different stimuli.

In all conducted trials, even a small amount of applied current cause activation of one neuron or several fibers parallel. Moreover, the most sensitive fiber is not necessarily the same for all four investigated stimulation types. The results presented in Table 7.5 additionally suggest that in some stimuli configurations non-neighboring reconstructed cochlear neurons were activated at threshold level which implies the infringement of the tonotopical principle. Threshold currents range from 30 to 60 μA whereas the vast majority of fibers are activated with a current between 40 and 45 μA.

When stimulating with electrodes located between 870° and 840° as well as between 720° and 540°, subpopulations of neighboring fibers were additionally activated as illustrated in Figure 7.12A (right plot) and Figure 7.12B (left plot). However, it was observed that the three electrodes between 810° and 750° also excite non-neighboring nerve fibers when firing with diverse stimuli configurations. Figure 7.14B illustrates as an example the temporal change of the transmembrane potential for traced fibers apical 1 and 5 after a 0.05 mA BIC stimulus of the electrode located at 780° was fired. Both fibers are activated showing different IS along the neurons: apical 5 is activated near the peripheral end, whereas apical 1 is excited at the unmyelinated presomatic compartment. Furthermore, this behavior of the mentioned two fibers was seen with several other stimuli configurations when only fiber apical 1 or 5 was stimulated. The varying IS along the investigated neurons cause additionally deviations in the durations of the APs need to reach the model end: in the presented case, the AP of apical 5 needs about a third longer than the one of apical 1 which features a 40% longer peripheral process (see Table 7.2).

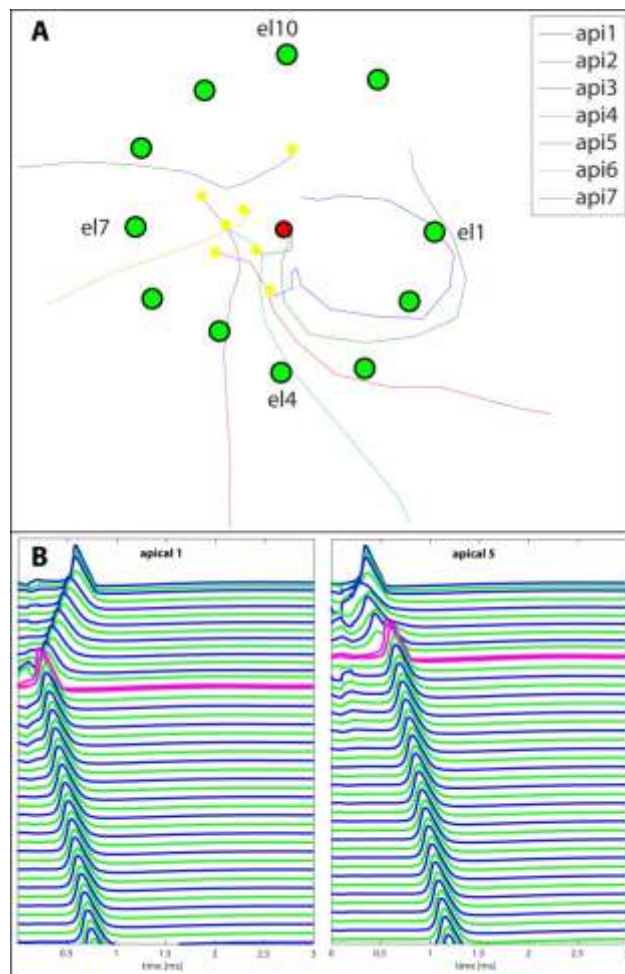


Figure 7.14: Evaluation of the spiral nature of apical fibers. A top view of the seven reconstructed fiber bundles (yellow spheres indicate the unmyelinated soma) is presented in (A) where the midmodiolar axis is represented by the red circle. Green spheres denote active electrodes whereas el1 is situated in the most apical, possible point (at about 870°) within the narrowing *S. tympani*. Subsequent electrodes were positioned every 30° along the lateral wall of *S. tympani* in basal direction until about 570° represented by el11. The excitation profile of apical fibers 1 and 5 is presented in (B). Both fibers were stimulated by the electrode at 780° with a 0.05 mA BIC stimulus. The unmyelinated somatic region is visualized in magenta.

7.5 Discussion

The main weakness of existing numerical models of the human cochlea and electrical circuit models of human auditory nerve fibers is the lack of anatomical precision of inner ear geometrical models and the unavailability of three dimensional pathways of the signal transmitting neurons through the hearing organ. Numerous numerical models were developed in consideration of simplifying assumptions of complex human cochlea geometry and fiber pathways in the past to investigate the relation of the electrode position, stimuli configurations and neural excitation pattern (Spelman et al., 1980; Black et al., 1983; Finley et al., 1990; Suesserman & Spelman, 1993; Frijns et al., 1995; Briaire & Frijns, 2005; Hanekom, 2001; Rattay et al., 2001b). However, simplification of cochlear geometry may impacts the spreading profile of the induced electrical potential by an active electrode. This is especially the case for the high-frequency regions due to reported non-uniform rise of the S. tympani within the basal turn (Cohen et al., 1996) which cannot be considered when reconstructing a human cochlea from a single 2D section.

This paper presents an anatomical accurate FEM of the human cochlea considering the coiled shape and its natural dimension used to calculate the distribution of the intracochlear electrical potential induced by distinct electrodes. Furthermore, the reconstructed three dimensional pathways of tonotopically organized auditory nerve fiber bundles over a range of about eight octaves provide the fundament for subsequent conducted analysis of the activation profiles and the temporal fine structure of selected normal and degenerated human auditory neurons to microstimulation.

Particularly these three dimensional pathways of the neurons are of prime importance for simulating the realistic neuronal behavior to microstimulation in the human cochlea. Rattay et al. (2001a) reported that fiber regions featuring strong curvatures are more easily excitable than fibers that run more linear. Our analysis showed that even tangential running basal fibers show a slightly spiral characteristic in their central process ($\geq 180^\circ$) due to their helical pathway around the modiolar axis. This effect increases steadily in direction to low-frequency fibers which additionally feature this distinction in their peripheral process. The reason for this peripheral spiral course can be found in the snail-shaped geometry resulting in narrowing microanatomical structures. Due to the shortage of space, the spiral canal housing the bipolar cell bodies of middle- and apical cochlear neurons ends densely crowded in a blind-ending bulge at the level of the middle turn ((Glueckert et al., 2005b), Fig.3b) after about $1\frac{3}{4}$ turns. This extraordinary region starts at around 600 Hz which is represented by traced fiber bundle middle 5 (Table 7.3). Consequently, the APs generated by lower frequencies are transmitted down the helical structure by significantly longer peripheral processes in a spiral manner to the somata.

The spiraling peripheral processes of apical neurons are additionally the main reason for infringing the tonotopical principle when stimulated artificially. Our investigations of the apical turn showed that even stimulating at threshold level will activate non-neighboring at different regions altering the temporal fine structure and infringing the tonotopical principle observed for monophasic as well as biphasic stimulation. The reason can be found again in the spiraling peripheral processes which cause relatively small distances to the active electrodes. Consequently, the probability for these neurons of being excited by those electrodes increases, even with a small amount of current.

However, neither the deep-insertion nor the perimodiolar located electrode array reached the investigated region. It should be noted in this context that the length of the scanned cochlea which was used for developing the FEM was determined at 40mm at the level of the OC. This value is settled in the upper limit of reported length for the human hearing organ (Wright et al., 1987).

Stimulation of the low frequencies was hypothesized to increase the perception of background noise which negatively affects speech recognition (Wilson, 2004). This theory is supported by results presented by Lazard et al. (Lazard et al., 2012) who stimulated selectively the apical region of several implantees with pulse trains by perimodiolar CIs. The resulting hearing sensation was an inharmonic sound with a spectral envelope peak at ~ 520 Hz. This physiological perception and the determined peak energy of this complex sound can be a consequence of infringing the tonotopical principle at this remarkable cochlea region.

According to our conducted computer simulations, remarkable differences are predicted in the activation pattern of the reconstructed neurons when excited with varying stimuli configurations. Especially the applied current strength affects the excitation pattern of cochlear neurons. This effect (compare Figure 7.12 and Figure 7.13) is intensified by the position of the firing electrode: a 3-fold CAT threshold stimulus fired by a perimodiolar located electrode in the middle turn activates up to 87% of the traced population from all cochlea regions infringing the tonotopical principle. In this electrode-stimuli configuration, the AP transmitted to the auditory cortex was induced in all neurons at the somatic region or in the central process respectively. These regions are closest to the electrode and tremendously influence the IS and therefore, the temporal pattern of electrical signals sent to the CNS. As shown by Rattay et al. (2001a) (see Table 7.2) for the homogeneous case, increasing stimuli strength will activate neurons at the central process influencing the temporal fine structure delivered to the brain. This conclusion can be also drawn with our human auditory model as shown by our results presented in Figure 7.12B (right plot) and Figure 7.13 (middle and right plot). The highly spiral pathways of apical fibers (see Figure 7.6), especially of their central process, ensure that they come quite close to the medial side of the RC in the middle turn. As a result, these fibers as well as fibers originating from the actual stimulated region are quite simultaneously activated by the same electrode. Consequently, the activation of a large population at the same time impacts the expected delay pattern of neurons from different cochlea regions which will subsequently confuse the temporal fine pattern of the neural code in CI implantees.

The temporal fine structure of the neural code plays an important role in speech understanding and is of prime importance in noisy environment (Friesen et al., 2001; Zeng et al., 2005). These fast variations carry information concerning the pitch for pure and complex tones and the localization of sound (Nelson et al., 2003; Stickney et al., 2005; Qin & Oxenham, 2006). Changings in this information tremendously impacts tonal and sound perception in general, leading to misinterpretation by the auditory cortex. Computer simulations predict remarkable alterations of the temporal fine structure of the analyzed target neurons from the basal- and middle turn especially when comparing the normal with the degenerated case. Due to the much higher currents needed to successfully activate a degenerated neuron, APs are substantially earlier generated. Consequently, these signals reach earlier the model neurons' end compared to the normal simulated case. Quantitative evaluation of peripheral process fibers running in the spiral lamina, cell bodies in the spiral canal and central processes of SGNs in the VIIIth cranial nerve in deaf and hearing impaired people respectively indicate that the number of periphearal processes is much smaller compared to the central processes (Spoendlin & Schrott, 1988; Spoendlin & Schrott, 1989; Felix et al., 1997; Felder et al., 1997; Felix et al., 2002). However, the results presented in these studies suggest that both anatomical variations of human cochlear neurons exist parallel along the whole spiral organ. Together with the predicted infringement the tonotopical principle induced by microstimulation, our conducted computer simulations suggest that the auditory cortex receives not only partially wrong auditory spectral input due to infringement of the tonotopical principle but also a confused temporal fine structure of the transmitted auditory neural code due to varying IS, PTs and ETs. These

disturbances in the temporal pattern are a result by the coexistent of normal and degenerated neurons within the pathological, electrically stimulated human cochlea.

The presented model offers the possibility to simulate the auditory behavior to microstimulation with an unprecedented accuracy considering the human cochlea anatomy. However, a future refined model should include (i) new and systematic measured conductive properties describing the conductive behavior of the modeled compartments and (ii) it should be embedded in a 'natural' environment.

Besides the anatomical situation, the dielectrical properties of cochlea tissues and fluids compose the core of the model and determine the spreading of the electrical potential induced by active electrodes. Large differences of these values are found in literature and partly adapted values are used, e.g. for the bone or the peri- and endolymph (Von Békésy, 1952; Kosterich et al., 1983; Suesserman & Spelman, 1993; Frijns et al., 1995; Rattay et al., 2001b; van Rienen et al., 2005). To increase model accuracy, conductivity values for the heavy mineralized otic capsule, known to be the hardest bone within the human body (Kalwani et al., 2013) and for the highly porous bony column are essential. Besides room temperature, measurements should also be conducted at body temperature due to reported significant differences in resulting conductance (Baumann et al., 1997; Schmid et al., 2007) to get physiological correct values to complete the important cochlea conductivity pattern.

As mentioned in a second point, the FEM should be embedded in a, e.g. reconstructed human head including the approximated bony and soft compartments. This would mimic the geometrical proportions between the cochlea, the implant and the head resulting in realistic positioning of the, e.g. ground electrode.

In this paper, we present the first computational human cochlea environment that is based on a high-resolution micro CT scan. Data extraction of this isotropic spatial data set enables simulations of (i) the spreading of the electrical potential induced by CIs conducted on a newly developed FEM and (ii) the resulting auditory response of selected cochlear neurons to microstimulation. The presented model can be used to mimic complex stimulation strategies, develop optimized electrode configurations and positions within the cochlea as well as analyzing the resulting impact on the neural excitation profiles and the temporal fine structure of the neural code in an adapted electrical circuit model of a human auditory neuron.

Bibliography

- Aarhus, 2010. Cochlear implantation ved børn. Available at: http://e-dok.rm.dk/e-dok/e_700301.nsf/UI2/82CC57D1D7DD6221C12577960043AD23?OpenDocument, access on: August 17, 2013
- Adams, J. & Liberman, C., 2010. Anatomy. In Schuknecht's Pathology of the Ear. Peoples Medical Publishing House, USA.
- Aesch, E. & Büchl-Zimmermann, S., 2010. Präparationsmethoden. In: Romeis Mikroskopische Technik. Spektrum Akademischer Verlag GmbH.
- Alberti, P., 2006. The Anatomy and Physiology of the Ear and Hearing. Available at: http://www.who.int/occupational_health/publications/noise2.pdf, access on: August 10, 2013
- Amira, V.S., 2009. Amira reference Guide. Available at: <http://www2.udel.edu/ctcr/sites/udel.edu.ctcr/files/Amira%20Reference%20Guide.pdf>, access on: June 25, 2013
- Anastassiou, C.A., Perin, R., Markram, H. & Koch, C., 2011. Ephaptic coupling of cortical neurons. *Nat Neurosci*, 14(2), pp.217-23. Available at: <http://dx.doi.org/10.1038/nn.2727>.
- Arnold, W.J., 1982. The spiral ganglion of the newborn baby. *Am J Otol*, 3(3), pp.266-69.
- Arnold, W., 1987. Myelination of the human spiral ganglion. *Acta Otolaryngol Suppl*, 436, pp.76-84.
- Bartscher, M., Staude, A., Ehrig, K. & Ramsey, A., 2012. The Influence of Data Filtering on Dimensional Measurements with CT. Available at: http://www.ndt.net/article/wcndt2012/papers/429_wcndtfinal00429.pdf, access on: June 15, 2013. Durban, South Africa.
- Bast, T., 1942. Development of the otic capsule. *Ann Otol Rhinol Laryngol*, 51, pp.343-57.
- Baumann, S.B., Wozny, D.R., Kelly, S.K. & Meno, F.M., 1997. The electrical conductivity of human cerebrospinal fluid at body temperature. *IEEE Trans Biomed Eng*, 44(3), pp.220-23. Available at: <http://dx.doi.org/10.1109/10.554770>.
- Bean, B.P., 2007. The action potential in mammalian central neurons. *Nat Rev Neurosci*, 8(6), pp.451-65. Available at: <http://dx.doi.org/10.1038/nrn2148>.
- Bennett, M.V.L. & Zukin, R.S., 2004. Electrical coupling and neuronal synchronization in the Mammalian brain. *Neuron*, 41(4), pp.495-511.
- Berglund, A.M. & Ryugo, D.K., 1991. Neurofilament antibodies and spiral ganglion neurons of the mammalian cochlea. *J Comp Neurol*, 306(3), pp.393-408. Available at: <http://dx.doi.org/10.1002/cne.903060304>.
- Bernard, P.A. & Spöndlin, H., 1973. Unmyelinated fibers in the cochlea. *JFORL J Fr Otorhinolaryngol Audiophonol Chir Maxillofac*, 22(1), pp.39-42.
- Berthold, C., Rydmark, M. & Corneliussen, O., 1982. Estimation of sectioning compression and thickness of ultrathin sections through Vestopal-W-embedded cat spinal roots. *J Ultrastruct Res*, 80(1), pp.42-52.

- Bierer, J.A., 2007. Threshold and channel interaction in cochlear implant users: evaluation of the tripolar electrode configuration. *J Acoust Soc Am*, 121(3), pp.1642-53.
- Binczak, S., Eilbeck, J. & Scott, A., 2001. Ephaptic coupling of myelinated nerve fibers. *Physica D*, 148(1-2), pp.159-74.
- Bitter, R., Mohiuddin, T. & Nawrocki, M., 2007. Object-Orientated Programming in LabVIEW. In: *LabVIEW™ Advanced Programming Techniques*. 2nd ed. Boca Raton: CRC Press LLC.
- Black, R., Clark, G., Tong, Y. & Patrick, J., 1983. Current distributions in cochlear stimulation. *Ann N Y Acad Sci.*, 405, pp.137-45.
- Boyd, I.A. & Kalu, K.U., 1979. Scaling factor relating conduction velocity and diameter for myelinated afferent nerve fibres in the cat hind limb. *J Physiol*, 289, pp.277-97.
- Braun, K., Böhnke, F. & Stark, T., 2012. Three-dimensional representation of the human cochlea using micro-computed tomography data: presenting an anatomical model for further numerical calculations. *Acta Otolaryngol*, 132(6), pp.603-13. Available at: <http://dx.doi.org/10.3109/00016489.2011.653670>.
- Briaire, J.J. & Frijns, J.H., 2000. Field patterns in a 3D tapered spiral model of the electrically stimulated cochlea. *Hear Res*, 148(1-2), pp.18-30.
- Briaire, J.J. & Frijns, J.H.M., 2005. Unraveling the electrically evoked compound action potential. *Hear Res*, 205(1-2), pp.143-56. Available at: <http://dx.doi.org/10.1016/j.heares.2005.03.020>.
- Burns, M., 1993. *Automated Fabrication: Improving Productivity in Manufacturing*. New Jersey: Prentice Hall.
- Cantrell, C., 2000. Chebyshev Approximations. In: *Modern Mathematical Methods for Physicists and Engineers*. Cambridge University Press.
- Cattell, R., 1966. The Scree Test for the Number of Factors. *Multivariate Behavioral Research*, 1, pp.245-76.
- Charles, T. & Yi-Hsuan, L., 2012. A Review of Stimulating Strategies for Cochlear Implants, Cochlear Implant Research Updates. INTECH.
- Chiu, S.Y., Ritchie, J.M., Rogart, R.B. & Stagg, D., 1979. A quantitative description of membrane currents in rabbit myelinated nerve. *J Physiol*, 292, pp.149-66.
- Claxton, N., Fellers, T. & Davidson, M., 2005. *Laser Scanning Confocal Microscopy*. Available at: <http://www.olympusfluoview.com/theory/LSCMIntro.pdf>, access on: April 14, 2013
- Cochlear, 2012. Cochlear™ Nucleus® Cochlear Implants. Available at: <http://professionals.cochlearamericas.com/cochlear-products/nucleus-cochlear-implants/surgical-support/contour-advance-images>, access on: September 24, 2012
- Cohen, L.T., Xu, J., Xu, S.A. & Clark, G.M., 1996. Improved and simplified methods for specifying positions of the electrode bands of a cochlear implant array. *Am J Otol*, 17(6), pp.859-65.
- Coleman, B., Rickard, N.A., de Silva, M.G. & Shepherd, R.K., 2009. A protocol for cryoembedding the adult guinea pig cochlea for fluorescence immunohistology. *J Neurosci Methods*, 176(2), pp.144-51. Available at: <http://dx.doi.org/10.1016/j.jneumeth.2008.09.007>.

- COMSOL, M., 2012. AC/DC Module User's Guide. Available at: <http://hpc.mtech.edu/comsol/pdf/acdc/ACDCModuleUsersGuide.pdf>, access on: June 25, 2013
- Coons, A., Creech, H. & Jones, R., 1941. Immunological properties of an antibody containing a fluorescent group. *Proceedings of the Society for Experimental Biology and Medicine*, 47, pp.200-02.
- Costello, A. & Osborne, J., 2005. Best Practices in Exploratory Factor Analysis: Four Recommendations for Getting the Most From Your Analysis. *Practical Assessment, Research & Evaluation*, 10, pp.1-9.
- Dallos, P., 1992. The active cochlea. *J Neurosci*, 12(12), pp.4575-85.
- Dallos, P. & Corey, M.E., 1991. The role of outer hair cell motility in cochlear tuning. *Curr Opin Neurobiol*, 1(2), pp.215-20.
- Davis, R.L. & Liu, Q., 2011. Complex primary afferents: What the distribution of electrophysiologically-relevant phenotypes within the spiral ganglion tells us about peripheral neural coding. *Hear Res*, 276(1-2), pp.34-43. Available at: <http://dx.doi.org/10.1016/j.heares.2011.01.014>.
- de Crespigny, A. et al., 2008. 3D micro-CT imaging of the postmortem brain. *J Neurosci Methods*, 171(2), pp.207-13. Available at: <http://dx.doi.org/10.1016/j.jneumeth.2008.03.006>.
- Deverell, M., Bailey, N. & Whimster, W., 1989. Tissue distortion in three-dimensional reconstruction of wax or plastic embedded microscopic structures. *Pathol Res Pract.*, 185(5), pp.598-601.
- Drennan, W., Won, J., Dasika, V. & Rubinstein, J., 2007. Drennan WR, Won JH, Dasika VK, Rubinstein JT Effects of temporal fine structure on the lateralization of speech and on speech understanding in noise. *J Assoc Res Otolaryngol*, 8, pp.373-83.
- Dunn, O., 1961. Multiple comparisons among means. *J Am Stat Assoc*, 56, pp.52-64.
- Elliott, J.C. & Dover, S.D., 1982. X-ray microtomography. *J Microsc*, 126(Pt 2), pp.211-13.
- Engel, D. & Jonas, P., 2005. Presynaptic action potential amplification by voltage-gated Na⁺ channels in hippocampal mossy fiber boutons. *Neuron*, 45(3), pp.405-17. Available at: <http://dx.doi.org/10.1016/j.neuron.2004.12.048>.
- Erixon, E., Högstorp, H., Wadin, K. & Rask-Andersen, H., 2009. Variational anatomy of the human cochlea: implications for cochlear implantation. *Otol Neurotol*, 30(1), pp.14-22. Available at: <http://dx.doi.org/10.1097/MAO.0b013e31818a08e8>.
- Esteves, M. et al., 2009. Brainstem evoked response audiometry in normal hearing subjects. *Braz J Otorhinolaryngol*, 75, pp.420-25.
- ETH, 2010. Scientific Visualization Group. Available at: <http://www.scivis.ethz.ch/>, access on: April 14, 2013
- Felder, E. et al., 1997. Quantitative evaluation of cochlear neurons and computer-aided three-dimensional reconstruction of spiral ganglion cells in humans with a peripheral loss of nerve fibres. *Hear Res*, 105(1-2), pp.183-90.
- Felix, H., Gleeson, M., Pollak, A. & Johnsson, L., 1997. The cochlear neurons in humans. In: *Progress in Human Auditory and Vestibular Histopathology*. Amsterdam: Kugler Publications.

- Felix, H. et al., 1992. Morphometric analysis of the cochlear nerve in man. *Acta Otolaryngol*, 112(2), pp.284-87.
- Felix, H., Pollak, A., Gleeson, M. & Johnsson, L.-G., 2002. Degeneration pattern of human first-order cochlear neurons. *Adv Otorhinolaryngol*, 59, pp.116-23.
- Finley, C., Wilson, B. & White, M., 1990. Models of neural responsiveness to electrical stimulation. In: *Cochlear Implants: Models of the Electrically Stimulated Ear*. New York: Springer.
- Flock, A. et al., 1999. Supporting cells contribute to control of hearing sensitivity. *J Neurosci*, 19(11), pp.4498-507.
- Fohlmeister, J.F., 2009. A nerve model of greatly increased energy-efficiency and encoding flexibility over the Hodgkin-Huxley model. *Brain Res*, 1296, pp.225-33. Available at: <http://dx.doi.org/10.1016/j.brainres.2009.06.101>.
- Frankenhaeuser, B. & Huxley, A., 1964. The Action Potential in the Myelinated Nerve Fiber of *Xenopus Laevis* As Computed on the Basis of Voltage Clamp Data. *J Physiol*, 171, pp.302-15.
- Friendly, M., 2008. Milestones in the history of thematic cartography, statistical graphics and data visualization. *Engineering*, 9(2), p.2008.
- Friesen, L.M., Shannon, R.V., Baskent, D. & Wang, X., 2001. Speech recognition in noise as a function of the number of spectral channels: comparison of acoustic hearing and cochlear implants. *J Acoust Soc Am*, 110(2), pp.1150-63.
- Frijns, J.H., de Snoo, S.L. & Schoonhoven, R., 1995. Potential distributions and neural excitation patterns in a rotationally symmetric model of the electrically stimulated cochlea. *Hear Res*, 87(1-2), pp.170-86.
- Frijns, J.H., Mooij, J. & ten Kate, J.H., 1994. A quantitative approach to modeling mammalian myelinated nerve fibers for electrical prosthesis design. *IEEE Trans Biomed Eng*, 41(6), pp.556-66. Available at: <http://dx.doi.org/10.1109/10.293243>.
- Frolenkov, G.I., 2006. Regulation of electromotility in the cochlear outer hair cell. *J Physiol*, 576(Pt 1), pp.43-48. Available at: <http://dx.doi.org/10.1113/jphysiol.2006.114975>.
- Füllgrabe, C., Berthommier, F. & Lorenzi, C., 2006. Masking release for consonant features in temporally fluctuating background noise. *Hear Res*, 211(1-2), pp.74-84. Available at: <http://dx.doi.org/10.1016/j.heares.2005.09.001>.
- Ghitza, O., 1994. Auditory models and human performances in tasks related to speech coding and speech recognition. *IEEE Trans. Speech Audio Proc.*, 2, pp.115-32.
- Gillespie, L.N. & Shepherd, R.K., 2005. Clinical application of neurotrophic factors: the potential for primary auditory neuron protection. *Eur J Neurosci*, 22(9), pp.2123-33. Available at: <http://dx.doi.org/10.1111/j.1460-9568.2005.04430.x>.
- Glueckert, R., 2013. Skriptum zu Histologischen Analyseverfahren. 7. Ausgabe.
- Glueckert, R. et al., 2005b. The human spiral ganglion: new insights into ultrastructure, survival rate and implications for cochlear implants. *Audiol Neurootol*, 10(5), pp.258-73. Available at: <http://dx.doi.org/10.1159/000086000>.

- Glueckert, R. et al., 2005a. High resolution scanning electron microscopy of the human organ of Corti. A study using freshly fixed surgical specimens. *Hear Res*, 199(1-2), pp.40-56. Available at: <http://dx.doi.org/10.1016/j.heares.2004.05.006>.
- Golding, N., Ferragamo, M. & Oertel, D., 1999. Role of intrinsic conductances underlying responses to transients in octopus cells of the cochlear nucleus. *J Neurosci*, pp.2897-905.
- Goldwyn, J.H., Bierer, S.M. & Bierer, J.A., 2010. Modeling the electrode-neuron interface of cochlear implants: effects of neural survival, electrode placement, and the partial tripolar configuration. *Hear Res*, 268(1-2), pp.93-104. Available at: <http://dx.doi.org/10.1016/j.heares.2010.05.005>.
- Grant, L., Yi, E. & Glowatzki, E., 2010. Two modes of release shape the postsynaptic response at the inner hair cell ribbon synapse. *J Neurosci*, 30(12), pp.4210-20. Available at: <http://dx.doi.org/10.1523/JNEUROSCI.4439-09.2010>.
- Greenwood, D., 1961. Critical bandwidth and the frequency coordinates of the basilar membrane. *The Journal of the Acoustical Society of America*, 33, pp.1344-56.
- Greenwood, D., 1990. A cochlear frequency-position function for several species--29 years later. *J Acoust Soc Am*, 87(6), pp.2592-605.
- Hafidi, A., 1998. Peripherin-like immunoreactivity in type II spiral ganglion cell body and projections. *Brain Res*, 805(1-2), pp.181-90.
- Hanani, M., 2010. Satellite glial cells: more than just 'rings around the neuron'. *Neuron Glia Biol*, 6(1), pp.1-2. Available at: <http://dx.doi.org/10.1017/S1740925X10000104>.
- Hanekom, T., 2001. Three-dimensional spiraling finite element model of the electrically stimulated cochlea. *Ear Hear*, 22(4), pp.300-15.
- Hansen, C., 2005. *Visualization Handbook*. Oxford: Elsevier Butterworth-Heinemann.
- Hardie, N.A., MacDonald, G. & Rubel, E.W., 2004. A new method for imaging and 3D reconstruction of mammalian cochlea by fluorescent confocal microscopy. *Brain Res*, 1000(1-2), pp.200-10. Available at: <http://dx.doi.org/10.1016/j.brainres.2003.10.071>.
- Hartmann, R., Topp, G. & Klinke, R., 1984. Discharge patterns of cat primary auditory fibers with electrical stimulation of the cochlea. *Hear Res*, 13(1), pp.47-62.
- Hastie, T., Tibshirani, R. & Friedman, J., 2009. *Hierarchical Clustering*. In: *The Elements of Statistical Learning*. 2nd ed. New York: Springer.
- Hodgkin, A. & Huxley, A., 1952. A quantitative description of membrane current and its application to conduction and excitation in nerve. *J Physiol*, 117(4), pp.500-44.
- Hollien, H., Dew, D. & Philips, P., 1971. Phonational frequency ranges of adults. *J Speech Hear Res*, 14(4), pp.755-60.
- Holmes, T.J. & Liu, Y.H., 1989. Richardson-Lucy/maximum likelihood image restoration algorithm for fluorescence microscopy: further testing. *Appl Opt*, 28(22), pp.4930-38.
- Holt, G.R. & Koch, C., 1999. Electrical interactions via the extracellular potential near cell bodies. *J Comput Neurosci*, 6(2), pp.169-84.

- Hossain, W.A. et al., 2005. Where is the spike generator of the cochlear nerve? Voltage-gated sodium channels in the mouse cochlea. *J Neurosci*, 25(29), pp.6857-68. Available at: <http://dx.doi.org/10.1523/JNEUROSCI.0123-05.2005>.
- Hu, W. et al., 2009. Distinct contributions of Na(v)1.6 and Na(v)1.2 in action potential initiation and backpropagation. *Nat Neurosci*, 12(8), pp.996-1002. Available at: <http://dx.doi.org/10.1038/nn.2359>.
- Huxley, A.F. & Stämpfli, R., 1949. Evidence for saltatory conduction in peripheral myelinated nerve fibres. *J Physiol*, 108(3), pp.315-39.
- Jagger, D.J. & Housley, G.D., 2003. Membrane properties of type II spiral ganglion neurones identified in a neonatal rat cochlear slice. *J Physiol*, 552(Pt 2), pp.525-33. Available at: <http://dx.doi.org/10.1113/jphysiol.2003.052589>.
- Javel, E. & Shepherd, R.K., 2000. Electrical stimulation of the auditory nerve. III. Response initiation sites and temporal fine structure. *Hear Res*, 140(1-2), pp.45-76.
- Kalwani, N.M. et al., 2013. Quantitative polarized light microscopy of unstained mammalian cochlear sections. *J Biomed Opt*, 18(2), p.26021. Available at: <http://dx.doi.org/10.1117/1.JBO.18.2.026021>.
- Kandler, K. & Friauf, E., 1993. Pre- and postnatal development of efferent connections of the cochlear nucleus in the rat. *J Comp Neurol*, 328(2), pp.161-84. Available at: <http://dx.doi.org/10.1002/cne.903280202>.
- Kellerhals, B., Engström, H. & Ades, H., 1967. Die Morphologie des Ganglion Spirale Cochleae. *Acta Otolaryngol Suppl*, 226, pp.1-78.
- Kiang, N., 1965. Discharge pattern of single fibres in the cats auditory nerve. *Journal of Anatomy*, 101, pp.176-77.
- Kiang, N. et al., 1984. Afferent innervation of the mammalian cochlea. In: *Comparative Physiology of Sensory Systems*. Cambridge: Cambridge UP.
- Kiefer, J. et al., 2001. Comparison of speech recognition with different speech coding strategies (SPEAK, CIS, and ACE) and their relationship to telemetric measures of compound action potentials in the nucleus CI 24M cochlear implant system. *Audiology*, 40(1), pp.32-42.
- Kim, J. et al., 2008. *Data Visualization and Display*. In: *Biomedical Information Technology*. Oxford: Elsevier.
- Koch, D.B., Osberger, M.J., Segel, P. & Kessler, D., 2004. HiResolution and conventional sound processing in the HiResolution bionic ear: using appropriate outcome measures to assess speech recognition ability. *Audiol Neurootol*, 9(4), pp.214-23. Available at: <http://dx.doi.org/10.1159/000078391>.
- Kolb, B. & Whishaw, I., 2011. *An Introduction to Brain and Behaviour*. 2nd ed. New York City: Worth Publishers.
- Kosterich, J.D., Foster, K.R. & Pollack, S.R., 1983. Dielectric permittivity and electrical conductivity of fluid saturated bone. *IEEE Trans Biomed Eng*, 30(2), pp.81-86.
- Kozubek, M., 2001. Theoretical versus experimental resolution in optical microscopy. *Microsc Res Tech*, 53(2), pp.157-66. Available at: <http://dx.doi.org/10.1002/jemt.1080>.

- Kress, G.J. & Mennerick, S., 2009. Action potential initiation and propagation: upstream influences on neurotransmission. *Neuroscience*, 158(1), pp.211-22. Available at: <http://dx.doi.org/10.1016/j.neuroscience.2008.03.021>.
- Kuijpers, W., Tonnaer, E.L., Peters, T.A. & Ramaekers, F.C., 1991. Expression of intermediate filament proteins in the mature inner ear of the rat and guinea pig. *Hear Res*, 52(1), pp.133-46.
- Lareida, A. et al., 2009. High-resolution X-ray tomography of the human inner ear: synchrotron radiation-based study of nerve fibre bundles, membranes and ganglion cells. *J Microsc*, 234(1), pp.95-102. Available at: <http://dx.doi.org/10.1111/j.1365-2818.2009.03143.x>.
- Lazard, D.S., Marozeau, J. & McDermott, H.J., 2012. The sound sensation of apical electric stimulation in cochlear implant recipients with contralateral residual hearing. *PLoS One*, 7(6), p.e38687. Available at: <http://dx.doi.org/10.1371/journal.pone.0038687>.
- Lieberman, M.C., 1980a. Efferent synapses in the inner hair cell area of the cat cochlea: an electron microscopic study of serial sections. *Hear Res*, 3(3), pp.189-204.
- Lieberman, M.C., 1980b. Morphological differences among radial afferent fibers in the cat cochlea: an electron-microscopic study of serial sections. *Hear Res*, 3(1), pp.45-63.
- Lieberman, M.C., 1982. The cochlear frequency map for the cat: labeling auditory-nerve fibers of known characteristic frequency. *J Acoust Soc Am*, 72(5), pp.1441-49.
- Lieberman, M.C., Dodds, L.W. & Pierce, S., 1990. Afferent and efferent innervation of the cat cochlea: quantitative analysis with light and electron microscopy. *J Comp Neurol*, 301(3), pp.443-60. Available at: <http://dx.doi.org/10.1002/cne.903010309>.
- Lieberman, M.C. & Kiang, N.Y., 1978. Acoustic trauma in cats. Cochlear pathology and auditory-nerve activity. *Acta Otolaryngol Suppl*, 358, pp.1-63.
- Lieberman, M.C. & Oliver, M.E., 1984. Morphometry of intracellularly labeled neurons of the auditory nerve: correlations with functional properties. *J Comp Neurol*, 223(2), pp.163-76. Available at: <http://dx.doi.org/10.1002/cne.902230203>.
- Liu, W. et al., 2012. Expression of myelin basic protein in the human auditory nerve - an immunohistochemical and comparative study. *Auris Nasus Larynx*, 39(1), pp.18-24. Available at: <http://dx.doi.org/10.1016/j.anl.2011.04.007>.
- Liu, W., Boström, M., Kinnefors, A. & Rask-Andersen, H., 2009a. Unique expression of connexins in the human cochlea. *Hear Res*, 250(1-2), pp.55-62. Available at: <http://dx.doi.org/10.1016/j.heares.2009.01.010>.
- Liu, W., Boström, M. & Rask-Andersen, H., 2009b. Expression of peripherin in the pig spiral ganglion--aspects of nerve injury and regeneration. *Acta Otolaryngol*, 129(6), pp.608-14. Available at: <http://dx.doi.org/10.1080/00016480802369294>.
- Liu, W., Kinnefors, A., Boström, M. & Rask-Andersen, H., 2010. Expression of peripherin in human cochlea. *Cell Tissue Res*, 342(3), pp.345-51. Available at: <http://dx.doi.org/10.1007/s00441-010-1081-6>.
- Loizou, P.C., 1999. Introduction to cochlear implants. *IEEE Eng Med Biol Mag*, 18(1), pp.32-42.

- Lu, J., Fiala, J.C. & Lichtman, J.W., 2009. Semi-automated reconstruction of neural processes from large numbers of fluorescence images. *PLoS One*, 4(5), p.e5655. Available at: <http://dx.doi.org/10.1371/journal.pone.0005655>.
- Maalouf, E., 2010. Contribution to fluorescence microscopy, 3D thick samples deconvolution and depth-variant PSF. PhD - thesis, Haute Alsace University. Available at: http://tel.archives-ouvertes.fr/docs/00/59/42/47/PDF/2010MULH2458_these_Maalouf.pdf, access on July 25, 2013
- Macherey, O. et al., 2008. Higher sensitivity of human auditory nerve fibers to positive electrical currents. *J Assoc Res Otolaryngol*, 9(2), pp.241-51. Available at: <http://dx.doi.org/10.1007/s10162-008-0112-4>.
- Mainen, Z.F. & Sejnowski, T.J., 1996. Influence of dendritic structure on firing pattern in model neocortical neurons. *Nature*, 382(6589), pp.363-66. Available at: <http://dx.doi.org/10.1038/382363a0>.
- Makary, C.A. et al., 2011. Age-related primary cochlear neuronal degeneration in human temporal bones. *J Assoc Res Otolaryngol*, 12(6), pp.711-17. Available at: <http://dx.doi.org/10.1007/s10162-011-0283-2>.
- Malherbe, T.K., Hanekom, T. & Hanekom, J.J., 2013. Can subject-specific single-fibre electrically evoked auditory brainstem response data be predicted from a model? *Med Eng Phys*, 35(7), pp.926-36. Available at: <http://dx.doi.org/10.1016/j.medengphy.2012.09.001>.
- MathWorks, 2013. Object-Oriented Programming in MATLAB. Available at: <http://www.mathworks.com/discovery/object-oriented-programming.html>, access on: April 18, 2013
- McFadden, S.L., Ding, D., Jiang, H. & Salvi, R.J., 2004. Time course of efferent fiber and spiral ganglion cell degeneration following complete hair cell loss in the chinchilla. *Brain Res*, 997(1), pp.40-51.
- Med-El, 2012. FLEX Elektrodenträger. Available at: <http://www.medel.com/data/pdf/22946.pdf>, access on: July 23, 2012
- Meeks, J. & Mennerick, S., 2007. Action potential initiation and propagation in ca3 pyramidal axons. *J Neurophysiol*, pp.3460-72. Available at: <http://dx.doi.org/10.1113/jphysiol.2005.089086>.
- Metscher, B.D., 2009. MicroCT for comparative morphology: simple staining methods allow high-contrast 3D imaging of diverse non-mineralized animal tissues. *BMC Physiol*, 9, p.11. Available at: <http://dx.doi.org/10.1186/1472-6793-9-11>.
- Miller, C.A. et al., 2004. Intracochlear and extracochlear ECAPs suggest antidromic action potentials. *Hear Res*, 198(1-2), pp.75-86. Available at: <http://dx.doi.org/10.1016/j.heares.2004.07.005>.
- Miller, C.A. et al., 1999. Electrically evoked single-fiber action potentials from cat: responses to monopolar, monophasic stimulation. *Hear Res*, 130(1-2), pp.197-218.
- Miller, J.M. et al., 1997. Neurotrophins can enhance spiral ganglion cell survival after inner hair cell loss. *Int J Dev Neurosci*, 15(4-5), pp.631-43.
- Miller, A.L., Morris, D.J. & Pflugst, B.E., 1997. Interactions between pulse separation and pulse polarity order in cochlear implants. *Hear Res*, 109(1-2), pp.21-33.

- Miller, C.A. et al., 2001. Auditory nerve responses to monophasic and biphasic electric stimuli. *Hear Res*, 151(1-2), pp.79-94.
- Mino, H., Rubinstein, J.T., Miller, C.A. & Abbas, P.J., 2004. Effects of electrode-to-fiber distance on temporal neural response with electrical stimulation. *IEEE Trans Biomed Eng*, 51(1), pp.13-20. Available at: <http://dx.doi.org/10.1109/TBME.2003.820383>.
- Miura, M., Sando, I., Hirsch, B.E. & Orita, Y., 2002. Analysis of spiral ganglion cell populations in children with normal and pathological ears. *Ann Otol Rhinol Laryngol*, 111(12 Pt 1), pp.1059-65.
- Moore, B., 2007. *Cochlear Hearing Loss: physiological, psychological and technical issues*. 2nd ed. Chichester: John Wiley & Sons Ltd.
- Moore, B.C.J., 2008. The role of temporal fine structure processing in pitch perception, masking, and speech perception for normal-hearing and hearing-impaired people. *J Assoc Res Otolaryngol*, 9(4), pp.399-406. Available at: <http://dx.doi.org/10.1007/s10162-008-0143-x>.
- Moore, J. et al., 1978. Simulations of conduction in uniform myelinated fibers. Relative sensitivity to changes in nodal and internodal parameters. *Biophys J*, pp.147-60.
- Motz, H. & Rattay, F., 1986. A study of the application of the Hodgkin-Huxley and the Frankenhaeuser-Huxley model for electrostimulation of the acoustic nerve. *Neuroscience*, 18(3), pp.699-712.
- Mudry, A. & Mills, M., 2013. The early history of the cochlear implant: a retrospective. *JAMA Otolaryngol Head Neck Surg*, 139(5), pp.446-53. Available at: <http://dx.doi.org/10.1001/jamaoto.2013.293>.
- Müller, M., 2006. *Introduction to Confocal Fluorescence Microscopy*. 2nd ed. Washington: The International Society for Optical Engineering.
- Murtagh, M., 1984. Complexities of Hierarchical Clustering Algorithms: the state of the art. *Computational Statistics Quarterly*, 1, pp.101-13.
- Nadol, J.J., 1988a. Quantification of human spiral ganglion cells by serial section reconstruction and segmental density estimates. *Am J Otolaryngol*, 9(2), pp.47-51.
- Nadol, J.J., 1988b. Comparative anatomy of the cochlea and auditory nerve in mammals. *Hear Res*, 34(3), pp.253-66.
- Nadol, J.J., 1997. Patterns of neural degeneration in the human cochlea and auditory nerve: implications for cochlear implantation. *Otolaryngol Head Neck Surg*, 117(3 Pt 1), pp.220-28.
- Nadol, J.J., 2010. Disorders of Aging. In: *Schuhknecht's Pathology of the Ear*. 3rd ed. People's Medical Publishing House, USA.
- Nadol, J.J., Burgess, B.J. & Reisser, C., 1990. Morphometric analysis of normal human spiral ganglion cells. *Ann Otol Rhinol Laryngol*, 99(5 Pt 1), pp.340-48.
- Nadol, J.J. et al., 2001. Histopathology of cochlear implants in humans. *Ann Otol Rhinol Laryngol*, 110(9), pp.883-91.
- Nakai, Y., 1970. An electron microscopic study of the human fetus cochlea. *Pract Otorhinolaryngol (Basel)*, 32(5), pp.257-67.

- Namasivayam, A., 2004. Cochlear Implant Technical Issues: Electrodes, Channels, Stimulation Modes and more. Available at: <http://www.audiologyonline.com/articles/cochlear-implant-technical-issues-electrodes-1081>, access on: August 18, 2013
- Negm, M. & Bruce, I., 2008. Effects of I(h) and I(KLT) on the response of the auditory nerve to electrical stimulation in a stochastic Hodgkin-Huxley model. *Conf Proc IEEE Eng Med Biol Soc.*, 2008, pp.5539-42.
- Nelson, L., 2005. Some observations on the scree test, and on coefficient alpha. *Thai Journal of Educational Research and Measurement*, 3, pp.1-17.
- Nelson, P.B., Jin, S.-H., Carney, A.E. & Nelson, D.A., 2003. Understanding speech in modulated interference: cochlear implant users and normal-hearing listeners. *J Acoust Soc Am*, 113(2), pp.961-68.
- NIDCD, 2011. Cochlear Implants - NIH Publication No. 11-4798. Available at: <http://www.nidcd.nih.gov/staticresources/health/hearing/FactSheetCochlearImplant.pdf>, access on: August 13, 2013
- Osen, K.K., 1970. Course and termination of the primary afferents in the cochlear nuclei of the cat. An experimental anatomical study. *Arch Ital Biol*, 108(1), pp.21-51.
- Ota, C.Y. & Kimura, R.S., 1980. Ultrastructural study of the human spiral ganglion. *Acta Otolaryngol*, 89(1-2), pp.53-62.
- Petrou, M. & Petrou, C., 2010. *Image Processing: The Fundamentals*. 2nd ed. Chichester: John Wiley & Sons Ltd.
- Pharr, M. & Humphreys, G., 2010. Sampling and Reconstruction. In: *Physically Based Rendering: From Theory to Implementation*. Burlington: Elsevier.
- Piegl, L. & Tiller, W., 1997. *The NURBS Book*. Springer.
- Popa, R., Anniko, M., Takumida, M. & Arnold, W., 2001. Localization of nitric oxide synthase isoforms in the human cochlea. *Acta Otolaryngol*, 121(4), pp.454-59.
- Poznyakovskiy, A.A. et al., 2008. The creation of geometric three-dimensional models of the inner ear based on micro computer tomography data. *Hear Res*, 243(1-2), pp.95-104. Available at: <http://dx.doi.org/10.1016/j.heares.2008.06.008>.
- Qin, M.K. & Oxenham, A.J., 2006. Effects of introducing unprocessed low-frequency information on the reception of envelope-vocoder processed speech. *J Acoust Soc Am*, 119(4), pp.2417-26.
- Ramos-Vara, J.A., 2005. Technical aspects of immunohistochemistry. *Vet Pathol*, 42(4), pp.405-26. Available at: <http://dx.doi.org/10.1354/vp.42-4-405>.
- Randolph, K. & Myers, L., 2013. Analysis of Variance (ANOVA) and Covariance (ANCOVA). In: *Basis Statistics in Multivariate Analysis*. New York: Oxford University Press.
- Rao, S., 2005. *The finite Element Method in Engineering*. 4th ed. Oxford: Elsevier Butterworth-Heinemann.

- Rask-Andersen, H. et al., 2012. Human cochlea: anatomical characteristics and their relevance for cochlear implantation. *Anat Rec (Hoboken)*, 295(11), pp.1791-811. Available at: <http://dx.doi.org/10.1002/ar.22599>.
- Rattay, F., 1990. *Electrical nerve stimulation, theory, experiments and applications*. New York: Springer.
- Rattay, F., 1995. Propagation and distribution of neural signals: A modeling study of axonal transport. *Phys Alive*, 3, pp.60-66.
- Rattay, F., 1999. The basic mechanism for the electrical stimulation of the nervous system. *Neuroscience*, 89(2), pp.335-46.
- Rattay, F., 2004. Central nervous system stimulation. In: *Neuroprosthetics: Theory and Practice*. World Scientific Publishing.
- Rattay, F. & Aberham, M., 1993. Modeling axon membranes for functional electrical stimulation. *IEEE Trans Biomed Eng*, 40(12), pp.1201-09. Available at: <http://dx.doi.org/10.1109/10.250575>.
- Rattay, F., Greenberg, R. & Resatz, S., 2003. Neuron modeling. In: *Handbook of Neuroprosthetic Methods*. CRC press LLC.
- Rattay, F., Leao, R.N. & Felix, H., 2001b. A model of the electrically excited human cochlear neuron. II. Influence of the three-dimensional cochlear structure on neural excitability. *Hear Res*, 153(1-2), pp.64-79.
- Rattay, F. & Lutter, P., 1997. Speech Sound Representation in the Auditory Nerve: Computer Simulation Studies on Inner Ear Mechanisms. *ZAMM-Journal of Applied Mathematics and Mechanics*, 77, pp.935-43.
- Rattay, F., Lutter, P. & Felix, H., 2001a. A model of the electrically excited human cochlear neuron. I. Contribution of neural substructures to the generation and propagation of spikes. *Hear Res*, 153(1-2), pp.43-63.
- Rattay, F. et al., 2003. Mechanisms of electrical stimulation with neural prostheses. *Neuromodulation*, 6(1), pp.42-56. Available at: <http://dx.doi.org/10.1046/j.1525-1403.2003.03006.x>.
- Rattay, F. & Wenger, C., 2010. Which elements of the mammalian central nervous system are excited by low current stimulation with microelectrodes? *Neuroscience*, 170(2), pp.399-407. Available at: <http://dx.doi.org/10.1016/j.neuroscience.2010.07.032>.
- Retzius, G., 1884. *Das Gehörorgan der Wirbeltiere. II. Das Gehörorgan der Reptilien, der Vögel und der Säugetiere*. Stockholm.
- Rosbe, K.W., Burgess, B.J., Glynn, R.J. & Nadol, J.J., 1996. Morphologic evidence for three cell types in the human spiral ganglion. *Hear Res*, 93(1-2), pp.120-27.
- Rusznák, Z. & Szucs, G., 2009. Spiral ganglion neurones: an overview of morphology, firing behaviour, ionic channels and function. *Pflugers Arch*, 457(6), pp.1303-25. Available at: <http://dx.doi.org/10.1007/s00424-008-0586-2>.
- Ryugo, D.K. et al., 1998. Single unit recordings in the auditory nerve of congenitally deaf white cats: morphological correlates in the cochlea and cochlear nucleus. *J Comp Neurol*, 397(4), pp.532-48.

- Saba, R., 2012. Cochlear Implant Modelling: Stimulation and Power Consumption. PhD - Thesis, University of Southampton. Available at: eprints.soton.ac.uk/348818/1/Rami%20Saba%20Thesis%202012.pdf, access on April 25, 2013.
- Sachs, M.B. & Abbas, P.J., 1974. Rate versus level functions for auditory-nerve fibers in cats: tone-burst stimuli. *J Acoust Soc Am*, 56(6), pp.1835-47.
- Sato, M., Henson, M.M., Henson, J.O. & Smith, D.W., 1999. The innervation of outer hair cells: 3D reconstruction from TEM serial sections in the Japanese macaque. *Hear Res*, 135(1-2), pp.29-38.
- Schindelin, J. et al., 2012. Fiji: an open-source platform for biological-image analysis. *Nat Methods*, 9(7), pp.676-82. Available at: <http://dx.doi.org/10.1038/nmeth.2019>.
- Schmid, G. et al., 2007. High-resolution numerical model of the middle and inner ear for a detailed analysis of radio frequency absorption. *Phys Med Biol*, 52(7), pp.1771-81. Available at: <http://dx.doi.org/10.1088/0031-9155/52/7/001>.
- Schnabl, J. et al., 2012. Sheep as a large animal model for middle and inner ear implantable hearing devices: a feasibility study in cadavers. *Otol Neurotol*, 33(3), pp.481-89. Available at: <http://dx.doi.org/10.1097/MAO.0b013e318248ee3a>.
- Schormann, T., Dabringhaus, A. & Zilles, K., 1995. Statistics of deformations in histology and application to improved alignment with MRI. *IEEE Trans Med Imaging*, 14(1), pp.25-35.
- Schwarz, J.R. & Eikhof, G., 1987. Na currents and action potentials in rat myelinated nerve fibres at 20 and 37 degrees C. *Pflugers Arch*, 409(6), pp.569-77.
- Shamma, S.A., 1985. Speech processing in the auditory system. I: The representation of speech sounds in the responses of the auditory nerve. *J Acoust Soc Am*, 78(5), pp.1612-21.
- Shepherd, R.K. & Javel, E., 1999. Electrical stimulation of the auditory nerve: II. Effect of stimulus waveshape on single fibre response properties. *Hear Res*, 130(1-2), pp.171-88.
- Shibata, T., Matsumoto, S., Agishi, T. & Nagano, T., 2009. Visualization of Reissner membrane and the spiral ganglion in human fetal cochlea by micro-computed tomography. *Am J Otolaryngol*, 30(2), pp.112-20. Available at: <http://dx.doi.org/10.1016/j.amjoto.2008.07.012>.
- Shin, K.-J. et al., 2013. Quantitative analysis of the cochlea using three-dimensional reconstruction based on microcomputed tomographic images. *Anat Rec (Hoboken)*, 296(7), pp.1083-88. Available at: <http://dx.doi.org/10.1002/ar.22714>.
- Sibarita, J.-B., 2005. Deconvolution microscopy. *Adv Biochem Eng Biotechnol*, 95, pp.201-43.
- Simbürger, E., Hehl, S. & Hessling, R., 2013. Zeiss LSM 510 Meta – Guided Tour. Available at: <http://www.olympusfluoview.com/theory/LSCMIntro.pdf>, access on: April 14, 2013
- Simmons, F.B., 1966. Electrical stimulation of the auditory nerve in man. *Arch Otolaryngol*, 84(1), pp.2-54.
- Simmons, D. & Liberman, M., 1988. Afferent innervation of outer hair cells in adult cats: I. Light microscopic analysis of fibers labeled with horseradish peroxidase. *J Comp Neurol*, pp.132-44.

- Smit, J.E., Hanekom, T. & Hanekom, J.J., 2009. Estimation of stimulus attenuation in cochlear implants. *J Neurosci Methods*, 180(2), pp.363-73. Available at: <http://dx.doi.org/10.1016/j.jneumeth.2009.03.024>.
- Song, Y., Treanor, D., Bulpitt, A.J. & Magee, D.R., 2013. 3D reconstruction of multiple stained histology images. *J Pathol Inform*, 4(Suppl), p.S7. Available at: <http://dx.doi.org/10.4103/2153-3539.109864>.
- Spelman, F., Clopton, B., Pfingst, B. & Miller, J., 1980. Design of the cochlear prosthesis: effects of the flow of current in the implanted ear. *Ann Otol Rhinol Laryngol Suppl.*, 89(2), pp.8-10.
- Spoendlin, H., 1969. Innervation patterns in the organ of corti of the cat. *Acta Otolaryngol*, 67(2), pp.239-54.
- Spoendlin, H., 1981. Differentiation of cochlear afferent neurons. *Acta Otolaryngol*, 91(5-6), pp.451-56.
- Spoendlin, H., 1984. Factors inducing retrograde degeneration of the cochlear nerve. *Ann Otol Rhinol Laryngol Suppl*, 112, pp.76-82.
- Spoendlin, H., 1985. Anatomy of cochlear innervation. *Am J Otolaryngol*, 6(6), pp.453-67.
- Spoendlin, H. & Brun, J.P., 1974. The block-surface technique for evaluation of cochlear pathology. *Arch Otorhinolaryngol*, 208(2), pp.137-45.
- Spoendlin, H. & Schrott, A., 1987. The block surface method for evaluation of human inner ears. *Acta Otolaryngol Suppl*, 436, pp.25-36.
- Spoendlin, H. & Schrott, A., 1988. The spiral ganglion and the innervation of the human organ of Corti. *Acta Otolaryngol*, 105(5-6), pp.403-10.
- Spoendlin, H. & Schrott, A., 1989. Analysis of the human auditory nerve. *Hear Res*, 43(1), pp.25-38.
- Spoendlin, H. & Schrott, A., 1990. Quantitative evaluation of the human cochlear nerve. *Acta Otolaryngol Suppl*, 470, pp.61--9; discussion 69-70.
- Stakhovskaya, O., Sridhar, D., Bonham, B. & Leake, P., 2007. Frequency map for the human cochlear spiral ganglion: implications for cochlear implants. *J Assoc Res Otolaryngol.*, 8(2), pp.220-33.
- Stickney, G.S., Nie, K. & Zeng, F.-G., 2005. Contribution of frequency modulation to speech recognition in noise. *J Acoust Soc Am*, 118(4), pp.2412-20.
- Suesserman, M.F. & Spelman, F.A., 1993. Lumped-parameter model for in vivo cochlear stimulation. *IEEE Trans Biomed Eng*, 40(3), pp.237-45. Available at: <http://dx.doi.org/10.1109/10.216407>.
- Sweeney, J., Mortimer, J. & Durnand, D., 1987. Modeling of mammalian myelinated nerve for functional neuromuscular electrostimulation. *IEEE 9th Ann. Conf. Eng. Med Biol. Soc.*, -, pp.1577-78.
- Thiers, F.A., Burgess, B.J. & Nadol, J.J., 2000. Prevalence and ultrastructural morphology of axosomatic synapses on spiral ganglion cells in humans of different ages. *Hear Res*, 150(1-2), pp.119-31.
- Thode, H., 2002. Plots, Probability Plots and Regression Tests. In: *Testing for normality*. New York: Marcel Dekker.

- Trevisi, M., Pagani, P.A. & Sirigu, P., 1972. Comparative research on the size of neurons of the cochlear ganglion in various species of mammals. *Arch Sci Biol (Bologna)*, 56(2), pp.91-96.
- Tylstedt, S., Kinnefors, A. & Rask-Andersen, H., 1997. Neural interaction in the human spiral ganglion: a TEM study. *Acta Otolaryngol*, 117(4), pp.505-12.
- Tylstedt, S. & Rask-Andersen, H., 2001. A 3-D model of membrane specializations between human auditory spiral ganglion cells. *J Neurocytol*, 30(6), pp.465-73.
- Undurraga, J.A., Carlyon, R.P., Wouters, J. & van Wieringen, A., 2013. The polarity sensitivity of the electrically stimulated human auditory nerve measured at the level of the brainstem. *J Assoc Res Otolaryngol*, 14(3), pp.359-77. Available at: <http://dx.doi.org/10.1007/s10162-013-0377-0>.
- van den Honert, C. & Stypulkowski, P.H., 1984. Physiological properties of the electrically stimulated auditory nerve. II. Single fiber recordings. *Hear Res*, 14(3), pp.225-43.
- van den Honert, C. & Stypulkowski, P.H., 1986. Characterization of the electrically evoked auditory brainstem response (ABR) in cats and humans. *Hear Res*, 21(2), pp.109-26.
- van den Honert, C. & Stypulkowski, P.H., 1987. Temporal response patterns of single auditory nerve fibers elicited by periodic electrical stimuli. *Hear Res*, 29(2-3), pp.207-22.
- van Kempen, G., 1999. Image Restoration in Fluorescence Microscopy. PhD - Thesis, Delft University of Technology, Delft University Press.
- van Rienen, U. et al., 2005. Electro-Quasistatic Simulations in Bio-Systems Engineering and Medical Engineering. *Advances in Radio Science*, 3, pp.39-49.
- Van Spaendonck, M.P. et al., 2000. High resolution imaging of the mouse inner ear by microtomography: a new tool in inner ear research. *Anat Rec*, 259(2), pp.229-36.
- van Wieringen, A., Carlyon, R.P., Macherey, O. & Wouters, J., 2006. Effects of pulse rate on thresholds and loudness of biphasic and alternating monophasic pulse trains in electrical hearing. *Hear Res*, 220(1-2), pp.49-60. Available at: <http://dx.doi.org/10.1016/j.heares.2006.06.015>.
- Veninga, T., Huisman, H., van der Maazen, R. & Huizenga, H., 2004. Clinical validation of the normalized mutual information method for registration of CT and MR images in radiotherapy of brain tumors. *J Appl Clin Med Phys*, 5, pp.66-79.
- Von Békésy, G., 1952. Gross Localization of the Place of Origin of the Cochlear Microphonics. *Journal of the Acoustical Society of America*, 24, pp.399-409.
- von Ilberg, C.A. et al., 2011. Electric-acoustic stimulation of the auditory system: a review of the first decade. *Audiol Neurootol*, 16 Suppl 2, pp.1-30. Available at: <http://dx.doi.org/10.1159/000327765>.
- Wangemann, P. & Schacht, J., 1996. Homeostatic mechanisms in the cochlea. In *Springer Handbook of Auditory Research: The Cochlea*. Springer-Verlag New York, Inc.
- Weinstein, M. & Castleman, K., 1971. Reconstruction 3-D Specimens from 2-D Section Images. *Proc. SPIE 0026, Quantitative Imagery in the Biomedical Sciences I*, 131, pp.-.
- Weisz, C., Glowatzki, E. & Fuchs, P., 2009. The postsynaptic function of type II cochlear afferents. *Nature*, 461(7267), pp.1126-29. Available at: <http://dx.doi.org/10.1038/nature08487>.

- Weisz, C.J.C. et al., 2012. Synaptic transfer from outer hair cells to type II afferent fibers in the rat cochlea. *J Neurosci*, 32(28), pp.9528-36. Available at: <http://dx.doi.org/10.1523/JNEUROSCI.6194-11.2012>.
- Wever, E. & Bray, C., 1930. Action Currents in the Auditory Nerve in Response to Acoustical Stimulation. *Proc Natl Acad Sci U S A*, 16(5), pp.344-50.
- WHO, 2013. Deafness and hearing loss. Available at: <http://www.who.int/mediacentre/factsheets/fs300/en>, access on: June 26, 2013
- Wilson, B., 2004. Engineering Design of Cochlear Implants. In: *Cochlear Implants: Auditory Prostheses and Electric Hearing*. New York: Springer.
- Wilson, B.S. & Dorman, M.F., 2008. Cochlear implants: current designs and future possibilities. *J Rehabil Res Dev*, 45(5), pp.695-730.
- Woo, J., Miller, C.A. & Abbas, P.J., 2009a. Biophysical model of an auditory nerve fiber with a novel adaptation component. *IEEE Trans Biomed Eng*, 56(9), pp.2177-80. Available at: <http://dx.doi.org/10.1109/TBME.2009.2023978>.
- Woo, J., Miller, C.A. & Abbas, P.J., 2009b. Simulation of the electrically stimulated cochlear neuron: modeling adaptation to trains of electric pulses. *IEEE Trans Biomed Eng*, 56(5), pp.1348-59. Available at: <http://dx.doi.org/10.1109/TBME.2008.2005782>.
- Worrall, D., 2000. The Physiology of Hearing. Online from: The Physics and Psychophysics of Sound & Music. Available at: <http://www.avatar.com.au/courses/PPofM/index.html>, access on: August 11, 2013.
- Wright, A. et al., 1987. Hair cell distributions in the normal human cochlea. A report of a European working group. *Acta Otolaryngol Suppl*, 436, pp.15-24.
- Yadav, P., 2003. *Histology*. Discovery Publishing House.
- Yi, E., Roux, I. & Glowatzki, E., 2010. Dendritic HCN channels shape excitatory postsynaptic potentials at the inner hair cell afferent synapse in the mammalian cochlea. *J Neurophysiol*, 103(5), pp.2532-43. Available at: <http://dx.doi.org/10.1152/jn.00506.2009>.
- Young, E., 1998. The cochlear nucleus. In: *The Synaptic Organization of the Brain*. New York: Oxford Univ. Press.
- Young, B. & Heath, J., 2000. *Wheater's Functional Histology: A Text and Colour Atlas*. 4th ed. Elsevier Limited.
- Young, E. & Sachs, M., 1979. Representation of steady-state vowels in the temporal aspects of the discharge patterns of populations of auditory-nerve fibers. *J Acoust Soc Am*, 66(5), pp.1381-403.
- Yu, N. & Zhao, H.-B., 2009. Modulation of outer hair cell electromotility by cochlear supporting cells and gap junctions. *PLoS One*, 4(11), p.e7923. Available at: <http://dx.doi.org/10.1371/journal.pone.0007923>.
- Zeng, F., 2004. Past, Present, and Future. In: *Cochlear Implants: Auditory Prosthesis and Electric Hearing*. New York: Springer.

Zeng, F.-G. et al., 2005. Speech recognition with amplitude and frequency modulations. Proc Natl Acad Sci U S A, 102(7), pp.2293-98. Available at: <http://dx.doi.org/10.1073/pnas.0406460102>.

Zenner, H., 2005. Die Kommunikation des Menschen. In: Physiologie des Menschen. 29th ed. Heidelberg: Springer.

Zheng, J. et al., 2000. Prestin is the motor protein of cochlear outer hair cells. Nature, 405(6783), pp.149-55. Available at: <http://dx.doi.org/10.1038/35012009>.

Zhu, Z. et al., 2012. Cochlear-implant spatial selectivity with monopolar, bipolar and tripolar stimulation. Hear Res, 283(1-2), pp.45-58. Available at: <http://dx.doi.org/10.1016/j.heares.2011.11.005>.

Curriculum Vitae

Personal Data

Name Thomas Potrusil
Nationality Austria
Date and 22.03.1979
Place of birth Freistadt, OÖ, Austria
Email thomas.potrusil@gmx.at

Education

2007 - 2009 Master program ‚Biomedical Engineering Sciences‘ at the University of Applied Sciences Technikum Wien with a focus on Medical Engineering, passed with merit
2004 - 2007 Bachelor program ‚Biomedical Engineering‘ at the University of Applied Sciences Technikum Wien with a focus on Medical Engineering

Professional Experience

Since 2010 Project Assistant (FWF), Laboratory for Inner Ear Biology, Innsbruck Medical University
Projekt: Human Cochlea Nerve Model (FWF number: P21848)
2007 - 2010 Carl Reiner GmbH, Vienna. Research & Development in the field of Superimposed Highfrequency Jet Ventilation

Publications

Journals

Frank Rattay, Thomas Potrusil, Cornelia Wenger, Andrew K. Wise, Rudolf Glueckert, Anneliese Schrott-Fischer, 2013. Impact of Morphometry, Myelination and Synaptic Current Strength on Spike Conduction in Human and Cat Spiral Ganglion Neurons. PLOS ONE (accepted at September 23, 2013)

Potrusil, T., Wenger, C., Glueckert, R., Schrott-Fischer, A., Rattay, F., 2012. Morphometric Classification and Spatial Organization of Spiral Ganglion Neurons in the Human Cochlea: Consequences for Single Fiber Response to Electrical Stimulation. Neuroscience, 12;214:120-135

Schnabl, J., Glueckert, R., Wolf-Magele A., Feuchtner, G., Recheis W., Potrusil, T., Schrott-Fischer A., Riechelmann, H., Sprinzl, G., 2011. Sheep as an Animal Model for Middle- and Inner Ear Implantable Hearing Devices: A Feasibility Study. Otology & Neurotology, 33(3):481-489

Bitsche, M., Dudas, J., Roy, S., Potrusil, T., Schmutzhard, J., Schrott-Fischer, A., 2011. Neurotrophic receptors as potential therapy targets in postnatal development, in adult, and in hearing-loss-affected inner ear. Otology & Neurotology, 32(5):761-73

Oral Presentations

Potrusil Thomas, Wenger C, Kuhn V, Glueckert R, Schrott-Fischer A, Rattay F. Imaging the Human Cochlea using micro-CT: Tracing of Human Cochleas Neuron Fiber Bundles an Development of a Finite Element Model. Wissenschaftstag der Universitätsklinik für HNO Innsbruck, Krankenhaus Hochzierl, Austria, 26.11.2012

Thomas Potrusil, Cornelia Wenger, Rudolf Glueckert, Frank Rattay, Anneliese Schrott-Fischer. The Unmyelinated Perikarya of Human Spiral Ganglion Neurons: Impact on Action Potential Propagation. Neuroscience Day 2012 of the Innsbruck Medical University & the University of Innsbruck. Grillhof, Innsbruck, Austria, 20.04.2012

Potrusil Thomas, Wenger C, Glueckert R, Schrott-Fischer A, Rattay F. Morphological differences and distributions of spiral ganglion cells in the human cochlea and simulation of single neuron response to microstimulation Wissenschaftstag der Universitätsklinik für HNO Innsbruck, Stift Stams, Austria, 14.10.2011

Potrusil T, Wenger C, Glueckert R, Schrott-Fischer A, Rattay F. Morphometrical Differences of Human Spiral Ganglion Cells: What does it mean for Electrical Stimulation? 48th Inner Ear Biology Workshop 2011, Lisbon, Portugal, 18th to 21st September 2011

Potrusil Thomas. Human Cochlea Nerve Model: Data Collection and Simulation. Wissenschaftstag der Universitätsklinik für HNO Innsbruck, Stift Stams, Austria, 29.10.2010

Poster Presentations

T. Potrusil, C. Wenger, F. Rattay, V. Kuhn, R. Glueckert, A. Schrott-Fischer. Acquisition and Implementation of 3D-Data from Human Cochlear Neurons Fiber Bundles using μ CT-Imaging. 8th Meeting of Doctoral Students, Innsbruck, Austria, 05.10.2012

Potrusil T., Wenger C., Glueckert R., Rattay F., Schrott-Fischer A. Perisomatic Myelinization Of Human Spiral Ganglion Neurons: Impact On Action Potential Propagation. 8th FENS Forum for Neuroscience, Barcelona, Spain, 14.-18.07.2012